Koutsonas, Spiridon (2015) Race-track modelling and variability in RTM for advanced composites structures. PhD thesis, University of Nottingham.

Division of Materials, Mechanics & Structures

Faculty of Engineering

*"*Race-track modelling and variability in RTM for advanced composites structures*"*

by

Spiridon Koutsonas

MRes(Phy)

Thesis submitted to The University of Nottingham

for the degree of Doctor of Philosophy

April 2015

Spiridon Koutsonas

Abstract

The Resin Transfer Moulding (RTM) process is one of the most common manufacturing routes for composites. The challenge in the present work is to be able to predict the flow behaviour in order to manufacture advanced composites truss structures. To that end, there is a lack of an advanced simulation tool capable to predict void formations for the manufacture of three dimensional, multi-layer woven textile composites like the Advanced Composites Truss Structure (ACTS) generic node TSB-funded project that is presented in this thesis. Industrial experience has shown that during mould filling, due to race-tracking and stochastic variability in the material properties, the filling patterns and arising cycle times are rarely the same between a given set of apparently identical mouldings.

The objectives of this thesis were 2D, 3D racetrack prediction of textile reinforcements for RTM processes and 3D variability prediction at the component scale. A model that predicts the resin rich zone along a component edge was developed for this purpose. The issue of 2D, 3D racetrack prediction was firstly investigated along a 90° edge for three different geometry, architectures and material preforms, on a generic composite node 3D. Variability was also investigated through the same CAD model with the use of the FE/CV technique.

A novel numerical approach for 3D FE CAD modelling was developed in order to predict race-tracking and variability for advanced composites structures. A stochastic analysis technique was developed to account for the effect of node

variability during the fabrication process by RTM. The study based on this technique provided important insights into flow filling variations, voidage formation and optimization on a generic advanced composite truss structure.

The model developed from this work can be used to account for the effects of race-tracking and variability on any other composite component at the macroscale level. The predicted race-track and variability data can complement experimental data in order to enhance flow simulations at the component scale.

"Dedicated to my Father, Mr Georgios Koutsonas"

(1939-2007)

Acknowledgements

Sincere thanks are extended to my supervisor of this project, Prof. Andrew Long for giving me the opportunity to work on composite materials and particularly on modelling variability and race-tracking topics in which I am interested.

Furthermore, I would like also to express my sincere gratitude to Mr Roger Smith our ex laboratory technician (in retirement), and Dr Kok H. Wong, Dr Kevin Brown, Dr Tom Turner and all members of the Polymer Composites Group at the University of Nottingham. Moreover, I want to acknowledge with gratefulness the support of my family and in particular the encouragement of my mother Maria Koutsona and my brother Dr Yannis Koutsonas. Undoubtedly, without them I would not have been here today.

Finally, the financial support of the Technology Strategy Board (TSB) and all industrial partners Airbus, Bentley Motors Ltd, Composites Integration Ltd, Network Rail, NP-Aerospace, Pipex, QinetiQ, Tony Gee, Sigmatex, Oxford Brooks University and of course The University of Nottingham on the ACTS project are greatly acknowledged.

Table of contents:

Chapter 1: Background

Chapter 2: Literature review

Chapter 5: Fabric bending model development

Chapter 6: Analysis of flow for a 90° curved plate

Chapter 7: **Node modelling**

Chapter 8: **Node variability modelling**

Chapter 9: Node manufacturing

Chapter 10: Conclusions and future work

Appendix : A Publications and achivements

Abbreviations

ACTS…..Advanced Composites Truss Structures

BEM.…………..Boundary Element Method

CFRP………………………………………...…..Carbon Fibre Reinforced Plastics

CRTM...Compression Resin Transfer Moulding

CV/FE...Control Volume /Finite Element method

DCFP……………………….........................Directed Carbon Fibre Preforming

DSC..Differential Scanning Calorimetry

FCDD………………………………...Fibre Composites Design and Development

FEM.…………...Finite Element Method

FDM...Finite Difference Method

GFRP…………………………………………..Glass Fibres Reinforced Plastics

I/CM..Injection/Compression Moulding

LCM…………………………………………….Liquid Composite Moulding

RTM...Resin Transfer Moulding

NDT...Non Destructive Testing

SD...Standard Deviation

VARTM...Vacuum Assisted Resin Transfer Moulding

Nomenclature

A   Area   m^2

α   Empirical material constant   -

α_c	Empirical material constant	-
β	Empirical material constant	-
C	Kozeny-Carman constant	m^2
D_p	Diameter	m
ε_r	Sphericity	-
f	Force	N
H	Fabric thickness (height)	m
h	Distance between upper moulder wall and fabric	m
K	Permeability	m^2
$[K]$	Permeability tensor	m^2
K_1	In-plain Warp/Weft permeability	m^2
K_2	In-plain Warp/Weft permeability	m^2
K_3	Through-thickness permeability	m^2
L	Height	m
m	Mass	Kg
v_0	Superficial velocity	m/s
P	Pressure	Pa
r	Radius	m
t	Time	sec
t_{ff}	Analytical filling time	sec
V_f	Fibre volume fraction	-
$\vec{V}$	Velocity vector	m/s
u	Darcy's velocity	m/s
μ	Viscosity	Pa s
θ	Angle between Warp direction and K_1 flow direction	deg
φ	Angle of preform bending	deg
Φ	Porosity	-
ρ	Density	Kg/m^3
x_{ff}	Filling distance	m
x, y, z	Cartesian coordinates	-

Chapter 1

1. Background

1.1 Introduction

Over the last few years economic pressure and increasingly stringent environmental requirements have increased the usage of polymer composite materials in industrial applications such as vehicles, aircraft substructures and rail footbridges. This is primarily due to their advantageous properties, namely they are lightweight have very good mechanical properties and are resistant to corrosion, which when combined with new cost-effective (or improved existing) manufacturing techniques, make such materials attractive for a wide range of applications in industry as mentioned by Advani, S. G., [1].

Polymer composites manufacturing techniques may be categorized into three groups:

i)   techniques that involve short fibre suspension flows (e.g. injection, compression moulding)

ii) those that utilise sheets containing preimpregnated highly viscous resins (thermoplastics or partially cured thermosets)

iii) manufacturing processes with the use of flow through porous media

The first group is the manufacturing of composites with the use of fibre processes and involves the transport of fibres and resin as a suspension into a mould or through a die to form the composite final shape.

The second group involves preimpregnated reinforcements or prepregs. Here resin and fibres deform together under high applied pressure in order to form

the desired final composite shape. The last group are well known as liquid moulding processes and contain continuous and nearly stationary fibre networks into which a viscous resin is impregnated in a mould in order to displace the air inside the reinforcement forming a composite. The last process may take place on an open or closed mould studied by Advani, S. G., [1] and Rudd, C. D., et al [2].

The resin transfer moulding (RTM) process belongs to this category that involve porous media and out of a considerable number of competing processing methods, it has the potential of becoming the dominant relatively low-cost process for the fabrication of large, high performance products. Advantages of RTM over alternative manufacturing processes like VARTM and compression moulding, include for example: design flexibility with a good surface finish, high number production, the incorporation of pressure transducers and inserts in order to monitor the flow front during manufacturing process, a tight control over fibre placement and resin volume fraction and the possibility of embedding sensors into manufactured components for structural health monitoring, control of dimensional tolerances, lower material waste. Disadvantages include: the higher tool cost, the greater tooling design and construction skills required, complex mould design and reinforcement loading that may be difficult with complex parts. But generally the main reason that this process has not received widespread usage is primarily due to its relatively trial and error nature, racetracking, washout, high cycle time and void formation. The basic operation of the RTM process involves loading a fibre reinforcement preform into a mould cavity, closing the mould, injecting resin

into the mould and allowing the resin to cure reported by Wong, C. C., [3] and Shojaei, A., et al [4].

Advanced Composites Truss Structures (ACTS) was a multi-sector collaborative research project with the following aims:

- Characterise permeability of candidate 3D woven reinforcement

- Characterise variability in preform architecture and permeability: local tow waviness, variable compaction, race-tracking

- Develop stochastic modelling methodology incorporating the above defects within resin flow simulations

These attributes are preferred in order to develop, an understanding of likelihood of defect formation within 3D woven composites, demonstrate and validate above issues for the ACTS generic node.

Collaborative ACTS partners were the Technology Strategy Board (TSB) and industrial partners Airbus, Bentley Motors Ltd, Composites Integration Ltd, Network Rail, NP-Aerospace, Pipex, QinetiQ, Tony Gee, Sigmatex Ltd, Oxford Brooks University, and The University of Nottingham.

Design and geometrical details for the ACTS generic Node are as following and can be shown in Fig. 1.1(a), 1.1(b), 1.2.

- Bond length: 150 mm

- Strut dimension: Square 51.8 mm (2.00") as shown Fig. 1.1(a)

- Fillet radius at internal corners: 3.2 mm (Lower moulder moulder)

- Fillet radius at external corners: 5.95 mm (Upper moulder surface)

- 8 layers thickness = 5.5mm
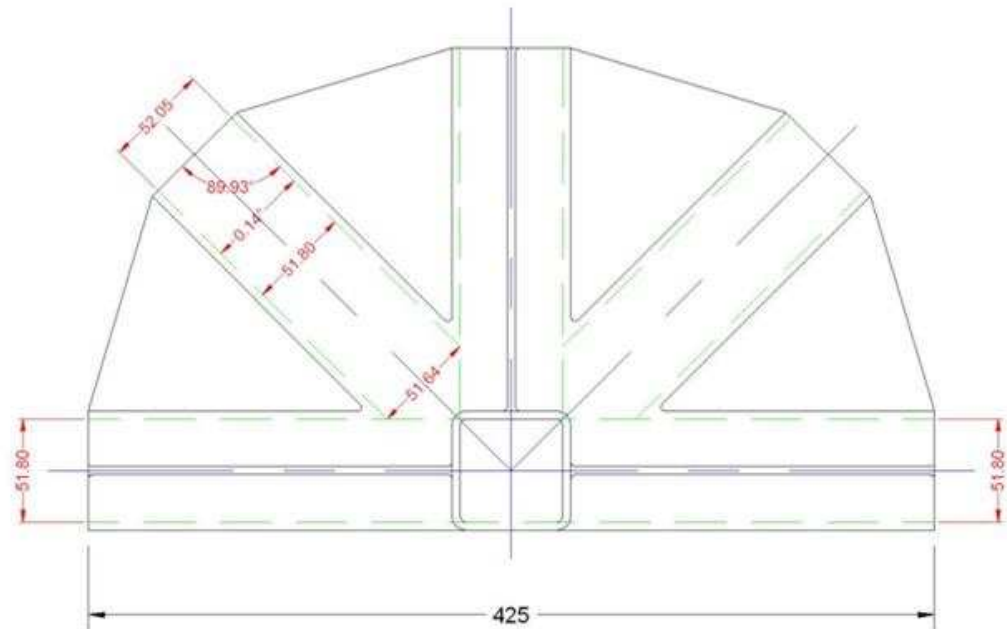
Fig. 1.1 (a): ACTS generic node length in mm upper view.
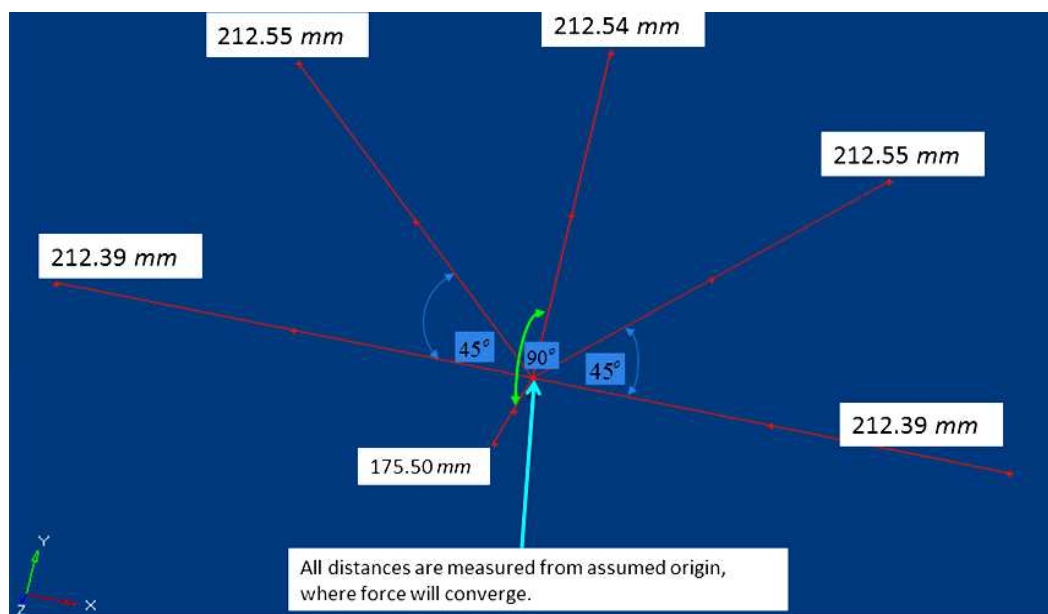
Fig. 1.1 (b): ACTS generic node angular and length dimensions.
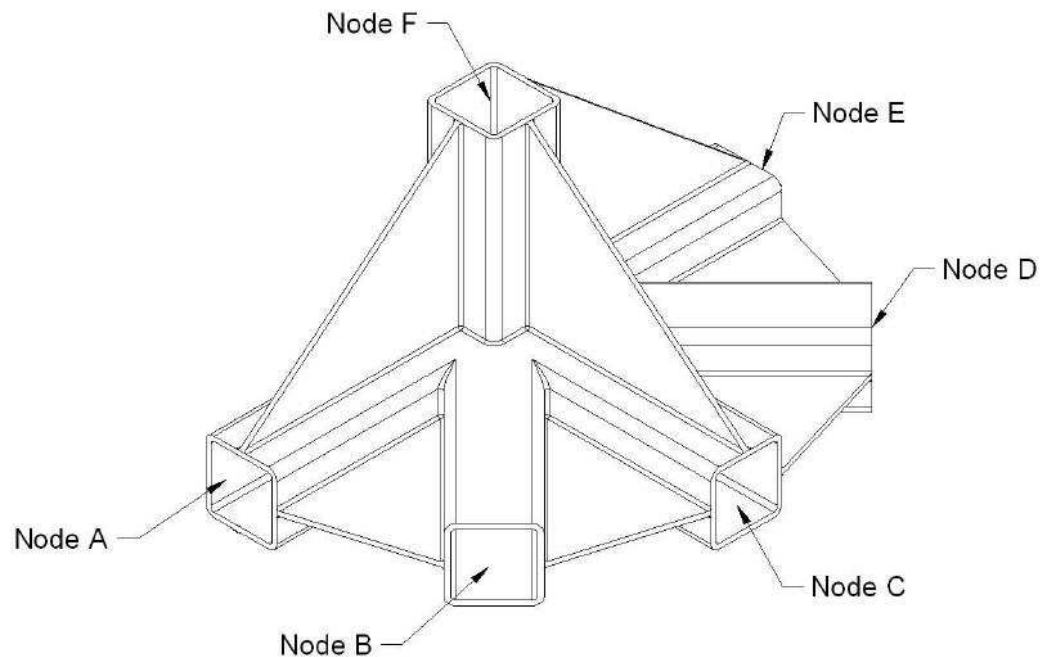
Fig. 1.2: ACTS generic node strut members A to F.

Construction materials of the generic node:

In the ACTS project the preform for the generic node is 3D woven using yarns made of 12K High Tensile Strength (HTS) carbon fibre. Yarns were manufactured by Toho Tenex and commercially known as Tenax®HTS40 F13. The 3D woven preform was impregnated in an epoxy based resin system, commercially known as ACG MVR444® and manufactured by Advanced Composites Group Ltd (Now Cytec). All material properties are presented from the manufactured web site [5, 6].

The fabrication of the generic node was performed using the RTM process. The preform was assembled from HTS40 F13 (8-layers) and the sockets

created from the textile manufacturer (Sigmatex Ltd). The mould is as shown

in Figures 1.3, 1.4,

Fig. 1.3: ACTS generic node preform with HTS40 F13.
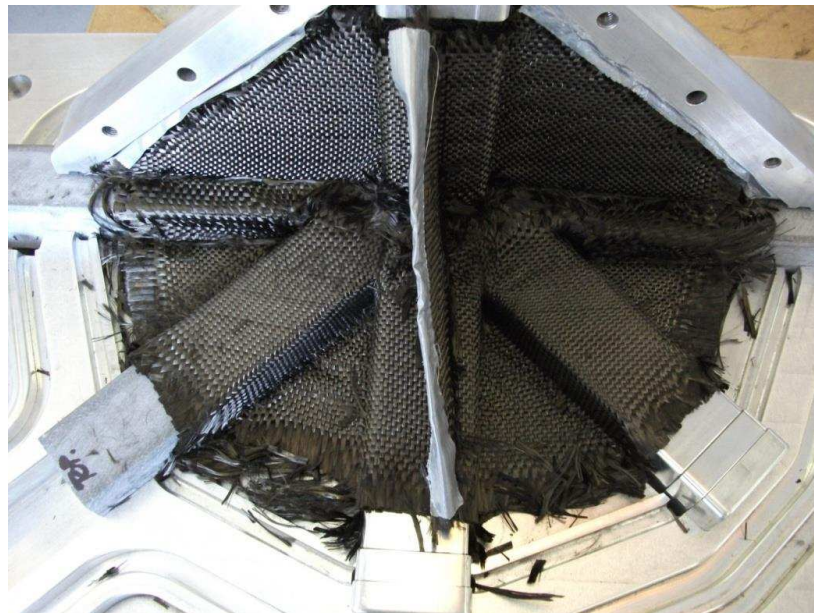
Fig. 1.4: Top view of ACTS generic node HTS40 F13 fabric inside the moulder before injection moulding.

with fabric thickness as shown in Figures 1.5, 1.6.

Colour	No. of Layers (mm)
	3=2.06mm
	4=2.75mm
	6=4.13mm
	8=5.5mm
	Pi Clip

Scale 1:5
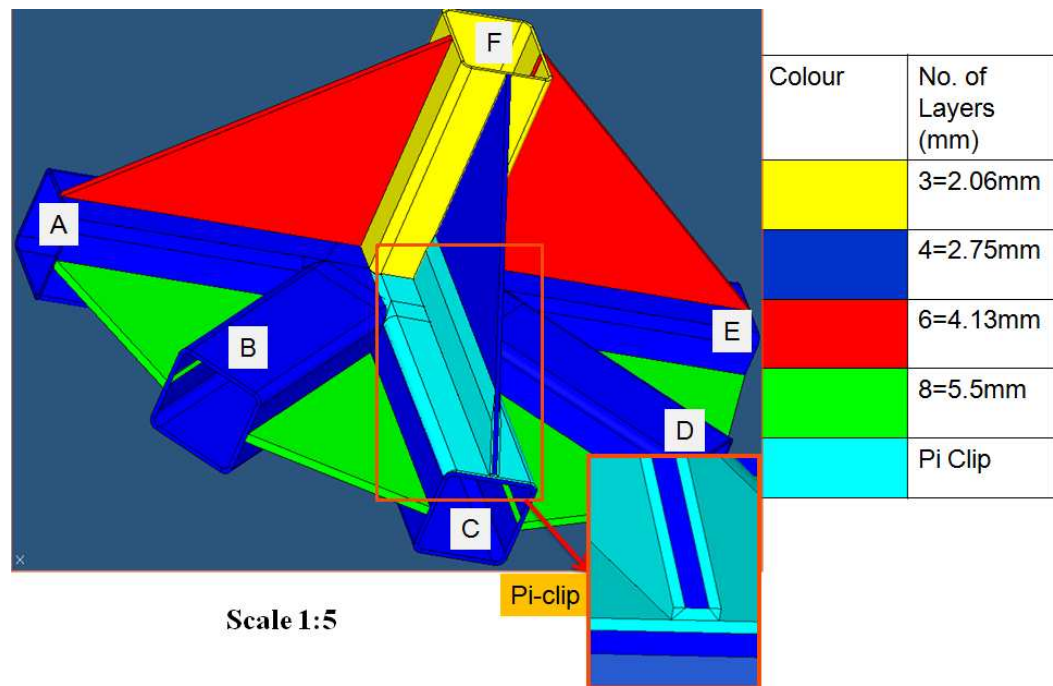
Fig. 1.5: ACTS generic node CAD model showing the reinforcement layers distribution.

In order to hold the front upright flange on the shear web of the generic node it is fixed with a 'pi clip' see Fig. 1.6. Node members C and F are bonded. Node members A/E, B and D are directly connected and four layers HTS40 F13 fabric are used. The height of the 'pi clip' is 2.75±0.05mm, of 2 layers. The horizontal layers are blend into the corner radius. All flanges to wall sections have a 1.0mm radius as shown in Fig. 1.6.
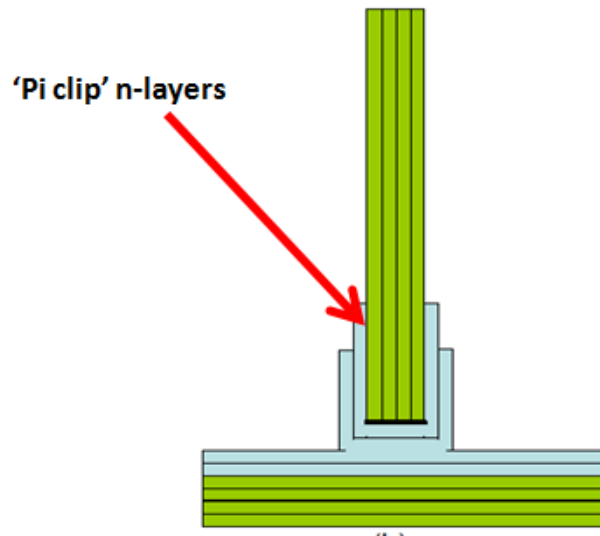
Fig. 1.6: Schematic representation of 'Pi clip' geometry and number of layers with the 3D woven HTS40 F13 reinforcement.

The characterization of preform permeability and race-tracking are considered to be the key parameters in the fabrication of a composite part. It can be shown that assuming an incompressible Newtonian liquid the flow behaviour of resin during liquid infusion is governed by Darcy's law [7]:

$$\bar{u} = -\frac{1}{\mu}[K]\nabla P \qquad \text{(1-1)}$$

which calculates the flow of the fluid through the fabric by relating the velocity to the pressure drop, and the fabric's permeability which is resistance to flow. The permeability is actually a second order tensor, meaning its value depends on the direction of the flow.

On (1-1) equation $\bar{u}$ is the fluid velocity, μ is the resin viscosity, [K] the permeability tensor and ∇P is the pressure gradient. The minus sign in front of this equation is stated to indicate that the flow is produced by a pressure drop.

In this research work the experimentally measured permeability of three preforms will be assessed in the framework of Darcy's law through the

application of the ESI PAM-RTM® software in order to simulate the fluid flow behaviour firstly for a 90° curve plate and secondly for the node in the ACTS project [8].

1.2 Motivation

In this research the phenomenon of race-tracking and variability during the RTM manufacturing process of a generic node is studied.

To date very little was understood regarding local permeability i.e. the relationship between racetrack and variability to the reinforcement structure for a successful subsequent composite manufacturing process.

The main motivation on this project was to develop, validate and apply simulation tools for race-tracking and variability for RTM during the manufacturing process, and model the flow behaviour of the resin as the node is manufactured.

With this in mind, a new method, able to predict race-tracking and variability computationally has been developed in order to represent new classes of composite materials for the study of the internal structure and the determination of the fundamental material properties. Therefore, by the end of this investigation it will be possible to validate and predict with good accuracy the preform local permeability that causes race-tracking and void formation due to flow behaviour for the node and any other component.

This work has also addressed some other aspects of RTM, ranging from the physics of flow behaviour in 2D, 3D flow modelling capabilities and manufacturing reliability issues.

Furthermore the necessary materials such as 3D woven carbon fabric HTS 5631 800tex (also known as HTS40 F13 the 2/2 twill (carbon 12K) and triaxial (E-glass stitched) were also studied. Through these the flow behaviour, race-tracking and variability for a novel generic component and material combination was investigated and simulated.

1.3 Thesis overview

The Thesis consists of 10 Chapters.

Chapter 1: Gives a general introduction and background to the research subject in addition to motivation and Thesis overview.

Chapter 2: Contains the literature review.

Chapter 3: The compaction behaviour was experimentally determined and fitted with an empirical power law model for each of the tested fabrics. The bending behaviour of each fabric was measured. Compaction tables made it possible to predict the gap between the fabric and the mould wall where race-tracking would occur.

Chapter 4: Experimental determination of the 3D permeability, (K_1, K_2, K_3) of the 3 different fabrics followed by fitting of a power law model in order to be able to predict the permeability of the above fabrics at any V_f.

Chapter 5: A model was developed in order to predict the compaction behaviour of the fabric along the 90° angle bend. The model was then fitted with experimental compaction behaviour data of preforms to allow the race-tracking gap to be predicted.

Chapter 6: A transparent tool (with a 90° curved plate cavity) was designed and fabricated. The flow behaviour of the three textiles were tested experimentally with a known viscosity commercial oil. The latter was performed with the use of two web cams connected with a personal computer so that the flow could be recorded.

Race-tracking was modelled for 2D, 3D models on 90°angle preform bending. For 3D a number of models were created with three racetrack zones (top part higher local permeability) and three zones with higher volume fractions V_f (lower part local permeability) under the racetrack channel. The gap height of the 3D models was determined by taking into account the experimental gap statistical distributions from the bending experiments (Chapter 3). Simulated flows of the FE CAD models were compared with experimental investigation results with the Perspex tool.

Chapter 7: 2D, 3D CAD node models were designed and meshed for the node. Then the node was simulated firstly with ACTS 2D, 3D woven carbon fabric material properties for the isotropic and with 3D anisotropic case. Furthermore for the anisotropic case possible

void formation were identified from converging flow fronts within the node geometry.

Chapter 8: A new 3D node CAD model was created with a modified mesh in order to represent twenty-three racetrack node curve plate zones of the structural elements A, B, C, D, E, and F, and a random gap number generator for each zone represented the variability for each fabric based on bending measurements from Chapter 3. The node was then simulated for the detection of void formation with PAM-RTM software with material properties calculated from Chapters 3, 4. Node variability, frequency of void formation, void volume, and number of voids were predicted for ten cases on each of the three different fabrics. Finally an optimisation process was considered for the worst case filling output (i.e. the case with the maximum void volume and the highest unfilled area). Injection gates were modified and extra vents were positioned on the node for these cases and the simulations were repeated. The whole process was repeated until the total void formation was reduced significantly in volume (m^3) for the ACTS generic node.

Chapter 9: The ACTS node mould tool was modified and node prototypes were successfully manufactured.

Chapter 10: Here conclusions from Chapters 1-9 are discussed and finite mesh is proposed.

1.4 Conclusions

Summarising Chapter 1 of this thesis, this research aims to develop a model in order to be able with simulation tools to:

1. Predict the 2D, 3D local permeability and its variation as a function of the textile bending deformation along the edge of any reinforcement;

2. Predict the 3D variability of a generic node reinforcement, based on its internal complex geometry, by taking in to account twenty three 90° edges for the node where race-tracking can occur;

3. Optimize void formation due to converging flow front during resin filling of the generic node by considering the above cases for the node geometry;

4. Extend this research in order to be able to predict and optimize the race-tracking and variability during the manufacturing of any composite at component scale.

References

[1]Advani, S. G., "Flow and Rheology in polymer composites manufacturing" Elsevier Science B.V. All right reserved 1994; p 466-479, ISBN: 0 444 89347 4.

[2]Rudd, C.D., Long, A.C., Kendall, K.N., Mangin, C.G.E., "Liquid moulding technologies. Resin transfer moulding, structural reaction injection moulding and related processing techniques." Woodhead Publishing, 1997; p 254-280, ISBN 1 85573 242 4, Society of Automotive Engineers ISBN: 0 7680b0016 5.

[3]Wong, C.C.,"Modelling the effects of textile preform architecture on permeability." PhD Thesis, University of Nottingham 2006.

[4]Shojaei, A., Ghaffarian, S.R. and Karimian, S.M.H., "Modeling and *Simulation Approaches in the Resin Transfer Molding Process: A Review"*, Polymer Composites, Vol. **24**, No.4: (2003); p 525-544.

[5]http://www.tohotenaxamerica.com/products/pls020.pdf "Last accessed 13.07.2014".

[6]http://www.advancedcomposites.co.uk/data_catalogue/catalogue%20files/p ds/PDS1190_MVR444_Issue1a.pdf "Last accessed 13.07.2014".

[7]Darcy, H., "Les Fontaines Publiques de la Villa de Dijon 1856'', http://biosystems.okstate.edu/darcy/index.htm "Last accessed 13.07.2014".

[8]www.esi-group.com "Last accessed 19.09.2014".

Chapter 2

Literature Review

2.1 Composite Materials

Composite materials are engineered materials made from the combination of at least two different materials that are distinct on a microscopic level while forming a single component. Generally composites comprise a reinforcement part and a binding material called the matrix. These materials may be typically from glass fibres and polyester, resin or carbon fibres and epoxy resin presented by Campbell, F.C., [1].

Products made from composite materials can offer significant benefits because of their characteristically low weight, good mechanical properties and excellent resistance to corrosion. For example, composites used in cars can reduce the overall weight of the car and so offer fuel savings through the lifetime of the vehicle. In civil and aerospace applications, development of composite structures is advancing as mentioned Advani, S. G., et al [2] and presented by Long, A. C., [3].

2.2 Polymer Matrix

Polymer matrix consists of polymeric chains which are made up of 10^3 to 10^6 monomer units, assembled through chemical reactions. The type of bond formed between these chains, categorises the polymer matrix as either a thermoplastic or a thermoset. Thermoplastics are materials that do not undergo chemical change in their composition when heated and can be moulded again

and again. Thermosets can take shape once; after they have cured, they stay solid. In the thermosetting process, a chemical reaction occurs that is irreversible Elias, H-G., [4].

Thermosets offer high quality composites with better mechanical properties and better thermal stability compared to thermoplastics; hence, they are used widely in the composites industry. However, they undergo chemical reactions during curing, an irreversible process in which the matrix is thermally and chemically activated to form strong covalent bonds and cross-links between polymer chains Foote, B., et al [5], Carey, F. A., [6].

2.3 Textile reinforcements

Textile reinforced composites are structured fibre materials; they are a subclass of composites where the reinforcement is the material that comprises natural or artificial fibres, typically arranged in tows or yarns. Textiles are formed by weaving, knitting, braiding, crocheting, knotting or pressing fibres together. Most fabrics can bend and fold easily. The name textile was originally reserved only for woven fabrics but nowadays comprises all fibres, filaments and yarns, natural or synthetic and in any textile fibres are assembled first into yarns [7].

In hierarchical terms we may distinguish three scales (i) fibres at microscopic scale, (ii) yarn repeat at mesoscopic scale, (iii) fabric at macroscopic scale Long, A. C., [3].

The diversity of textile technologies has resulted in a large variety of available textile geometries.

The simplest of fabrics consist of warp and weft yarns, interlaced to form a self-supporting textile structure. There are a number of possible interlacing patterns, of which in the plain weave warp yarns interlaces with weft yarns. For the plain wave each weft thread crosses the warp threads by going over one, then under the next, and so on. The next weft thread goes under the warp threads that its neighbour went over, and vice versa.

More complex interlacing patterns for 2D woven fabric can be categorised as twill, satin etc. A twill weave is the second most basic weave that can be made on a fairly simple loom. In a twill weave, each weft or filling yarn floats across the warp yarns in a progression of interlacing to the right or left, forming a distinct diagonal line called a 'wale'. A float is the portion of a yarn that crosses over two or more yarns from the opposite direction.

Twill weave is often designated as a fraction, such as 2/1, 2/2 ... in which the numerator indicates the number of lifting yarns that are raised when a weft yarn is inserted.

Non-crimp fabrics consist of layers of long fibres held in place by a secondary non-structural stitching thread (usually polyester) for these materials biaxial, triaxial or even quadriaxial arrangements are possible presented by Coman F., Plast J R. [10]. Typical textiles weaves are shown in Fig. 2.1.

2D 2/1 Twill woven   2D Triaxial woven
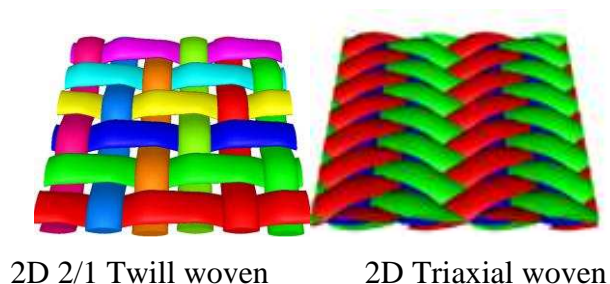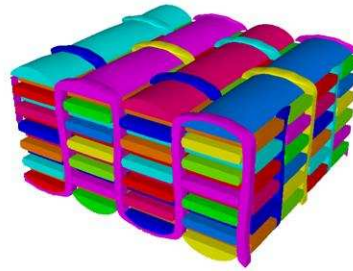
3D Orthogonal woven

Fig. 2.1: Textile Geometry of some woven fabrics [3].

According to Huang, G., and Zhong, Z., [8] 2D fabrics may be woven, knitted or non-woven. In a composite after the fabrication process, the space between the filaments and two adjacent fabric layers would be filled with resin; this would form distinctive layers in the composite. When the composite is bent, interlaminar shear force is created. Because of the lower shearing strength of the resin, delamination would become the main failure mode for 2D composites. 3D woven composites are an effective alternative for laminated products. In a 3D woven preform, layers are joined together by filaments through thickness. Therefore the preform becomes a solid entity, so it is difficult for the layers to separate. In addition 3D woven structures are arranged in weft, warp and through thickness directions, which provides strength in three directions. Thus 3D woven composites exhibit better mechanical properties in all directions than conventional 2D woven laminates as mentioned by Hill, B, J., [9]

2.4 Resin Transfer Moulding (RTM)

RTM is a common route for manufacturing complex and high quality composite parts. With RTM, initially the preform (reinforcement) is prepared and located in the mould. The mould is then closed and the preform is

compressed to a defined fibre volume fraction. The resin is injected in the mould and the reinforcement is impregnated. Finally, after cure of the resin, the mould is opened and the part is removed. If necessary, the part may be submitted to post-cure in order to reach the maximum properties. The RTM mould must have at least one vent to allow, during the injection of the resin, the exit of existing air in the interior of the mould by Li, J., [11]. In larger parts, it is common to include several vents Fig. 2.2 shows the RTM process.
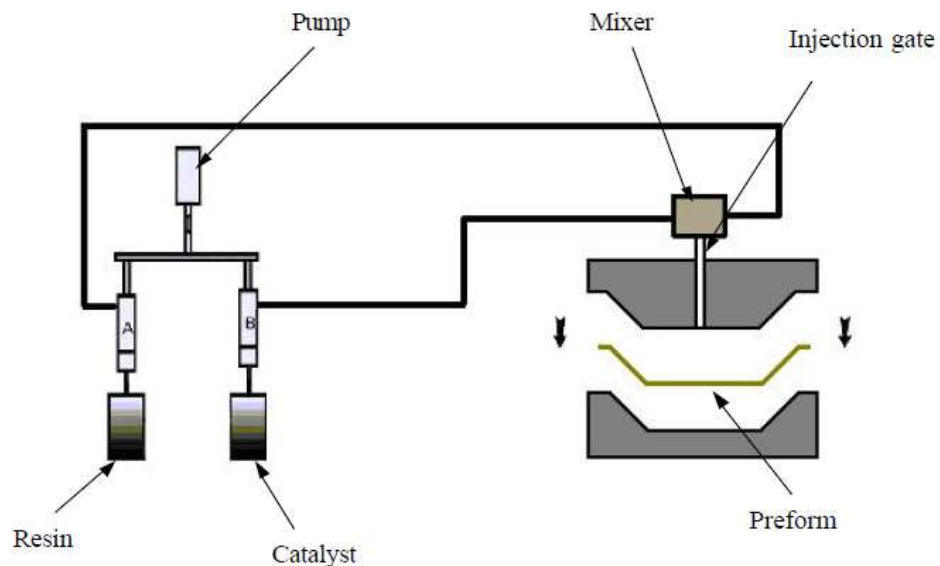
Fig. 2.2: RTM process [11].

RTM improves the manufacturing process and reduces the cost and time to manufacture, making it an increasingly common route for textile composites. Other notable advantages in using RTM are the large and complex shapes that can be made efficiently and inexpensively with better reproducibility due to the high dimensional accuracy of the mould.

The RTM process eliminates the labour and skill that is required in hand lay-up and reduces the exposure to volatile organic compounds as mentioned by Beckwith, S. W., and Hyland, C. R., [12].

The RTM process will be used for manufacture the node in ACTS. Fig. 2.3 shows the mould manufactured by Composites Integration Ltd for the fabrication of the node.

Disadvantages of the RTM process are the mould design which may be critical and expensive, and the phenomenon of race-tracking leading resin rich areas especially at the curved radii edges of the composite. Gonzalez, R., and Macosko, C. W., [13] presented a study of the process parameters estimation for structural reaction injection moulding and RTM.

The moulding of impregnation process during RTM has been studied from Chan, A.W., [14], while Lee, J., et al [15] studied the mould filling and cure modelling of RTM process.
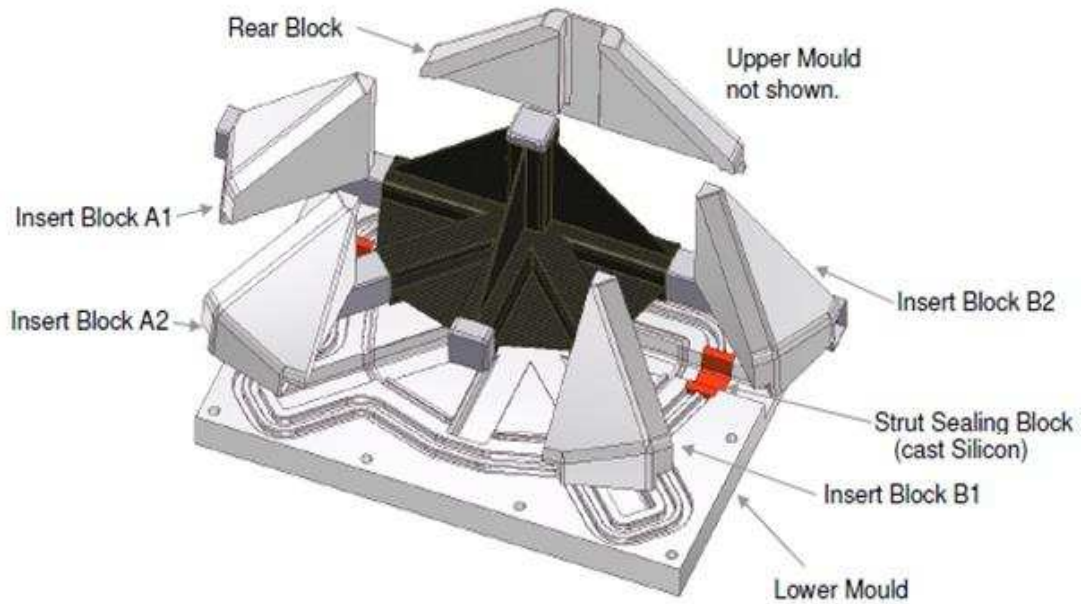
Fig. 2.3: Moulder for Composite Node in ACTS project provided by Composite Integration Ltd, with gates and vents suggested by the University of Nottingham (Chapter 9).

The RTM process has drawn a considerable amount of attention from different perspectives, and several software systems have been developed to simulate the RTM flow behaviour, optimize the process and find the best tooling design. The difficulty of obtaining the accurate permeability of the preform impedes the further development of RTM simulation packages. For flow simulation analysis, the predicted results will be valid only if accurate local permeability values for the actual material are supplied. Surface density variations, compression variations and race-tracking affect significantly the permeability for the actual process. For example, to get accurate permeability values, special care must be taken to avoid or minimize the edge effect or race-tracking; however, variability is almost always present in the actual manufacturing process. This may cause flow front variation for two identical

textile fillings on the same moulding and thus a the different voidage formation during RTM process.

 Whenever the permeability changes for the same part, the optimal set-up will also change. Hammami, A., and Gebart, B. R., [16], attempted to model the equivalent permeability by analysing the infusion moulding process under vacuum conditions. Hammami, A., and Gauvin, R., et al [17] studied the permeability change analysing the edge effect on various flow patterns in the LCM process. Bickerton, S., and Advani, S. G., [18] characterized and modelled the race-tracking in liquid composite moulding processes by taking into account the local permeability variations.

Subsequently Bickerton, S., Advani, S. G., et al [19] made an experimental analysis and numerical modelling of flow channel effects in RTM. Hubert, P., et al [20] generated a two-dimensional flow model for the process simulation of complex shape composite laminates. Brillant, M., [21] in his thesis studied the out of autoclave manufacturing of complex shape laminates.

Finally Dong, C., [22], attempted to model the permeability changes for edge effects with vacuum-assisted RTM (VARTM) at curved edges.

   Existence of race-tracking increases the errors for permeability measurement, on the other hand, race-tracking can offer benefits in real situations: the regions with race-tracking provide low resistance during resin flow and reduce the mould filling time.

2.5 Modelling and simulations of Liquid Composites Moulding (LCM)

LCM processes describe various moulding processes ranging from traditional RTM to VARTM, and other RTM variations. No matter how complex these LCM techniques are, they involve similar basic processes: mould filling and resin curing. Over the last few decades many research studies has been conducted by a series of researchers in order to model computationally LCM and predict race-tracking during filling of composites. During this period of time experiments and computational approaches has been reported in studying resin impregnation behaviour at microscopic, mesoscopic and macroscopic level. The microscopic, mesoscopic studies addressing issues like voidage due to insufficient fibre wetting caused by the local fibrous preform geometry presented by Kang, M.K., et al [23] while Patel, N., and Lee, L.J., [24] studied the effects of fibre mat architecture on void formation and removal in LCM. Binetruy, C., et al [25] studied the influence of fibre wetting in RTM.

Mesolevel analysis during the LCM process was done by Dimitrovova, Z., and Advani, S.G., [26] while Lekakou, C., and Bader, M.G., [27] provided a mathematical modelling of macro and micro-infiltration in resin transfer moulding RTM. Parnas, R.S., [28] provided insights of the interaction between microscopic and macroscopic flow in RTM.

Macroscopic process models deal with the 2D, 3D flow front filling, these models predict the flow front movement during the impregnation inside the mould geometry and try to avoid a converging flow front that may lead to air

entrapment and thus formation of voids. Simacek, P., and Advani, S. G., [29] paper described desirable features (such as design optimization and control of the impregnation process in order to avoid variability and race-tracking during the manufacturing of composites). Trochu, F., et al [30] report, on numerical simulation of liquid composite moulding for process analysis and optimization. Riuz, E., et al [31] research the optimization of injection flow rate in order to minimize micro and macro-voids formation in RTM manufacturing. Riuz, E., et al optimization was based on the analysis of the capillary number at the fluid flow front position. Once this capillary number is calculated, the injection flow rate is corrected at each time step to ensure an optimal capillary number at the flow front (i.e., the capillary number for which the fibrous preform is totally impregnated). To demonstrate the abilities of the numerical method, two test cases were presented: an isothermal and a non-isothermal three-dimensional injection optimization. The two optimizations were compared with filling simulations at constant injection pressure and flow rate. In the two tested cases, the optimization showed a minimization of the macro/micro-voids for similar filling times.

While Buntain, M. J., and Bickerton, S., [32] model forces generated within LCM tools. The authors have presented a detailed study on the evolution of total clamping force during resin transfer moulding (RTM) and injection/compression moulding (I/CM) cycles. The influence of the complex compaction response of two different reinforcements was demonstrated, showing important effects including stress relaxation, an apparent lubrication

by the injected fluid, and permanent deformation. In this paper an attempt was made to model clamping force evolution utilizing elastic reinforcement compaction models. The predictions are shown to have significant qualitative errors if a single elastic model is applied, particularly if forces due to reinforcement compaction dominate those due to fluid pressure. By using a combination of elastic models significant qualitative and quantitative improvements were made to the predictions. It is concluded that careful characterization of both reinforcement permeability and compaction response are required for an accurate LCM tooling force analysis.

Kelly, P.A., and Bickerton, the S., [33] presented a comprehensive filling and tooling force analysis for rigid mould LCM processes. This has been implemented with a generic LCM filling simulation. The simulation has been verified against existing analytic and semi-analytic solutions, considering fill times and clamping force due to reinforcement compaction. Industrial application is demonstrated through consideration of a fireman's helmet, which has demonstrated the complex evolution of both local and global tooling forces during RTM and I/CM (Injection against Compression Moulding) cycles. Resultant forces are computed in the closing and lateral directions, having practical benefits for design of moulds and supporting equipment. The evolution of tooling forces has been shown to be sensitive to the accuracy of the applied fibre reinforcement compaction model, which is used to predict normal and tangential stresses exerted on mould surfaces.

Bicherton, S., and Abdullah, M. Z., [34] on modelling and evaluation of the filling stage of injection, compression moulding. A series of parametric studies are presented on this research, considering the effects of process parameters on mould filling times, and internal tooling forces. Two modes of compression flow are considered, constant speed, and constant force. While significant reductions in fill time can be achieved, these gains are balanced by increased clamping force, or increased internal stress applied to the mould. Constant force compression is shown to minimise fill times, using the full capacity of the clamping device. An experimental study was completed to verify the applied models. Comparisons to predicted fluid pressure histories are very good, verifying the applied pressure governing equations. Total clamping force predictions have shown important qualitative differences, which have been related to the use of elastic preform deformation models. Significant viscoelastic stress response was exhibited by the reinforcement studied, in the absence of any resin. Due to the similar time scales of (I/CM) (Injection against Compression Moulding) filling and preform stress relaxation behaviour, viscoelastic deformation models are required to improve filling simulations.

Shojaei, A., [35] on a numerical study of filling process through multilayer preforms in resin injection, compression moulding. In this article, numerical simulation is utilized to investigate the filling process in an heterogeneous porous medium. The filling stage simulated in a full three-dimensional space by using CV/FE method and based upon an appropriate filling algorithm. The flow in the open gap which may be present in the mould cavity is modelled by

Darcy's law using an equivalent permeability. Numerical simulations of filling process for preforms containing two and three layers of different reinforcements in various stacking sequences are conducted with the aid of computer code developed in this study. Results shown that the injection time as well as flow front progression depends on fibre types in the whole preform, fibre stacking sequence and open gap provided in the mould cavity. Simulated results also suggest that the presence of open gap at top of reinforcement can lead to both low injection time and uniform flow pattern.

Laurenzi, S., et al [36] studied process simulation for a large composite aeronautic beam by resin transfer moulding. This paper presented the numerical process analysis and the experimental investigation. The component is a primary structure characterized by several thick sections with abrupt changes in shape that complicates the resin impregnation of the preform. Process simulations based on a finite element method-modified control volume (CV/FE) were conducted in order to investigate the resin flow front patterns and find the injection scheme that guarantees both a complete impregnation of the preform and a filling time compatible with the resin gel time. The beam component was successfully manufactured, and a good agreement between the numerical analysis and the fabrication process was demonstrated.

Shojaei, A., [37] studied numerical simulation of three-dimensional flow and analysis of filling process in compression resin transfer moulding. This paper studies the numerical simulation of filling process of CRTM in full three-dimensional domain. A mathematical model of three-dimensional resin flow

inside the CRTM mould is presented. An effective elastic modulus is introduced for multi-layer preforms connecting the mould closing speed to deformation rate of individual layers. Control volume/finite element method (CV/FE) is used and the numerical algorithm developed to progress the flow front is based on a quasi-steady state approach, previously employed for resin transfer moulding (RTM), which is here modified for a deformable medium. Element characteristic height (ECH) and element characteristic surface area (ECSA) are introduced to take into account irregular elements in the simulation which are often observed in complex mould cavity. The numerical algorithm presented is coded and the resulting computer code is used to predict the necessary filling parameters such as flow progression, pressure distribution and mould clamping force. The validity of the numerical algorithm is verified by comparison with analytical solutions for simple moulds. Computer code developed is also used to analyse the CRTM process with different filling modes by providing various numerical examples. The results show the effectiveness of the numerical simulation in predicting the CRTM process.

Merotte, J., et al [38] made a resin flow analysis with fibre preform deformation in the through-thickness direction during CRTM. Resin flow during Compression Resin Transfer Moulding (CRTM) described and analysed in three phases on this research paper. In the first phase, a gap is created by holding the upper mould platen parallel to the preform surface at a fixed distance from it. The desired amount of resin injected into the gap quickly flows primarily over the preform. The second phase initiates when the

injection is discontinued and the upper mould platen moves down squeezing the resin into the deforming preform until the mould surface comes in contact with the preform. Further mould closure during the final phase will compact the preform to the desired thickness and redistribute the resin to fill all empty spaces. This paper describes the second phase of the infusion. In which assume that at the end of phase one; there is a uniform resin layer that covers the entire preform surface. This constrains the resin to flow in through-thickness direction during the second phase. This through-thickness flow is modelled as the load on the upper mould forces the resin into the preform, simultaneously compact, in the preform. The constitutive equations describing the compaction of the fabric as well as its permeability are included in the analysis. A numerical solution predicting the flow front progression and the deformation is developed and experimentally verified. Non-dimensional analysis is carried out and the role of important non-dimensional parameters is investigated to identify their correlations for process optimization.

Finally Poodts, E., et al [39] wrote a research on fabrication, process simulation and testing of a thick CFRP component using the RTM process. This paper introduces the case of a CFRP con-rod beam, and describes many aspects regarding its production with the Resin Transfer Moulding (RTM) process. The objective was to find the best process parameters of the injection and curing stages in order to manufacture the 20 mm thick CFRP part. The results are analysed in terms of the aesthetic aspect, the porosity and the mechanical properties of the final component. For the resin injection stage,

results obtained from production experiences are presented, which have been performed with different set-ups, and simulations of the resin flow are used to analyse them. The results show that the resin flow during injection could be rather unpredictable, probably because of the fibre rearrangement and race tracking effects. Improvements in terms of aesthetic aspect and porosity of the part could be achieved by a process which included final compaction of the cavity by means of compressed air. Regarding the curing stage, the article presents the simulation results of a curing cycle, and it's validation through DSC analysis of specimens obtained from the finished component.

Finally, results of tensile mechanical tests are provided, performed on finished components produced by RTM and compared to others produced with the method of hand lay-up of pre-impregnated plies and curing in autoclave. The results confirm that it is possible to achieve components through RTM with comparable mechanical performance to those produced with the prepreg plus autoclave process.

For computational modelling the permeability K can be obtained experimentally and fitted with an empirically derived (from the fibres volume fraction V_f) power law which is discussed in details, non-isotropic behaviour and the preform compaction numerical methods such as Finite Difference Method (FDM) and Control Volume/Finite Element Method (CV/FEM), can successfully model the LCM.

Successful moulding of a composite during any RTM process should take into account the fabric variability. Under ideal conditions the fabric must fit

exactly inside the mould and the distance between the fabric and the mould, must be zero hence the flow behaviour depends upon the porous media only. However, due to mould complex geometry and preform imperfections or deformations from fabric cutting in order to fit into the mould, gaps and channels may arise along a component, offering a path with less resistance for resin flow.

The faster advance of resin due to different local permeability through these gaps and channels is a common disturbance known as race-tracking. Preform deformations and discontinuity may cause a converging flow front around all the mentioned areas creating air entrapments, so lower quality composites result from the manufacturing process as mentioned by Poodts, E., et al [39].

Approaches to estimate race-tracking and local permeability during the impregnation of a composite have been studied by several researchers where the influences of various race-tracking situations on the flow pattern have been addressed by Devillard, M., et al [40] on-line characterization of bulk permeability and race-tracking during the filling stage in RTM process. Andersson, H.M., et al [41] wrote a paper on numerical model for vacuum infusion manufacturing of polymer composite. Their paper is focused on the development and evaluation of a numerical model describing the impregnation stage of fibre reinforced polymer composites, during manufacturing process of vacuum infusion. Examples of items made with this process are hulls for sailing yachts and containers for the transportation industry. The impregnation is characterised by a full 3D flow in a porous medium having an anisotropic, spatial- and time-dependent permeability. The numerical model has been

implemented in a general and commercial computational fluid dynamic software through custom written subroutines that: couple the flow equations to the equations describing the stiffness of the fibre reinforcement; modify the momentum equations to account for the porous medium flow; re-mesh the computational domain in each time step to account for the deformation by pressure change. The verification of the code showed excellent agreement with analytical solutions and very good agreement with experiments. The numerical model can easily be extended to more complex geometry and to other constitutive equations for the permeability and the compressibility of the reinforcement.

Anderson, H.M., et al [42] outlined the application of digital speckle photography to measure thickness variations in the vacuum infusion process. A method to measure the movement of the flexible bag used in vacuum infusion is presented in this paper. The method is based on developed stereoscopic digital speckle photography system (DSP). The advantage with this optical method, which is based on cross-correlation, is that the deflection of a large area can be continuously measured with a great accuracy (down to 10 pm). The method is at this stage most suited for research but can in the long run also be adopted in production control and optimization. By use of the method it was confirmed that a local deformation is formed at the resin flow front and that there can be a considerable and seemingly perpetual compaction after complete filling. The existence of the deformation demonstrates that the stiffness of the reinforcement can be considerably reduced when it is wetted. Hence, the

maximum fibre volume fraction can be larger than predicted from dry measurements of preform elasticity. It is likely that the overall thickness reduction after complete filling is caused by lubrication of the fibres combined with an outflow of the resin. In addition, the cross-linking starts and the polymer shrinks. Hence, the alteration in height will continue until complete crosslinking is reached.

Hammami, A., et al [43] made a study on modelling the edge effect in LCM. Their paper presents an analysis of the flow patterns using appropriate flow equations to simulate the open channel and Darcy's law in the porous medium. From this an equivalent porous medium is defined for the channel for which an equivalent permeability tensor can be computed. Two geometric models to predict the edge effect are presented. The first model is derived from the Navier-Stokes equation in the channel. In the second model, the flow is assumed to take place in an equivalent cylindrical channel as in Poiseuille flow. To evaluate the applicability of these simple models, a parameter called the transverse flow factor is defined. For finite element flow simulation an equation to define the equivalent permeability of the first row of elements encompassing the open channel is given. Experimental as well as simulation results are presented.

Sozera, E.M., et al [44] studied on-line strategic control of LCM process.
In this paper an on-line strategic controller with in situ sensor data influenced the flow front pattern during mould filling and drove the process towards successful completion. Variability analysis was performed during the

moulding filling. Some of these variabilities are considered in off-line mould filling simulations. By analysing the simulation results, the sensors are placed inside the mould to identify the variabilities and take corrective action(s) to eliminate voids. Sensor data and the control actions were cast in the form of a decision tree. Data acquisition software collected the in situ sensor data and implements the control actions from this decision tree. A case study was included in which various race-tracking and bulk permeability variations can be expected during manufacturing. The proposed controller is described in detail for this selected case study and its usefulness is verified with experiments.

Gokce, A., and Advani, S. G., [45] researched on vent location optimization using map-based exhaustive search in LCM. In this paper, probabilistic race-tracking modelling is used to capture last-filled region distribution over the mould geometry. Success criteria for mould filling are defined in terms of dry spot tolerances, and vent fitness maps, which display potential vent locations, are created. Next, exhaustive search algorithm is coupled with vent fitness maps to determine optimal vent configurations. The map-based exhaustive search is demonstrated on three geometries and results are compared with existing combinatorial search results. The performance of the optimal vent configurations is evaluated in a virtual manufacturing environment. Sensitivity analyses are conducted to determine the influence of optimization parameters on the results.

Lawrence, J. M., et al [46] write on automated manufacturing environment to address bulk permeability variations and race tracking in RTM by redirecting flow with auxiliary gates. In this paper an automated RTM apparatus was designed and built, containing all of the necessary components. Flow sensors used in order to allow the monitoring of the fluid advancement. Individually controllable injection gates and vents allowed geometrical flexibility and flow control. The following study demonstrates usefulness of the manufacturing tool to implement, validate and uncover limitations of a scenario-based flow control approach with geometries of increasing complexity.

Lawrence, J. M., et al [47] made an approach to couple mould design and on-line control to manufacture complex composite parts by RTM. In this paper, used a mould filling simulation tool was used to develop a design and control methodology that, with the help of sensors and actuators, identifies the flow disturbance and redirects the resin flow to successfully complete the mould filling process without any voids. The methodology is implemented and experimentally validated for a mould geometry that contains complex features such as tapered regions, rib structures, and thick regions. The flow modelling for features such as ribs and tapered sections are validated independently before integrating them into the mould geometry. The approach encompasses creation of software tools that find the position of the sensors in the mould to identify anticipated disturbances and suggest flow control actions for additional actuators at auxiliary locations to redirect the flow. Laboratory hardware is selected and integrated to automate the filling process. The

effectiveness of the methodology is demonstrated by conducting experiments that, with feedback from the sensors, can automate and actively control the flow of the resin to consistently impregnate all the fibres completely despite disturbances in the process. Devillard, M., et al [48] wrote a paper on flow sensing and control strategies to address race-tracking disturbances in resin transfer moulding. In this paper part-II, an automated system designed to implement the on-line control strategy of part-I is demonstrated. Once the design of on-line control strategy is completed, the results seamlessly interfaced with the manufacturing platform to communicate with the sensors in the mould and control the injection and vent valves on an experimental platform. Thus, this streamlines the feedback control in RTM from the design stage to the automation stage. An experimental case study is presented to validate the use of model based on-line control of the RTM process and to demonstrate how it lends itself to automation in the manufacturing process.

Endruweit, A., et al [49] studied random discontinuous carbon fibre preform and provided a permeability modelling and resin injection simulation. In this paper the distribution of fibre bundles in short chopped carbon fibre preforms was described using a stochastic model, as a function of geometrical and preform processing parameters. Local permeability distributions were generated from this, based on Gebart's model for the permeability of aligned fibres. Resin injection simulations were evaluated statistically based on these permeability distributions. Results indicate that, as expected, the macroscopic preform permeability decreases with increasing the average fibre volume

fraction. It is independent of the tow filament count and the fibre length within the ranges investigated. The observed coefficient of variation of the permeability increases with increasing filament count, fibre bundle length and superficial density. At constant preform superficial density, variation of the preform processing parameters (fibre spray path offset, spray tool elevation, and spray path pattern) affects the fibre bundle distribution and thus the flow front patterns. Different combinations of the processing parameters have different effects on the mould fill times.

Pillai, K.M., et al [50] model the heterogeneities present in preforms during mould filling in RTM. This paper presents developments in the manufacturing process of RTM flow modelling with fibre reinforcements. Studies on measuring the permeability of the tested fibre preforms using the conventional RTM flow model are presented including heterogeneities in the flow process which are also discussed with analytical solutions for simple 2-D flows under constant pressure and constant flow-rate conditions. Approaches to numerically simulate the RTM process in fibre based materials reinforcements are presented.

Li, J., et al [51] made a research on statistical characterization and robust design of RTM processes. In this research, a comprehensive study was conducted to investigate the statistical property of the typical flow disturbance due to race-tracking in RTM processes. It was found that the ratio of the permeability values caused by race-tracking over average value for a rectangular mould could be represented as Weibull variables. With the

statistical analysis results, a robust RTM process design method was introduced and illustrated. This new process design approach can help design RTM processes to be insensitive to preform permeability variations coming from materials and processing. Therefore, high quality composite components can be made consistently.

However, because of the randomness of the variability it is a challenge to model local permeability conditions in a mould, firstly locally in the above areas of interest where the probability of converging flow is high and thereafter globally, in order to develop a probabilistic measure to forecast variability in the mould. This will facilitate optimization of the node during the impregnation process in the present study.

Starting with 1-D isotropic model, Gonzalez, R., [13] and Chan, A. W., [14] studied RTM in a disk shaped mould and a rectangular mould, respectively. By neglecting the chemical reaction and heat transfer during the filling stage, both analytical and numerical methods were utilized to simulate the flow process. The porous media flow approach, i.e. applying Darcy's law, was used by Lee, J., et al [53] to model more complicated 2-D and 3-D flow problems. They took into account not only heat transfer but also curing and rheological changes for both isotropic and anisotropic scenarios. Experimental verifications of the current models were also performed to assess accuracy of the mathematical methods. Corresponding to different mathematical models, which consist of a set of partial differential equations, several methods including finite difference method (FDM), finite element method (FEM) and

boundary element method (BEM) were performed by Young, W-B., [54], Liu, B., et al [55] FDM was the first attempt used to simulate a two-dimensional RTM process. By comparing with experimental results, it was proven that considering variability in the experiments, the predictions were reasonable. Um, MK., and Lee, WI., et al [56] applied the boundary element method. The case was two-dimensional flat moulds where the permeability and the resin viscosity were constant. They reported that it took less time to generate the mesh at each time step than required by FDM or FEM. Yoo, Y.-Y. and Lee, Woo II., [57] and Osswald, T., and Tucker, C., [58] determined that under the limitations of simple geometry parts and isothermal Newtonian problems, the BEM method gave very accurate simulation results. Finite element method (FEM) and control volume (CV), i.e. FE/CV, have been applied by Bruschke, MV., [59] with his predictive model for permeability and non-isothermal flow of viscous and shear-thinning fluids in anisotropic fibrous media. Varma, RR., [60] made research on three-dimensional simulations of filling in RTM with advances in FEA in fluid dynamics. Phelan, FR. Jr., [61] made simulations of the injection process in RTM.

Since the resin flow front advances, the calculation domain should be redefined and the numerical mesh should be regenerated, which results in a very time-consuming procedure. A major advantage of FE/CV is that simulating of the flow front can be carried out without re-meshing. Joshi, S. C., et al. [62] concluded that three major steps are needed in the FE/CV flow simulation: (1) use the FE solution to obtain the pressure distribution in the

resin-filled region; (2) calculate the resin flow rates; and (3) trace the resin flow front and update the computational domain.

Some unique techniques emerged in RTM simulation research. Ismail Y. and Springer, G. S., [63] developed an interactive simulation technique in which during the simulation process, the user can: (1) change the locations of the inlet and vents; (2) remove, open and close inlet and vents; and (3) change the inlet pressure or flow rate at the inlets Kanapady, R., et al [64, 65] two papers developed a new, implicit, pure finite-element approach in symmetric multiprocessor machines for large scale RTM process simulation which has been successfully applied to practical large-scale problems.

Lin, M. and Hahn, H.T., [66] used RTM process optimization while Padmanabhan, S. K., and Pitchumani, R., [67] using stochastic modelling investigated the effects of process and material uncertainties on the variability of fill time and degree of cure in RTM. Also work has been done by Fernlund, G., et al [68] on determining variability in process-induced deformations by simply performing parametric studies of the influence of input variables using a deterministic analysis.

Successful mould filling modelling has been done by several researchers over the last few years where the influence of variability and race-tracking situations on the flow pattern was investigated Jiang, S., et al [69] studied optimum arrangement of gate and vent locations for RTM process design using a mesh distance-based approach" .Gauvin, R., et al [70] studied key issues in

numerical simulation for LCM processes, and Parnas, R. S., et al [71] created a permeability database for composites manufacturing processes.

2.6 Optimisation of the RTM process

Designing optimal RTM processes in terms of minimizing cycle time, avoiding dry spots, and increasing the yield of successful parts has been considered. Lawrence, J., et al [47] developed a design and control methodology. By taking advantage of sensors and actuators, the flow disturbance was identified and the resin flow was redirected to complete the mould filling without any voids. They developed software for finding the position of the sensors in the mould to identify disturbances and suggest flow control actions for adding actuators at auxiliary locations to change the direction of flow. In their work, complex mould features, including tapered regions, rib structures, and thick regions, were tested to validate the effectiveness of the methodology. They documented that the feedback from sensors did have the ability to automate and actively control the flow of the resin, which led to consistently impregnating all the reinforcements even though disturbances were present in the process. Liu, B., et al [55] implemented a mould filling simulation code to deal with the processing issues, including gate control, venting and dry spot formation. They used numerical sensors to design a control strategy to optimize mould filling time or reduce the required injection pressure. With specified vent location, they simulated the predicted changes in the pressure distribution and mould filling pattern. The simulation code checked if air was trapped in the mould and kept track of these trapped air pockets. Lin, M., and Hahn, H. T., [66] discussed the strengths and

weaknesses of a genetic algorithm and gradient based algorithms. Two different types of RTM process optimization have been documented. In the first case, the Quasi-Newtonian method was coupled in the code Global Local Optimizer (GLO), and gate locations were optimized to minimize the filling time. In the second case, a graphical search was explored for adding the varied high permeability layers to minimize resin waste in addition to minimizing the filling time. They reported that these two methods have their specialties, and if the design variables are discrete, for example number of gates and vents, the combination of two methods should be used. In addition, they also pointed out the limitation of the finite element method used in the analysis, i.e. a noticeable error was incurred if a single node was used to model the gate. Jiang, S., et al [69] introduced a new mesh distance-based approach of genetic algorithm. The basic idea for this method was to find the optimum arrangement of gates and vents to achieve the objective of minimizing the maximum distance between gates and vents to avoid dry spot formation. By comparing with the examples in the literature, it was found that this method was very efficient and effective in optimizing the locations of gates and vents and saving computation time.

As pointed out by Gauvin, R., et al [70] and Parnas, R. S., et al [71], on permeability measurements three types of errors are likely to occur during resin flow: (1) edge effect, (2) initial effect and (3) mould deflection. In unidirectional flow experiments, achieving perfect fit of the test preform and mould edges is difficult, leading to the fluid flowing into the channel between preform and mould edges. Under this situation, the fluid flows faster along edges making the flow front a curved shape instead of a straight line. Some

researchers have done extensively work on edge effects in permeability measurements. Hammami, A., et al [43] presented a model to describe the edge effect. The model was derived using Navier-Stokes equations in the open channel and Darcy's law in the porous preform simultaneously characterize the flow in the channel and through the reinforcement. They defined an equivalent porous media for which an equivalent permeability can be computed as a function of the channel geometry eq. (2-1).

$$K = \frac{h^2}{12} \hspace{4cm} (2\text{-}1)$$

where K is the equivalent average permeability of the channel and h is the channel height (gap between the preform and the mould wall). This model was validated by their experiments in the case of neglecting the transverse flow.

Bickerton, S., and Advani, S. G., [18] took into account a more complex situation, studying the regions within the mould cavity where free channel with high porosity exist, for example, near corners, bends, air-gaps and other features involving sharp curvatures. They demonstrated the role of flow channels in reducing the injection and mould pressures and redistributing the flow. Unexpected air was trapped in the mould cavity during saturated flow experiments. The air expands and contracts resulting in non-Darcy behaviour and measurement errors.

2.7 Finite Element Method (FEM) in RTM

Simulations of the RTM process provide the capability to predict the flow pattern and any air entrapment and void formation during the manufacturing process.

The Finite Element Method (FEM), or Finite Element Analysis (FEA), is based on the principle that is possible to divide an object with complex geometry in small parts (elements or mesh) and consequently describe the behaviour of each single element of the body by assigning to it equations and relationships that accurately describe the element behaviour. As the size of these elements is made smaller and smaller we may obtain a more accurate numerical solution for the entire complex object. However this has the effect of increasing the computation time Hieber, S. A., and Shen, S. F., [72].

2.8 Control Volume Finite Element Method (CV/FE)

The combination of the finite element method with the control volume technique in order to determine the pressure field for flow front advancement is called the Control Volume/Finite Element method. Control Volume/Finite Element method has been implemented successfully by Hieber C.A. and Shen S.F. [72] they provide a paper on finite element/finite difference simulation of the injection mould filling process. Frederick, R., and Phelan, JR., [73] researched simulations of the injection process in resin transfer moulding with the use of CV/FE. Trochu, F., et al [74] presented a paper on numerical analysis of the resin transfer moulding process by the Finite Element Method. Long, A. C., [75] presents in details the CV/FE method. Initially, the entire

flow field is discretized into a finite element mesh. Each element is sub-divided by lines connecting the centroid, to the midpoint of each side as shown in Fig. 2.4. A control volume is composed of several sub-areas surrounding a single node. A fill factor is associated with each control volume, which represents the degree of resin saturation of the region and is equal to the volume of the resin divided by the original pore volume of the control volume. Therefore a fill factor of zero shows that the control volume is empty and a factor of one show that it is fully saturated. An intermediate value indicates that the flow front passes through the control volume in question. Nodes within these flow front control volumes are assigned the appropriate boundary condition. With this method the mass conservation is achieved locally at the expense of a slight increase in geometric feature complexity.
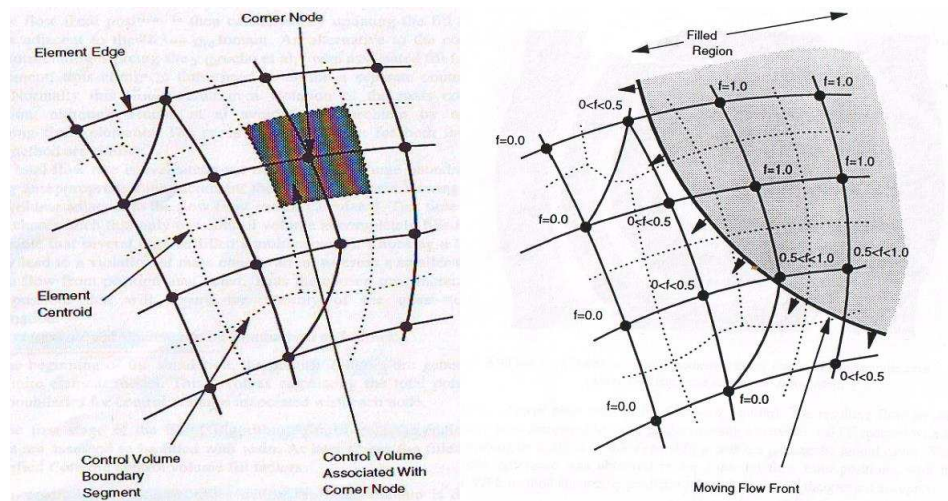
Fig. 2.4: CV/FE method (left), CV/FE method moving flow front (right) [52].

The 3D form of Darcy's law (equation 1.1) may be combined with the assumption of conservation of fluid volume:

$$\nabla\left(\frac{1}{\mu}[\text{K}]\nabla\text{P}\right) = 0 \qquad\qquad \text{(2-2)}$$

In the general case, the permeability [K] tensor in eq. (2-2) and its components in three-dimensional space may be written as:

$$[K] = \begin{bmatrix} K_{xx} & K_{xy} & K_{xz} \\ K_{yx} & K_{yy} & K_{yz} \\ K_{zx} & K_{zy} & K_{zz} \end{bmatrix} \qquad\qquad \text{(2-3)}$$

For a woven fabric, considering the axes of coordinates oriented along the principal directions of anisotropy, for an anisotropic formation $K_x \neq K_y \neq K_z$, and the permeability as a tensor with 3 components one on each x, y, z axis: The permeability tensor is orthotropic where $K_{xy} = K_{yx}, K_{xz} = K_{zx}, K_{yz} = K_{zy}$, and there exists a principal coordinate system with a principal permeability tensor so eq. (2-3) can be written:

$$[K] = \begin{bmatrix} K_{xx} & 0 & 0 \\ 0 & K_{yy} & 0 \\ 0 & 0 & K_{zz} \end{bmatrix} \qquad\qquad \text{(2-4)}$$

So eq. (2-4) may be reformulated with (2-2) as:

$$\nabla\left(\frac{1}{\mu}\begin{bmatrix} K_{xx} & 0 & 0 \\ 0 & K_{yy} & 0 \\ 0 & 0 & K_{zz} \end{bmatrix}\nabla\text{P}\right) = 0 \qquad\qquad \text{(2-5)}$$

The computational approach may be summarised as followed according to Rudd C. D., et al [52] :

    a. The control volume is generated by the FE model.

b. Control volumes enclosing inlet nodes are assumed to be filled with resin and the filled region is identified by the control volume fill factors.

c. The pressure equation (2-5) at nodes within the filled domain is solved by the FE method by applying the appropriate boundary conditions.

d. The pressure gradients at the flow front are calculated by differentiating the element shape functions and the velocity field is then determined by Darcy's law. Hence the volumetric flow rate between control volumes is calculated by multiplying the connecting area with the normal fluid velocity.

e. The appropriate time increment is calculated to fill at least one control volume each time and the fill factors are updated at the flow front.

f. The whole process is repeated from stage (b) for the newly filled domain, until the mould cavity is completely filled with resin.

The approximate flow front position at any time may be determined by identifying nodes within control volumes which are between 0 and 1.

2.9 Race-tracking

During the mould filling stage of the RTM process the textile must be completely saturated with resin. Considering that gates and vents have been placed appropriately in order to ensure complete saturation, without any air entrapments inside the mould, the next step is to increase the yield of successful parts by taking into account phenomena such as preform variability

and race-tracking as mentioned by Anderson, H.M., et al [42], Hammami, A., et al [43], Sozera, E.M., et al [44].

A race-tracking channel may exist because of the fabric compaction across an angle at the edges of the preform. On this gap area the fluid usually meets lower flow resistance than the textile preform; hence permeability along a race-tracking channel is higher. For a complex geometry part like the ACTS node, more complexity also introduces higher probability of variability and race-tracking of resin during impregnation along preform radii. This may lead to incomplete saturation, forming dry spots in the composite. The strength and existence of race-tracking is a function of the fabric architecture and their placement in the mould. The race-tracking and preform variability are random phenomena and may vary from part to part due to fabric different volume fractions or gaps that may arise from the textile bending in the angles, and are therefore generally not repeatable from one part to the next. Therefore the optimization of the race-tracking phenomenon is of high importance for the manufacturing process of any composite material. Over the past few years an extensive amount of experimental and modelling research around the race-tracking phenomenon has been performed by Bickerton, S., Advani, S. G., [18] paper on characterization and modelling of race-tracking in liquid composite moulding processes. Gokce, A., and Advani, S. G., [45], Lawrence, J. M., et al [46], Lawrence, J. M., et al [47], Devillard, M., et al [48], Pillai, K.M., et al [50] paper on modelling the heterogeneities present in preforms during mould filling in RTM as described previously on Section 2.5 on this Chapter. Figures

2.5 and 2.6 demonstrate that race-tracking and local permeability may alter the flow pattern and cause the resin to reach the vent before the entire preform has been saturated.
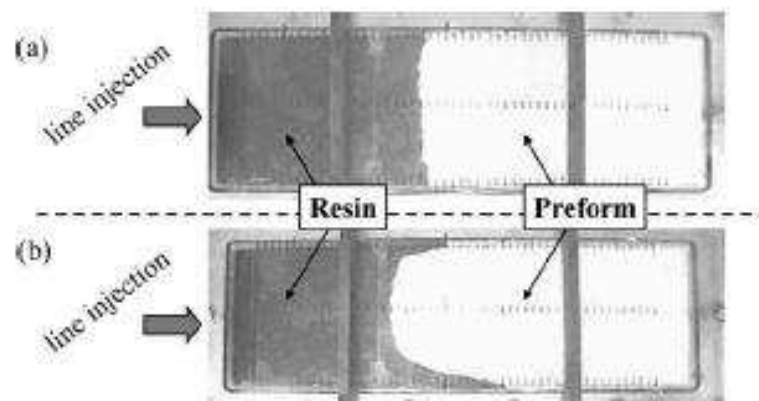
Fig. 2.5: RTM on a woven fabric (a) no race-tracking filling and (b) with race-tracking along the top and bottom edges in 1-d flow [76].
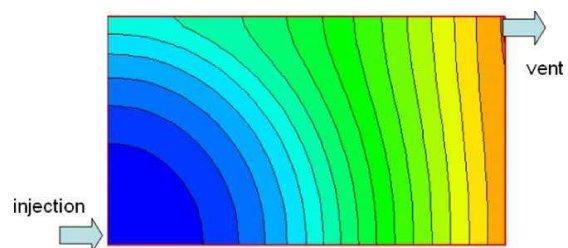
(a)
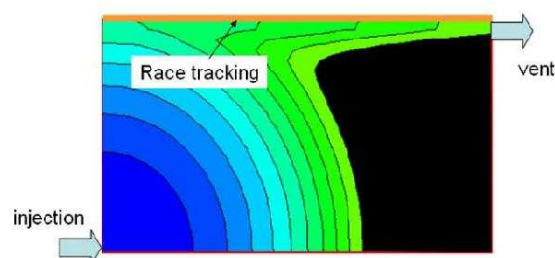
(b)

Fig. 2.6: RTM on a woven fabric (a) with no race-tracking and (b) with race-tracking along the top edge [77].

Therefore it follows that characterization of the preform local permeability and race-tracking locations are key elements in order to apply simulation tools for the complete filling of any composite part. Thus, with the study of race-tracking and variability one may optimise gates, vent locations and flow control strategies to minimise the change of defect deformation as mentioned by Lawrence, J.M., et al [76]. The characterization of preform permeability in the presence of race-tracking is repeated by Bickerton, S., et al [77], giving fabric structure and mould curvature effects on preform permeability and mould filling in the RTM process.

2.10 Void formation and characterization

Dry spots, which are inside a composite part devoid of resin, degrade the composite's properties significantly and affecting negatively the final quality of the part as studied by Liu, B., et al [55] and other researchers' papers mentioned previously on this Chapter: Lekakou, C., and Bader, M.G., [27], Parnas, R.S., [28], Riuz, E., et al [31].

During the RTM process the resin flows through a complex network of the fabric. As a result of this channels and paths are formed by the architecture of the textile inside the mould cavity. The dimensions of these channels are several orders of magnitude smaller than the thickness of the mould. Therefore the resin flow through the fibre textile may be characterized as a complex, micro-scale, and meso-scale flow as shown in Fig. 2.7 to 2.8. Optical microscopy and microscopic image analysis can be utilized to investigate average void content and spatial void distribution through the thickness of the

composite material studied by Liu, B., et al [55]. Moreover, image analysis offers the advantage of providing detailed information of other important parameters such as void location, void shape and size distribution.
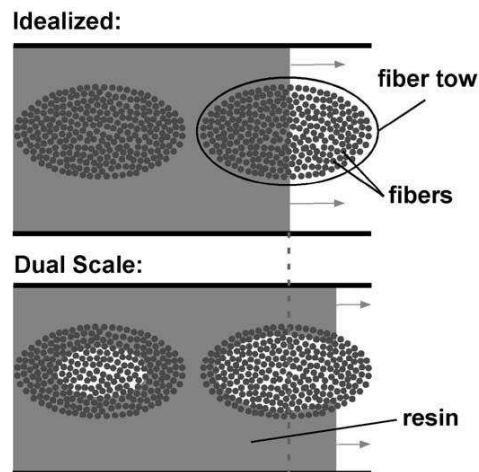
Fig. 2.7: Idealized and dual scale flow in micro-scale textile preforms [55].

However, void measurement by optical imaging is generally performed on limited sample surface area. Statistical averaging is therefore commonly used from random acquisition of pictures over the larger area of interest investigated by Penga, X. Q., et al [78].
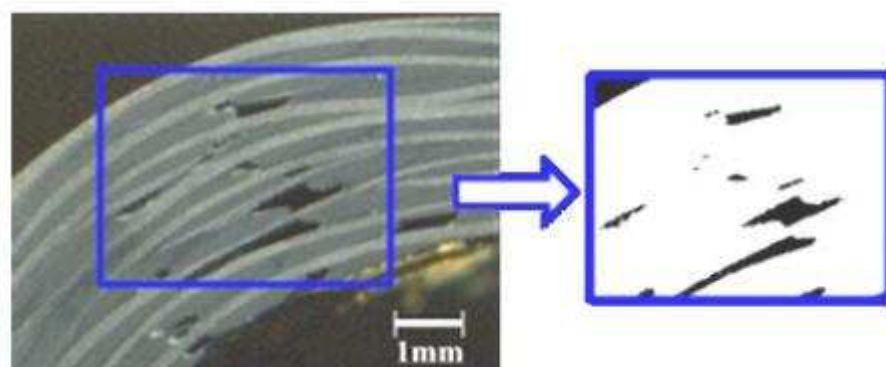
Fig. 2.8: Void formation on a curved plate composite sample [21].

During mould filling in RTM two types of flow at different scales occur simultaneously in the fibrous reinforcement: the advance of resin through the air channels, which is a meso-scale flow between the yarns and a microscopic flow within the yarns. As a result of this we can categorize void formation in three scales:

      i)   Microscopic Scale < Unit Cell

      ii)   Mesoscopic Scale = Unit Cell

     iii)   Macroscopic Scale > Unit Cell

The unit cell is the smallest geometry of the textile reinforcement which is repeated in a regular manner.

While theoretically it is possible to analyse the complex process of microscale and mesoscale void formation in detail the immense computational power required to solve the problem makes any prediction modelling approach towards this direction not an easy task. However a detailed macroscale prediction modelling study, which is absolutely necessary, may be done computationally with the ESI PAM-RTM® commercial software [79].

Red arrows represent void locations
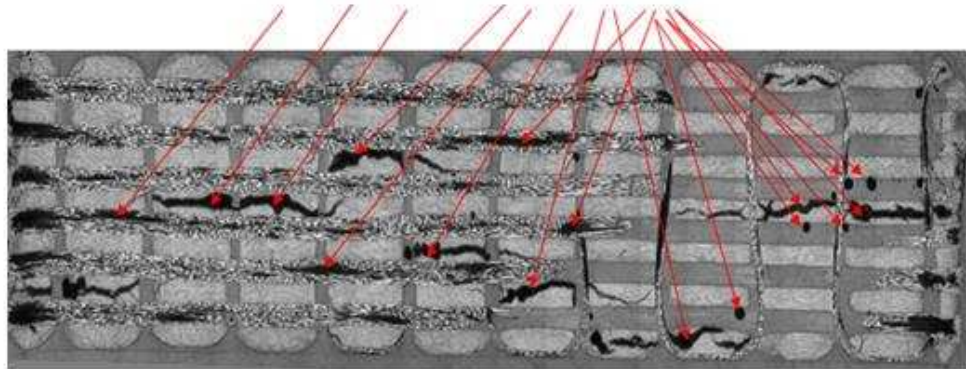
Fig. 2.9: Red arrows indicated void formation in 3D woven orthogonal fabric 6x7 layers (Sample for void experimental observation with optical microscopy done at the University of Nottingham) [80].

Void formation occurs during the impregnation process when the flow front merges due to the presence of inserts, ribs, and heterogeneity in the preform as shown for a 3D woven orthogonal fabric up in Fig. 2.9.

2.11 Composite Truss Structures

In this section a number of research studies on the use and design of truss structures will be presented. These modular structures can lead to reduced weight and cost and increased strength. Fibre composite truss structures already exist in various industries such as aerospace, automobile, satellites, marine, offshore and civil infrastructures. These trusses commonly employ discontinuous mechanical node configurations, which often prevent the truss members from reaching their ultimate strength to weight ratio.

In case of composite truss structures, nodes are often made of different materials and mechanically joined causing stress discontinuity according to Varvill, R., et al [81], Darooka, D. K., et al [82]. There are two different types

of structure, either 2-dimensional, plane trusses, where the struts and the applied forces all lie in a plane, or 3-dimensional trusses. The simplest structure is a triangular plane truss, which has three struts and three nodes and can be lengthened, by repeating appropriately, with the addition of two further struts and a node. Two structures that have gained widespread use are both based on the triangular truss. The much lighter weight expected, in comparison to the other structures, was not found in practice due to the inherent weight disadvantage of the metallic nodes by Varvill, R., [81].

Removing the truss structure's weight disadvantage, with an optimized load bearing composite nodal structure, would be a big step forward for truss structures in applications where lightweight is an important parameter. Current joining technologies of nodes and struts can lead to further disadvantages of high cost and manufacturing time and the possible requirement of specialised tooling.

Bildstein, M., [84] examined the choice of different materials and structural design for lightweight structures. Advantages and disadvantages of possible materials were considered based on weight, cost, stiffness, strength and manufacturability. Dow, M. B., and Dexter, H. B., [85] developed a series of stitched, braided and woven composites in the ACT Programme and at Langley Research Centre. Schütze, R., [86] and designed and tested light weight carbon fibre rods and truss structure materials, Fig. 2.10-2.11.
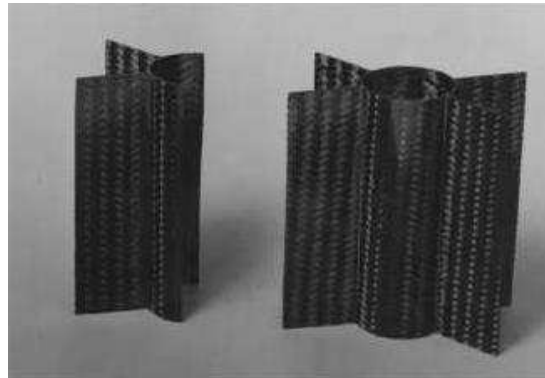
Fig. 2.10: Connection element with nodal plates, on right is finished connection element [86].
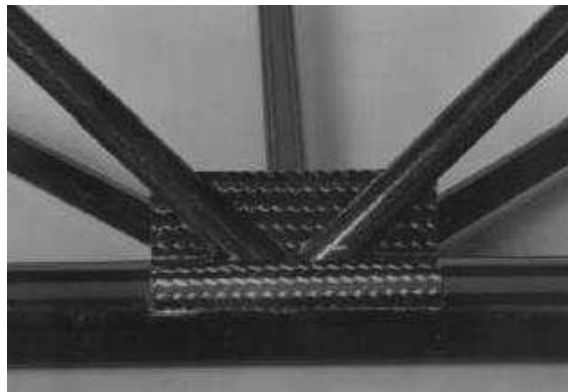
Fig. 2.11: Nodal point [86].

Node-strut joining becomes particularly important for self-erecting by Lindberg, C., [87] or deployable structures by Mikulas, M. M. Jr., and Crawford, R. F., [88] as well as connecting apparatus by Lange F A. [89] and modular spacecraft structures by Ganssle, E. R., and Samhammer, N. F., [90] Joints in the form of fasteners can result in an increase of total structural weight, a large parts count, and a high cost in terms of labour and manufacturing time. Often struts and nodes, when both are metallic, are manufactured as modules in order to minimise the total part count. Adhesive bonding can be used with composite struts giving an additional weight advantage over metallic truss structures, where bolts and mechanical fastening

are a necessary additional weight by Glaessgen, E. H., et al [91]. Uozumi, T., and Kito, A., [92] manufactured braided preforms, which have multiple joint parts made of carbon fibre and moulded them using RTM for investigating their mechanical and thermal properties. Members of the truss structure were integrated together during preforming to obtain a single piece integral truss unit as shown in Fig. 2.12. Struts in the structure were connected using adhesive bonding. Composite joints showed superior performance compared to aluminium and titanium joints.
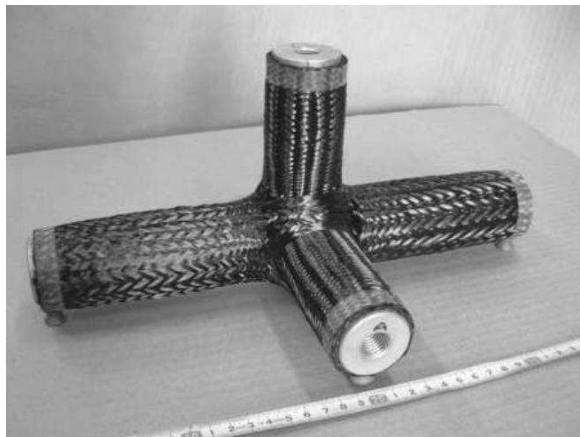
Fig. 2.12: Braided preform of tri-axial joint for satellite application [92].

Thuis, H. G. S. J., and Biemans, C., [93] designed a composite bracket made of carbon fibres to replace a metal bracket for an aerospace application using RTM. They tested the bracket under tensile and compressive static load, which matched the performance of a metallic bracket with a weight reduction of 43%. Researchers at University of Southern Queensland designed a 15 m long composite truss structure, to provide access from waterfront onto a floating walkway for nearly 20000 pedestrian trips per day. The large part of the truss structure was submerged in saltwater and subjected to extremely high

dynamic load from the sea as well as pedestrians. This design was adopted in order to achieve a 100 year design life span for the walkway. This design was proposed as an alternative to traditional structures, which have short life span and need replacement every 10-15 years.

Triangular braidns truss elements used to support a bridge deck in military and offshore applications were joined together using adhesive Brown, R., [94]. First, six of these elements were bonded to form a truss section, which was followed by bonding of top and bottom plates using a pneumatic press. Carrion, J. E., et al [95] constructed E-glass nodes and GFRP struts.

The existence of joints (truss structure discontinuity) are potential weak points in the structure and are sites of possible failure, whether attributable to high stress concentrations around fastener holes, or an all-adhesive failure due to either high stresses or environmental effects. Problems can arise, with a conventional truss structure when using composite struts and metallic nodes, due to thermal expansion differences. These problems are eliminated when using, all composite or monocoque truss designs. The use of fibre composite materials in the field of civil engineering has created the opportunity for new and innovative approaches to conventional truss design, particularly the suitability of fibre composites for monocoque construction where truss joints are eliminated resulting in more efficient structures. The localised stresses that usually occur in mechanically fastened joints can be reduced by using a monocoque design where the structure is continuous. This is the basis of the innovative monocoque composite truss currently being investigated by the

Fibre Composites Design and Development (FCDD) research group at the University of Southern Queensland in Australia where, for a bridge application, strength, stiffness, cost and manufacturability were considered more important than weight. The monocoque construction allows fabrication of the truss and joints in one operation. Detailed analysis and testing of different types of monocoque joints is reported in 2005 by Erp, G. V., et al [96].

From the research papers [81-96] a series of different advanced truss structures has been designed and manufactured. Mechanical testing analysis showed significant advantages of the composites truss structure in comparison to the previous used materials in terms of stress against strain properties, light weight and resistant to corrosion.

2.12 Conclusions

In this Chapter a detailed discussion of composite materials, polymer matrix and textiles, as well as the techniques of Control Volume Finite Element Method (CV/FE)/Finite Element Method (FEM) were provided, which will be central to this work. Furthermore a review was presented the processes of: Resin Transfer, Moulding and optimisation, variability and race-tracking, void formation and characterization the Chapter concluded with a description of composite truss structures. The key findings to be carried forward can be summarised as follows:

- RTM is an important process for manufacturing composite structures.

- Control Volume /Finite Element Method (CV/FE) can provide suitable computational solutions.

- Variability and race-tracking are the key elements in improving the real life accuracy of computational modelling.

- Whole Composites (truss) structures offer significant advantages.

References

[1]Campbell, F.C., "Manufacturing Processes for *Advanced Composites*", FC Campbell 2004, ISBN 1856174158.

[2]Advani, S. G., Sozer, E. M., "Process Modelling in Composites *Manufacturing",* Marcel Dekker, Inc (2003); p 1-2, ISBN 0-8247-0860-1.

[3]Long, A. C., (Ed). "Design and manufacture of textile composites*",* Woodhead Publishing Ltd. 2005, p 259-287, 492, ISBN 1 85573 744 2.

[4]Elias. H-G., "Plastics, General Survey" in Ullmann's Encyclopedia of Industrial Chemistry: a20: 2005; p 543.Wiley-VCH, Weinheim doi: 10.1002/14356007.

[5]Foote, B., Anslyn, I., "Organic Chemistry 5th Edition: © 2009, 2005". Brooks/Cole Cengage Learning. ISBN-13: 978-0-495-38857-9, ISBN-10: 0-495-38857-2.

[6]Carey, F. A., "Organic Chemistry, University of Virginia 7th *Edition"* Published by McGraw-Hill 2008; p.1203-9 ISBN 978-0-07-110225-4.

[7]http://textiles.nottingham.ac.uk/ "Last accessed 13.03.2014".

[8]Huang, G. and Zhong, Z., "Tensile behaviour of 3D woven composites by *using different fabric structures"*, Materials and Design **23**: (2000); p 671-674.

[9]Hill, B.J., "Effect of internal structural changes on the properties of multi-*layer fabrics for composite reinforcement".* Polymer Composites **3**(2): (1995); p 105 –115.

[10]Coman, F., Plast, J. R., "*Design and analysis of 3D woven composites".* Composites **17**(6): (1998); p 545 –577.

[11]Li, J., Thesis: "Modeling, design and control of Vacuum assisted resin *transfer molding",* Manufacturing Engineering 2006.

[12] Beckwith, S. W., and Hyland, C. R.., "Resin Transfer Molding (RTM) Technology Overview," Composites Fabrication, March (1998); p 24-27.

[13]Gonzalez, R., and Macosko, C. W., "Process Parameters Estimation for Structural Reaction Injection Molding and Resin Transfer Molding," Polymer 104 Engineering and Science, Vol. **30** Mid-Feb., (1990); p 142-146.

[14]Chan, A.W., *"Molding of Impr*egnation Process During Resin Transfer *Molding,"* Polymer Engineering and Science, Vol. **31** Mid-Aug., (1991); p 1149-1156.

[15]Lee, J., Young, W.B., and Lin, R.J., *"Mold Filling and Cure Modeling of RTM and SCRIM Processes,"* Composites Structure, **27**; (1994); p 109-120.

[16]Hammami, A., and Gebart, B.R., "Analysis of the vacuum infusion *moulding process".* Polymer Composites, **21**(1): (2000); p 28-40.

[17]Hammami, A., Gauvin, R., Trochu, F., Truret, O., and Ferland, P., *"Analysis of the Edge Effect on Flow Patterns in Liquid Composites Molding".* Applied Composite Materials **5**: (1998); p 161-173.

[18]Bickerton, S., Advani, S. G., "Characterization and modelling of race-*tracking in liquid composite molding processes".* Composites Science and Technology **59**: (1999); p 2215-2229.

[19]Bickerton, S., Advani, S.G., Mohan, R.V., and Shires, D.R., *"Experimental Analysis and Numerical Modeling of Flow Channel Effects in Resin Transfer Molding",* Polymer Composites, Vol. **21**, No. 1: (Feb. 2000); p 134-153.

[20]Hubert, P., Vaziri, R., and Poursartira, A., "Two-dimensional flow model for the process simulation of complex shape composite laminates", International Journal for numerical methods in Engineering (Int. J. Numer. Meth. Eng. **44**: (1999); 1D26.

[21]Brillant, M., Thesis: "Out of Autoclave manufacturing of complex shape laminates", Department of Mechanical Engineering McGill University Montreal Canada, (December 2010); p 32.

[22]Dong, C., "Model development for the formation of resin-rich zones in composites processing". Composites: Part A **42**; (2011); p 419–424.

[23]Kang, M.K., Lee, W.I., and Hahn H.T., "Formation of microvoids during resin-transfer molding process". Composites Science and Technology, **60**(12-13): (2000); p 2427-2434.

[24]Patel, N., and Lee, L.J., "Effects of Fiber Mat Architecture on Void Formation and Removal in Liquid Composite Molding". Polymer Composites, **16**(5): (1995); p 386-399.

[25]Binetruy, C., Hilaire, B., and Pabiot, J., "The influence of fiber wetting in resin transfer molding": Scale effects. Polymer Composites, **21**(4): (2000); p 548-557.

[26]Dimitrovova, Z., and Advani, S.G., "Mesolevel analysis of the transition region formation and evolution during the Liquid Composite Molding process". Computers & Structures, **82**(17-19): (2004); p 1333-1347.

[27]Lekakou, C., and Bader, M.G., "Mathematical modelling of macro-and micro-infiltration in resin transfer moulding RTM". Composites Part A-Applied Science and Manufacturing, **29**(1-2): (1998); p 29-37.

[28]Parnas, R.S., "The Interaction between Microscopic and Macroscopic Flow in Rtm Preforms". Composite Structures, **27**(1-2): (1994); p 93-107.

[29]Simacek, P., Advani, S. G., "Desiderable Features in Mold Fill Simulation in LCM", Vol. **25**, Issue 4: (27 Jul 2004); p 355-367.

[30]Trochu, F., Edu, R., Achim. V., Soukane, S., "Advanced numerical simulation of liquid composite molding for process analysis and optimization", Composites: Part A **37**: (2006): p 890–902.

[31]Riuz, E., Achim, V., Soukane, S., Trochu, F., Breard, J., "Optimization of injection flow rate to minimize micro/macro-voids formation in resin transfer molded composites", Composites Science and Technology **66**: (2006); p 475–486.

[32]Buntain, M. J., Bickerton, S., "Modeling forces generated within LCM tools" Part A: Experimental study, Volume **38**, Issue 7: (July 2007); p 1729–1741.

[33]Kelly, P.A., Bickerton, S., "A comprehensive filling and tooling force analysis for rigid mould LCM processes", Volume **40**, Issue 11: (November 2009); p 1685–1697.

[34]Bicherton, S., Abdullah, M. Z., "Modelling and evaluation of the filling stage of injection, compression moulding", Composites Science and Technology **63**: (2003); p 1359–1375.

[35]Shojaei, A., "A numerical study of filling process through multilayer preforms in resin injection, compression moulding", Composites Science and Technology **66**: (2006); p 1546–1557.

[36]Laurenzi, S., Grilli, A., Pinna, M., De Nicolab, F., Cattaneo, G., Marchetti, M., "Process simulation for a large composite aeronautic beam by resin transfer molding" Volume **57**: (February 2014); p 47–55.

[37]Shojaei, A., "Numerical simulation of three-dimensional flow and analysis of filling process in compression resin transfer moulding", Composites: Part A **37**: (2006); p 1434–1450.

[38]Merotte, J., Simacek, P., Advani, S. G., "Resin flow analysis with fiber preform deformation in through thickness direction during Compression Resin Transfer Molding" Volume **41**, Issue 7: (July 2010); p 881–887.

[39]Poodts, E., Minak, G., Mazzocchetti, L., Giorgini, L., "Fabrication, process simulation and testing of a thick CFRP component using the RTM process", Volume **56**: (January 2014); p 673–680.

[40]Devillard, M., Hsiao, K-T., Gokce, A., and Advan,i S. G., *"On*-line Characterization of Bulk Permeability and Race-Tracking during the Filling *Stage in Resin Transfer Molding Process".* Journal of Composite Materials **37**: (2003); p 1525, DOI: 10.1177/0021998303034459.

[41]Andersson, H.M, Lundstrom, T.S., and Gebart, B.R., "Numerical model for vacuum infusion manufacturing of polymer composites". Polymer composites **13** (2-3): (2003); p 383-394.

[42]Anderson, H.M, Lundstrom, T.S., and Gebart, B.R., Synnergren, P., "Application of Digital Speckle Photography To Measure Thickness Variations in the Vacuum Infusion Process". Polymer composites **24** (3): (2003); p 448-455.

[43]Hammami, A., Gauvin, R., and Trochu, F., "Modelling the edge effect in liquid composites molding". Composites: Part A, **29** (5-6): (1998); p 603-609.

[44]Sozer, E.M., Bickerton, S., Advani, S.G., "On-line strategic control of liquid composite mould filling process", Composites: Part A **31**: (2000); p 1383–1394.

[45]Gokce, A., and Advani, S. G., "Vent Location Optimization Using Map-Based Exhausive Search in Liquid Composite Moulding Processes", Materials and Manufacturing Processes Vol. **19**, No.3: (2004); p 523-548.

[46]Lawrence, J. M., Fried, P., Advani, S. G. "Automated manufacturing environment to address bulk permeability variations and race tracking in resin transfer molding by red*irecting flow with auxiliary gates"*. Composites: Part A, **36**: (2005); p 1128–1141.

[47]Lawrence, J. M., Hsiao, K-T., Don R. C., Simacek P., Estrada G., Sozer, H. C., Stadtfeld, E. M., Advani, S. G., "An approach to couple mold design and on-line control to manufacture complex composite parts by resin transfer molding". Composites: Part A, **33**: (2002); p 981–990.

[48]Devillard, M., Hsiao, K-T., Advani, S. G., "Flow sensing and control strategies to address race-tracking disturbances in resin transfer molding-part II": automation and validation. Composites: Part A **36**: (2005); p 1581–1589.

[49]Endruweit, A., Harper, L.T., Turner, T.A., Warrior, N.A., Long, A.C., "Random discontinuous carbon fibre preform: Permeability modelling and resin injection simulation", Composites Part A, **39**: (2008); p 1660-1669.

[50]Pillai, K.M., Luce, T.L., Bruschke, M.V., Parnas, R.S., and Advani, S. G., "Modelling the Heterogeneities present in Preforms during Mold Filling in RTM", 25th International SAMPLE Conference paper (26-28 October 1993); p 279-293.

[51]Li, J., Zhang, C., Liang, R., Wang, B., "Statistical characterization and robust design of RTM processes", Composites Part A, **36**: (2005); p 564-580.

[52]Rudd, C. D., Long, A. C., Kendall, K. N., Mangin, C., "Liquid moulding technologies: Resin transfer moulding, structural reaction injection moulding and related processing techniques", Woodhead Publishing Ltd, (1997); p. 258, 270-273, ISBN 1 85573 242 4.

[53]Lee, J., Young, W.B., and Lin, R.J., *"Mold Filling and Cure Modelling of RTM and SCRIM Processes,"* Composites Structure, **27**: (1994); p 109-120.

[54]Young, W-B., *"Three-*dimensional Nonisothermal Mold Filling *Simulations in Resin Transfer Molding,"* Polymer Composites, Vol. **15**, No. 2: (April 1994); p 118-127.

[55]Liu, B., Bickerton, S., Advani, S. G., *"Modeling and Simulation of Resin* Transfer Molding (RTM) – *Gate Control, Venting and Dry Spot Prediction,"* Composites. Part A, Vol. **274**, No. 2: (1996); p 135-141.

[56]Um, MK., and Lee, WI., *"A Study on Mold Filling Process in Resin Transfer Molding,"* Polymer Engineering and Science, Vol. **31**: (1991); p 765-771.

[57]Yoo, Y-Y., and Lee, Woo II., *"Numerical Simulation of the Resin Transfer Mold Filling Process Using Boundary Element Method,"* Polymer Composites, Vol. **17**, No. 3: (1996); p 368-374.

[58]Osswald, T., and Tucker, C., *"A Boundary Element Simulation of Compression Mold Filling,"* Polymer Engineering and Science, Vol. **28**, No. 7: (Mid-Apr. 1998); p 413-420.

[59]Bruschke MV., *"A Predictive Model for Permeability and Non*-isothermal Flow of Viscous and Shear-*thinning Fluids in Anisotropic Fibrous Media"* CCM Report 56: (1992); p 992.

[60]Varma RR., *"Three*-dimensional Simulations of Filling in Resin Transfer *Molding"* Advances in Finite Element Analysis in Fluid Dynamics (ASME): FED **200**: (1994); p 21–27.

[61]Phelan, FR. Jr., *"Simulation of the Injection Process in Resin Transfer Mold*ing*"* Polymer Composites **4**(18): (1997); p 460–476.

[62]Joshi, S. C., Lam, Y.C. and Liu, X.L., *"Mass Conservation in Numerical Simulation of Resin Flow"* Composites. Part A, Vol. **31**: (2000); p 1061-1068.

[63]Ismail, Y., Springer, G.S., *"Interactive Simulation of Resin Transfer Molding,"* Journal of Composite Materials, Vol. **31**, No. 10: (1997); p 954-980.

[64]Kanapady, R., Tamma, K., Baddourah, M., and Mark, A., *"High* Performance 105 Computing on a Symmetric Multiprocessor (SMP) Environment for RTM Process Modeling of Large Complex Structural *Geometries,"* Advances in Engineering Software, Vol. **29**, 3-6: (1998); p 399-408.

[65]Kanapady, R., Tamma, K., and Mark, A., *"Highly Scalable Parallel* Computational Models for Large-scale RTM Process Modeling Simulation, *Part 3: Validation and Performance Results,"* Numerical Heat Transfer, Part V: Fundamentals, Vol. **36**, 4: (1999); p 351-386.

[66]Lin, M., and Hahn, H.T., *"Resin Transfer Molding Process Optimization,"* Composites. Part A, Vol. **31**: (2000); p 361-371.

[67]Padmanabhan, S.K., and Pitchumani, R., "Stochastic Modelling of Nonisothermal Flow During Resin Transfer Molding", International Journal Heat Mass Transfer, **42**: (1999); p 3057–3070.

[68]Fernlund, G., Poursartip, A., Russell, J., Nelson, K., Wilenski, M., Swanstrom, F. "Process Modelling For Dimensional Control – Sensitivity Analysis of a Composite Spar Process". May 23–27 (1999); In: Proceedings of 44th Int. SAMPE Symp. and Exhibition, Long Beach, California.

[69]Jiang S., Zhang C., and Wang B., *"Optimum Arrangement of Gate and* Vent Locations for RTM Process Design Using a Mesh Distance-based *Approach",* Composites. Part A, Vol. **33**: (2002); p 471-481.

[70]Gauvin, R., and Trochu, F., *"Key Issues in Numerical Simulation for Liquid Composite Molding Processes,"* Polymer Composites, vol. **19**, No. 3: (June 1998); p 233-240.

[71]Parnas, R. S., Flynn, K. M., and Dal Favero, M. E*., "A Permeability Database for Composites Manufacturing",* Polymer Composites, Vol. **18**, No. 5: (Oct. 1997); p 623-632.

[72]Hieber, C.A., and Shen S.F. "A finite element/finite difference simulation of the injection mold filling process", J. Non-Newtonian Fluid Mesh. **7**(1): (1980); p 1-31.

[**73**]Frederick, R., Phelan, JR., "Simulation of the injection process in resin transfer molding". Polymer Composites **18**(4): (1997); p 460–476.

[**74**]Trochu, F., Gauvin, R., and Gao, D-M., *"Numerical analysis of the resin transfer molding process by the Finite Elements method".* Advantages in Polymer Technology **12**: (1993); p 329-342.

[**75**]Long, A. C., (Ed). "Composites forming technologies", Woodhead Publishing Ltd, (2007); p 344, ISBN 1 84569 033 8.

[**76**]Lawrence, J.M., Barr, J., Karmakar, R., and Advani, S.G., *"Characterization of preform permeability in the presence of race tracking",* Composites Part A: Applied Science Manufacturing **35**: (2004); p. 1393–1405.

[**77**]Bickerton, S., Sozer, E. M., Graham, P. J., and Advani, S. G., "Fabric structure and mold curvature effects on preform permeability and mold filling *in the RTM process". Part II.* Experiment. Composites: Part A, **36**: (2005); p 1128–1141.

[**78**]Penga, X.Q., Caoa, J., Chenb, J., Xuea, P., Lussierb, D.S., Liub, L., "Experimental and numerical analysis on normalization of picture frame tests for composite materials", Composites Science and Technology **64**: (2004); p 11–21.

[**79**]www.esi-group.com "Last accessed 19.09.2014".

[**80**]Endruweit, A., and Long, A. C., "Analysis of compressibility and permeability of selected 3D woven reinforcements*".* Journal of Composite Materials, **44**(24): (2010); p 2833-2862.

[**81**]Varvill, R., "Application of Unidirectional Carbon Fibre Truss Technology to the Fuselage Structure of the Skylon Spaceplane", October 1999; 50th International Astronautical Congress.

[82] Darooka, D. K., and Jensen, D. W., *"Advanced Space Structure Concepts and their Developme*nt*"*, American Insitute of Aeronautics and Astronautics, AIAA2001: (2001); p 1257.

[83] Francom, L. R., & Jensen, D. W., *"Three*-Dimensional Iso-Truss *structure",* July 1999; US Patent No. 5921048.

[84] Bildstein, M., *"Receiver Structure of a Radio Telescope",* PhD thesis 1996; University of British Columbia, Vancouver sponsored by AGRA Coast Steel Fabricators Ltd.

[85] Dow, M. B., Dexter, H. B., *" Development of Stitched, Braided and Woven Composites in the ACT Programme and at Langley Research Centre"*, 1997; NASA TP-97-206234.

[86] Schütze, R., "*Lightweight Carbon Fibre Rods and Truss Structures"*, Materials and Design, Vol **18**, Ns. 4/6: (1997); p 231-238.

[87] Lindbergh, C., *"Self – erecting aircraft structure",* US Patent No. 3940892, 1976.

[88] Mikulas, M. M. Jr, & Crawford, R. F., "Sequentially Deployable *Manoeuvrable Tetrahedral Beam",* 1985; US Patent No. 4557097.

[89] Lange, F. A., *"Connecting Apparatus",* 1987; US Patent No. 4637193.

[90] Ganssle, E. R., Samhammer, N. F., *"Modular Spacecraft Structures",* 1983; US Patent No. 4395004.

[91]Glaessgen, E.H., Raju, I.S., and Poe, C.C. Jr., "Debond Analyses of

Composites Stitched Structures"

http://techreports.larc.nasa.gov/ltrs/PDF/1998/mtg/NASA-98-icces-ehg.pdf

"Last accessed 19.09.2014" .

[92]Uozumi, T., and Kito, A., " Carbon fibre-reinforced plastic truss

structures for satellite using braiding/resin transfer moulding process",

Proceedings of Institution of Mechanical Engineering Part L: J. Materials:

Design and Applications, Vol. **221**: (2007); p 93-101.

[93]Thuis, H. G. S. J., and Biemans, C., *"De*sign, fabrication and testing of a

composite bracket for aerospace applications", Composite Structures, Vol. **38**:

(1997); p 91-98.

[94]Brown, R., "Automatic through-the-thickness braiding", 37th International

SAMPE Symposium and Exhibition, Vol. **37**: (1992); p 832.

[95]Carrion, J. E., La Fave, J. M., and Hjelmstad, K. D., *"Experimental*

behaviour of monolithic composite cuff connections for fiber reinforced plastic

box sections", Composite Structures, Vol. **67**: (2005); p 333-345.

[96]Erp, G. V., Cattell, C., and Ayers, S., *"The Australian approach to*

composites in civil engineering", Reinforced plastics, Vol. **49**, No. 6: (2005); p

20-26.

Chapter 3

Compaction and bending tests

3.1 Introduction

The first objective of this Chapter is to model with an empirical power law the compaction behaviour of the three textiles mentioned in section 2.3. In order to study race-tracking and variability, in the manufacture of the generic node the relationship of the preform thickness against pressure is required. The second objective was to measure the preform thickness variation along a 90° curved plate. This information will be used for simulating flow for a 90° model curved plate (representing the preform bending along the 90° angle) in the generic node variability model.

3.2 Background

In the RTM manufacturing process preform compaction plays a significant role in the final composite part quality and performance. With this process the preform of solid fibres is placed inside a mould which is closed and by the application of pressure the desired height and so fibre volume fraction (V_f) of the final composite part is achieved.

Considering composites, the preform compaction response represents how the fabric volume fraction changes with applied pressure. Volume fraction is a governing factor in preform permeability and therefore the fabric compaction

behaviour needs to be correctly addressed in order to solve Darcy's law eq. (1-1).

Compaction behaviour inside the mould cavity and corresponding V_f determines the local fabric permeability and so is directly related to race-tracking and preform variability. In order to address preform compaction a number of models by Chen B., et al [1] have been proposed with a paper on experimental and theoretical studies of fabric compaction behaviour in RTM. Hubert, P., Poursartip, A., [2, 3] wrote a method for the direct measurement of the fibre bed compaction curve of composite prepregs and a review of flow and compaction modelling to thermoset matrix laminate processing. Saunders, R. A., et al [4, 5] provided insights into the compaction of 2D woven fabric preforms. They modelled the yarn compaction in woven composites from a geometrical consideration without treating the fabric pressure against thickness relationship. Somashekar, A.A., et al [6] explored the non-elastic compression deformation of dry glass fibre reinforcements. Compaction on a porous media (wool fibres) was first studied in 1946 by Van Wyk, C., [7]. He developed the idea that the transverse elastic behaviour of a bundle of fibres is controlled by a fibre bending mechanism and his work was concentrated on wool compaction. Simacek P., Karbhari, V. M., et al [8, 9], made theoretical modeling of fabric compressibility based upon beam theory. Cai, Z., et al [10], used structural analysis in order to derive a nonlinear, elastic approach based on beam theory of lubricated fibre bundles in the 3D state. They considered both elastic and viscous responses of aligned transversely isotropic preforms and validated their models experimentally. Gutowski, T.G., et al [11, 12] made experiments

in composites consolidation by considering fibre deformation. Chen, Z.R.., et al [13] theorised micromechanical models for single layer and multi-layer preforms. Chen, B., et al [14] also looked at woven, multi-layer fibre preforms and considered the three stages of the compaction pressure versus V_f curve; the initial linear region, a nonlinear middle region of fibre reorganisation and a final linear compaction stage. Experimental work was carried out studying parameters of a fabric's mechanical behaviour by Matsudaira, M., and Qin, H., [15]. By analysing their experimental work they theorised models regarding the compression behaviour of fabrics and separated the compression and recovery curves of the compression load as a function of deformation into three steps. The first step of the recovery curve was approximated by linear relations. The second step was approximated by exponential relations. In the third stage of the recovery step, they concluded that instantaneous recovery was impossible.

Pearce, N., and Summerscales, J., [16] confirmed with their empirical compaction model the Quinn, J.A., and Randall, J.E., [17] fitted square root law.

Robitaille, F., and Gauvin, R., [18–20] published studies of the compaction of textile reinforcements for composites manufacturing. They observed the effects of various process parameters on both dry and wet reinforcements. Specimens were subjected to cyclic loading tests and the existence of relaxation and differing reorganization of the fibre network during compaction and relaxation. The power law suggested eq. (3-1), has been used as the base

for unsaturated and saturated empirical compaction models by Govignon Q., et al [21] in simulation of the reinforcement compaction and resin flow during the complete resin infusion process, and also by Bickerton, S., Buntain, M.J., [22], Correia, N., [23], Endruweit, A., and Long, A.C., [24].

$$V_f = \alpha_c P^{\beta} \qquad \textbf{(3-1)}$$

In eq. (3-1) V_f is the fibre volume fraction, P is the pressure, α_c and β are empirical material constants. Further verification of Robitaille, F., and Gauvin, R., [18-20] eq. (3-1) was done on Chapter 3 of Correia's, thesis, [23].

3.3 Methodology and materials

Composite process modelling requires effective materials characterisation. Testing environments need to be representative of the manufacturing method since the results will be used in simulation tools. In this way, it is necessary to understand the main factors affecting the material property and design a test routine that takes these factors into consideration. Compaction characterisation for this study was conducted in a similar fashion by Correia, N., [23]. A purpose build machined test rig, (see Fig. 3.1) consisted of a matched top moving part and a lower fixed 50mm internal diameter circular fitting, which were fixed to a dual-column, Instron tester. For consistency and to reflect previous findings on layer effects, reinforcement samples were press-cut into 50mm discs and loaded into the lower fixed plate sample fitting cavity, see Fig. 3.2. Dry samples of three different architecture woven fabrics were compacted

at a rate of 1kN/second, from zero to 10kN static load capacity. An auto-ranging load cell was used to measure force.

Fig. 3.1: Compaction testing rig.

To enable the determination of absolute distance (specimen height H) between the upper moving plate and the lower fixed plate cavity of the rig during testing, a linear displacement transducer was used in order to calculate the fibre volume fraction at each state of compression according to eq. (3-2) Endruweit, A., [24].

$$V_f = \frac{m}{\rho A H} \tag{3-2}$$

where m is the specimen mass, A is the specimen area, and ρ is the density of the carbon fibres. With the combination of (3-1) and (3-2):

$$H_{fabricthickness} = \alpha P^{-\beta} \tag{3-3}$$

In equation (3-3) the preform thickness H is related to a given compaction

pressure P, where $\alpha = \dfrac{m}{\rho A}\dfrac{1}{\alpha_c}$ and β are empirical material constants.
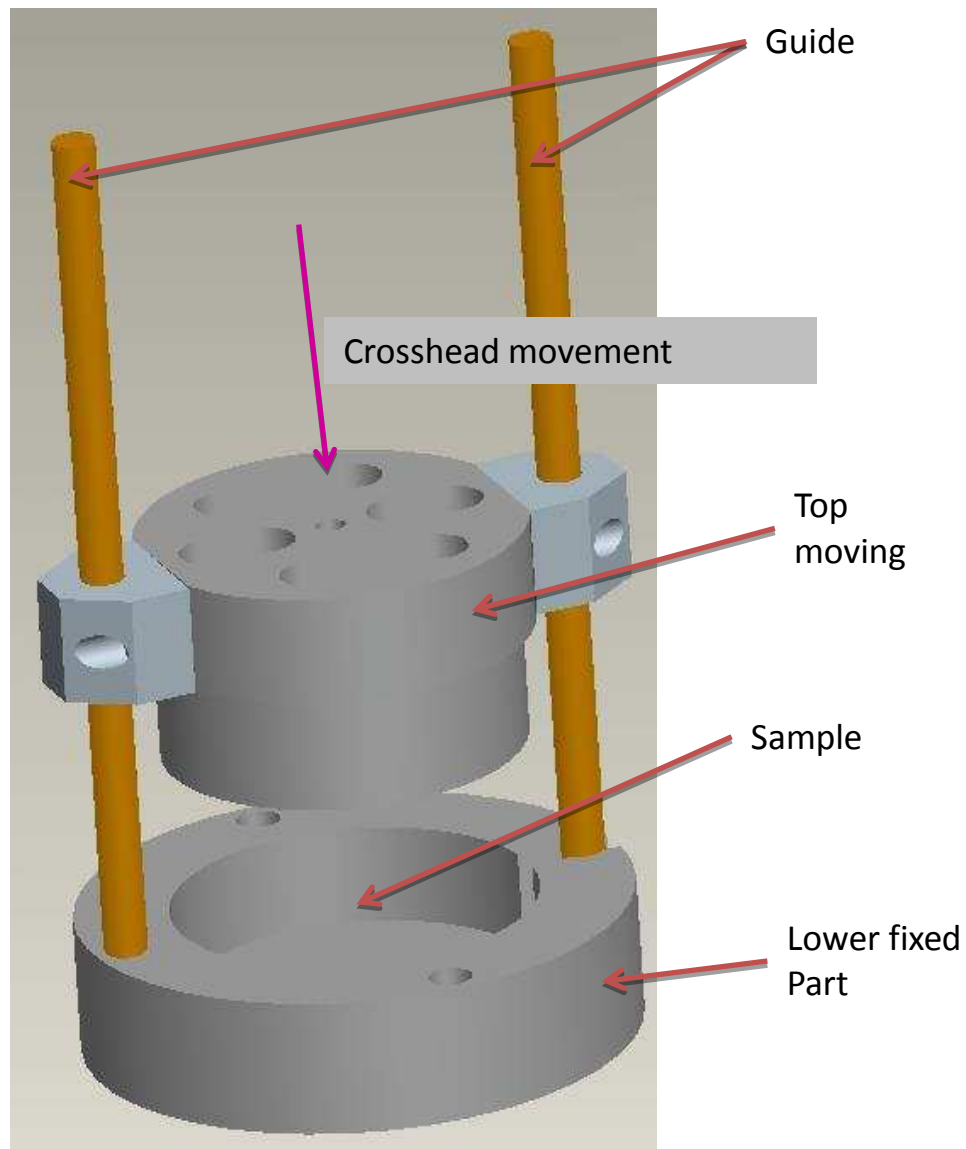
Fig. 3.2: Schematic of fabric compression test.

The materials tested are presented in Fig. 3.3 and the material properties in table 3.1 that follows.
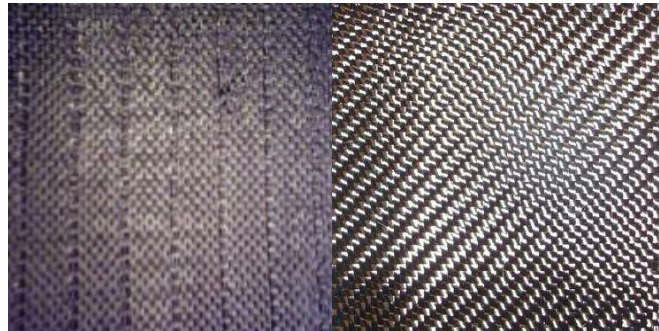
i) 3D woven HTS40 F13   ii) 2/2 Twill
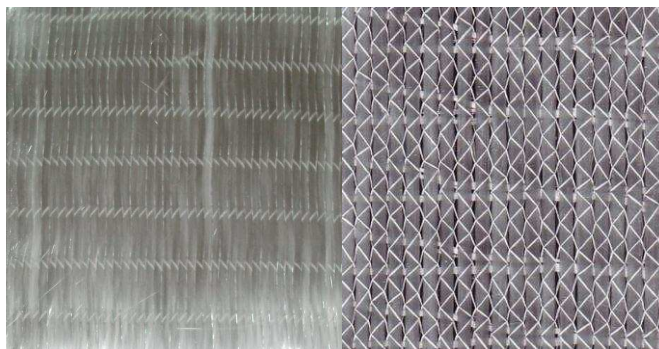
iii) Triaxial (one side)   iv) Triaxial (stitched other side)

Fig. 3.3: Reinforcements used for compaction tests.

The ACTS generic node fabric (fig. 3.4) is one layer composed of eight weft yarns with measured thickness of (5.85±0.05) mm. The density of the 3D woven HTS40 F13 carbon fibre's textile provided by Sigmatex is $\rho=1760$ Kg/m³.

Table 3.1: Textiles with properties used in compaction tests.

Textile type	Textile commercial name	Manufacturer	Aerial mass (Kg/m^2)
3D- woven	HTS40 F13	Sigmatex Ltd	5.3 (8-layers)
3D- woven	HTS40 F13	Sigmatex Ltd	2.284 (4-layers)
3D- woven	HTS40 F13	Sigmatex Ltd	1.713 (3-layers)[1]
2/2 Twill	38391 (12K)	Car reinforcements	0.686 (1-layer)
Triaxial	FGE 0/±45°	Formax	1.2 (1-layer)

The aerial mass was calculated as the ratio of mass, m, over surface area, A, and it was found to be: 5.30 Kg/m². The fibre volume fraction was calculated from equation (3-2). The 3D woven fabric known as Tenax® HTS40 F13 is made of commercial high strength aerospace grade carbon fibres (12K for yarn) 4-layer and 3-layer variant of the same fabric was also tested.
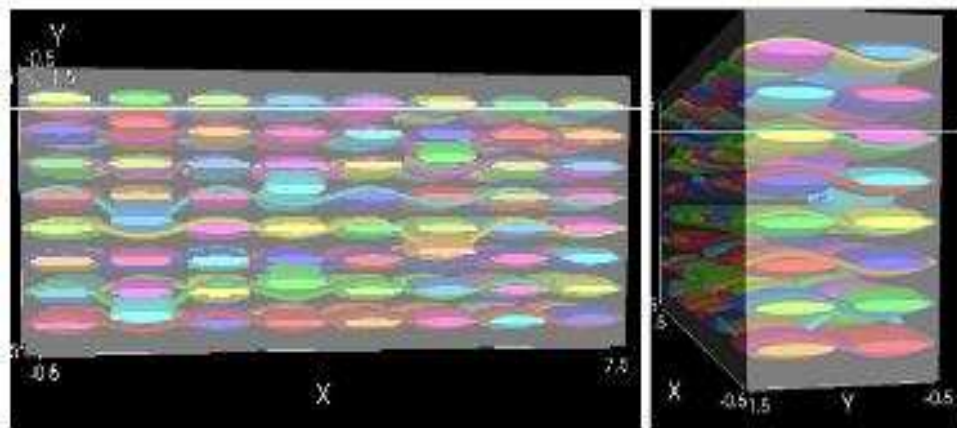
Fig. 3.4: Design of the Sigmatex textile used for permeability measurements. Image generated using Tex-Gen software. X axis coincides with the weft direction and Y axes coincide with the warp direction of the fabric.

---

[1]ACTS 3-layers 3D woven HTS40 F13 fabric is not provided by the manufacturer therefore all material properties in following chapters extrapolated in comparison to measurements done at ACTS 4-layers 3D woven HTS40 F13 fabric.

3.4 Compaction results and discussion

After preform characterisation was completed the results of compaction tests were collected to a PC, to which the Instron tester was connected. The empirical power law was then fitted and the pressure (bar) against fabric thickness (mm) plotted. The results are presented in Fig. 3.5, (nesting is considered negligible due to the fact that we have 3D woven fabric).

Plot showing H_{ACTS} fabric Thickness (mm) against Pressure (Bar) with three curves:

8-layers: $y = 5.1643x^{-0.071}$, $R^2 = 0.9939$

4-layers: $y = 2.6051x^{-0.073}$, $R^2 = 1$

3-layers: $y = 1.9538x^{-0.073}$, $R^2 = 1$
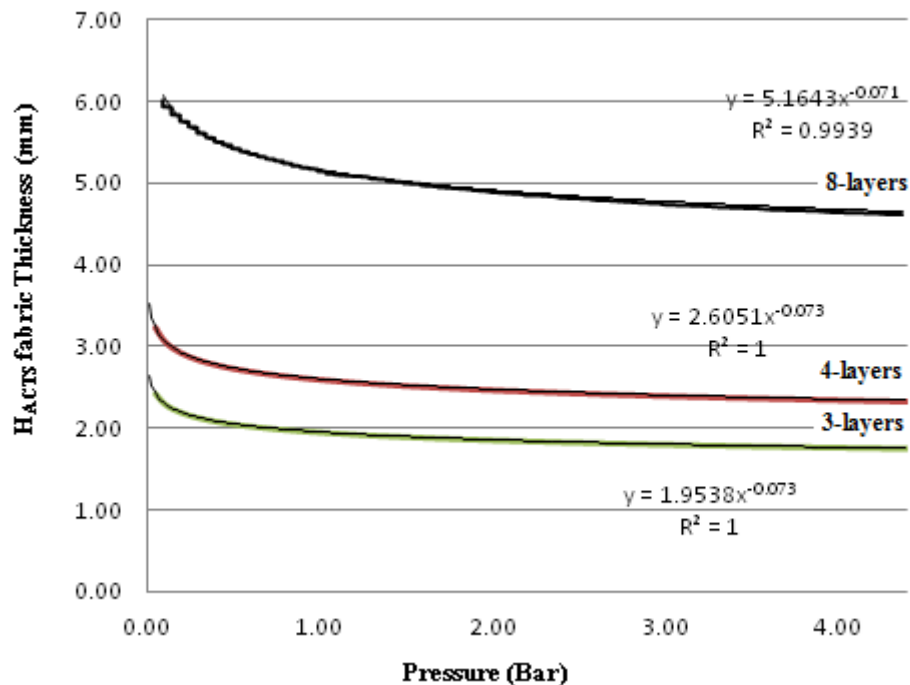
Fig. 3.5: Plot of ACTS (HTS40 F13) 8 layers (upper), 4 layers (middle), and 3 layers (lower) curve for fabric thickness against applied pressure.

In the same way, the 2/2 twill and the triaxial fabric, was fitted with eq. (3-3). Nesting of plies was not considered as previous studies by Pearce, N., and Summerscales, J., [16], Quinn, J.A., and Randall, J.E., [17], Robitaille, F., and Gauvin, R., [18-20], Govignon, Q., et al [21], Bickerton, S., et al [22] had suggested this to be negligible, for two neighbouring layers of the same plain

Spiridon Koutsonas

woven fabric. Therefore by considering two layers of thickness eq. (3-3) was fitted for the 2/2 twill and the triaxial fabric. The calculation was conducted similarly to the ACTS fabric. The results are presented in Figures 3.6 and 3.7 respectively:
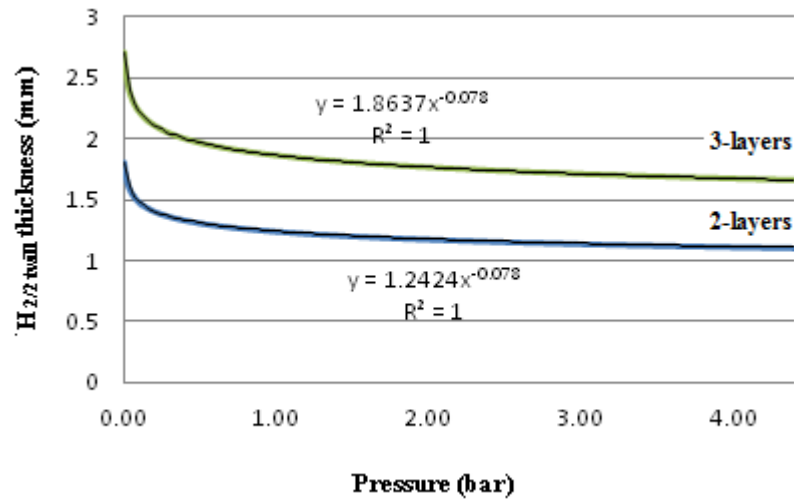
Fig. 3.6: Plot of 2/2 twill 3 layers (upper), 2 layers (lower) curve for preform thickness against applied pressure.
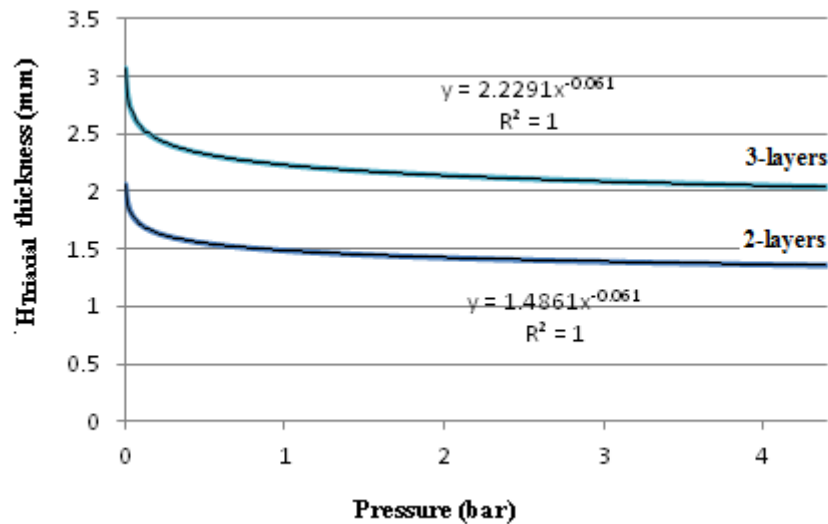
Fig. 3.7: Plot of triaxial 3 layers (upper), 2 layers (lower) curve for preform thickness against applied pressure.

The experimental results with the above three fabrics are collected and presented on Table 3.2.

Table 3.2: Compaction tests power law fitting.

Preform	Layers	H_{height} (mm)
ACTS fabric	4-layers	$2.6051\,P^{(-0.073)}$
ACTS fabric	3-layers	$1.9538\,P^{(-0.073)}$
2.2 Twill	3-layers	$1.8637\,P^{(-0.078)}$
2.2 Twill	2-layers	$1.2424\,P^{(-0.078)}$
Triaxial	3-layers	$2.2291\,P^{(-0.061)}$
Triaxial	2-layers	$1.4861\,P^{(-0.061)}$

In this way it will be possible to evaluate the preform thickness at any pressure value. Compaction results from Table 3.2 have been used for a model generation in Chapter 5, racetrack prediction of the 90° curve plate in Chapter 6, and ACTS node variability modelling in Chapter 8.

3.5 Bending

When a fibrous preform bends around a radius it is compacted radially at the bend part due to in-plain tension caused by friction between the compacted preform and the tool as discussed by Dong, C., [25]. In order to measure the bending behaviour relevant to the generic node in the ACTS project an aluminium 3D base with a 90° curved plate and 3.2mm radius (same material and geometry as the node mould presented on Fig. 7.9 (a), (b)) was designed and constructed, shown on Fig. 3.8. The aluminium base dimensions on xyz

axis were 48×19x39mm. The thickness of the aluminium base was 19 mm and the radius 3.2mm, as per the ACTS node aluminium mould.

Fig. 3.8: Aluminium curve plate xyz axis 48×19x39mm used for bending tests.

3.6 Experimental non-contact techniques

3.6.1 Photography

The specimen was bent around the aluminium base and a series of experiments in order to measure the fabric thickness variation of the fixed samples, were carried out unsuccessfully. Photography was used as a starting method, shown on Fig. 3.9.

(a)   (b)

Fig. 3.9: Aluminium curved plate bended (a) with 2/2 twill 1-layer, (b) with ACTS 8-layer carbon fibre preform on millimetre scale paper.

Photography was not good enough on this case to measure with precision the fabric's compaction along the 90° curved plate as shown in Fig. 3.9. The triaxial glass fabric was even more difficult because of the glass fibres reflection with the aluminium curve plate used for bending tests.

3.6.2 Optical microscopy

Following this, optical microscopy was used to measure the fabric's compaction, as shown Fig. 3.10.
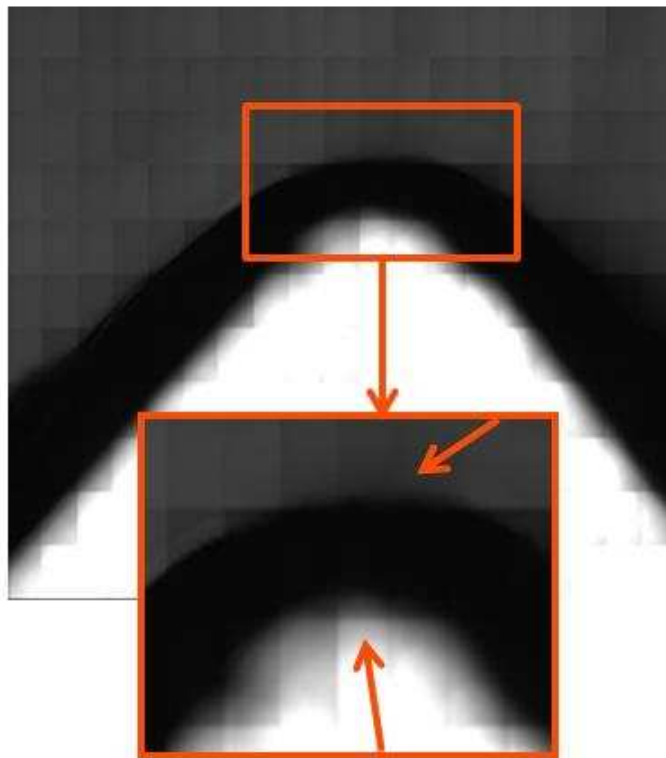
Fig. 3.10: Optical microscopy on aluminium curved plate base with 2/2 twill fabric (arrows shown the zones of uncertainty).

The optical microscopy images as shows Fig. 3.10 revealed again localized fabric compression along the bend radii of the 2/2 twill and HTS40 F13

preform. However there was always an uncertain zone between the aluminium and the fabric. This is due to the fact that the carbon fabric on its extremities had lost its geometrical properties because of bending and there were free yarn bundles in this zone. The same conditions were observed on the upper part of the specimen. So the determination of the compacted area was unclear or in any case showed high inaccuracy. The triaxial glass fabric was not possible to be visualised with the optical microscopy technique. Another problem was that the sample dimensions on xyz axis 48×19x39mm were big and therefore the magnification was not good.

Due to these drawbacks it was decided to carry on with Coordinate Measuring Machine (CMM) contact measurement method.

3.7 Coordinate Measuring Machine (CMM) tests

A coordinate measuring machine (CMM) is a 3D device for measuring the physical geometrical characteristics of an object. Measurements are defined by a probe attached to the third moving axis of this machine.

Probes may be mechanical, optical, laser, or white light, amongst others. In modern machines, the gantry type superstructure has two legs and is called a bridge. This moves freely along a granite table with one leg following a guide rail attached to one side of the granite table. The opposite leg (outside leg) simply rests on the granite table following the vertical surface contour [26, 27].

Fig. 3.11: Mitutoyo coordinate measuring machine, with scanning probe, (right).

Scanning probe surface techniques are methods that use a physical probe to scan the specimen. A line of the surface is obtained by mechanically moving the probe on the specimen, and recording the probe-surface interaction as a function of position. A scanning measurement instrument is capable of achieving high accuracy and high speed in scanning measurement [26]. Using scanning probes of CMM inspection is more accurate than the conventional touch-probe method and also faster [26]. A purpose machined test rig consisting of Mitutoyo CMM and a scanning probe is shown in Fig. 3.11. A similar model of CMM is available at the University of Nottingham. The precision of measurements using the above scanning device is of the order of 0.9 μm according to specifications in respective manufacturer datasheets [27]. With the use of the above mentioned instrumentation the bending behaviour of the 3 textiles in Table 3.1 was tested. Firstly, the curve plate aluminium base was fixed and scanned in order to define the 3D coordinate system of reference as shown in Fig. 3.12. Each sample was fixed on the aluminium 90° curve

plate with an adhesive in order to reproduce the bending behaviour inside the mould.

<div align="center">(a)   (b)</div>

Fig. 3.12: CMM test on: (a) on the aluminium 90° curve plate used as zero (reference), (b) on bend 2/2 twill 3-layers sample 5 results presented on Fig. 3.13 (c).

Secondly, a number of least five bending tests (warp, weft) with the textiles mentioned in table 3.1 (4-layers ACTS fabric, 3 layers with 2/2 twill and triaxial fabric) were conducted. The output file was collected on a PC to which the CMM was connected.

3.7.1 CMM results

The output bending test data (2-lines for each specimen) had to be reprocessed in order to calculate the fabric thickness for each specimen.

Bending tests results are presented in following Fig. 3.13 (a) to 3.13 (e) where the gap between the fabric and the upper mould h_{gap} is plotted against the angle ϕ along the curved plate bend.
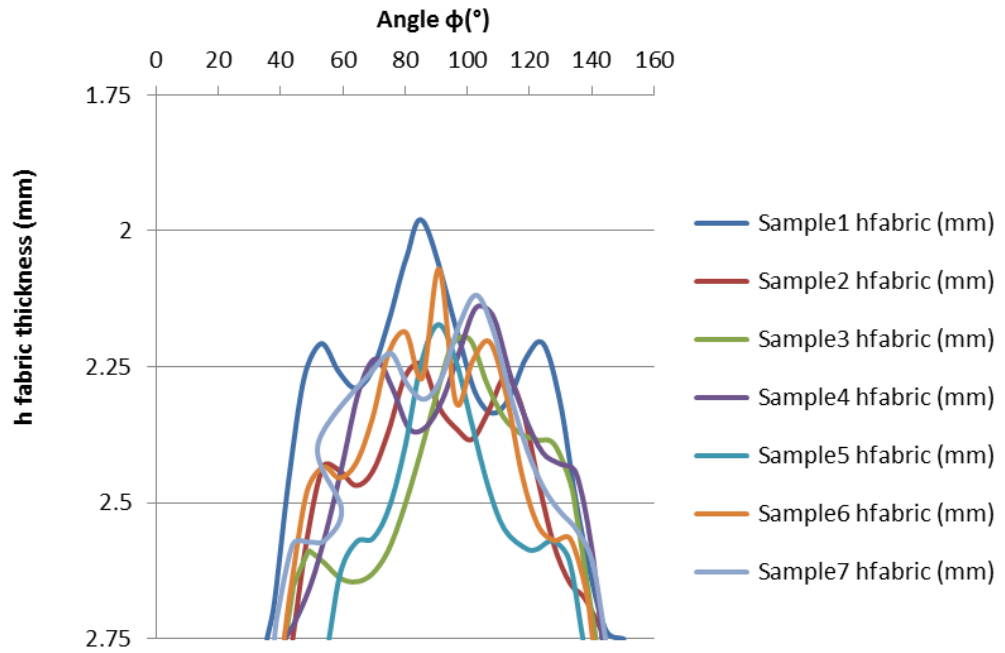
Fig. 3.13 (a): Measured fabric thickness variation on bending with HTS40 F13 3D woven samples warp 4-layers preform.
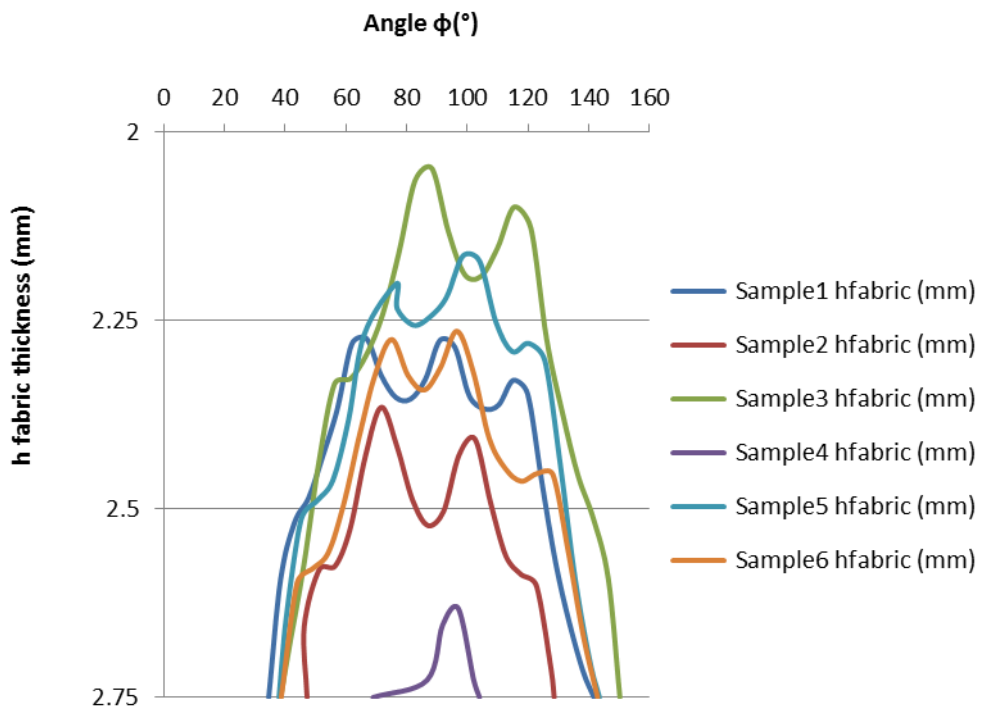
Fig. 3.13 (b): Measured fabric thickness variation on bending with HTS40 F13 3D woven samples weft 4-layers preform.
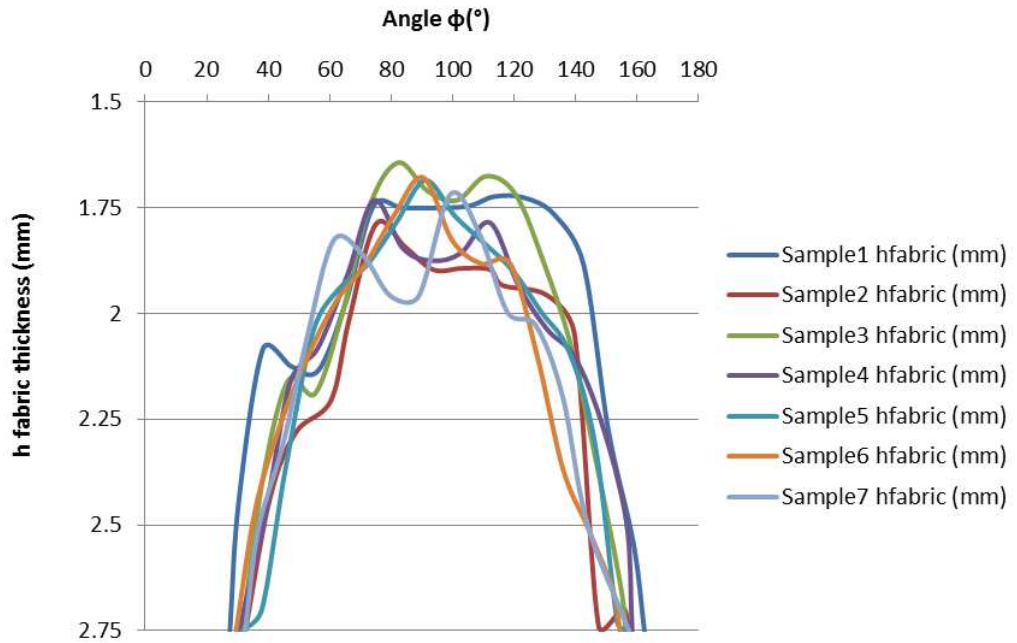
Fig. 3.13 (c): Measured fabric thickness variation on bending with 2/2 twill samples 3-layers preform.
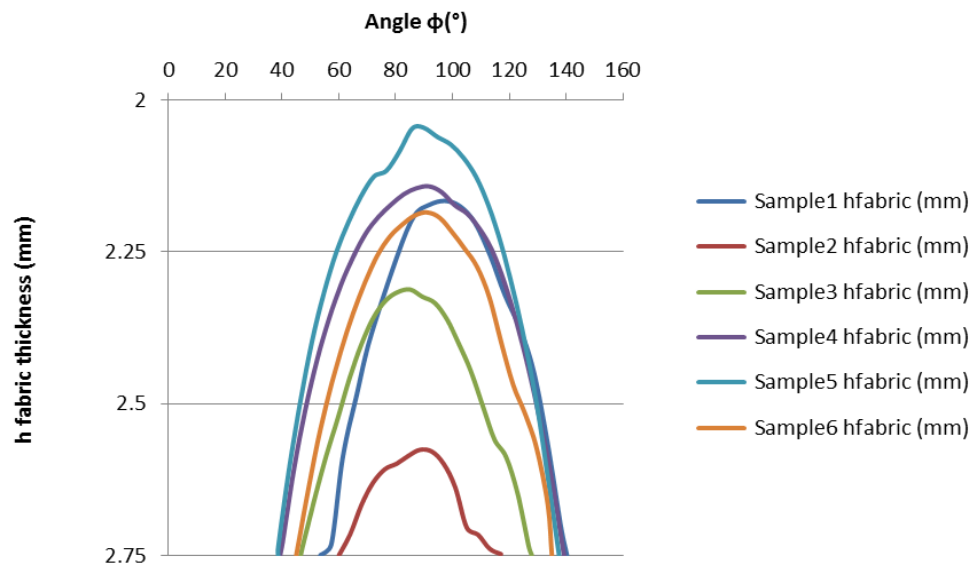
Fig. 3.13 (d): Measured fabric thickness variation on bending with triaxial warp samples 3-layers preform.
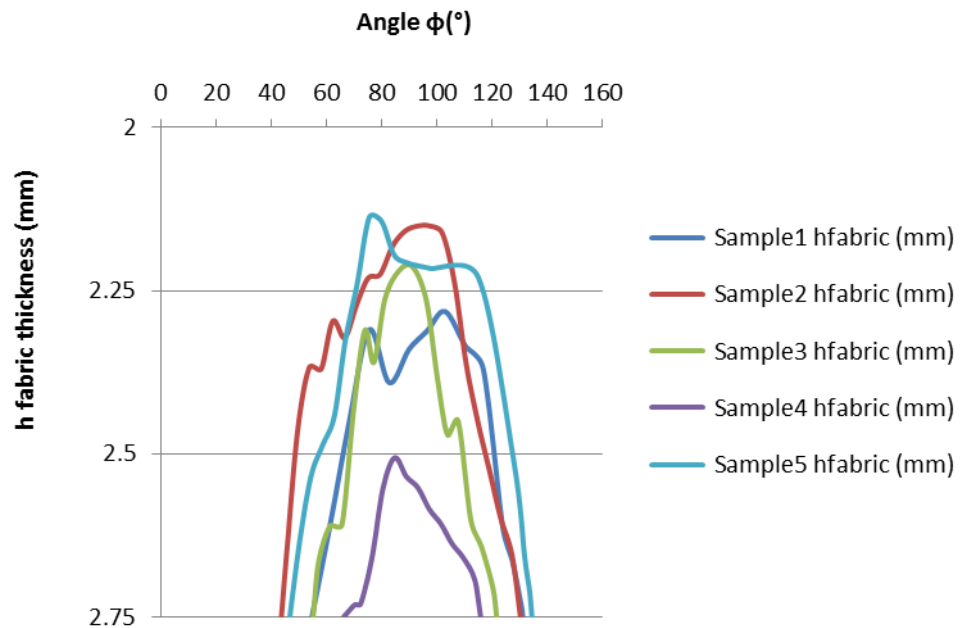
Fig. 3.13 (e): Measured fabric thickness variation on bending with triaxial weft samples 3-layers preform.

3.8 CMM results discussion

Preform thickness measured variations Figures 3.13 (a) – 3.13 (e) were used to generate tables with h_{min} fabric thickness on the 90° bend with approximation up to ±0.1 mm (show in Appendix B Tables B (a) - B (e)).

The preform thickness inside mould is 2.75mm but on the bend angle was measured to be lower in all tested fabrics. Therefore the h_{min} fabric thickness on bend Appendix B Tables B (a) - B (e) revealed the gap height (h_{gap}) variation on the bend.

All preform measured fabric thickness on bend presented in Fig. 3.13 (a) -3.13 (e) section 3.7.1 were considered in Chapter 5 for fitting with the model developed in order to predict the gap height and in Chapters 6, 8 for racetrack and variability simulations modelling on RTM.

3.9 Conclusion

In Chapter 3 experimental non-contact and contact techniques were used in order to investigate the compaction and bending behaviour of three different composites textiles. Firstly through-thickness against compression tests were carried out on an Instron testing machine and the compressibility of the tested fabrics was measured. The empirically derived power law models allowed the determination of the height, H(mm), of the preforms against pressure, P(bar), and $\alpha = \dfrac{m}{\rho A} \dfrac{1}{\alpha_c}$ and β empirical material constants. With the use of the CMM the bending behaviour was measured for each of the tested fabrics. The final results provided detailed information about the compaction behaviour and thickness reduction in bending of the textiles. These data will be used to validate a model for bending (Chapter 5) and so input to simulations of resin flow with PAM-RTM$^{®}$ (Chapters 6, 8).

In this chapter:

- Generated tables with h_{min} thickness on the 90° bend from the samples of the tested preforms.

References

[1]Chen, B., Lang, E. J., Chou, T-W., "Experimental and theoretical studies of *fabric compaction behavior in resin transfer molding''* Materials Science and Engineering: A **317** (2001); p 188–196.

[2]Hubert, P., Poursartip, A., *"A method for the direct measurement of the fibre bed compaction curve of composite prepregs''* Composites: Part A **32**: (2001); p 179–187.

[3]Hubert, P., Poursartip, A., *"A review of flow and compaction modelling* relevant to thermoset matrix laminate processing". Journal of Reinforced Plastics and Composites **17**(4): (1998); p 286–318.

[4]Saunders, R. A., Lekakou, C., and Bader, M. G., *"Compression in the* processing of polymer composites 1. A mechanical and microstructural study for *different glass fabrics and resins''* Composites Science and Technology **59** (1999); p 983-993.

[5]Saunders, R. A., Lekakou, C., and Bader, M. G., *"Compression and* microstructure of fibre plain woven cloths in the processing of polymer *composites''* Composites Part A **29**A (1998); p 443-454.

[6]Somashekar, A.A., Bickerton, S., Bhattacharyya, D., *"Exploring the non-elastic compression deformation of dry glass fibre reinforcements''* Composites Science and Technology **67** (2007); p 183–200.

[7]Van Wyk, C., "A note *on the compressibility of wool".* The Journal of the Textile Institute, **37** (1946); p 285-292.

[8] Simacek, P., Karbhari, V.M., Journal of Reinforced Plastics Composites. **15** (1996); p 86–122.

[9] Karbhari, V.M., Simacek, P., Journal of Reinforced Plastics Composites. **15** (1996); p 837–861.

[10] Cai, Z., and Gutowski, T.G., "The 3-D Deformation-Behavior of a *Lubricated Fiber Bundle"*. Journal of Composite Materials, **26**(8): (1992); p 1207-1237.

[11] Gutowski, T.G., Morigaki, T., Cai, Z., "The consolidation of laminate *composites"*. Journal of Composite Materials **21**(2): (1987); p 172–88.

[12] Gutowski, T.G., Kingery, J., Boucher, D., "Experiments in composites *consolidation: fiber deformation"*. Society of Plastic Engineers. Annual Technical Conference (1986); p 1316–20.

[13] Chen, Z.R., Ye, L., and Kruckenberg, T., "A micromechanical compaction *model for woven fabric preforms". Part I: Single layer.* Composites Science and Technology, **66**(16): 2006; p 3254-3262.

[14] Chen, B., Cheng, A.H.D., and Chou, T.W., "A nonlinear compaction *model for fibrous preforms"*. Composites Part A. Applied Science and Manufacturing, **32**(5): (2001); p 701-707.

[15] Matsudaira, M., Qin, H., "Features and mechanical parameters of a *fabrics mechanical behaviour"*. Journal of the Textile Institute **86**(3): (1995); p 476-86.

[16] Pearce, N., Summerscales, J., "The compressibility of a reinforcement *fabric"*. Composites Manufacturing, **6**: (1995); p 15-21.

[17]Quinn, J.A., and Randall, J.E., "Compliance of composite reinforcement

materials". Proceedings of the Institution of Mechanical Engineers, **3**: (1990);

p 105-112.

[18]Robitaille, F., and Gauvin, R., "Compaction of textile reinforcements for

composites manufacturing. I: Review of experi*mental results"*. Polymer

Composites, **19**(2): (1998); p 198-216.

[19]Robitaille, F., and Gauvin, R., "Compaction of textile reinforcements for

composites manufacturing. II: Compaction and relaxation of dry and H2O-

saturated woven reinforcements". Polymer Composites, **19**(5): (1998); p 543-

557.

[20]Robitaille, F., and Gauvin, R., "Compaction of textile reinforcements for

composites manufacturing. III. Reorganization of the fiber network". Polymer

Composites, **20**(1): (1999); p 48-61.

[21]Govignon, Q., Bickerton, S., and Kelly, P.A., "Simulation of the

reinforcement compaction and resin flow during the complete resin infusion

process". Composites Part a-Applied Science and Manufacturing, **41**(1):

(2010); p 45-57.

[22]Bickerton, S., and Buntain, M.J., "Modeling forces generated within rigid

liquid composite molding tools. P*art B: Numerical analysis"*. Composites Part

a-Applied Science and Manufacturing, **38**(7): (2007); p 1742-1754.

[23]Correia, N., Thesis *"Analysis of the vacuum infusion moulding process"*

University of Nottingham, School of Mechanics Materials, Manufacturing

Engineering and Management Chapter **3**: (April 2004); p 40-73.

[24]Endruweit, A., and Long, A.C., "Analysis of Compressibility and

Permeability of Selected 3D Woven Reinforcements". Journal of Composite

Materials **44**(24): (2010); p 2833-2862.

[25]Dong, C., "Model development for the formation of resin-rich zones in

composites processing". Composites: Part A **42** (2011) p 419–424.

[26]http://en.wikipedia.org/wiki/Coordinate-measuring_machine. "Last

accessed 13.04.2014".

[27]http://www2.mitutoyo.de/fileadmin/user_upload/pdf/prospekte/0ENGLIS

H/kmg_en/Strato_Apex_PRE.pdf. "Last accessed 13.04.2014".

Chapter 4

Permeability measurement

4.1 Introduction

The objective of this chapter is to measure the permeability of the three textiles introduced in section 2.3 against the V_f for the in-plane (K_1, K_2) and the through thickness permeability (K_3). This is in order to model 3D race-tracking along a 90° curved plate preform bending in Chapter 6 and the variability of the generic node in Chapters 7, 8. Therefore the development of a fitting equation curve in order to predict the relationship between the preform permeability at any fibre volume fraction is one of the most important issues.

4.2 Background

The permeability is defined as the property of a porous material which characterizes the ease with which a fluid may be made to flow through the material due to an applied pressure gradient. Flow through porous media was first analysed by Darcy and characterised by Darcy's law, equation (1-1). It is extremely difficult to predict analytically the permeability of a preform with a complicated architecture. Several models have been proposed that relate the permeability to fibre volume fraction reported by Endruweit, A., et al [1-4], Lawrence, J. M., et al [5] with the characterization of preform permeability in the presence of race tracking. Weitzenböck, J.R., [6, 7, 11] studied the radial flow permeability and 3D permeability. Baiju, Z. B., and Pillai, K. M., [8] made an experimental investigation of the effect of fibre-mat architecture on the unsaturated flow in LCM. Carter, E.J. et al [9] wrote a paper on data

validation procedures for the automated determination of the 2-dimensional permeability tensor of a fabric reinforcement. Ferland, P., et al [10] Concurrent Methods for Permeability Measurement in RTM. Gauvin, R., et al [12, 13] with two research papers studied firstly key issues in numerical simulations for LCM and permeability and secondly flow simulation through fibre reinforcement. Hammami, A., et al [14] wrote a journal paper on directional permeability measurement of deformed reinforcement. Lekakou, C., et al [15] provided a research paper on measurement techniques and effects on in-plane permeability of woven cloths in RTM. Models for permeability measurement were provided by Kozeny, J. [16], Carman, P.C., [17],

Kozeny J. firstly, made a series of studies on the capillary transportation of groundwater in soil [16], and developed a model for the permeability of a randomly packed porous bed based on geometric parameters. Later Carman, P.C. [17] modified his model, resulting in the Kozeny-Carman (K-C) equation (4-1) which relates the variation of pressure along the medium to the fluid velocity.

$$\frac{\Delta P}{L} = \frac{180 v_0 \mu}{\varepsilon^2_r D^2_p} \frac{(1-\Phi)^2}{\Phi^3} \qquad \textbf{(4-1)}$$

ΔP is the change in pressure, L is the bed height, v_0 is the superficial velocity, μ is the fluid viscosity, Φ is the bed porosity, ε_r is the sphericity of the random particles, D_p is the diameter of the random particles.

In another notation the above form can be seen written as:

$$K = \frac{r^2}{4C_0} \frac{(1-V_f)^3}{V^2_f} \qquad \textbf{(4-2)}$$

where K is the bed permeability, r is the radius of the random particles, V_f is the volume fraction of the particles in the bed, and C_0 is the material Kozeny constant.

By defining the constant coefficient C in (4-2) in equation as:

$$C = \frac{r^2}{4C_0} \qquad \text{(4-3)}$$

one can rewrite:

$$K = C\frac{(1-V_f)^3}{V_f^2} \qquad \text{(4-4)}$$

Where the preform permeability depends only upon a constant C and the fabric's V_f. as reported in three paper research by Endruweit, A., et al [2-4].

The constant C in equation (4-4) is a material-dependant geometrical description of the randomly packed bed architecture, which includes terms for the shape (k_0) and tortuosity (L_e/L) of the pore path.

$$C = k_0(\frac{L_0}{L})^2 \qquad \text{(4-5)}$$

k_0 is the shape factor, L_e is the effective length of flow, L is the superficial length. Equation (4-4) has been applied to the laminar flow of resin through fibrous preforms during liquid composite infusion by Endruweit, A., et al [1-4], Lawrence, J.M., et al [5], Carman, P.C., [17], Gebart, B.R., et al [18].

Gebart, B.R., et al [18] derived models for intra-yarn permeability in the aligned and transverse directions for UD fabric. By replacing the fibre radius term in the shape factor k_0 with the yarn radius, the K-C law can be applied to

98

inter-yarn flow, allowing determination of a preform's macro permeability. Pomeroy, R., [19] characterised permeability of continuous filament mats for RTM.

Williams, J.G., et al., [20] early work on permeability looked at liquid and gas flow through aligned fibre beds. Their experimental study involved unidirectional silane glass fibres packed into glass hollow tubes. In an initial unsaturated experiment, nitrogen gas was passed through the tubes parallel to the sized UD fibres. The coherence caused by the sizing was believed to be responsible for a significant non-uniformity in fibre distribution giving rise to large porosity variations. This was confirmed by photo-micrographic analysis of cured cross sections of the packed tube beds, and resulted in low permeability values when calculated from the K-C equation. The higher observed flow rates compared to those predicted by the K-C approach were also attributed to the variance in porosity. Water, ethanol, silicone and mineral oils, glycerol and an epoxy resin were also passed through the fibres in both unsaturated and pre-saturated states. It was noted that re-distribution of the UD fibres was reduced significantly, in particular by the liquids with higher surface tensions (epoxy resin and glycerol). It was also suggested that the additional presence of air pockets in the dry tests, caused by the increased liquid surface tension, resulting in higher resistance to liquid flow and giving slower flow rates compared to the pre-wetted experiments.

Young, W-B., [21] determined permeability for 3-dimensional non isothermal mould filling simulations in RTM.

At present the most commonly used techniques in order to measure the permeability of a fibrous material are the advancing front technique and the steady state permeability technique.

In the advancing front technique, a fluid is introduced into a dry preform at either a constant flow rate or a constant pressure condition. The flow front may be measured by visual means and/or by the use of pressure transducers. The permeability is then calculated by the use of Darcy's law. This technique has the advantage of accounting for capillary and gravitational effects, which are essential in either low flow rate or low pressure injection processing techniques. However, it is time consuming because of the use of a new preform for every fibre volume fraction tested.

Steady state permeability is measured under constant flow rate conditions using a saturated preform. The pressure differential across the preform is measured, and the permeability is calculated using Darcy's law. This technique has the advantage of the need for only one preform to measure the permeability of all the fibre volume fractions desired. The disadvantage is that it sometimes does not resemble the actual composite processing conditions, as reported by Endruweit, A., [1-4], Lawrence, J.M., et al [5], Weitzenböck, J.R., et al [6, 7], Babu, Z. B., et al [8].

In this thesis the permeability of three different textiles (Fig. 3.3) is measured. The in-plane permeability at, at least three different fibre volume fractions was measured with the advancing front technique with constant inlet pressure, and the through thickness permeability was measured with a steady state permeability technique.

4.3 Apparatus

4.3.1 In-plane permeability K_1, K_2 measurements

The instrumentation used for this experimental investigation includes:

(i)   The in-plane permeability test rig.

(ii)   A pressure pot able to provide a constant pressure 1-7 bar.

(iii)   Trent HDX30 oil as the infusion liquid in order to simulate the commercial ACG MVR444 resin that will be used for the generic node manufacturing process.(viscosity data Appendix H)

(iv)   A precision balance.

(v)   A personal computer with LABVIEW software connected to the permeability rig (see Fig. 4.1-4.3).

The tool for the experiments consisted of two horizontal plates. The base plate is prepared for holding circular specimens with diameter D = 400 mm. When the tool is closed, the height of the cavity h can be adjusted in steps of Δh = 0.2 mm by inserting spacer frames, which ensure that the plates stay parallel. The fabric specimens are clamped between both plates and compressed to achieve a predefined thickness h. The radius R_0 of the central circular injection gate in the base plate is 5 mm. Thereafter the fabric specimens were injected with Trent HDX30 oil from the central hole at the bottom of the base plate under constant pressure (3 bar).
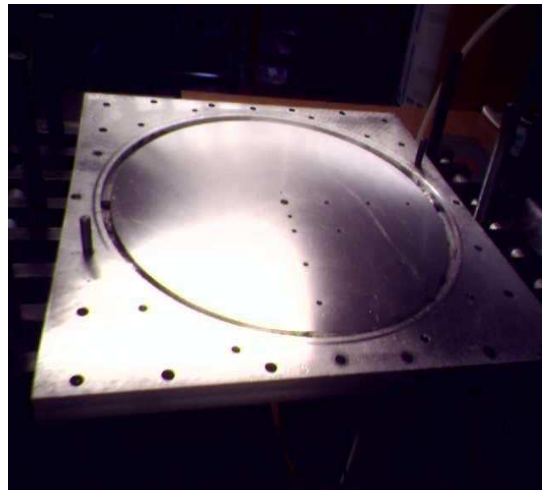
(a)
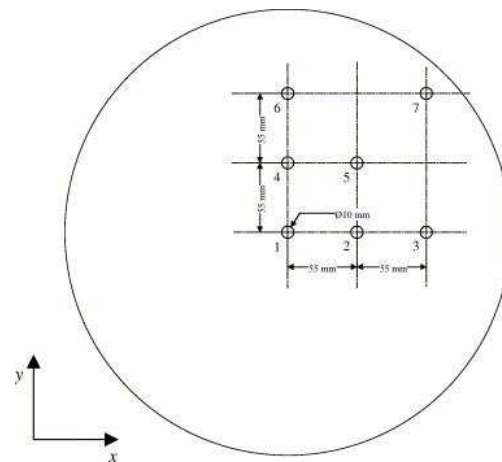
(b)

Fig. 4.1: Permeability radial rig. The injection gate is the central hole in the metallic plate; we may observe the pressure traducers in the lower plate (a). Schematic arrangement of the injection gate and pressure transducers in the in-plane flow tool (b).
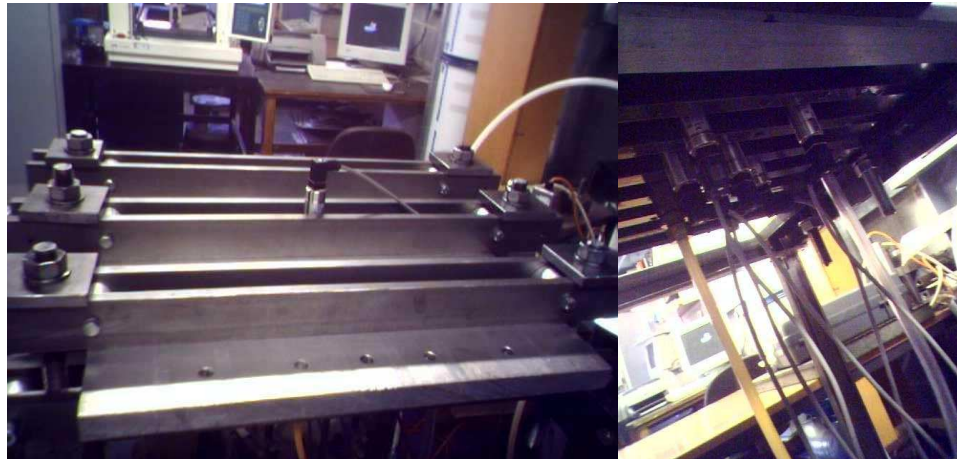
Fig. 4.2: In-plane permeability rig metallic cover provided constant thickness to the fabric. Also shown is the pressure transducer in the centre of the square metallic plate (left), Permeability rig lower view; observe the injection tube (yellow) in the centre of the lower plate and the pressure transducers to detect the oil flow front (right).
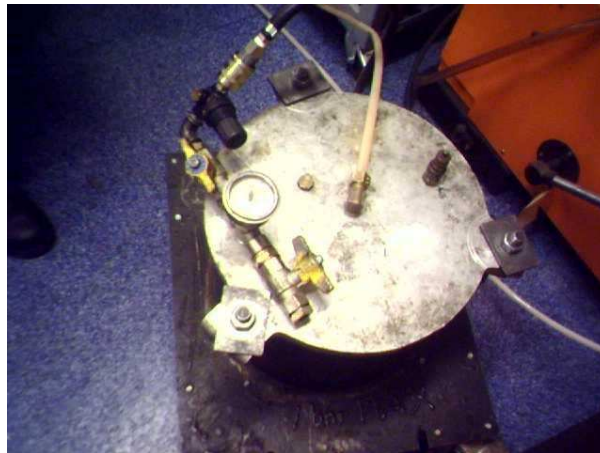
Fig. 4.3: The pressure pot with the meter that provides oil with constant pressure to the permeability rig. Experimental in-plane permeability was calculated from the flow front arrival times from the pressure readings against time during the experiment with the use of the eq. (4-4). All readings were transferred to a PC with LABVIEW software connected to the permeability rig (Fig 4.1, 4.2).

The flow front position was measured in three directions the weft (x), warp (y)

axes and at 45º between weft and warp. The 45º angle measurement between

the weft and warp direction allowed the angle (θ) between K_1 and the weft direction to be calculated for the fabric.

Fig. 4.6 shows the fabric before and after the in-plane permeability tests. Furthermore a schematic representation of the maximum principal permeability K_1 in weft direction and K_2 in warp direction is presented in Fig 4.6.

4.3.2 Through Thickness permeability K_3

The instrumentation used for the through thickness experimental investigation includes:

(i)   The through thickness steel cylinder test tool.

(ii)   A piston pump for constant flow rate.

(iii)   An oil container with oil with a constant viscosity.(Appendix H)

(iv)   A high precision balance ±0.1g.

(v)   A PC with LABVIEW software connected to the permeability rig.

(a)

(b)

Fig. 4.4: Through thickness permeability measurement apparatus (a), specimen holder of the through thickness permeability apparatus (b).

Fig. 4.5: ACTS fabric specimen before the through thickness permeability K_3 measurement.

The apparatus for the through thickness permeability measurement consists

of a steel cylinder with diameter of 250mm and height of 150mm with an

internal cylindrical cavity of 80mm diameter. The cylinder is split into an upper and lower part plate as seen in Fig. 4.4.

4.4 Methodology

4.4.1 Experimental K_1, K_2 in-plane permeability

Over the last two decades experimental permeability measurements has been extensively studied (reported on section 4.2) by Weitzenböck, J.R., et al [6, 7], Babu, Z. B., et al [8], Carter, E.J. et al [9], Ferland, P., et al [10], Gauvin, R., et al [12, 13], Hammami, A., et al [14], Lekakou, C., et al [15].

In this work the bidirectional flow experimental method was used for the in-plane permeability measurements: With this method the test fluid was injected from the centre of the mould cavity and the analytical solution was based on Darcy's law eq. (1-1). For an isotropic scenario, the flow front would advance as a circular shape, and the following solution has been proposed:

$$(\frac{R_f}{R_0})^2 \left[2\ln(\frac{R_f}{R_0}) - 1 \right] + 1 = \frac{4tK\Delta P}{\Phi \mu R_0^2} \qquad \textbf{(4-6)}$$

where: R_f is the flow front radius at time t, R_0 inlet radius, i.e. the radius of the hole where the reinforcement stack at the centre injection point, ΔP is the pressure gradient, t is the elapsed time, μ the fluid viscosity, Φ the porosity and K the isotropic permeability ($K = K_x = K_y$).

For the anisotropic case, $K_x \neq K_y$ results in the flow front having an elliptical shape. Several simplification methods exist in the literature as reported by Endruweit, A., et al [1-4], Lawrence, J. M., et al [5]. The procedures for one of simplified solutions are shown, which transforms the anisotropic permeability into an equivalent isotropic system, where the Laplace equation is utilized. A

point in the original domain is transformed to a new coordinate system: (x) (y) => (x_e y_e) by the relations:

$$x_e = \left(\frac{K_y}{K_x}\right)^{\frac{1}{4}} x \text{ and } y_e = \left(\frac{K_y}{K_x}\right)^{\frac{1}{4}} y \qquad \textbf{(4-7)}$$

In this equivalent isotropic system, the flow front is represented by a circular shape with $R = R_{xe} = R_{ye}$. Along with the relationship between x and y in original domain, the solution for permeability can be obtained by the following set of equations:

$$K_e = \sqrt{K_x K_y}$$

$$R_{x0,e} = \left(\frac{K_y}{K_x}\right)^{\frac{1}{4}} R_0 \qquad \textbf{(4-8)}$$

$$K_e = \frac{\Phi \mu R_{x0,e}^{\,2}}{4t\Delta P}\left\{(\frac{R_x}{R_0})^2\left[2\ln(\frac{R_x}{R_0})-1\right]+1\right\}$$

where R_x is the semi-major axis of the flow front ellipse at time t, K_e the tested preform permeability and $R_{x0,e}$, is the equivalent injection gate dimension in direction R_x for a circular injection gate in elliptical co-ordinates reported by Endruweit, A., et al [1-4], Lawrence, J. M., et al [5].

With the above method a series of five specimens for each different volume fractions for each preform, was tested.

ACTS 3D woven HTS40 F13 preform required a better determination of the K_1, K_2, K_3 (due to the fact that the node was made of this textile) therefore this was tested for four different V_f. 2/2 twill, triaxial was tested for three different V_f.

Tested specimens for 3D woven HTS40 F13 and triaxial fabric are presented in

Fig. 4.6.
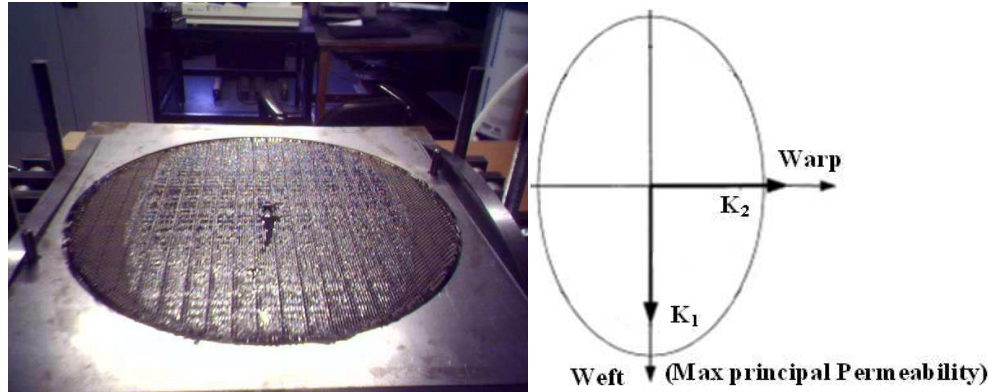
a)   3D woven HTS40 F13 sample
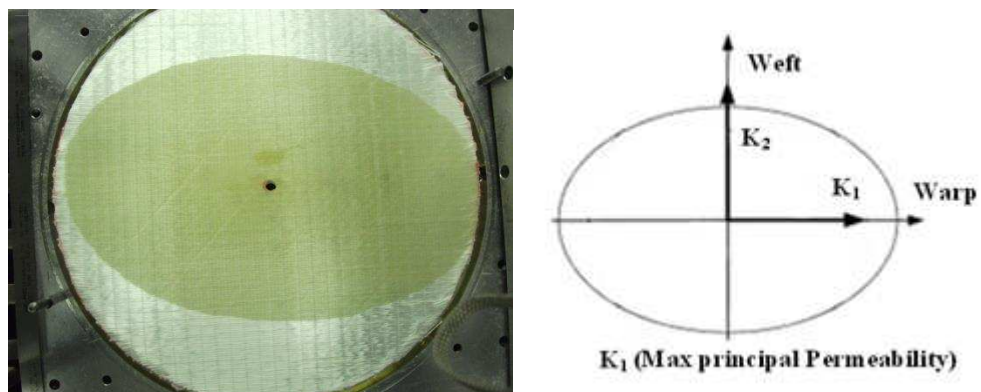
b)   Triaxial sample

Fig. 4.6: a) 3D woven HTS40 F13 sample with V_f=52%, weight=0.667Kg after the permeability test (left), schematic representation of the maximum principal permeability K_1 in weft direction and K_2 in warp direction for the tested sample (right).

b) Triaxial sample with V_f=60%, weight=0.672Kg after the permeability test (left), schematic representation of the maximum principal permeability K_1 in warp direction and K_2 in weft direction for the tested sample (right).

4.4.2 Experimental K_3 through-thickness permeability

The need to manufacture by the RTM process increasingly complex, large,

thick components has made the knowledge of through-thickness permeability

an important issue. Therefore research attention has been drawn to three-

108

dimensional flow experiments as proposed by Endruweit, A., et al [1-4], Weitzenböck, J.R., et al [11], Carman, P.C., [17], Young, W-B., [21].

The channel flow apparatus is the most common method to measure permeability in the through-thickness direction. Darcy's law plays a governing role in computing the permeability as for two-dimensional flow. Inside the through thickness permeability measurement cylinder there are two circular plates with holes to support the specimen. The specimen is first weighed with a high precision balance in order to calculate accurately the V_f, and is then fixed inside the 80mm cavity. Spacers with different thickness are used in order to achieve the desired fibre volume fraction V_f. The V_f calculation was done in the same way as for in the in-plane permeability measurements with equation (3-2). A piston pump with constant flow rate supplies through one side (upper side) inside the cylindrical cavity, and the oil flows through the porous medium into the other side of the sample chamber in order to ensure continuous fluid flow rate inside the specimen. Near the upper and lower side of the steel cylinder (Fig. 4.4) are two pressure transducers to measure the pressure difference along the flow direction. The numerical difference information of the two pressure transducers is then transferred to a PC with LABVIEW software and two graphs of pressure against time are automatically plotted. When the two curves show that there is a constant pressure drop the test is stopped. Thereafter from Darcy's law, K_3 is calculated since all the other factors such as fluid velocity (constant) and Trent HDX30 oil viscosity are known.

4.5 Results

4.5.1 In-plane permeability K_1, K_2

A series of measurements at different fibre volume fractions with the three preforms was carried out as explained in the previous section. Five specimens of each preform with different V_f were tested. Thereafter K_1, K_2 and K_1/K_2 were calculated. With the above experimental output a series of tables were created (Tables: 4.1 to 4.7). The angle θ between weft and K_1 was observed in each case. This measurement indicated the maximum principal permeability K_1 of each tested fabric. From the experimental results it is seen that K_1, K_2 permeability values decrease with increasing volume fraction according to the curves in Figures 4.7 and 4.8.

4.5.2 In-plane permeability K_1, K_2 for 3D woven HTS40 F13

From the experimental results it is seen firstly that K_1, K_2 decrease with increasing volume fraction according to the curves in Fig. 4.7, 4.8 and secondly that the ratio K_1/K_2 for increasing volume fractions is approximately constant (as shown in Table 4.1) the weft direction. In-plane reproducibility and data consistency for K_1 and K_2 were observed at the higher volume fractions 0.59, 0.63 with small standard deviation (SD). Higher errors were observed at lower volume fractions 0.52, 0.55. The angle θ between weft (K_1) and warp (K_2) was observed to be 5 ° at V_f of 0.59 and less than that in any other case, as show in Table 4.1, Fig. 4.7-4.8. This indicates that the maximum principal flow direction is approximately parallel to the weft.

Table 4.1: Experimental θ, K_1, K_2, K_1/K_2 of 3D woven fabric results.

$\theta(°)$	V_f	$K_1 / 10^{-10}$ m^2	SD	$K_2 / 10^{-10}$ m^2	SD	K_1/K_2	SD
-4	0.52	9.373	0.846	4.854	1.166	1.967	0.298
1	0.55	5.207	1.737	2.221	1.084	2.452	0.349
5	0.59	1.823	0.686	0.589	0.083	3.233	1.578
4	0.63	1.113	0.115	0.52	0.035	2.152	0.368

In order to ensure a more accurate RTM simulations at different zones and volumes fractions for the generic node an empirical power law fitting equation was adopted. With the use of equations $K_1 = 0.005V_f^{-11.55}$, $K_2 = 0.0013V_f^{-12.41}$ values were closer to the experimental K_1, K_2 permeability results than those resolved from the K-C equation (4-4).

Fig. 4.7: Power law fitting equation for K_1 experimental permeability for the 3D woven fabric as a function of the volume fraction V_f. Comparison with the Kozeny-Carman [16, 17] model (orange) curve.

Fig. 4.8: Power law fitting equation for K_2 experimental permeability for the 3D woven fabric as a function of the volume fraction V_f. Comparison with the Kozeny-Carman [16, 17] model (orange) curve.

4.5.3 In-plane permeability K_1, K_2 for 2/2 twill fabric

From the experimental results it is seen firstly that the values K_1, K_2 decrease with increasing volume fraction according to the curves in Fig. 4.9, 4.10 and secondly the ratio K_1/K_2 for increasing volume fractions is approximately constant see Table 4.2.

Flow in the 2/2 twill preform has approximately a circular shape. In this case in-plane reproducibility and data consistency for K_1 and K_2 were observed at the higher volume fraction 0.58 with small standard deviation (SD). Higher errors were observed at lower volume fractions 0.44, 0.5, see Table 4.2, Fig. 4.9, 4.10.

Table 4.2: Experimental θ, K_1, K_2, K_1/K_2 of 2/2 twill fabric results.

$\theta(°)$	V_f	K_1	SD	K_2	SD	K_1/K_2	SD
100	0.44	11.355	2.508	8.956	1.897	1.271	0.12
-18	0.5	2.216	0.473	1.631	0.372	1.373	0.194
101	0.58	0.499	0.126	0.455	0.114	1.095	0.026

112

Again in this case in order to ensure more accurate RTM simulations at different zones and volumes fractions for the modelling a power law fitting equation was adopted.
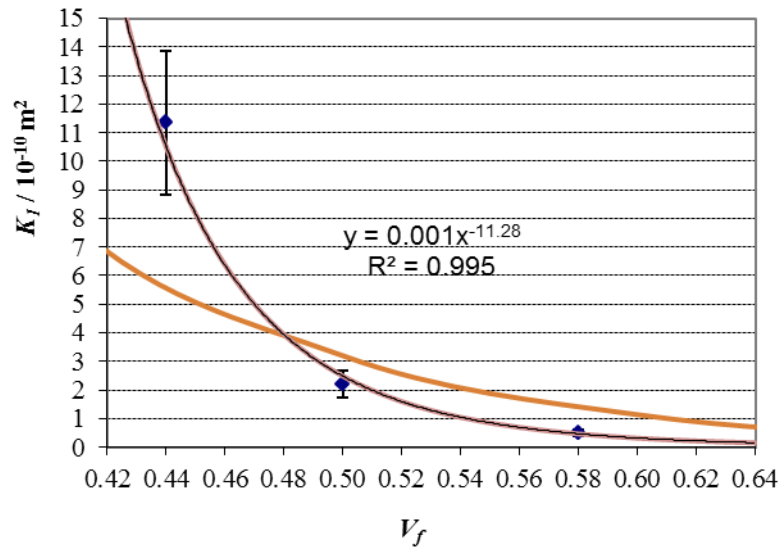
Fig. 4.9: Power law fitting equation for K_I experimental permeability for 2/2 twill fabric as a function of the volume fraction V_f. Comparison with the Kozeny-Carman [16, 17] model (orange) curve.
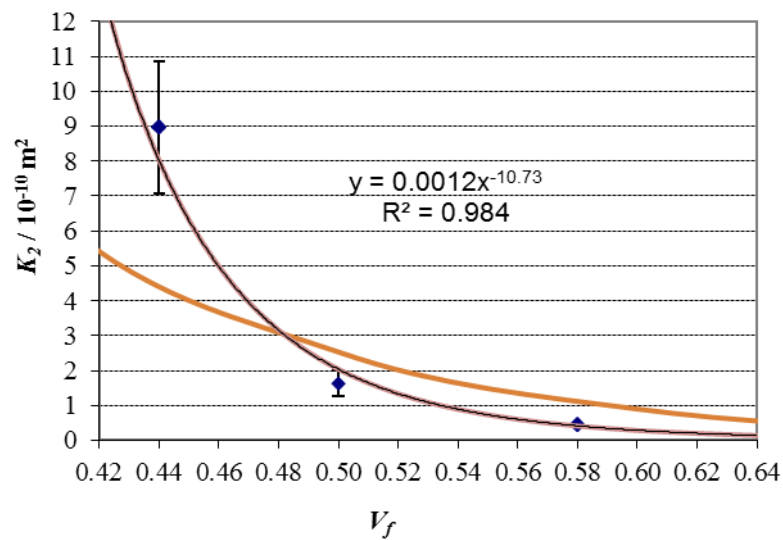
Fig. 4.10: Power law fitting equation for K_2 experimental permeability for the 2/2 twill fabric as a function of the volume fraction V_f. Comparison with the Kozeny-Carman [16, 17] model (orange) curve.

113

The modelling equations $K_1 = 0.001 V_f^{-11.28}$ and $K_2 = 0.0012 V_f^{-10.73}$ yielded

permeability values closer to the experimental K_1, K_2 permeability results than

those resolved from the K-C equation (4-4).

4.5.4 In-plane permeability K_1, K_2 for triaxial fabric

From the experimental results it is seen firstly that K_1, K_2 decrease with

increasing volume fraction according to Fig. 4.11, 4.12 and secondly the ratio

K_1/K_2 for increasing volume fractions is approximately constant see Table 4.3.

For the triaxial preform the axial fibres are in the warp direction, hence this

is the maximum principal flow direction. Also in this case, in-plane

reproducibility and data consistency for K_1 and K_2 were observed at the higher

volume fraction 0.6 with small standard deviation (SD). Higher errors were

observed at lower volume fractions 0.46, 0.53. The angle θ between warp (K_1)

and weft (K_2) was observed to be 83º at 0.53 of V_f and 79º, 81º at 0.46 and 0.6

successively, see Table 4.3, Fig. 4.11, 4.12.

Table 4.3: Experimental K_1, K_2, K_1/K_2 of triaxial fabric results.

$\theta(°)$	V_f	K_1	SD	K_2	SD	K_1/K_2	SD
79	0.46	5.01	0.968	2.244	0.569	2.267	0.277
83	0.53	1.394	0.312	0.365	0.075	3.829	0.547
81	0.6	0.35	0.051	0.122	0.01	2.884	0.478

Again in this case in order to ensure more accurate RTM simulations at

different zones and volumes fractions a power law fitting equation was adopted.
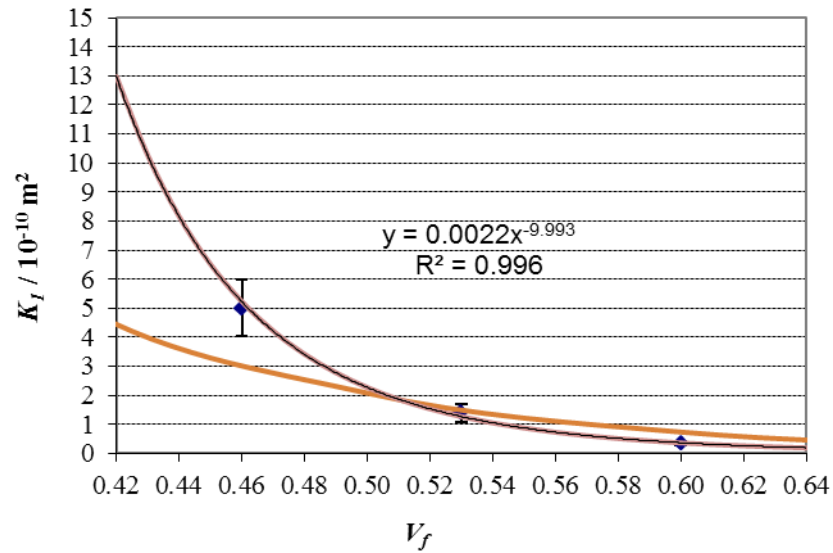
Fig. 4.11: Power law fitting equation for K_1 experimental permeability for the triaxial fabric as a function of the volume fraction V_f. Comparison with the Kozeny-Carman [16, 17] model (orange) curve.
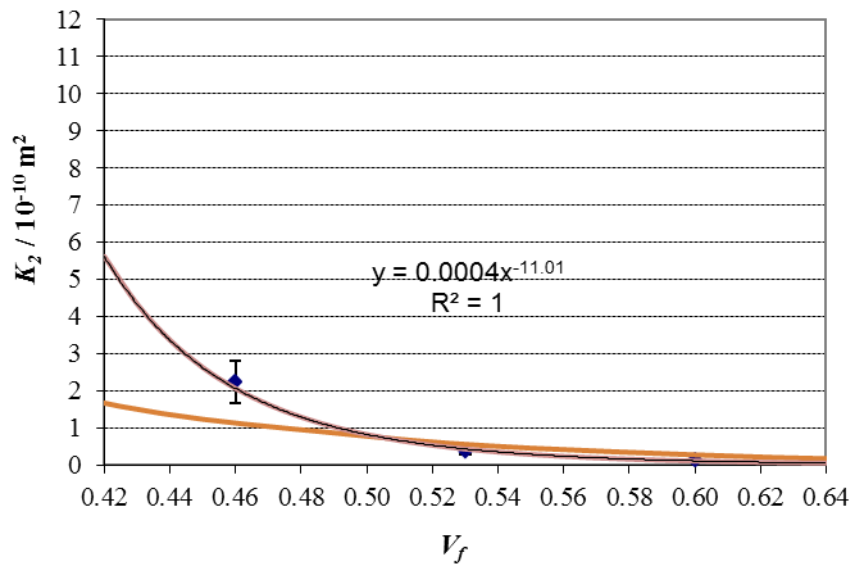
Fig. 4.12: Power law fitting equation for K_2 experimental permeability for the triaxial fabric as a function of the volume fraction V_f. Comparison with the Kozeny-Carman [16, 17] model (orange) curve.

In this case the power law $K_1 = 0.0022V_f^{-9.993}$ and $K_2 = 0.00043V_f^{-11.01}$ produced better fit to the experimental permeability K_1 and K_2 than those coming out of the K-C model.

4.6 Through-thickness permeability K_3

4.6.1 Through-thickness permeability K_3 for 3D woven HTS40F13

By the use of the appropriate experimental set up (see section 4.3.2), a series of specimens at different volume fractions (V_f) of 0.5, 0.54, 0.58, 0.6 respectively were measured for through-thickness permeability.

The experimental results are provided in Table 4.4 and Fig. 4.13.

Table 4.4: Experimental K_3 of 3D woven fabric results.

V_f	K_3 (10^{-12} m^2)	SD
0.5	8.405	1.083
0.54	5.515	0.191
0.58	5.83	0.968
0.6	3.05	0.863

From the experimental results it is seen that the K_3 values decrease with increasing volume fraction as in Fig. 4.13.

These are compared with the Kozeny-Carman model. From the graph it appears that the empirical power law for the 3D woven HTS40 F13 is closer to the experimental results in lower volume fractions up to $V_f = 0.58$ whereas in higher volume fractions $V_f > 0.58$ the K-C equation seems to provide a better fit.
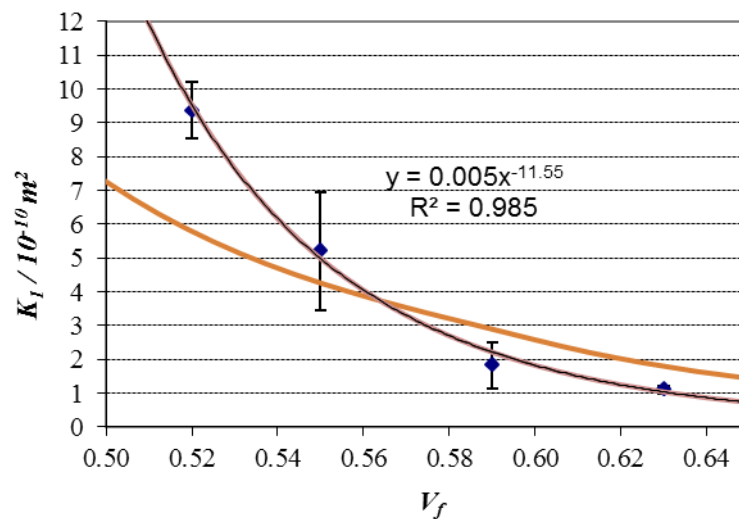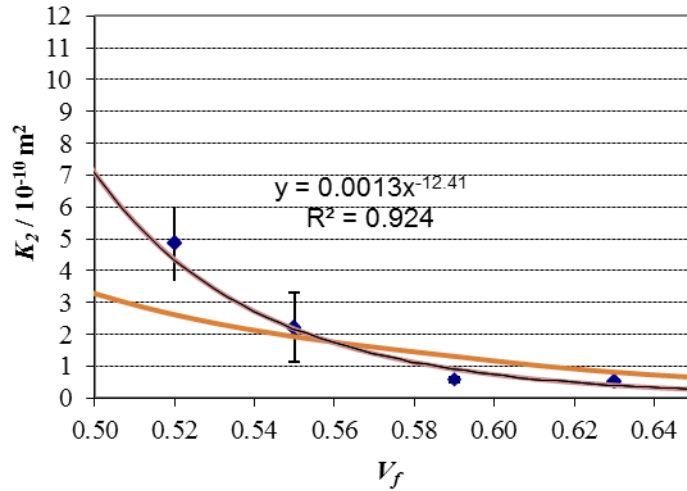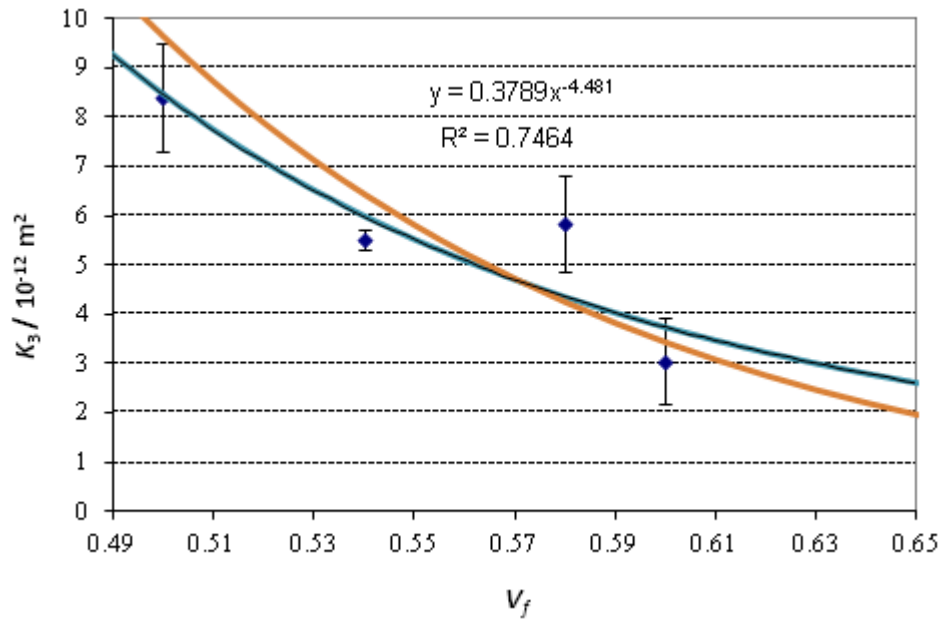
Fig. 4.13: Power law fitting equation for K_3 experimental permeability for the 3D woven HTS40 F13 carbon fabric as a function of the volume fraction V_f. Comparison with the Kozeny-Carman [16, 17] model (orange).

Therefore again in order to ensure consistency with K_1 and K_2 on RTM simulation at different zones and volume fractions, fitting through a power law was again attempted (Fig. 4.13).

Based on the fit provided by $K_3 = 0.3789 V_f^{-4.481}$ the permeability values were used for RTM simulations at different zones and volumes fractions.

4.6.2 Through-thickness permeability K_3 for 2/2 twill fabric

A series of specimens at different volume fractions V_f of 0.42, 0.47, 0.55 respectively, has been used to measure the through-thickness permeability. The experimental results are presented in Table 4.5 and Fig. 4.14. From of the 2/2 twill both table and graph it is seen that K_3 decreases with increasing volume fraction.

Table 4.5: Experimental K₃ of 2/2 twill fabric results.

V_f	K_3 (10^{-12} m^2)	SD
0.42	15.282	5.263
0.47	12.836	4.324
0.55	2.705	0.799

Comparison of the experimental results of the 2/2 twill, with the Kozeny-Carman model shows a better fit of the K-C equation at lower volume fractions up to V_f =0.47 but at higher volume fractions $V_f > 0.46$ the power law $K_3 = 0.05939 V_f^{-6.644}$ is seen to approach the experimental measurement better. Hence the permeability values resulting from this equation were used for RTM simulations.
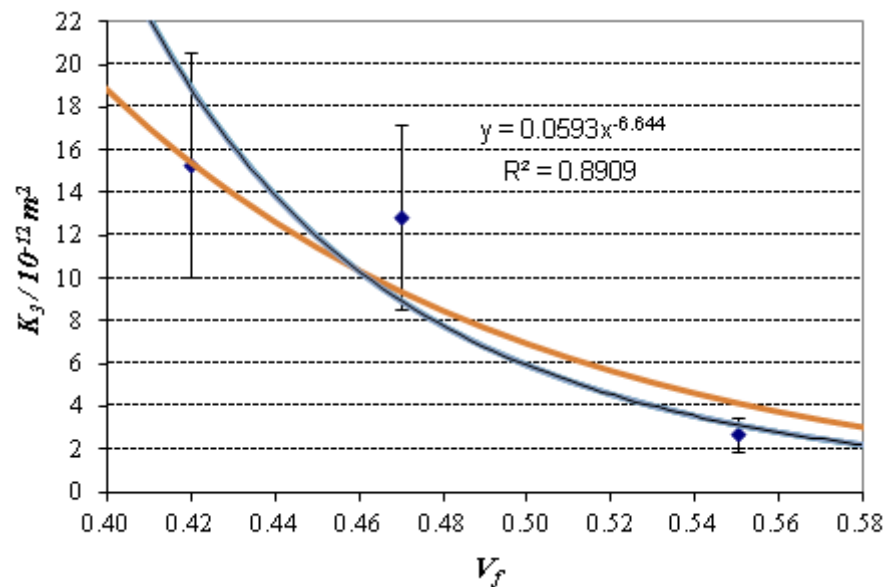
Fig. 4.14: Power law fitting equation for K₃ experimental permeability for the 2/2 twill carbon fabric as a function of the volume fraction V_f. Comparison with the Kozeny-Carman [16, 17] model (orange).

4.6.3 Through-thickness permeability K_3 for triaxial fabric

Using the triaxial fabric, a series of specimens at volume fractions V_f 0.46, 0.53 and 0.6 were tested to assess the through-thickness permeability (shown on Table 4.6 and Fig. 4.16).

It is seen that K_3 permeability values decrease with increasing volume fraction according to Fig. 4.15.

Table 4.6: Experimental K_3 triaxial fabric results.

V_f	K_3 (10^{-12} m^2)	SD
0.46	2.65	1.19
0.53	1.823	1.194
0.6	0.815	1.193

From Fig. 4.15 it is seen that the power law $K_3 = 0.0945 V_f^{-4.396}$ for the triaxial preform is closer to the experimental results for lower volume fractions up to $V_f = 0.52$ whereas at higher volume fractions $V_f > 0.52$ the K-C equation is seen to approach the experimental data better.

Hence the permeability values of the above equation were used in RTM simulations in different zones and volume fractions for the 90° curve plate and the node.
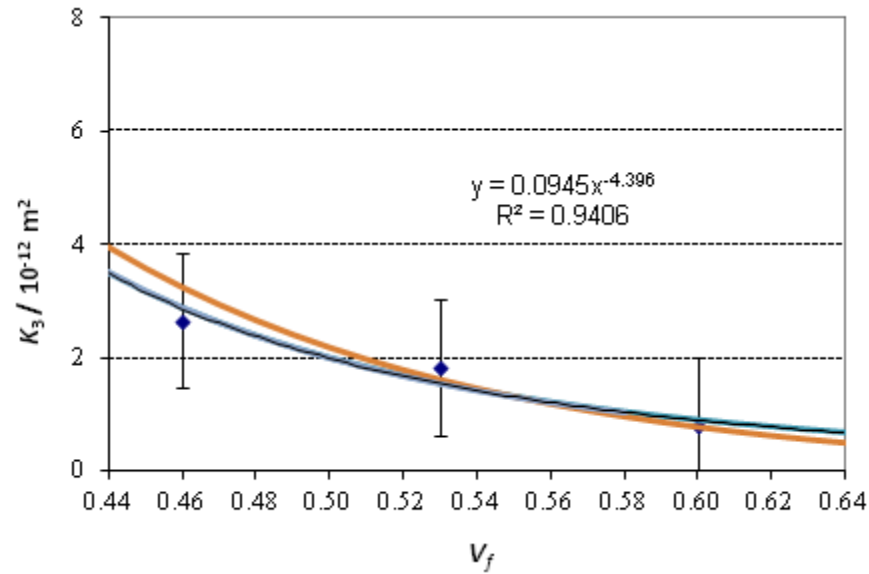
Fig. 4.15: Power law fitting equation for K_3 experimental permeability for the triaxial glass fabric as a function of the volume fraction V_f. Comparison with the Kozeny-Carman [16, 17] model (orange).

Therefore equation $K_3 = 0.0945V_f^{-4.396}$ permeability values were used for RTM simulations.

4.7 Discussion

The permeability of the 3D woven HTS40 F13 fabric that will be used for the fabrication of the generic ACTS node was measured. By increasing the fibre volume fraction for the in-plane permeability a decrease in K_1 (maximum principal permeability, weft direction) and K_2 (minimum permeability, warp direction) was observed. For the above volume fractions no unfilled fabric regions were observed. The graphs of K_1, K_2 against the volume fraction gave high standard deviations at lower volume fractions in between 52% and 55%. Reproducibility and data consistency was observed for the higher volume fractions see Fig. 4.7, 4.8. The ratio K_1/K_2 was measured against fibre volume fraction and observed to be constant. By increasing the volume fraction for the

through-thickness permeability a decrease in K_3 was observed, see (Fig 4.13).

The K_3 permeability for the above 3D woven HTS40 F13 fabric was measured

to be two orders of magnitude lower than the in-plane permeability, and in the

region of 10^{-12} m^2. From the above results it is concluded that the new

Sigmatex 3D woven HTS40 F13 textile can be used at a fibre volume fraction

of $V_f \geq 55\%$ as data are generally more consistent with less scatter suggesting a

lower possibility of defect formation due to manufacturing process variability.

Empirical permeability models for each fabric are summarised in Table 4.7.

Table 4.7: Preform permeability K_1, K_2, K_3 against V_f that may be used in simulation tools.

a) In-plain K_1, K_2 fitting equations:

Preform	K_1 fitting eq.(m^2)	K_2 fitting eq.(m^2)
3D woven HTS40 F13	$0.005 V_f^{(-11.55)}$	$0.0013 V_f^{(-12.41)}$
2/2 Twill (cf)	$0.001 V_f^{(-11.28)}$	$0.0012 V_f^{(-10.73)}$
Triaxial (gf)	$0.0022 V_f^{(-9.93)}$	$0.0004 V_f^{(-11.01)}$

b) Through thickness K_3 fitting equations:

Preform	K_3 fitting eq.(m^2)
3D woven HTS40 F13	$0.03789 V_f^{(-4.481)}$
2/2 Twill	$0.0593 V_f^{(-6.644)}$
Triaxial	$0.0945 V_f^{(-4.396)}$

The above information has been used as input data for RTM simulations for a

90° curved plate and the generic node.

4.8 Conclusions

In this chapter the permeabilities of the 3 different preforms that were discussed in Chapter 2 (section 2.3, table 3.1) were assessed.

In unsaturated radial flow the in-plane permeabilities (K_1, K_2) and flow orientation (θ) were measured. In saturated unidirectional flow at constant flow rate the through-thickness permeability K_3 was determined from the pressure variation across the specimen thickness.

With the information provided in Table 4.7 for K_1, K_2, K_3 in this chapter it is possible to predict the in-plane and through thickness permeability of the each fabric at any volume fraction within the range tested.

Therefore the preceding in-plane and through thickness permeability values will allow modelling the nature of the flow for various injection and venting scenarios for which the resin flow, and variability due to the complex geometry of the node, is not known a priori.

The key findings to be carried forward can be summarised as follows:

- In plane permeability characterization and power law curve fitting have been completed for three fabrics.
- Through-thickness permeability characterization and curve fitting have been completed for three fabrics.

The above key findings will be used for with FE analysis on Chapters 6, 7, 8 in order to predict the racetrack and the variability of the node.

References

[1]Endruweit, A., and Long, A.C., "Analysis of Compressibility and *Permeability of Selected 3D Woven Reinforcements"*. Journal of Composite Materials. **44** (24): (2010); p 2833-2862.

[2]Endruweit, A., Long, A. C., Robitaille, F., Rudd, C. D., "Influence of stochastic fibre angle variations on the permeability of bi-directional textile *fabrics"*. Composites: Part A **37**: (2006); p 122–132.

[3]Endruweit, A., McGregor, P., Long, A.C., and Johnson, M.S., "Influence of the fabric architecture on the variations in experimentally determined in-plane *permeability values"*. Composites Science and Technology. **66** (11-12): (2006); p 1778-1792.

[4]Endruweit, A., Harper, L.T., Turner, T.A, Warrior, N.A., and Long, A.C., *Random discontinuous carbon fiber preforms: "Experimental permeability* character*ization and local modelling"*. Polymer Composites. **31** (4): (2010); p 569-580.

[5]Lawrence, J.M., Barr, J., Karmakar, R., and Advani, S.G., *"Characterization of preform permeability in the presence of race tracking"*, Composites Part A: Applied Science Manufacturing **35:** (2004); p 1393–1405.

[6]Weitzenböck, J.R., Shenoi, R.A., Wilson, P.A., "Radial flow permeability *measurement"*. Part A: Composites: Part A **30:** (1999); p 781–796.

[7]Weitzenböck J.R., Shenoi R.A., Wilson P.A., "Radial flow permeability *measurement"*. Part B: Composites: Part A **30:** (1999); p 797–813.

[8]Babu, Z. B., and Pillai, K. M., "Experimental Investigation of the Effect of Fiber-mat Architecture on the Unsaturated Flow in Liquid Composite *Molding"*. Journal of Composite Materials **38**: (2004); p 57.

[9]Carter, EJ., Fell, AW., Griffin, P.R., and Summerscales, J., *"Data Validation Procedures for the Automated Determination of the Two-dimensional Permeability Tensor of a Fabric Reinforcement"*. Composites. Part A, Vol. **27**, Issue. 4: (1996); p 255-261.

[10]Ferland, P., Guitard, D., and Trochu, F., *"Concurrent Methods for* Permeability Measurement in Resin Transfer Moldi*ng"*. Polymer Composites, Vol. **17,** No. **1:** (Feb. 1996); p 149-158.

[11]Weitzenböck, J. R., Shenoi, R.A., Wilson, P.A., "Measurement of Three-dimen*sional Permeability"*. Composites Part A, Vol. **29**A: (1998); p 159-169.

[12]Gauvin, R., and Trochu, F., *"Key Issues in Numerical Simulation for Liquid Composite Molding Processes".* Polymer Composites, vol. **19**, No. **3**: (June 1998); p 233-240.

[13]Gauvin, R., Trochu, F., Lemenn, Y., and Diallo, L., *"Permeability Measurement and Flow Simulation Through Fiber Reinforcement"*. Polymer Composites, vol. **17**, No. **1**: (Feb. 1996); p 34-42.

[14]Hammami, A., Trochu, F., Gauvin, R., and Wirth, S., *"Directional* Permeability Measurement of Deformed Reinf*orcement"*. Journal of Reinforced Plastics and Composites, vol. **15**: (June 1996); p 552-562.

[15] Lekakou, C., Johari, M. A. K., Norman, D., and Bader, M. G., *"Measurement Techniques and Effects* on In-plane Permeability of Woven *Cloths in Resin Transfer Molding"* Composites. Part A, Vol. **27**, Issue **5**: (1996); p 401-408.

[16] Kozeny, J., *"*Uber die Kapillare Leitung des Wassers in Boden. Sitzungsberichte*"*. Akademie der Wissenschaft Wien Math-naturw, **136**: (1927); p 271-306.

[17] Carman, P.C., *"Fluid Flow Through a Granular Bed".* Transactions of the Institute of Chemical Engineers, **15**: (1937); p 150-166.

[18] Gebart, B.R., *"Permeability of Unidirectional Reinforcements for Rtm".* Journal of Composite Materials, **26**(8): (1992); p 1100-1133.

[19] Pomeroy, R., *"Permeability Characterisation of Continuous Filament Mats for Resin Transfer Moulding".* PhD Thesis, 2009.

[20] Williams, J.G., Morris, C.E.M., and Ennis, B.C., *"Liquid Flow through Aligned Fiber Beds".* Polymer Engineering and Science, **14**(6): (1974); p 413-419.

[21] Young, W-B., *"Three*-dimensional Nonisothermal Mold Filling *Simulations in Resin Transfer Molding".* Polymer Composites, Vol. **15**, No. 2: (April 1994); p 118-127.

Chapter 5

Fabric bending model development

5.1 Introduction

When the preform bends around an edge (inside the mould) it is compacted radially. This is due to the stiffness of the preform and forces of friction between the preform and the mould wall. As a result of this behaviour a gap between the preform and mould wall along the edge will be created. This can lead to resin rich zones, along the edges of the composite part. Existence of race-tracking is able to affect the filling and final mechanical properties of the composite. Resin rich zones are difficult to predict due to the height gap variation as studied by Dong, C. [1] with a model on VARTM experiments. Bickerton, S., et al [2-7] provided a series of experimental investigations on racetrack modelling, and mould curvature effects during RTM process. Curvature effects on preform permeability during filling on a closed mould were studied for a non-planar geometry. Numerical modelling of flow channel effects in RTM was studied as well. Devillard, M., et al [8-9] provided an on-line characterization of bulk permeability and race-tracking during the filling stage in RTM process. A paper with flow sensing and control strategies was presented. Hammami, A., et al [10] presented a research on edge effects modelling in LCM for composites.

A model in order to predict the formation of resin rich zones for a curved plate representing an edge in the generic node mould is presented in this Chapter. The relationship between gap thickness and edge radius is also

investigated. This model is validated against experimental data taken from the experimental study with three different fabrics presented in Chapter 3.

5.2 Model analysis

The gap formation of resin rich zones on a 90 ° curved plate may be seen schematically in Fig. 5.1.
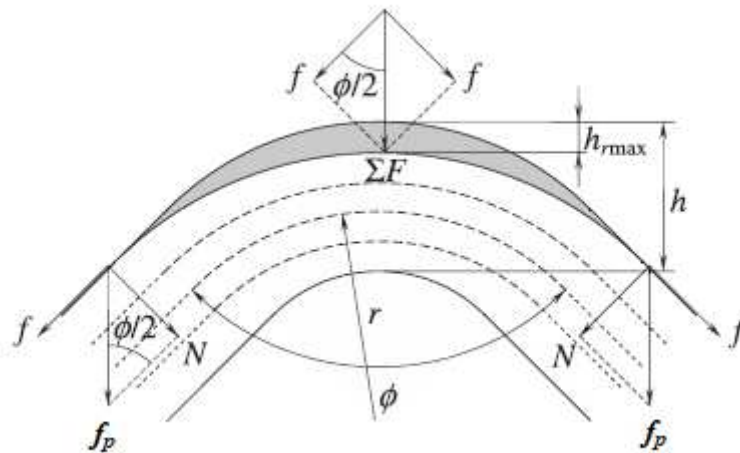
Fig. 5.1: Forces for gap formation at corner radii of preform [1].

When a preform textile is placed around an edge inside a mould a static friction force f appears as shown in eq. (5-1).

$$f = N\mu \tag{5-1}$$

Where μ is the coefficient of friction between the preform fibres and mould, N is normal force. As a result of the enclosed curve angle $\varphi=90°$ the resultant force is reflected perpendicularly to the preform fibres across the edge of the curve plate and compresses the upper preform part. Therefore a force f_p multiplied by $sin \dfrac{\phi}{2}$ gives the normal force N at any angle. Because of the axis of symmetry on the curved plate at 90° from the horizontal line it is sufficient

to study only one half of the geometry and then applied the same mathematical equations to the other half. The normal force N in eq. (5-1) may be written from Fig.5.1 as:

$$N = f_p \sin\frac{\phi}{2} \tag{5-2}$$

It must be pointed out that the normal force N changes from point to point along the curved plate with angle φ, however it remains constant for a fixed angle and through the thickness of the preform fibres. The resultant force *Σf* Fig. 5.1 pulls down the fibre preform at the upper part of the corner radius and a gap is formed. So the frictional force of equation (5-1) is given by:

$$f = \mu f_p \sin(\frac{\phi}{2}) \tag{5-3}$$

where f is also equal to pressure (P) multiplied by area (A) so:

$$f = PA = \mu f_p \sin\frac{\phi}{2} \tag{5-4}$$

Finally the pressure contribution to the fabric's density variation on the 90° angle will be given by the equation

$$P = \frac{\mu f_p \sin\frac{\phi}{2}}{A} \tag{5-5}$$

On the other hand the fabric's compaction behaviour may be based on an empirical power law discussed in detail by Robitaille, F., et Gauvin, R., [11-13] with their three papers study that give the fabric thickness variation (H) against pressure, as discussed in Chapter 3.

$$H_{fabricthickness} = \alpha P^{-\beta} \qquad (3\text{-}3)$$

where α and β are material constants, and P is the dimensionless pressure,

By combining equations (5-5) and (3-3) eq. (5-6) was obtained:

$$\mu f_p = \frac{A\left(\dfrac{\alpha}{H_{Fabric\ thickness}}\right)^{\frac{1}{\beta}}}{sin\left(\dfrac{\phi}{2}\right)} \qquad (5\text{-}6)$$

By taking as reference the arc centre at $\dfrac{\phi}{2} = 90^{\circ}$, $H_{max\ fabric\ thickness}$ occurs at

$sin\dfrac{\phi}{2} = 1$, from the reference centre point, therefore equation **(5-6)** becomes:

$$\mu f_p = A\left(\frac{\alpha}{H_{maxfabric\ thickness}}\right)^{\frac{1}{\beta}} \qquad (5\text{-}7)$$

$H_{max\ fabric\ thickness}$ can be measured by bending tests (Chapter 3). The calculated μf_p product of equation (5-7) is considered to be the same for the same material properties, across the 90° curve plate. Rearranging equation (5-7) gives:

$$H_{Fabric\ thickness} = \alpha\left(\frac{A}{\mu f_p sin\left(\dfrac{\phi}{2}\right)}\right)^{\beta} \qquad (5\text{-}8)$$

Finally h $_{gap}$ will be the mould height minus the fabric thickness according to:

$$h_{gap} = H_{Mould} - H_{Fabric\ thickness.} \qquad (5\text{-}9)$$

Hence, considering the whole geometry with equations (5-8) and (5-9)**:**

$$h_{gap} = H_{Mould} - \alpha\left(\frac{A}{\mu f_p sin\left(\dfrac{\phi}{2}\right)}\right)^{\beta} \qquad (5\text{-}10)$$

So the height of the racetrack gap of eq. (5-10) depends upon the following factors: the mould height, the fabric's compaction behaviour, the area of the fabric, the static friction normal force reaction component μf_p and the angle variation through $\sin(\frac{\phi}{2})$.

By further combing (5-10) with (5-5):

$$h_{gap} = H_{Mould} - \alpha (P^{-1})^{\beta} \tag{5-11}$$

where the racetrack gap h $_{gap}$ depends only upon fabric's compaction behaviour, the material constants α, β and the pressure P shows on in eq. (5-11).

5.3 Discussion

Model numerical results were calculated by considering the fabric's compaction experimental power law equation (3-3), with numerical values from table (3-2). From equation (5-10) it becomes quite clear that the maximum gap of the race-tracking may be determined from the variation of μf_p considering that that all the remaining factors may be calculated or measured experimentally for a fixed angle. In an inverse way by measuring h_{max} each time we may obtain the value of the product μf_p. So measuring the gap variation for the 90° curved plane (bend angle) the gap variation of the generic node can be predicted. However this is true only in the cases where the same material is used for the bending test and the mould. Changing the material the product μf_p. from equation (5-10) will be different.

5.4 Model fitting

Considering that the experimental gap of the preform is well defined there are two available possibilities:

i)   Fit the model in the centre of the FE curved plate edge with maximum h_{gap} to try to achieve a good fitting to the experimental data.

ii)   Fit the model in the centre of the FE curved plate edge with accurate flow modelling, considering the total racetrack area.

case i) is the easier and most practical way to follow however due to inter-yarn forces both cases are to be used. Case i), ii) was used in model fitting for experimental data evaluation on Chapter 6. The above model was evaluated with the use of eq. (5-10) fitted to the experimental data obtained from separate measurements through scanning with a coordinate measurement machine (CMM) as described in Chapter 3. Taking into account the different reference measurements the experimental data for the centre of a curved plate of 3.2 mm in radius was obtained. Prior to this equation (5-10) had to be transformed. Firstly, by looking from the centre of the 3.2 mm radius curved plate, the angle of the scanning samples was 180° i.e. double of that considered in the 90° model curved plate. Hence $sin(\frac{\phi}{2})$ had to be replaced with $sin(\phi)$ shifted by 45°. The fabric's compressibility factors α and β the area A and static friction normal force reaction component μf_p are not affected by the change of the centre of origin. The model was fitted as described in section 5.4. Equation (5-10) was then fitted with the experimental coordinate measurement machine

Spiridon Koutsonas

(CMM) data for the ACTS 4-layers carbon fabric samples, shown Fig. 5.2 (a),

5.2 (b).
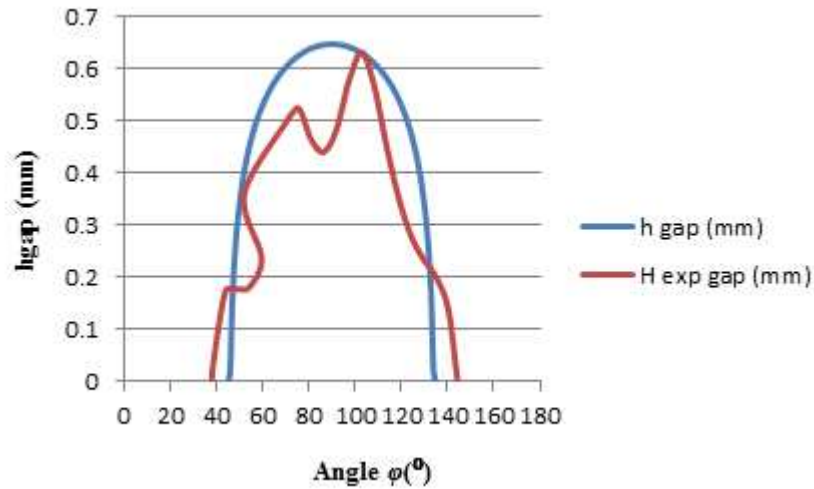
Fig. 5.2 (a): Model gap fitting with sample 7 on Fig. 3.13 (a) warp HTS40 F13 4-layers preform (CMM) on aluminium base.
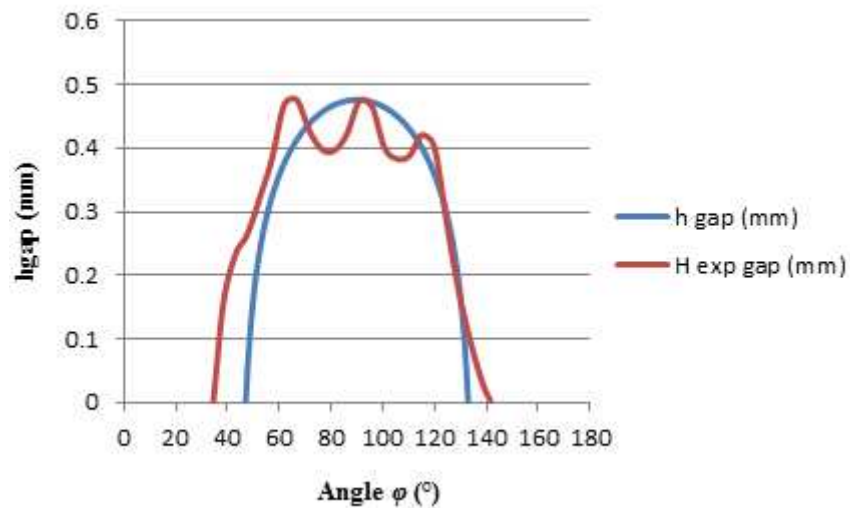
Fig. 5.2 (b): Model gap fitting with sample 1 on Fig. 3.13 (b) weft HTS40 F13) 4-layers preform (CMM) on aluminium base.

Secondly, equation **(5-10)** was then fitted with CMM data obtained from the

2/2 Twill 3-layer carbon fabric samples, shown Fig. 5.3.
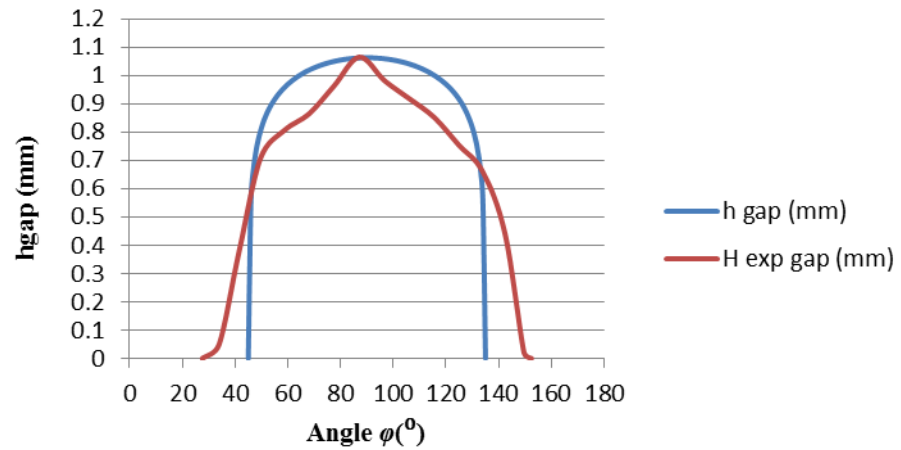
Fig. 5.3: Model gap fitting with sample 5 on Fig. 3.13 (c) of 2/2 twill 3-layers preform (CMM) on aluminium base.

Thirdly, equation (5-10) was also fitted with CMM data obtained from the triaxial 3-layer glass fabric samples, see Fig. 5.4 (a), 5.4 (b):
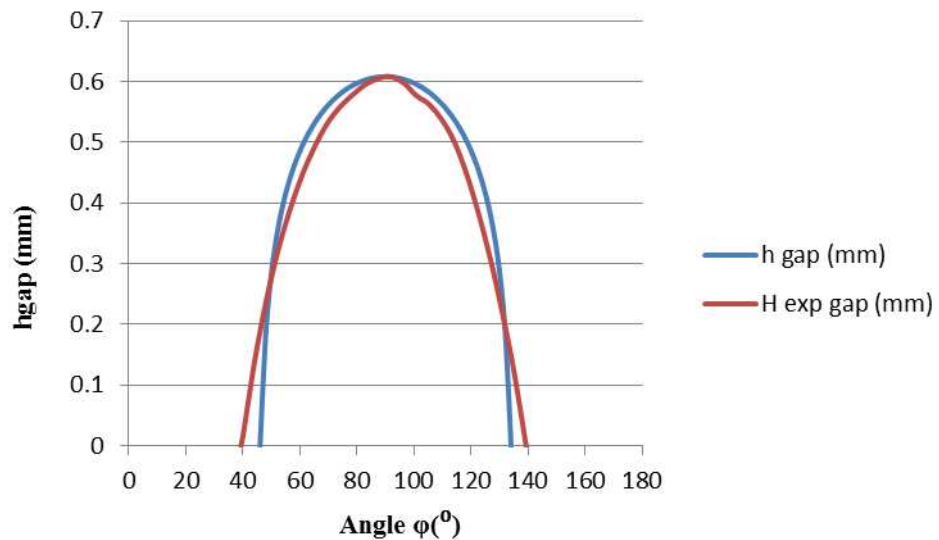
Fig. 5.4 (a): Model gap fitting with sample 4 on Fig. 3.13 (d) warp triaxial 3-layers preform (CMM) on aluminium base.
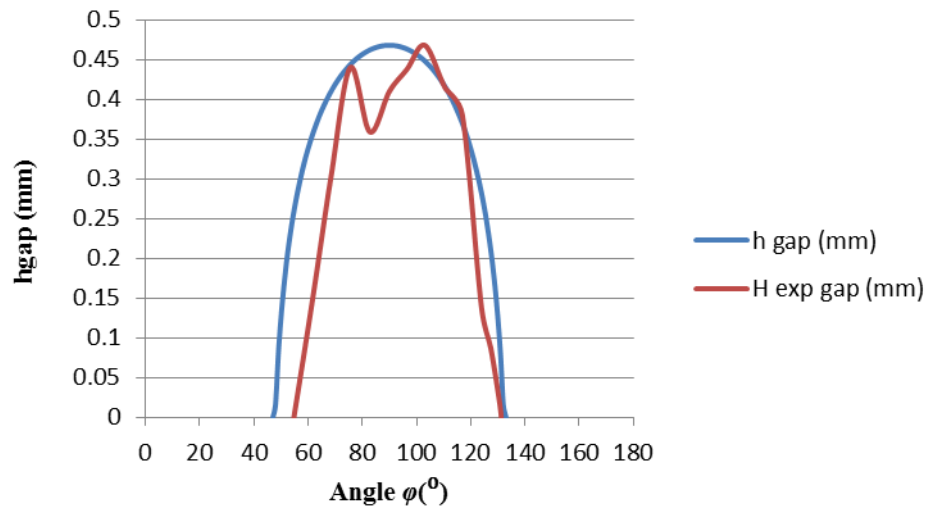
Fig. 5.4 (b): Model gap fitting with sample 1 on Fig. 3.13 (e) weft triaxial 3-layers preform (CMM) on aluminium base.

5.5 Observations

In almost all samples with the three tested fabrics at least one sharp peak was observed. Due to the random inter-yarn force distributions of each of the tested fabrics along the bend angle of the preform that said, in general the model probes a reasonable fit to the experimental data.

Experimentally measured (with CMM) small gaps (0.01-0.15mm) may contain only the sharp peak and therefore contain area significant small for race-tracking purposes. Gaps of height (0.01-0.15mm) size are difficult to observe experimentally. On these occasions more factors such as stochastic variability and race-tracking significantly affect the fluid behaviour during infusion and one has to take further issues into account (stochastic variability of preform permeability has not considered in this thesis). However for very small gaps due to sharp compression along the bend, this approach does not fit

so well. Therefore we proceeded with case ii) on section 5.4 as shown in Figures 5.5, 5.6.
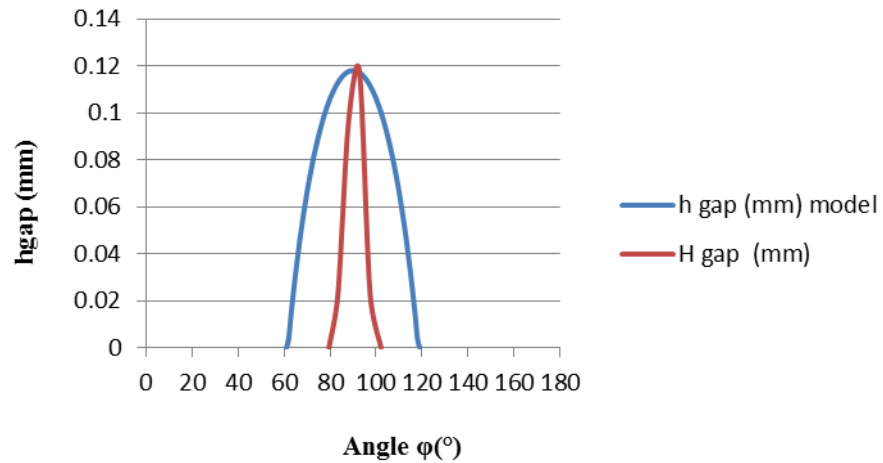
Fig. 5.5: Model gap (blue line) fitting case i) section 5.4 with sample 4 (red line) weft ACTS 4-layers preform (CMM) on aluminium base.

This allow the total racetrack area to be predicted accurately which is important for accurate flow modelling.
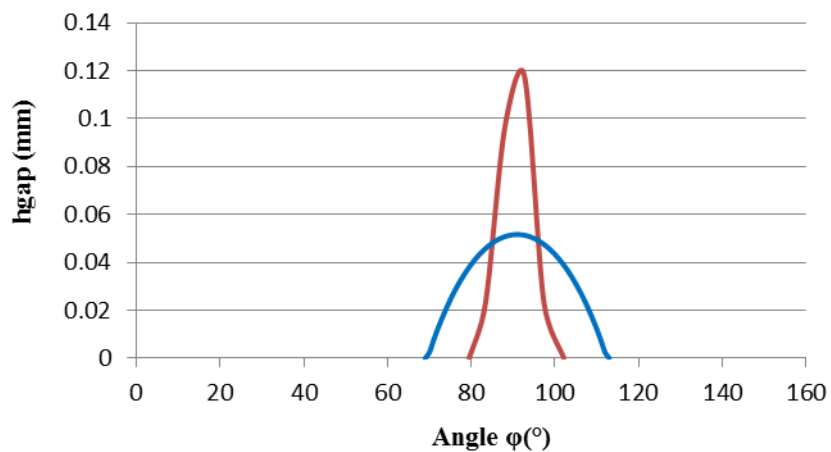
Fig. 5.6: Model gap (blue line) fitting with sample 4 (red line) weft ACTS 4-layers preform (CMM) on aluminium base.

5.6 Conclusions

A model for predicting the formation of resin rich zones in curved plate mouldings is presented in this Chapter representing the effect that may occur at edges in real composite parts. The functional relationship between gap thickness and radius, enclosed angle and preform compaction is derived by a mechanics based approach. The model quantitatively relates gap thickness with fibre volume fraction, along the enclosed bend preform angle eq. (5-10).

The model gives the relationship between gap thickness and curve plate radius. However this model does not consider the preform geometry and the flow inside the preform. For example for the through-thickness infusion of a $0°$ unidirectional preform, there will be race-tracking through the yarns of the preform that may influence the total flow inside the mould which should be verified experimentally with further investigation.

The key points of Chapter 5 can be summarised as follows:

- A model that may be used for FE modelling against the formation of resin rich zones along a 90° angle during infusion in RTM process, was presented.

- The model predictions fitted well with experimental CMM contact technique data for samples of three tested fabrics.

The above key findings will be used for with FE analysis on Chapters 6, 8 in order to predict the racetrack and the variability of the node.

References

[1]Dong, C., "Model development for the formation of resin-rich zones in *composites processing"* Composites, Part A **42**: (2011); p 419–424.

[2]Bickerton, S., Sozer, E. M, Graham, P. J., and Advani, S. G., "Fabric structure and mold curvature effects on preform permeability and mold filling in the RTM process Part II *Experiment"*. Composites, Part A **36**: (2005); p 1128–1141.

[3]Bickerton, S., Advani, S. G., "Characterization and modelling of race-tracking in liquid *composite molding processes"*. Composites Science and Technology, Vol. **59**: (1999); p 2215-2229.

[4]Bickerton, S., Sozer, E.M., S¡imacek, P., Advani, S.G., "Fabric structure and mold curvature effects on preform permeability and mold filling in the *RTM process"*. *Part II*. Predictions and comparisons with experiments, September 1999, Composites, Part A **31**: (2000); p 439–458.

[5]Bickerton, S., & Advani, S. G., "Experimental investigation and flow visualization of the resin transfer moldfilling process in a non-planar *geometry"*, July 1996, Composites Science and Technology, Vol. **51**: (1997); p 23-33.

[6]Bickerton, S., Advani, S. G., "Characterization and modeling of race-tracking in liquid composite m*olding processes"*. Composites Science and Technology, Vol. **59**: (1999); p 2215-2229.

[7]Bickerton, S., Advani, S.G., Mohan, R.V., and Shires, D.R., *"Ex*perimental Analysis and Numerical Modeling of Flow Channel Effects in Resin Transfer *Molding,"* Polymer Composites, Vol. **21**, No. 1: (Feb. 2000); p 134-153.

[8]Devillard, M., Hsiao, K-T., Gokce, A., and Advani, S. G., "On-line Characterization of Bulk Permeability and Race-Tracking during the Filling *Stage in Resin Transfer Molding Process"* Journal of Composite Materials, Vol. **37**: (2003); p 1525, DOI: 10.1177/0021998303034459.

[9]Devillard, M., Hsiao, K-T., Advani, S. G., "Flow sensing and control strategies to address race-tracking disturbances in resin transfer molding-part *II"*: automation and validation. Composites, Part A **36**: (2005); p 1581–1589.

[10]Hammami, A., Gauvin, R., and Trochu, F., "Modelling the edge effect in *liquid composites molding".* Composites, Part A, **29** (5-6): (1998); p 603-609.

[11]Robitaille, F., and Gauvin, R., "Compaction of textile reinforcements for *composites manufacturing. I: Review of experimental results".* Polymer Composites, **19** (2): (1998); p 198-216.

[12]Robitaille, F., and Gauvin, R., "Compaction of textile reinforcements for *composites manufacturing. II: "Compaction and relaxation of dry and H2O-saturated woven reinforcements".* Polymer Composites, **19** (5): (1998); p 543-557.

[13]Robitaille, F., and Gauvin, R., "Compaction of textile reinforcements for *composites manufacturing. III. Reorganization of the fiber network".* Polymer Composites, **20** (1): (1999); p 48-61.

Chapter 6

Analysis of flow for a 90° curved plate

6.1 Introduction

The objective of this chapter is to study race-tracking on a preform bend along 90° curved plate geometry. Analysis of flow for a 90° curved plate was conducted experimentally and computationally. Experimental analysis was performed with the use of a transparent tool that was designed and constructed for this purpose. The materials used for the experimental analysis are presented in Fig. 3.3 and table 3.1. Computationally the FE/CV method and a series of FE CAD models (in 2D, 3D) were used. Computational modelling was based on model in Chapter 5 and the experimental material properties.

6.1.1 Background

Approaches to estimate race-tracking and local permeability during the impregnation of a composite have been studied by Rudd C. D., et al [1]. Li, J., et al [2] used a stochastic simulation based approach for statistical analysis and composites characterization. Liu, B., et al [3] for modelled RTM gate control, venting and dry spot prediction. Schell, J.S.U., et al [4] published on numerical prediction and experimental characterisation of meso-scale voids in LCM process. Simacek, P., and Advani, S.G., [5] provided a numerical model in order to predict fibre tow saturation during LCM. Long, A. C., [6], [15] gave a description of race-tracking and what may happen during composites manufacturing process. Lawrence, J. M., et al [7] characterized the preform permeability in the presence of race-tracking. Bickerton, S., et al [8, 9]

researched fabric structure and mould curvature effects on preform permeability and mould filling during RTM process. Endruweit, A., et al [10], [22] showed firstly the influence of stochastic fibre angle variations on the permeability of bi-directional textile fabrics and secondly on random discontinuous carbon fibre preforms. Babu, Z. B. and Pillai, K. M., [11] presented an experimental investigation of the effects of fibre-mat architecture on the unsaturated flow during LCM process. Hieber, C. A., and Shen, S.F., [12] studied the injection moulding filling computationally with finite element and finite difference methods. Frederick, R., Phelan, JR., [13] provided further insights into computational modelling, Trochu, F., et al [14] used the FE method for numerical analysis of the RTM process. Devillard, M., et al [16] provided an on-line characterization of bulk permeability and race-tracking during in RTM process filling stage. Andersson, H.M., et al [17] provided a numerical model for vacuum infusion manufacturing of polymer composites. Hammami, A., et al [18, 19] modelled the edge effect in LCM and the vacuum infusion moulding process analysis. Lawrence, J. M., et al [20] studied automated manufacturing in order to address bulk permeability variations and race-tracking in RTM with auxiliary gates. Weimer, C., et al [21] provided a research on approach to net-shape preforming using textile technologies on the edges. Pillai, K.M., et al [23] modelled the heterogeneities presented in preforms during RTM during mould filling where the influences of various race-tracking situations on the flow pattern have been addressed as presented in the Literature Review, Sections 2.10-2.12.

In the present Chapter three different preforms were firstly tested experimentally with the use of a transparent tool and then simulated numerically with ESI PAM-RTM® group software. The simulations were performed by taking into account the material properties of Tables 3.2, 4.7 and the modelling methodology of Section 6.2. A linear injection gate on one side and linear vent on the other side were used in numerical simulations and experimental studies. In this way the pressure gradient was parallel to each preform's bend axis. With the use of two web cams, the flow front was visualised during the injections in a Perspex tool and recorded from a on a PC. The comparison of numerical simulations with experimental results allowed the model verifications to be validated and the calculation of the resin rich zone height.

6.2 Experimental Analysis of flow for a 90° curved plate

6.2.1 Race-tracking experimental procedure

Due to the fact that RTM experiments are expensive in terms of material consumption and instrumentation a limited number of experiments may be used to compare with the simulations. For this purpose and in order to demonstrate the implementation, a prototype mould transparent tool with a 90° curved plate cavity was designed and fabricated.

The objective was to create an apparatus with gates, vents, a preform cavity and fluid delivery (preferably oil) that would reproduce experimentally the 90° preform bending simulations referred to in Section 6.3 The transparent tool in use for infusion of the tested preforms along with its features are shown in Fig.

6.1. A description of its main components, i.e. the Perspex tool, the image visualization system and the personal computer, are briefly given here.

The Perspex mould shown in Fig. 6.1 was made of two pieces; one male and one female. The uniform cavity on the male part was manufactured with dimensions 150 ×150 mm and 2.75 mm height along a 90° curved plate. The radius of the male part was set at 3.20 mm while the radius of the female part was set at 5.95 mm to maintain a constant cavity thickness. More design specifications for the transparent tool are presented in the Appendix I.

Fig. 6.1: Transparent tooling (male left, female right) for the race-tracking study with a 90° curved plate. The cavity dimensions for the male part were: 150×150×2.75 mm.

The experimental setup of the apparatus for the racetrack image visualization is shown in Fig. 6.2 and consisted of:

(i) The Perspex rig.

(ii) An appropriately modified table that was hollow in the centre in order to visualise the flow from underneath.

(iii) A personal PC with MATLAB software installed.

(iv) A vacuum pump.

(v) A pressure pot indicator.

(vi) Metallic fixtures and two web cams, with one positioned above the mould and the other below.

(vii) Commercial motor oil type HDX30 (with measured viscosity Appendix H)

(viii) A tripod with a light
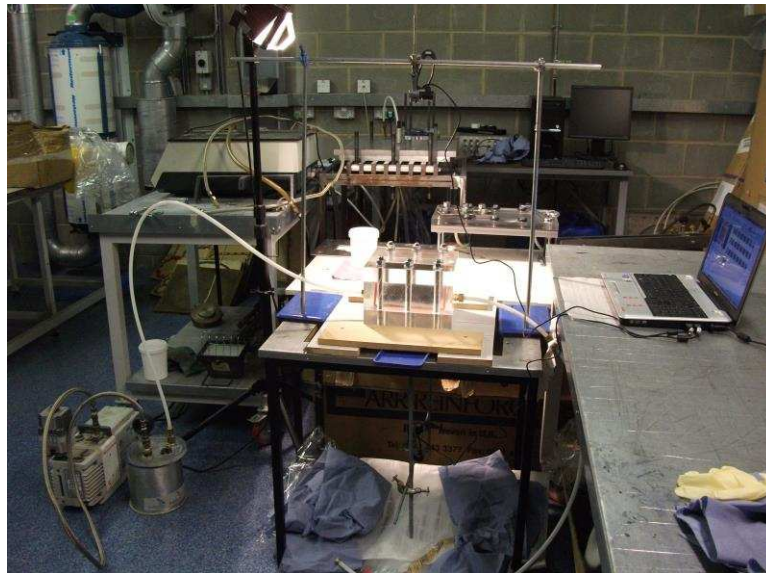
Fig. 6.2: Set up of the apparatus for preform infusion. The displayed instrumentation was used for the race-tracking image visualization along the 90° curved plate.

6.2.2 Experimental methodology for 90° 3D curved plate filling

The instrumentation used for the experimental comparison with numerical simulations was presented in Section 6.2.1 (Fig. 6.2). A transparent tool (Fig. 6.1) was used for visualization and validation of numerical simulations. Image visualization of the flow front propagation on both sides of the Perspex (top and bottom side) provided information about racetracking along the 90° curved

plate preform during liquid infusion with oil type HDX30 with a known viscosity (shown on Appendix H).

The methodology followed here was similar to that reported by Bickerton, S., et al [8, 9]. All experimental results were obtained according to the experimental set up Fig. 6.3.
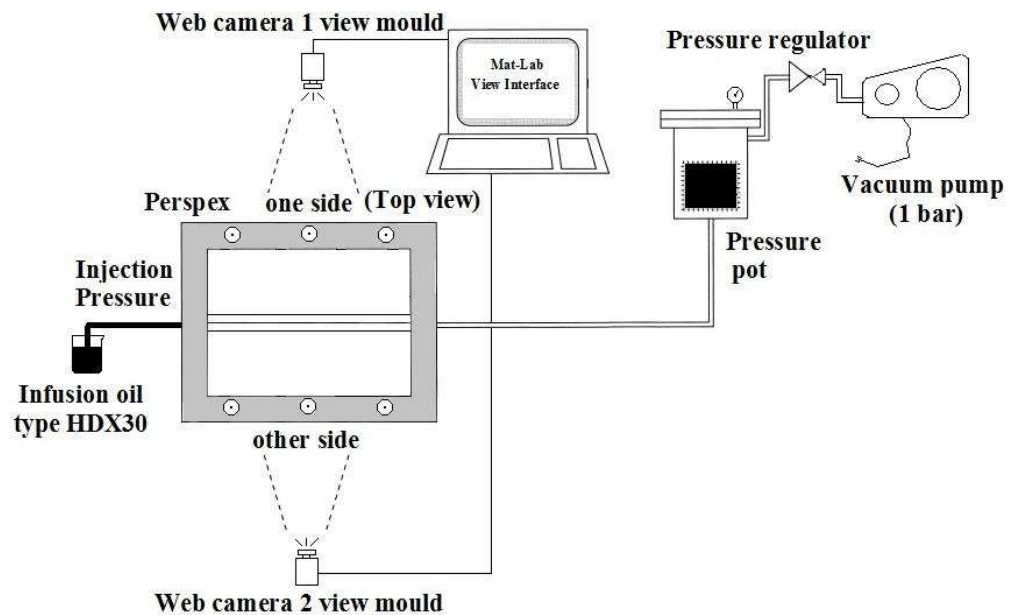
Fig. 6.3: Schematic for experimental flow visualization.

Initially the specimens were cut to the same dimensions as the Perspex cavity. Thereafter each fabric specimen was weighed with a precision scale ($\pm$0.1g) and placed inside the Perspex cavity. The transparent tool was shielded and the vacuum pump was set up at constant pressure (bar). When the two web cams, PC, and lights were set up the liquid infusion of known viscosity, oil type HDX30 started and so the image data collection was initialised. For visualization purposes a MATLAB view interface code was used. All experimental image visualization output files were collected on the PC.

Following the above method a number of 2/2 twill (3-layers) and triaxial (3-layers) in warp and weft direction were experimentally tested.

Thereafter the racetrack behaviour of a 3D woven HTS40 F13 (a preform made of 4-layers), was experimentally verified in warp and weft directions for one specimen for each case (due to limited quantity of 3D woven HTS40 F13 textile provided by the supplier). Selected experimental results are presented for comparison with the modelling results for each of the tested fabrics on Section 6.4 on this Chapter and on Appendix C.

6.3 Race-track modelling

6.3.1 Race-track modelling procedure

Macro-flow models consider flows through a fibre preform with a defined permeability in the present work the race-track effect was modelled, by grouping different zones on 90° curved plate reinforcement and by assigning to each of them a single local permeability. The modelling software used was PAM-RTM® developed by ESI group. [24] However despite its many advantages this software is also quite time consuming making 3D computations long enough and complex parts (such as the ACTS node) with multiple injection ports and vent gates, required high speed processing power to be used.

Within PAM-RTM® the saturated, partially saturated and unsaturated flow regions are modelled using the Finite Element Control Volume method, where each node is assigned a fill factor one (filled node), between zero and

one (partial filled node) and zero (unfilled node). In order to model flow for a given CAD geometry the following steps must be followed:

 (i) Create the CAD geometric model.

(ii) Mesh the CAD model and import to PAM-RTM® software.

(iii) Define the permeability $K_{fab}=f(V_f)$ throughout the CAD model on an element by element basis.

(iv) Define the 2D or 3D local permeability zones along the 90° angle preform bend elements and gap elements for racetrack purposes.

 (v) Set the vector orientations for each element model, reprocessing the reinforcement principal flow directions.

(vi) Set up injection gate and vent locations.

(vii) Run the model simulation.

6.3.2 FE CAD 90° curved plate race-track modelling

6.3.2.1 2D, FE CAD 90° curved plate race-track modelling

As soon as the resin flow front arrives in the mould at the 90° curve plate edges, (where gaps often exist between the preform and mould wall), the resin will tend to flow faster than elsewhere in the mould as reported for example by Liu, B. et al [3]. Bickerton, S., et al [8, 9] reported the mould curvature effects on preform permeability during mould filling in RTM with his experimental work. By taking into account this effect and in order to model the variability the following approach will be used: Firstly the critical variability areas (gap channels) of a component must be considered. At edges during the filling process, the local permeability may differ from the rest of the component. This is because of a free channel between the mould wall and the fabric. Thus the

local permeability may be given from the empirical equation reported by Endruweit, A., et al [22] and Pillai, K.M., et al [23]:

$$K = \frac{h^2}{12} \qquad \textbf{(6-1)}$$

Where K in (m^2) is the permeability of the gap and h (mm) is the gap between the fabric and mould wall. For all 2D, 3D curve plate models a linear injection gate (inlet) from one end and linear vent (outlet) from other end were used as shown in Fig. 6.4.
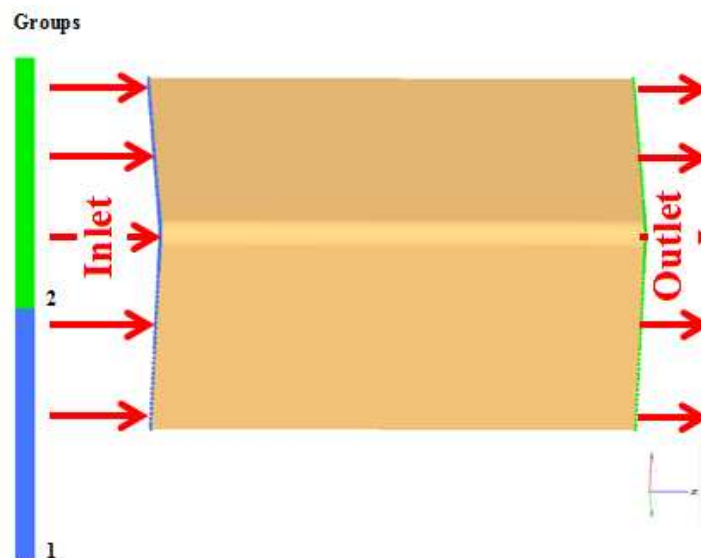
Fig. 6.4: Curved plate model injection gate (group 1, indicated by blue line left) and vent (group 2, indicated by green line right end). Red arrows shown the resin through thickness flow direction for all 2D, 3D 90° curve plate CAD models.

Firstly a 2D CAD model of 90° curve plate was designed and meshed with triangular finite elements in Altair Hyper-mesh software as shown in Fig. 6.5.
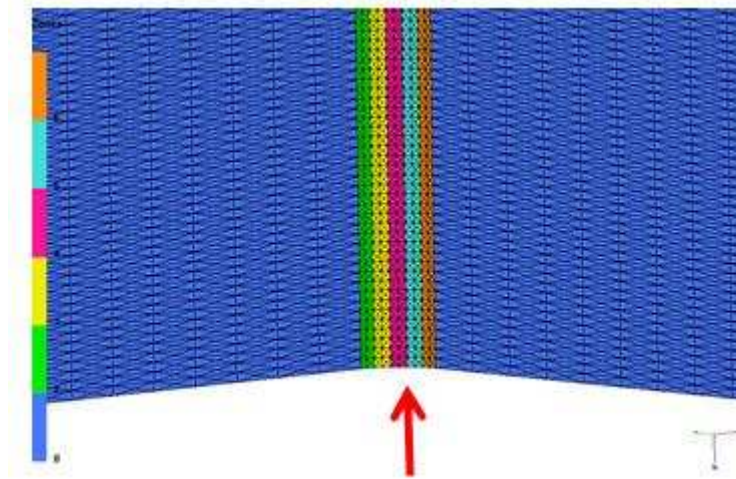
Fig. 6.5: 2D FE model with 9800 triangular elements (due to PAM-RTM) on a 90° curved plate, geometry with five zones see red arrow (green, yellow, purple, turquoise, orange) colours of different local permeability for race-track modelling and blue colour zone with the fabric's permeability.

Along the 90° curved plate a number of five different zones were generated. Element properties were determined by taking into account the weighted averaged permeability of the compacted preform and the gap and by assuming a good in-plane flow behaviour as suggested by Trochu, F., et al [14] according to:

$$K_{2D} = \frac{(h_{fabric}K_{fabric} + h_{gap}K_{gap})}{h_{fabric} + h_{gap}}$$ **(6-2)**

where K_{2D} in (m^2) is the average 2D-element permeability, K_{fabric} is the fabric permeability, K_{gap} is the gap permeability, h_{fabric} is the preform height and h_{gap} is the gap height between the preform and the mould wall. So for an anisotropic preform the in-plane permeability wil be Trochu, F., et al [14]:

$$K_{layer} = \frac{(h_{fabric}K_l + h_{gap}K_{gap})}{h_{fabric} + h_{gap}}$$

and **(6-3)**

$$K_{2\,aver} = \frac{(h_{fabric}K_2 + h_{gap}K_{gap})}{h_{fabric} + h_{gap}}$$

Furthermore, K_{1aver}, K_{2aver} were used as local permeability input data along with the material properties presented with power law in Tables 3.2, 4.7.

FE modelling in 2D provided an average estimation about how much local permeability may be affected by fabric's bending along a 90° angle during infusion in RTM process.

6.3.2.2 3D, FE CAD 90° curved plate race-track modelling

To model three-dimensional flow, 3D FE CAD models were designed and meshed with bend zone segmentation. For each zone the average fabric thickness H_{fabric} was determined with the equivalent preform permeability in relation to the fibre volume fraction V_f (Table 4.7) and the gap thickness h_{gap} with equivalent gap permeability according to Equation (6-1). In this case a mesh with tetrahedral finite elements was used allowing higher geometrical details in comparison to other types of finite elements. However the use of high element mesh density leads to an FE model which requires intensive computation. Therefore for practical reasons it was preferable to limit the mesh refinement on the FE CAD model and the number of zones along the curved plate see Fig. 6.6.
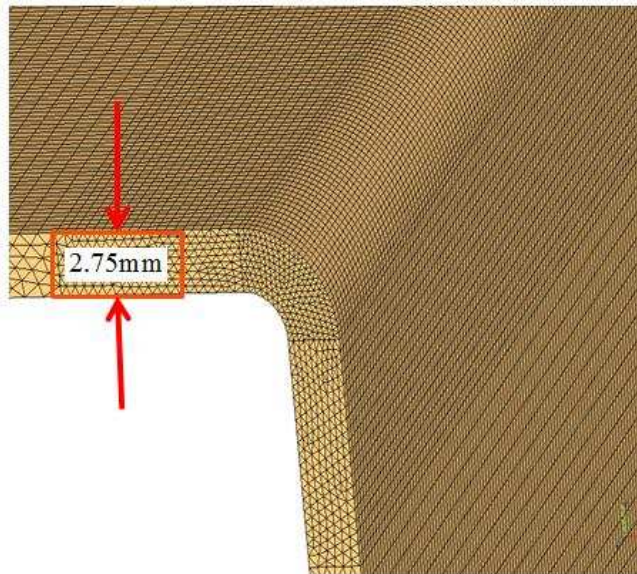
Fig. 6.6: 3D curve plate of 2.75mm thick with mesh refinement 1064399 tetrahedral with 10 elements through thickness along the 90° angle for race-track modelling study.

Thus 3D race-tracking was studied by creating a series of FE 3D CAD models of different gap heights (h_{max}). In Fig. 6.7 (a), 6.7 (b) the 2.75 mm radius height was divided in two sections:

(i)   a blue colour zone 1 with the fabric's permeability,

(ii)   an outer gap section with measured maximum gap height (h_{max}) of resin rich zones 2, 3 and 4 (green, yellow and purple),

(iii)   a compressed bent fabric section along the 90° curved plate zones 5, 6 and 7 (pink, orange and turquoise), under the racetrack channel of higher volume fraction V_f and with compressed fabric permeability.
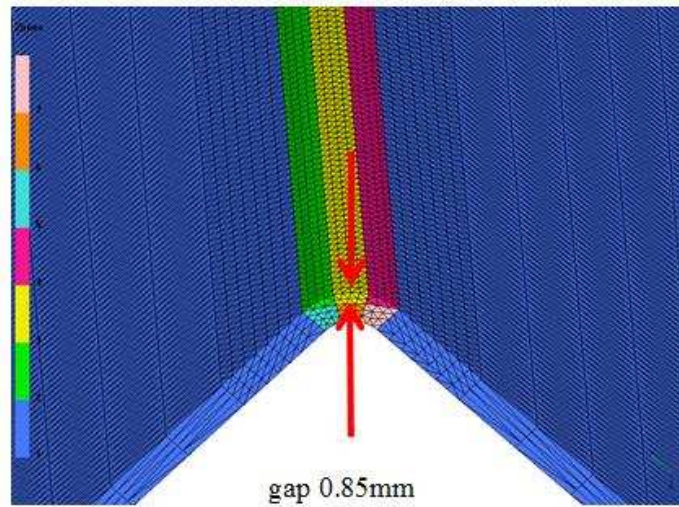
(a)
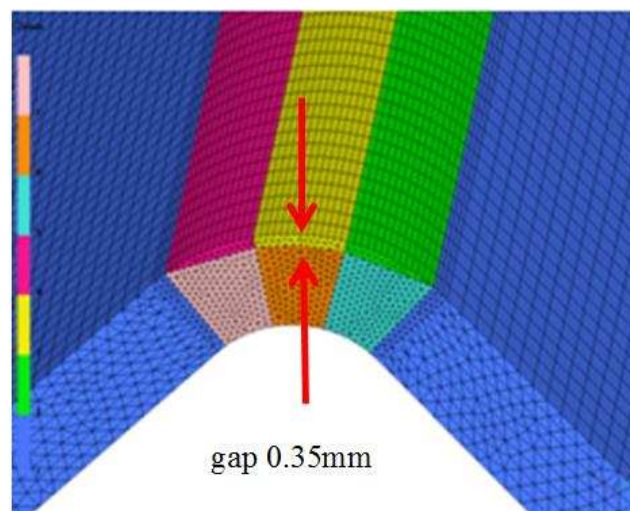
(b)

Fig. 6.7: 3D FE CAD 90° curved plate models meshed with seven zones geometry of different permeability, three h_{gap} zones (green, yellow, purple) see red arrows, three compressed zones with different V_f (turquoise, orange, pink) and blue colour zone with the fabric's permeability (a) with 154350 tetrahedral elements and h_{max} 0.85mm (b) with 300600 tetrahedral elements and h_{max} 0.35mm.

Within the zones the permeability of the gap was assigned according to Equation (6-1). The gap height was derived from Equation (5-11) model in Chapter 5. On the bent preform and along the 90° angle, the material properties

(Table 4.7) were assigned with the appropriate volume fraction V_f. Thereafter a series of eight FE 3D CAD models were designed and constructed with h_{max} = 0.35, 0.45, 0.65, 0.85, 0.95, 1.00, 1.10, 1.25 mm, i.e. values within the range of those measured with CMM in Chapter 3. Gaps with h_{max} less than 0.35 mm have not been modelled due to stochastic variability of the three tested preforms that made it impossible to quantify experimentally a small gap. The experimental behaviour of each of the tested fabrics was thereafter compared with the closest behaviour of the above generated FE 2D and 3D CAD models. FE modelling in 3D provided more detailed information about how much local permeability may be affected by fabric's bending along a 90° angle during infusion in RTM process.

For the flow behaviour during RTM, fluid mass conservation and equations of unsaturated flow of a viscous liquid through a porous medium were solved by PAM-RTM$^®$, based on an adaptive mesh as presented by Trochu, F., et al [14]. All the 2D, 3D FE CAD model simulations were scaled in the same dimensions as the Perspex cavity (i.e. 150x150 x2.75 mm).

6.3.3 Permeability vector orientations inside 90° 3D curved plate

For all the FE 3D CAD curved plate geometry models, (one of which is shown in Fig. 6.8), permeability vector orientations were incorporated for each tetrahedral element. For this, all tetrahedral elements assigned and the warp in-plane K_1-permeability orientations and the weft in-plane K_2-permeability orientations. These are shown in Fig.6.8. The through-thickness K_3-

permeability orientation was automatically considered by the PAM-RTM$^{®}$ software, to be perpendicular to K_1 and K_2 accordingly.
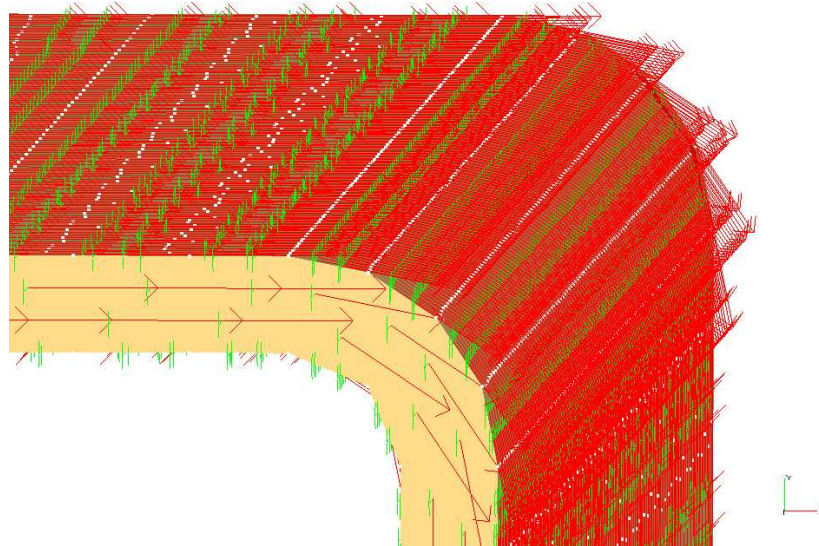
Fig. 6.8: Permeability vector orientations K_1 (red arrows), K_2 (green arrows) on a 3D curved plate model.

6.3.4 2/2 twill, triaxial, ACTS fabric Volume fractions for simulations

In order to evaluate the aerial density (d) of the tested fabrics (Fig. 3.3) a series of experimental measurements of mass (g) and area (m^2) were done for each preform. Thereafter the average aerial density of each preform was defined as the division of mass (g) against area (m^2) and shown in Tables 6.1-6.3. With the use of equation (3-2) the material properties and mould height, the fibre volume fraction was calculated as function of mould thickness as shown the Tables 6.1- 6.3.

i) 2/2 twill preform

Table 6.1: 2/2 twill aerial density measured experimentally.

Mass (g)	Area (mm)	d (m/A)
343	700x700	0.7
66.8	360x280	0.663
67.5	360x280	0.67
64	400x 230	0.696
65.8	400x 235	0.7
121.42		0.686

Volume fraction eq. (3-2) numerical calculation for 2/2 twill 3-layer

preform for 2.75mm thickness: $V_{f\,3layer} = 42.6\%$.

ii) ACTS 3D woven HTS40 F13 preform

Table 6.2: ACTS 3D woven HTS40 F13 fabric 4-layers aerial density measured experimentally.

Mass (g)	Area (mm)	d (m/A)
51.500	150x150	2.288
51.300	150x150	2.28
51.4		2.284

Volume fraction numerical calculation for 4-layer ACTS 3D woven

HTS40 F13 preform for 2.75mm thickness: $V_{f\,4layer} = 47.2\%$

iii) Triaxial preform

Table 6.3: Triaxial fabric aerial density measured experimentally.

Mass (g)	Area (mm)	d (m/A)
158.7	410x330	1.173
137.5	395x292	1.192
154.8	335x365	1.266
151.5	380x335	1.190
150.625		1.2

a) Volume fraction numerical calculation for triaxial 3-layer preform for 2.75mm thickness: $V_{f\,3layer} = 50.3\%$.

Fibre volume fractions calculated have been used as simulations input data with PAM-RTM$^{®}$ firstly for FE CAD 90° curve plate models in this Chapter and secondly for FE CAD generic node models in the following Chapter 7.

6.3.5 Mesh sensitivity

In this section the 2D, 3D 90° curved plate mesh sensitivity studies are presented. All sensitivity studies were performed for linear injection gate and vent along the preform bend geometry in 2D, 3D as shown in Fig. 6.3. The fill time (s) of each model was provided from the simulation. Analytical filling time was calculated with the use of equation (6-4)

$$t_{ff} = (\frac{\Phi\mu}{2KP_{inj}})x_{ff}^2 \qquad \textbf{(6-4)}$$

for rectilinear flow presented by Rudd C. D., et al [1] where Φ is the bed porosity, μ is the fluid viscosity, K is the permeability (m^2), P the injection pressure (bar), x_{ff} is the filling distance (m). All models had the same dimensions as the Perspex tool cavity.

6.3.6 2D, 3D 90° curved plate sensitivity

2D, 3D 90° curved plate models without the racetrack gap segmentation were studied for sensitivity verification using K principal permeability (m^2) as shown in Tables 6.4, 6.5. Models were simulated with 1 bar pressure and 0.3 Pa·s viscosity. All results agreed closely with the analytical fill time.

Table 6.4: 2D 90°curve plate sensitivity with 6899 triangular elements.

K Principal Permeability (m^2)	Filling Time (s)	Analytical Filling Time (s)
3.40E-10	8.79	8.82
2.22E-10	5.77	5.75
5.21E-12	13.36	13.5

Table 6.5: 3D 90°curve plate sensitivity with 169892 tetrahedral elements.

K Principal Permeability (m^2)	Filling Time (s)	Analytical Filling Time (s)
3.40E-10	8.69	8.82
2.22E-10	5.76	5.75
5.21E-12	13.29	13.5

6.3.7 2D, 3D race-tracking 90° curved plate sensitivity

2D racetrack sensitivity was verified for a series of models as shown in Tables 6.6 (first with one segment on bend geometry), Table 6.7 and Fig. 6.5, using, the permeability data presented in Tables 3.2, 4.7 for the 2/2 twill fabric and described in Chapter 6 section 6.3.4 i) 2D.

90° curved plate models with five segment racetrack zones as per Fig. 6.5 were simulated with 1 bar pressure and 0.3 Pa·s viscosity, as measured for the industrial oil HDX30 at lab temperature (19 ºC).

Table 6.7 shows racetrack fill time against number of elements, illustrating that convergence was seen for 93.600 triangular elements.

Table 6.6: 2D 90°curved plate with one segment racetrack zone.

No of Triag. Elem.	Racetrack fill time (s)	Edge fill time (s)	Δy lag position (cm)	Racetrack zones
22320	1.69	2.13	1.67	1 zone gap

For example in Table 6.6, racetrack fill time represents the fill time along the racetrack zone, edge fill time is the fill time at the edge of the mould, and Δy lag position the distance between them.

Table 6.7: 2D 90°curve plate 5 gap zone racetrack sensitivity studies.

No of Triag. Elem.	Racetrack fill time (s)	Edge fill time (s)	Δy lag position (cm)	Racetrack zones
9800	1.77	2.12	1.29	5 zones
28800	1.77	2.13	1.33	5 zones
50400	1.74	2.132	1.42	5 zones
93600	1.74	2.135	1.44	5 zones

Due to mesh refinement of the gap geometry which required a 3D structured mesh (highly time consuming and intensive computationally) race-tracking mesh sensitivity was only considered for two 3D models like those presented in Fig. 6.7.

The calculation of race-tracking was done at the end of the vent of the upper side of the 3D curved plate model.

The Δy lag racetrack position was calculated at the injection point of the opposite side (lower part) 3D curved plate model: Table 6.8 shows racetrack sensitivity for the upper side 3D curved plate models.

Table 6.8: 3D 90°curved plate upper side racetrack sensitivity.

No of Tetrah.elem.	Racetrack fill time (s)	Edge fill time (s)	Δy lag position edge (cm)	Racetrack zones
22680	0.736	2.13	6.17	3 out of 6
154350	0.755	2.15	6.2	3 out of 6

Table 6.9 shows lower side Δy lag racetrack sensitivity. The viscosity used for the 3D simulations was again equal to 0.3 Pa·s and the injection pressure was 1 bar.

Table 6.9: 3D 90°curve plate lower side racetrack sensitivity.

No of Tetrah. elem.	Racetrack fill time (s)	Edge fill time (s)	Δy lag position edge (cm)	Racetrack zones
22680	0.818	2.13	2.7	3 out of 6
154350	0.839	2.15	3.2	3 out of 6

Results of filling time of the edge for increasing number of tetrahedral elements comply well in both 3D and 2D cases with small variation which demonstrates acceptable level of mesh convergence.

6.4 Results and discussion

Considering different mould materials and testing the simile preforms, some small flow variations were expected, from the previously tested fabrics that were shown in Fig. 3.3 and Table 3.1. This was due to:

- Stochastic fabric variability that has not introduced on the 90° curved plate FEA model.

158

- Local variation of the friction-compression coefficient (μf_p), described in eq. (5-10).

- Lateral race-tracking on edges and corners of the model during infusion was not considered as well on FEA modelling.

However, the compaction behaviour of both the aluminium base tested fabrics and Perspex were not expected to differ considerably, as both surfaces were comparably smooth. Therefore the fluid flow behaviour observed under Perspex for the three tested fabrics was used in the optimization process of the node in ACTS.

The experimental flow behaviour was captured through imaging by the web cameras. Therefore, in the following sections, the simulation which was the closest match to a particular experiment is presented.

From this the racetrack gap height used in the simulation is presumed to determined represent that present in the experiment. This comparison yielded the racetrack behaviour of the tested fabrics along the 90° angle.

6.4.1 2/2 twill race-tracking

In this section 2D, 3D FE curved plate models via the PAM-RTM® software shown in Fig. 6.9 to 6.11 were compared with the experimental results for the 2/2 twill fabric.

6.4.1.1 2D 2/2 twill race-tracking for 0.85 mm gap FE model
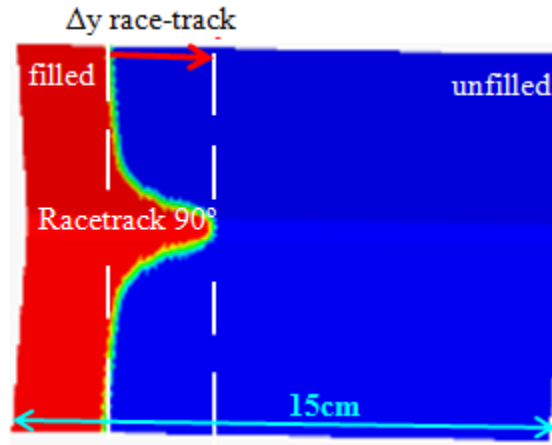
i) **At 5 cm from injection gate**
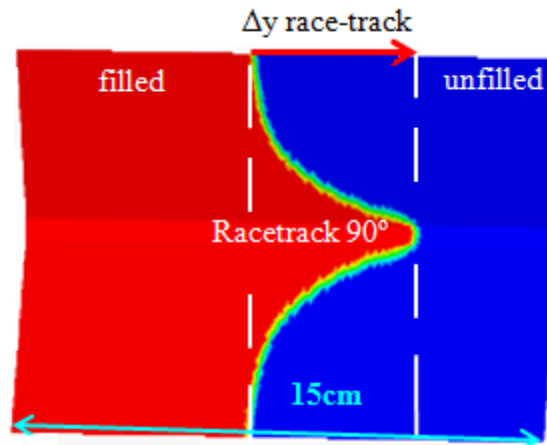
ii) **At 10 cm from injection gate**
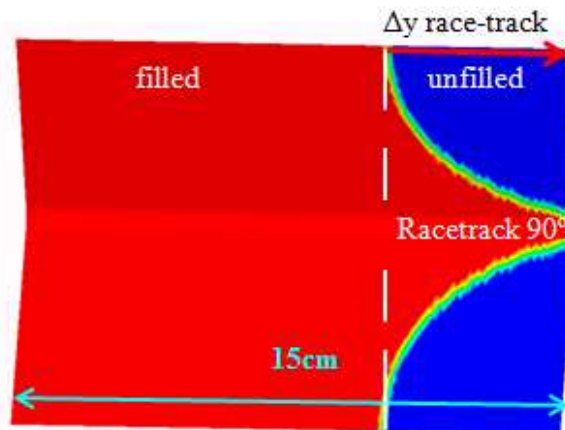
iii) **At 5 cm from injection gate**

Fig. 6.9: i), ii), iii) 2D 2/2 twill Δy racetrack evaluation for 0.85 mm gap modelled with the PAM-RTM software (red coloured filled area, blue unfilled, other colours half filled).

As input for 2D flow simulations, thickness-weighted averaging of the equivalent gap permeability shown in Fig. 6.5 and the permeability of the compressed fabric allows the effective permeability for each segment of the bend to be estimated. In the 2D racetrack model, the flow front (red colour filled area) is symetrical as shown Fig. 6.9. Table 6.10 presents y fit race-track analysis for Fig. 6.9.

Table 6.10: 2D 2/2 twill racetrack flow shape analysis from inlet for a 0.85 mm gap FE model of Fig. 6.9

y fill position 90° centre (cm)*	y fill position upper (cm)	y fill position lower (cm)	Δy race-track (fill 90° centre (-) fill average upper/lower) (cm)
5	2.42	2.42	2.58
10	5.98	5.98	4.02
15	9.99	9.99	5.01

* For briefly in the future only images y fit presented.

6.4.1.2 Results discussion 2D 2/2 twill 0.85 mm gap FE model

The simulated 2D average flow front position showing race-tracking, with lagging pressure gradient shapes reflect the dominating effect of race-tracking in the gap as shown Fig. 6.9 and numerically presented on Table 6.10.

For the 2D case simulated y fill position centre measured at 5, 10, 15 (cm) from the inlet at this point y fill position top-left and down-right was found to be 2.42, 5.98, 9.99 (cm) respectively increased Δy race-tracking flow front for 2.58, 4.02 and 5.01 (cm) at the outlet.

6.4.1.3 3D 2/2 twill race-tracking for 0.85 mm gap FE model

In order to obtain more accurate results through-thickness variations in permeability has to be taken into account in 3D FE model flow simulation. 3D 2/2 twill weave FE model shown in Fig. 6.10 for a 0.85mm gap height along the 90° angle compared with Perspex experiment revealed about the same fluid flow behaviour and so a gap of about the same height for the upper side bend of the tool.

i) Upper side PAM-RTM FE model   ii) Lower side PAM-RTM FE model

iii) Upper side Perspex   iv) Lower side Perspex
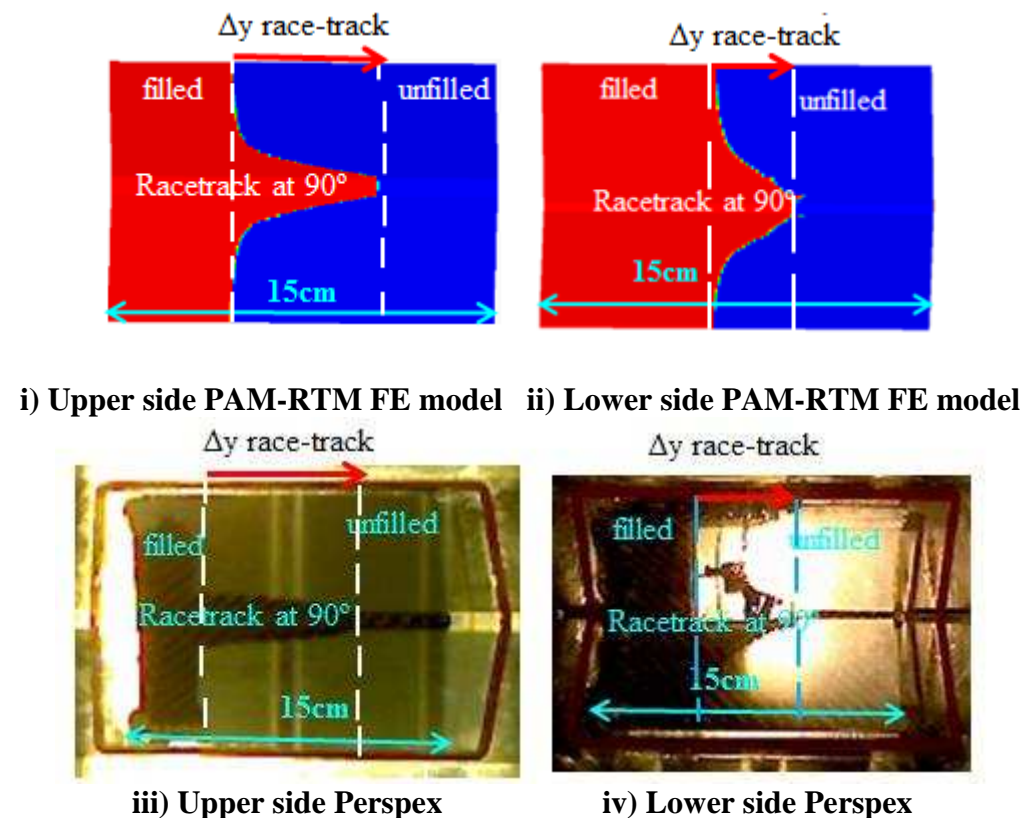
Fig. 6.10: 2/2 twill racetrack evaluation (at y=10cm of race-track) for 0.85 mm gap size, firstly obtained with the PAM-RTM software 3D FE CAD model (top images i), ii)) and secondly with the Perspex transparent tool (lower images iii), iv)).

Shape analysis on resin flow simulation based on 2/2 twill along the 90° angle on Fig. 6.10 presented on following Table 6.11.

Table 6.11: 2/2 twill racetrack flow shape analysis from inlet for a 0.85 mm gap FE model against 2/2 twill Perspex exp. i), ii) upper sides, iii), iv) lower sides related to Fig. 6.10.

i) 3D 2/2 twill FE (PAM-RTM) model shape analysis upper side:

y fill position 90° centre (cm)	y fill position upper (cm)	y fill position lower (cm)	Δy race-track (fill 90° centre (-) fill average upper/lower) (cm)
5	1.43	1.43	3.57
10	3.33	3.33	6.67
15	6.36	6.36	8.64

ii) 2/2 twill Perspex exp. shape analysis upper side:

y fill position 90° centre (cm)	y fill position upper (cm)	y fill position lower (cm)	Δy race-track (fill 90° centre (-) fill average upper/lower) (cm)
5	1.38	1.86	3.38
10	2.75	2.83	7.21
15	4.03	5.75	10.11

iii) 3D 2/2 twill FE (PAM-RTM) model shape analysis lower side:

y fill position 90° centre (cm)	y fill position upper (cm)	y fill position lower (cm)	Δy race-track (fill 90° centre (-) fill average upper/lower) (cm)
5	3.32	3.32	1.68
10	6.74	6.74	3.26
15	11.2	11.2	3.8

iv) 2/2 twill Perspex exp. shape analysis lower side:

y fill position 90° centre (cm)	y fill position upper (cm)	y fill position lower (cm)	Δy race-track (fill 90° centre (-) fill average upper/lower) (cm)
5	3.11	3.01	1.94
10	6.87	6.82	3.16
15	11.31	11.41	3.64

Comparing 3D modelling race-track results on Fig. 6.10 and Table 6.11 i) with 6.11 ii), Table 6.11 iii) with 6.11 iv) give close relation to the experimental results than those on 2D modelling on Table 6.10 as expected due to more realistic V_f along the 90° curved plate bending.

6.4.1.4 Results discussion 3D 2/2 twill 0.85 mm gap FE model

In this situation (case 1) the simulated flow front pressure gradient shapes reflect the dominating effect of race-tracking in the gap.

This observation indicated that the volume fraction modelling along the 90° angle with the 2/2 twill textile was correctly evaluated and that the fluid flow between the mould and the 2/2 twill fabric have been predicted more accurately with 3D FE modelling.

Modelling results of fluid flow agrees well with the experiment as shows Fig. 6.10 and Table 6.11.

Considering that the local variability of the fabric and the others phenomena in section 6.4 bullet points was not take on to account for the 3D FE model these are satisfactory results.

6.4.1.5 3D 2/2 twill race-tracking for 0.35 mm gap FE model

A further 2/2 twill weave Perspex experiment B2 revealed a fluid flow behaviour filling similar to 3D FE (PAM-RTM®) 0.35 mm gap height for the upper side bend of the tool.

i) Upper side PAM-RTM model　　**ii) Lower side PAM-RTM model**

iii) Upper side Perspex　　　　**iv) Lower side Perspex**
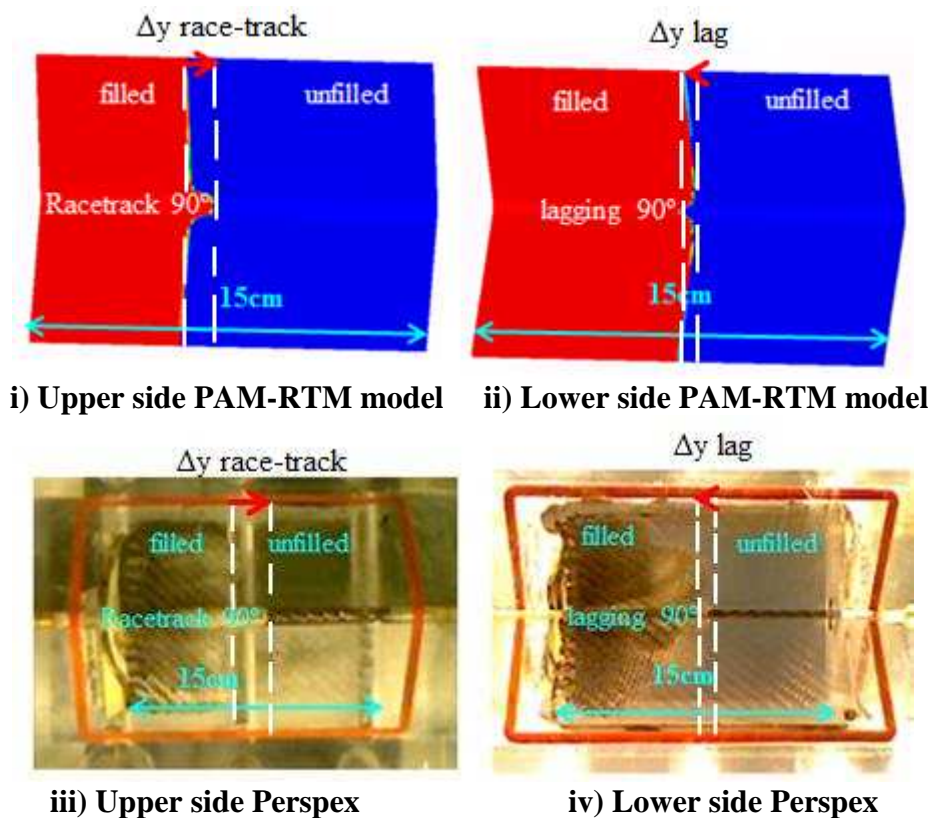
Fig. 6.11: 2/2 twill racetrack evaluation for the 0.35 mm gap size, obtained with the PAM-RTM software 3D FE CAD model (top images i), ii)) and with the Perspex transparent tool (lower images iii), iv)).

Fig. 6.11 shape analysis 3D 2/2 twill race-tracking for 0.35 mm gap FE model presented on following Table 6.12.

Table 6.12: 2/2 twill racetrack flow shape analysis from inlet for a 0.35 mm gap FE model against 2/2 twill Perspex exp. i), ii) upper sides, iii), iv) lower sides related to Fig. 6.11.

i) 3D 2/2 twill FE (PAM-RTM) model shape analysis upper side:

y fill position 90° centre (cm)	y fill position upper (cm)	y fill position lower (cm)	Δy race-track (fill 90° centre (-) fill average upper/lower) (cm)
5	3.94	3.94	1.06
10	8.7	8.7	1.3
15	13.7	13.7	1.3

ii) 2/2 twill Perspex exp. shape analysis upper side:

y fill position 90° centre (cm)	y fill position upper (cm)	y fill position lower (cm)	Δy race-track (fill 90° centre (-) fill average upper/lower) (cm)
5	4.86	4.2	0.47
10	8.93	8.82	1.13
15	13.45	12.6	1.97

iii) 3D 2/2 twill FE (PAM-RTM) model shape analysis lower side:

y fill position 90° centre (cm)	y fill position upper (cm)	y fill position lower (cm)	Δy lag (fill 90° centre (-) fill average upper/lower) (cm)
4.39	5	5	-0.61
9.38	10	10	-0.62
14.1	15	15	-0.9

iv) 2/2 twill Perspex exp. shape analysis lower side:

y fill position 90° centre (cm)	y fill position upper (cm)	y fill position lower (cm)	Δy lag (fill 90° centre (-) fill average upper/lower) (cm)
4.79	4.97	5.07	-0.23
9.36	9.87	10.05	-0.6
14.19	14.9	15.00	-0.77

3D modelling race-track results on Fig. 6.11 and Table 6.12 i), ii), Table 6.11 ii), iv) are more realistic due to more realistic V_f along the 90° curved plate bending.

6.4.1.6 Results discussion 3D 2/2 twill race-tracking for 0.35 mm gap FE model

3D simulation modelling results from PAM-RTM® with 2/2 twill properties, 0.35mm gap observed similar flow behaviour compared with Perspex experiment.

In this situation the through-thickness permeability K_3 is less dominant and therefore there is only a small racetrack on top of the tool along the bend angle and small lag of flow front at the opposite side of the tool.

Similar flow behaviour was obtained with the 3D FE CAD model for 0.35 mm gap with 2/2 twill material properties as shown Fig. 6.11 and Table 6.12 and in modelling results of fluid flow are in agreement with the experiment.

6.4.1.7 Results discussion 3D 2/2 twill race-tracking

Experimental observations with the Perspex transparent tool suggested that the racetrack gap on the upper part of the bend angle may vary between 0.85-0.35 mm.

The variation of the through thickness permeability K_3 against volume fraction V_f provided different shapes of race-tracking, which were modelled with the PAM-RTM® software.

Experimental results observation of the 2/2 twill preform with the Perspex tool on a 90° curve angle bend, suggested that during infusion there may be a centre gap of 0.85 mm between reinforcement and tool, which results in race-tracking at the upper radius of the bend.

In this case the through thickness permeability K_3 is reasonable high and therefore may allow an effective through thickness fluid exchange on both sides of the bend. The flow front shape at the top and the opposite side was dominated by the racetrack zone of the upper part. A similar behaviour was obtained for the 2/2 twill material properties of gap size 0.85 mm, but with the 3D FE CAD model as shown in Fig. 6.10.

For a 0.35mm centre gap observed (transient behaviour) the through thickness permeability K_3 is less dominant therefore there is only a small racetrack on top of the tool along the bend angle and small lag of flow front at the opposite side of the tool as presented in Fig 6.11.

6.4.2 3D woven HTS40 F13 race-track modelling

3D woven HTS40 F13 ACTS fabric was tested in same method as previously on section 6.4.1. Due to a lack of preform material only two experiments were conducted, one in the warp (K_2) and one in the weft (K_1) directions. 2D, 3D FE curved plate models via the PAM-RTM® software were compared with the experimental results.

6.4.2.1 2D FE model of 3D woven HTS40 F13 warp race-tracking for 0.65 mm gap

2D, FE curved plate PAM-RTM$^®$ software model was generated for the 3D woven HTS40 F13 warp fabric for comparison with experiment are presented in Fig. 6.12, and Fig. 6.13 for the warp permeability.
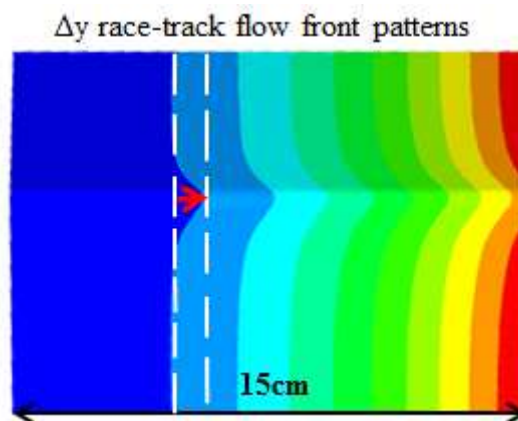
Fig. 6.12: 2D woven HTS40 F13 warp (K_2) racetrack evaluation (shown by red arrow) for the 0.65 mm gap size, modelled with the PAM-RTM software.

Input for 2D flow simulations, with 3D woven HTS40 F13 warp generated as shown in Fig. 6.5 and described previously in Section 6.4.1.1.

As per Fig. 6.12 in the 2D racetrack model, the flow front (in different colours blue, turquoise, aquamarine,..., etc.) is symmetrical due to uniform permeability through the thickness.

Table 6.13: 2D racetrack flow shape analysis from inlet for 3D woven HTS40 F13 warp 0.65 mm gap FE model related to Fig. 6.12

y fill position 90° centre (cm)	y fill position upper (cm)	y fill position lower (cm)	Δy race-track (fill 90° centre (-) fill average upper/lower) (cm)
5	4.29	4.29	0.71
10	9.17	9.17	0.83
15	14.14	14.14	0.86

2D race-track shape analysis on resin flow simulation based on 3D woven HTS40 F13 warp along the 90° angle on Fig. 6.12 presented on Table 6.13.

6.4.2.2 Results discussion 2D FE model of 3D woven HTS40 F13 warp race-tracking for 0.65 mm gap

The simulated 2D flow front position race-tracking pressure gradient shapes reflect the dominating effect of race-tracking in the 0.65mm centre gap as shown Fig. 6.12 and numerically presented on Table 6.13.

6.4.2.3 3D FE model of 3D woven HTS40 F13 warp race-tracking for 0.65 mm gap

Accurate results of through-thickness variations in permeability were obtained by taking in to account the 3D FE model simulation for the 3D woven HTS40 F13 warp fabric.

3D woven HTS40 F13 warp fabric FE model shown in Fig. 6.13 for a 0.65mm gap height along the 90° angle compared with Perspex experiment revealed about the same average fluid behaviour and so a gap of about the same height for the upper side bend of the tool.

i) Upper side PAM-RTM model   **ii) Lower side PAM-RTM model**

   iii) Upper side Perspex   **iv) Lower side Perspex**
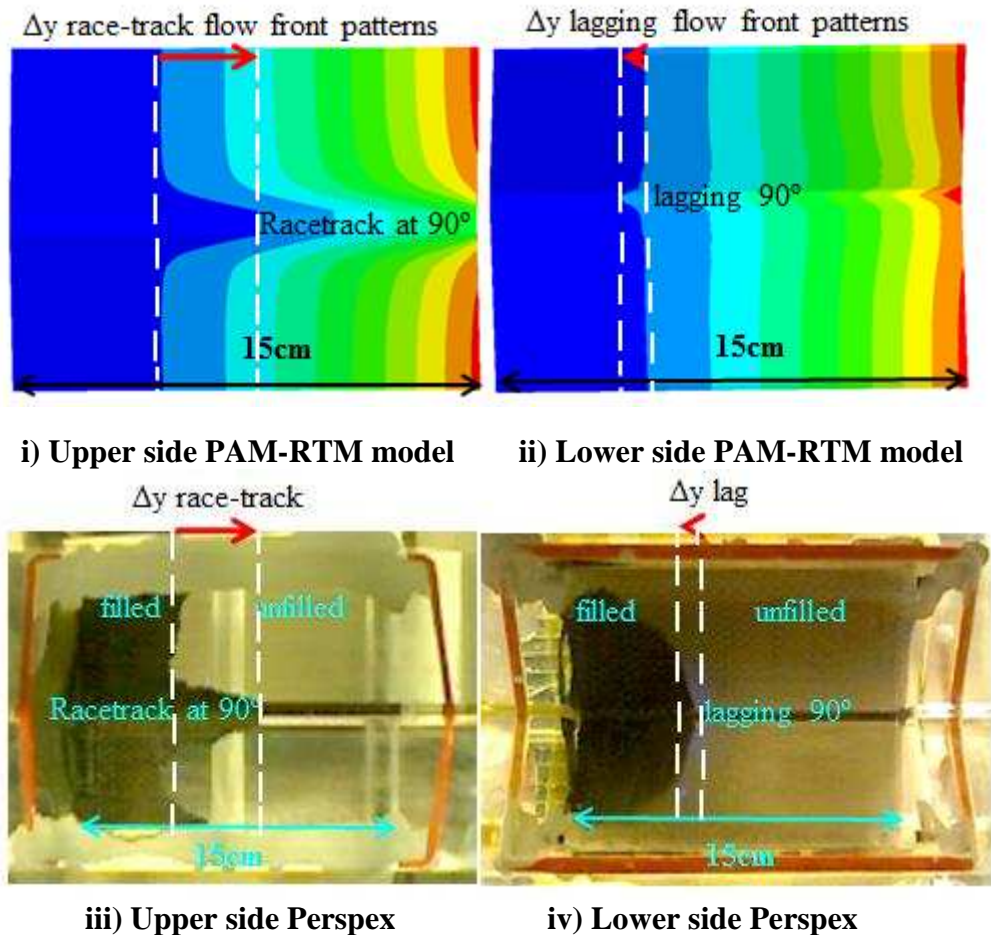
Fig. 6.13: Woven HTS40 F13 warp (K_2) racetrack evaluation for the 0.65 mm gap size, obtained with the PAM-RTM software 3D FE CAD model (top images i), ii)) and with the Perspex transparent tool (lower images iii), iv)).

Race-track shape analysis on resin flow simulation based on 3D woven HTS40

F13 warp along the 90° angle on Fig. 6.13 presented on following Table 6.14.

Table 6.14: 3D woven HTS40 F13 warp racetrack flow shape analysis from inlet for a 0.65 mm gap FE model against Perspex exp. i), ii) upper sides, iii), iv) lower sides related to Fig. 6.13.

i) 3D woven HTS40 F13 warp FE (PAM-RTM) model shape analysis upper side:

y fill position 90° centre (cm)	y fill position upper (cm)	y fill position lower (cm)	Δy race-track (fill 90° centre (-) fill average upper/lower) (cm)
5	2.92	2.92	2.08
10	7.27	7.27	2.73
15	11.59	11.59	3.41

ii) 3D woven HTS40 F13 warp Perspex exp. shape analysis upper side:

y fill position 90° centre (cm)	y fill position upper (cm)	y fill position lower (cm)	Δy race-track (fill 90° centre (-) fill average upper/lower) (cm)
5	3.31	2.77	1.96
10	5.95	7.73	3.16
15	8.45	9.95	5.8

iii) 3D woven HTS40 F13 warp FE (PAM-RTM) model shape analysis lower side:

y fill position 90° centre (cm)	y fill position upper (cm)	y fill position lower (cm)	Δy lag (fill 90° centre (-) fill average upper/lower) (cm)
4.29	5	5	-0.71
9.19	10	10	-0.81
14.18	15	15	-0.82

iv) 3D woven HTS40 F13 warp Perspex exp. shape analysis lower-side:

y fill position 90° centre (cm)	y fill position upper (cm)	y fill position lower (cm)	Δy lag (fill 90° centre (-) fill average upper/lower) (cm)
4.43	5	5.05	-0.57
9.36	10.37	10	-0.66
14.1	14.19	15	-0.82

3D modelling race-track results on Fig. 6.13 and Table 6.14 i), iii) are more realistic to the experimental results Table 6.11 ii), iv) than those on 2D modelling on Fig. 6.12 and Table 6.13 as expected due to 3D modelling with more realistic V_f along the 90° curved plate bending.

6.4.2.4 2D FE model of 3D woven HTS40 F13 weft race-tracking for 0.65 mm gap

As per section 6.4.2.1 2D, FE curved plate model 0.65 mm gap size via the PAM-RTM software generated for the 3D woven HTS40 F13 weft fabric in this section for comparison with 3D, FE curved plate model of 0.65 mm gap 3D woven HTS40 F13 weft racetrack and Perspex experiment are presented in Fig. 6.14, and Fig. 6.15 for the weft permeability.
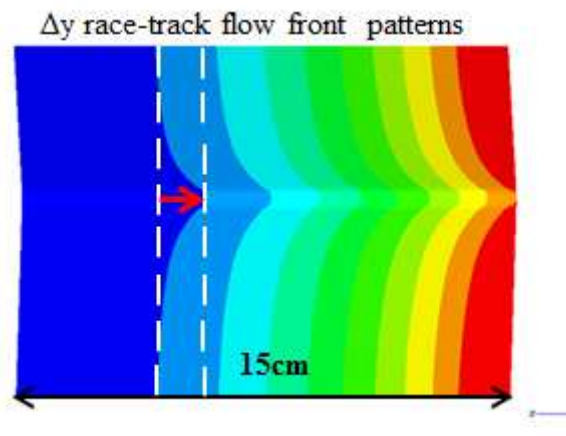
Fig. 6.14: 2D woven HTS40 F13 weft (K_l) racetrack evaluation (shown by red arrow) for the 0.65 mm gap size, modelled with the PAM-RTM software.

Input for 2D flow simulations, with 3D woven HTS40 F13 weft is shown in Fig. 6.5 and described previously in section 6.4.1.1. As per Fig. 6.14 in the 2D racetrack model, the flow front is symmetrical.

Table 6.15: 2D racetrack flow shape analysis from inlet for 3D woven HTS40 F13 weft 0.65 mm gap FE model related to Fig. 6.12.

y fill position 90° centre (cm)	y fill position upper (cm)	y fill position lower (cm)	Δy race-track (fill 90° centre (-) fill average upper/lower) (cm)
5	3.64	3.64	1.36
10	8.57	8.57	1.43
15	13.33	13.33	1.67

2D race-track shape analysis on resin flow simulation based on 3D woven HTS40 F13 weft along the 90° angle on Fig. 6.14 presented on Table 6.15.

6.4.2.5 Results discussion 2D FE model of 3D woven HTS40 F13 weft race-tracking for 0.65 mm gap

The simulated 2D flow front position race-tracking (with lagging on top left up and down-right) pressure gradient shapes reflect the dominating effect of race-tracking in the 0.65mm centre gap as shown Fig. 6.14 and numerically presented on Table 6.15.

6.4.2.6 3D FE model of 3D woven HTS40 F13 weft race-tracking for a 0.65 mm gap

Accurate results for through-thickness variations in permeability were obtained by taking on to account the 3D FE model simulation for the 3D woven HTS40 F13 weft fabric.

3D woven HTS40 F13 weft fabric FE model shown in Fig. 6.15 for a 0.65mm gap height along the 90° angle compared with Perspex experiment revealed a similar average fluid behaviour and so a gap of about the same height for the upper side bend of the tool.

i) Upper side PAM-RTM mode   **ii) Lower side PAM-RTM model**

iii) Upper side Perspex   **iv) Lower side Perspex**

Fig. 6.15: Woven HTS40 F13 weft (K_I) racetrack evaluation for the 0.65 mm gap size, obtained with the PAM-RTM software 3D FE CAD model (top images i), ii)) and with the Perspex transparent tool (lower images iii), iv)).

Race-track shape analysis on resin flow simulation based on 3D woven HTS40

F13 weft along the 90° angle on Fig. 6.15 presented on following Table 6.16.

Table 6.16: 3D woven HTS40 F13 weft racetrack flow shape analysis from inlet for a 0.65 mm gap FE model against Perspex exp. i), ii) upper sides, iii), iv) lower sides related to Fig. 6.15.

i) 3D woven HTS40 F13 warp FE (PAM-RTM) model shape analysis upper side:

y fill position 90° centre (cm)	y fill position upper (cm)	y fill position lower (cm)	Δy race-track (fill 90° centre (-) fill average upper/lower) (cm)
5	2.09	2.09	2.91
10	4.43	4.43	5.57
15	9.29	9.29	5.71

ii) 3D woven HTS40 F13 warp Perspex exp. shape analysis upper side:

y fill position 90° centre (cm)	y fill position upper (cm)	y fill position lower (cm)	Δy race-track (fill 90° centre (-) fill average upper/lower) (cm)
5	2.27	2.77	2.38
10	3.95	6.54	4.77
15	8.86	12.04	5.55

iii) 3D woven HTS40 F13 warp FE (PAM-RTM) model shape analysis lower side:

y fill position 90° centre (cm)	y fill position upper (cm)	y fill position lower (cm)	Δy lag (fill 90° centre (-) fill average upper/lower) (cm)
3.65	5	5	-1.35
8.62	10	10	-1.38
13.48	15	15	-1.52

iv) 3D woven HTS40 F13 warp Perspex exp. shape analysis lower side:

y fill position 90° centre (cm)	y fill position upper (cm)	y fill position lower (cm)	Δy lag (fill 90° centre (-) fill average upper/lower) (cm)
4.24	5	5.05	-0.76
9.3	10.17	10	-0.71
14.25	15	15	-0.75

3D modelling race-track results on Fig. 6.15 and Table 6.16 i), iii) are close more to the experimental results Table 6.11 ii), iv) than those from 2D modelling on Fig. 6.14 and Table 6.15 as expected due to 3D modelling with more realistic V_f along the 90° curved plate bending.

## 6.4.2.7 Results discussion 3D FE model of 3D woven HTS40 F13 warp/weft race-tracking for a 0.65 mm gap

Comparing the experimental observations of the 3D woven HTS40 F13 ACTS preform (in both warp and weft directions) with a Perspex tool on a 90° curved angle bend, suggests that during infusion the reinforcement resulted in racetracking at the upper radius of the bend. In the case of the of 3D woven ACTS preform the through thickness permeability K_3 was less dominant and therefore there was racetracking in the gap on top of the tool along the bend angle and a lag of flow front at the opposite side of the tool.

Along the weft (K_1) direction the racetrack of the above fabric was slightly larger due to the higher permeability in the weft for this fabric (this was also clearly stated in chapter 4 on Fig 4.6 a).

A similar flow behaviour was also observed with the 3D FE model for the 0.65 mm gap size with the 3D woven HTS40 F13 fabric displayed in Fig. 6.13, and 6.15.

In this case the measurement was within the gap range for this preform as assessed through the bending tests in Chapter 3. Discrepancies are due on reasons mentioned (with bullet points) in Section 6.4.

6.4.3 Triaxial race-tracking

Triaxial preform modelling simulations were conducted with the same methodology of sections 6.3.2.1, 6.3.2.2 and 6.3.3 incorporating the measured material properties presented in Tables 3.2, 4.7, Chapters 3, 4.

6.4.3.1 2D FE model of triaxial warp race-tracking for 0.35 mm gap

In 2D FE modelling of triaxial fabric with warp permeability 0.35 mm gap the flow front is shown Fig. 6.16.
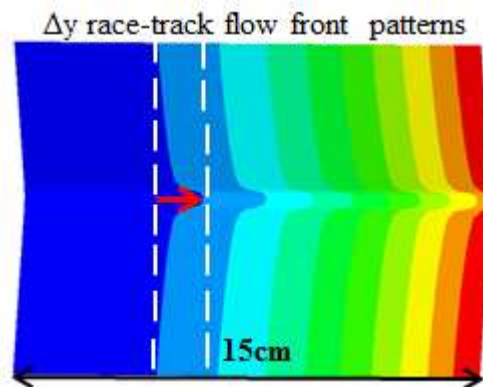
Fig. 6.16: 2D triaxial warp (K_l) racetrack evaluation (shown by red arrow) for the 0.35 mm gap modelled with the PAM-RTM software.

Input for 2D flow simulations, with triaxiax warp permeability generated as shown in Fig. 6.5 and described previously in section 6.4.1.1 is shown in Fig. 6.16. Shape analysis on resin flow simulation based on 2D triaxial fabric with warp permeability along the 90° angle with 0.35mm gap on Fig. 6.16 is presented on following Table 6.17.

Table 6.17: 2D racetrack flow shape analysis from inlet for 3D triaxial warp 0.35 mm gap FE model related to Fig. 6.16

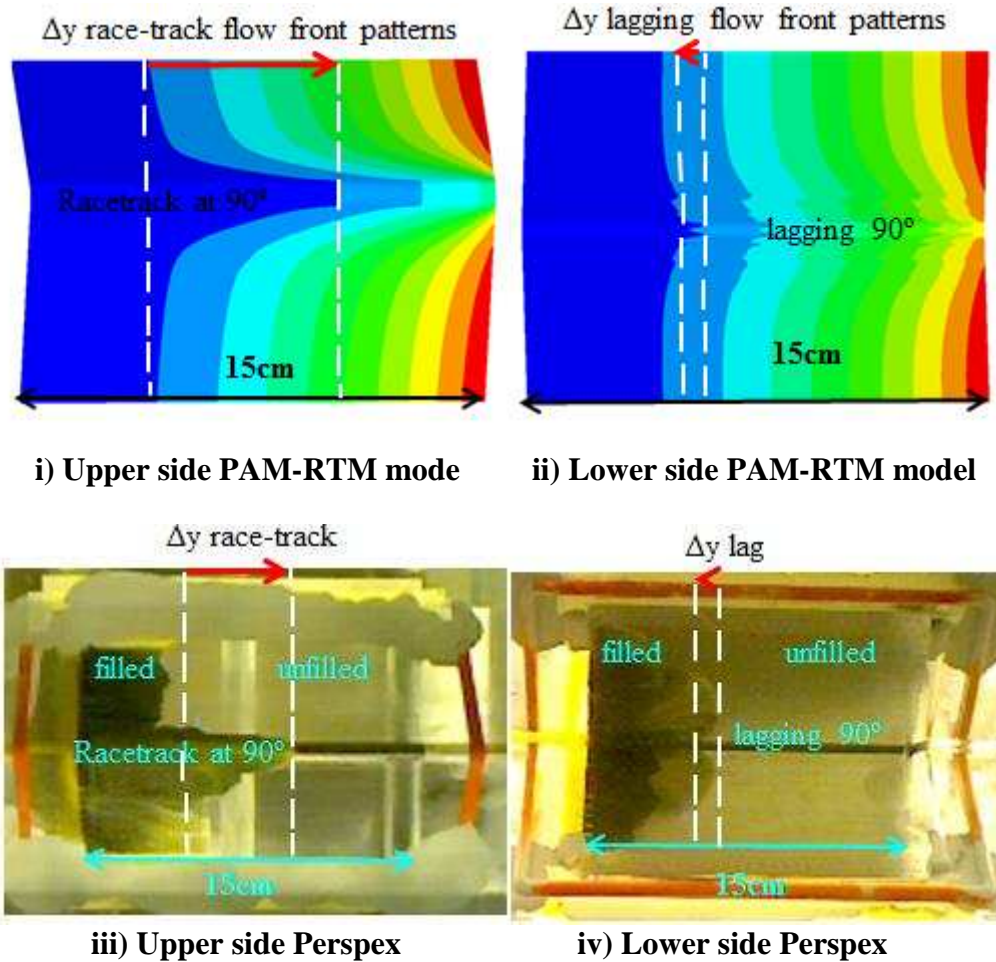| y fill position 90° centre (cm)	y fill position upper (cm)	y fill position lower (cm)	Δy race-track (fill 90° centre (-) fill average upper/lower) (cm)
5	4.09	4.09	0.91
10	9.07	9.07	0.93
15	13.35	13.35	1.65

6.4.3.2 Results discussion 2D FE model of triaxial warp race-tracking for 0.35 mm gap

The simulated 2D flow front position race-tracking (with lagging on top left up and down-right) pressure gradient shapes reflect the dominating effect of race-tracking in the 0.35mm gap as shown Fig. 6.16 and numerically presented on Table 6.17. For the 2D case simulated y fill position centre measured at 5, 10, 15 (cm) from the inlet at this point y lag position top-left and down-right was found to be 4.09, 9.07, 13.35 (cm) respectively. Δy race-tracking is also increased from 0.91 (cm) inlet to 1.65 (cm) at the outlet.

6.4.3.3 3D FE model of triaxial warp race-tracking for 0.35 mm gap

Accurate results of through-thickness variations in permeability were obtained by taking on to account the 3D FE model simulation for the triaxial warp fabric.

Triaxial warp fabric FE model shown in Fig. 6.17 for a 0.35mm gap height along the 90° angle compared with Perspex experiment revealed similar average fluid behaviour and so a gap of about the same height for the upper side bend of the tool.
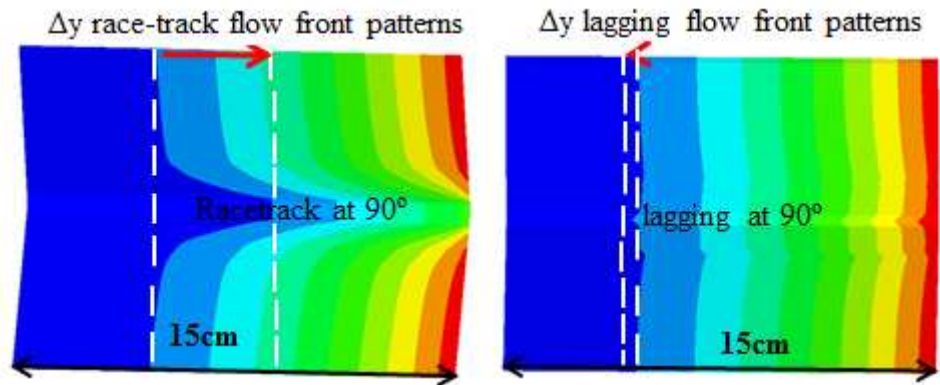
i) **Upper side PAM-RTM model** ii) **Lower side PAM-RTM model**
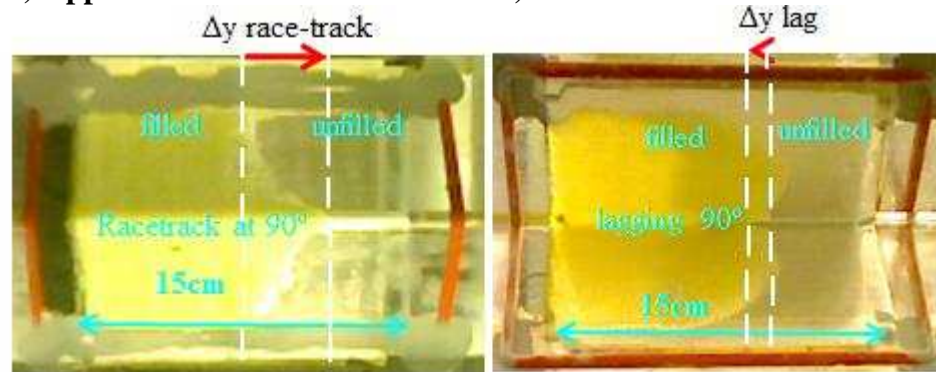
iii) **Upper side Perspex** iv) **Lower side Perspex**

Fig. 6.17: Triaxial warp (K_1) racetrack evaluation for 0.35 mm gap size, obtained with the PAM-RTM software 3D FE CAD model (top images i), ii)) and with the Perspex transparent tool (lower images iii), iv)).

Race-track shape analysis on resin flow simulation based on triaxial warp along the 90° angle on Fig. 6.17, is presented on following Table 6.18.

Table 6.18: Triaxial warp racetrack flow shape analysis from inlet for a 0.35 mm gap FE model against Perspex exp. with the same type fabric i), ii) upper sides, iii), iv) lower sides comparison related to Fig. 6.17.

i) Triaxial warp FE model(PAM-RTM) shape analysis upper side:

y fill position 90° centre (cm)	y fill position upper (cm)	y fill position lower (cm)	Δy race-track (fill 90° centre (-) fill average upper/lower) (cm)
5	3.11	3.11	1.89
10	7.98	7.98	2.02
15	12.7	12.7	2.3

ii) Triaxial warp Perspex exp. shape analysis upper side:

y fill position 90° centre (cm)	y fill position upper (cm)	y fill position lower (cm)	Δy race-track (fill 90° centre (-) fill average upper/lower) (cm)
5	3.61	4.07	1.16
10	7.48	8.17	2.18
15	11.67	12.99	2.67

iii) Triaxial warp FE model (PAM-RTM) shape analysis lower side:

y fill position 90° centre (cm)	y fill position upper (cm)	y fill position lower (cm)	Δy lag (fill 90° centre (-) fill average upper/lower) (cm)
3.85	5	5	-1.15
8.85	10	10	-1.15
13.85	15	15	-1.15

iv) Triaxial warp Perspex exp. shape analysis lower side:

y fill position 90° centre (cm)	y fill position upper (cm)	y fill position lower (cm)	Δy lag (fill 90° centre (-) fill average upper/lower) (cm)
4.63	5	5.14	-0.44
8.71	10.21	10	-1.42
13.56	15	14.42	-1.15

6.4.3.4 Results discussion 3D FE model of triaxial warp race-tracking for 0.35 mm gap

The flow behaviour in the Perspex transparent rig was similar to the 3D FE CAD model of the 0.35 mm gap size, along the 90° curved plate preform. In this case the through thickness permeability K_3 was less dominant and therefore there was racetracking in the gap on top of the tool along the bend angle and a lag of flow front at the opposite side of the tool, shown in Fig. 6.17 and Table 6.18.

6.4.3.5 2D FE model of triaxial weft race-tracking for 0.35 mm gap

2D FE modelling of triaxial fabric with weft permeability 0.35 mm gap the flow front is shown Fig. 6.18.
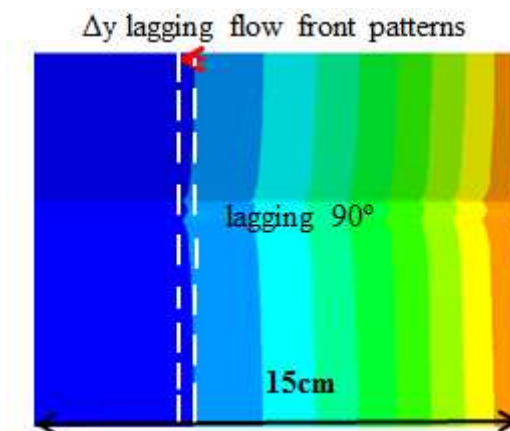
Fig. 6.18: The 2D triaxial weft (K_2) racetrack evaluation for the 0.35 mm gap size modelled with the PAM-RTM software.

Shape analysis on resin flow simulation based on 2D triaxial fabric with weft permeability along the 90° angle with 0.35mm gap on Fig. 6.18, is presented on following Table 6.19.

Table 6.19: 2D racetrack flow shape analysis from inlet for 3D triaxial weft 0.35 mm gap FE model related to Fig. 6.18

y fill position 90° centre (cm)	y fill position top-left (cm)	y fill position down-right (cm)	Δy lag (fill 90° centre (-) fill average top-left/down-right) (cm)
4.77	5	5	-0.23
9.77	10	10	-0.23
14.77	15	15	-0.23

6.4.3.6 Results discussion 2D FE model of triaxial weft race-tracking for 0.35 mm gap

In this case the simulated 2D flow front position, pressure gradient shapes reflect the dominating effect of a small lag fill position in the centre of the 90° curve plate (along the bending angle) for 0.35mm gap as shown Fig. 6.18 and numerically presented on Table 6.19.

6.4.3.7 3D FE model of triaxial weft race-tracking for 0.35 mm gap

Accurate results for through-thickness variations in permeability were obtained by taking on to account the 3D FE model simulation for the triaxial weft fabric.

Triaxial weft fabric FE model shown in Fig. 6.19 for a 0.35mm gap height along the 90° angle compared with Perspex experiment revealed about the same average fluid behaviour and so a gap of about the same height for the upper side bend of the tool.

i) Upper side PAM-RTM model   ii) Lower side PAM-RTM model

iii) Upper side Perspex   iv) Lower side Perspex
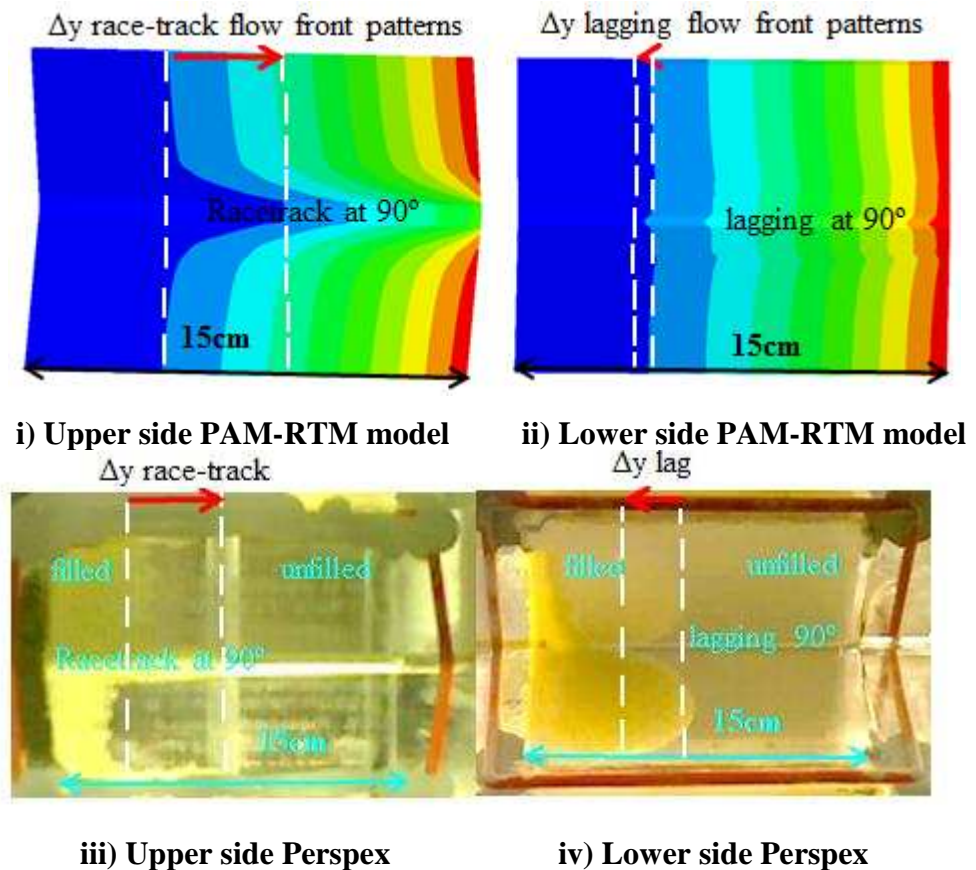
Fig. 6.19: Triaxial weft (K$_2$) racetrack evaluation for 0.35 mm gap size, obtained with the PAM-RTM software 3D FE CAD model (top images i), ii)) and with the Perspex transparent tool (lower images iii), iv)).

Race-track shape analysis on resin flow simulation based on triaxial warp along the 90° angle on Fig. 6.19 presented on following Table 6.20.

Table 6.20: Triaxial weft racetrack flow shape analysis from inlet for a 0.35 mm gap FE model against Perspex exp. with the same type fabric i), ii) upper sides, iii), iv) lower sides related to Fig. 6.19.

i)   Triaxial weft FE model(PAM-RTM) shape analysis upper side:

y fill position 90° centre (cm)	y fill position upper (cm)	y fill position lower (cm)	Δy race-track (fill 90° centre (-) fill average upper/lower) (cm)
5	2.93	2.93	2.07
10	6.89	6.89	3.11
15	11.87	11.87	3.13

ii) Triaxial weft Perspex exp. shape analysis upper side:

y fill position 90° centre (cm)	y fill position upper (cm)	y fill position lower (cm)	Δy race-track (fill 90° centre (-) fill average upper/lower) (cm)
5	3.25	2.48	2.14
10	7.44	5.46	3.55
15	14.25	9.53	3.11

iii) Triaxial weft FE model (PAM-RTM) shape analysis lower side:

y fill position 90° centre (cm)	y fill position upper (cm)	y fill position lower (cm)	Δy lag (fill 90° centre (-) fill average upper/lower) (cm)
4.34	5	5	-0.66
9.34	10	10	-0.66
14.34	15	15	-0.66

iv) Triaxial weft Perspex exp. shape analysis lower side:

y fill position 90° centre (cm)	y fill position upper (cm)	y fill position lower (cm)	Δy lag (fill 90° centre (-) fill average upper/lower) (cm)
4.18	5.09	5.3	-1.02
6.46	9.59	10.23	-3.45
13.06	14.05	15	-1.47

3D modelling race-track results comparison on Fig. 6.19 and Table 6.20 i) with iii), Table 6.20 ii) with iv) are more close to the experimental results than those on 2D modelling on Fig. 6.18 and Table 6.19 as expected due to 3D modelling with more realistic V_f along the 90° curved plate bending.

6.4.3.8 Results discussion 3D FE model of triaxial weft race-tracking for 0.35 mm gap

The flow behaviour in the Perspex transparent rig was similar to the 3D FE CAD model of the 0.35 mm gap size, along the 90° curved plate preform. In this case the through thickness permeability K_3 was less dominant (as per warp) and therefore there was race-tracking in the gap on top of the tool along the bend angle and a lag of flow front at the opposite side of the tool, shown in Fig. 6.19 and Table 6.20.

6.4.3.9 Triaxial warp/weft race-tracking results and discussion

Experimental results for the Perspex tool for the triaxial preform suggested a small gap between preform and the top Perspex wall due to the variation of the friction-compression (μf_p) coefficient described in eq. (5-10). Considering that the provided permeability values for the triaxial fabric were correct as mentioned in section 4.1, the PAM–RTM® model for 0.35 mm gap size was able to predict reasonably racetrack flow behaviour along the 90° angle bend.

Other experimental observations with the Perspex tool suggested lagging in the flow front at the top and opposite sides both in warp and weft directions, as shown in Fig. 6.20, 6.21.

Modelling the variability of the node geometry with the triaxial preform in Chapter 8, cases in Fig. 6.20, 6.21 were considered lagging at 90 ^{o} angle bend.

| i)Upper side Perspex | ii) Lower side Perspex |
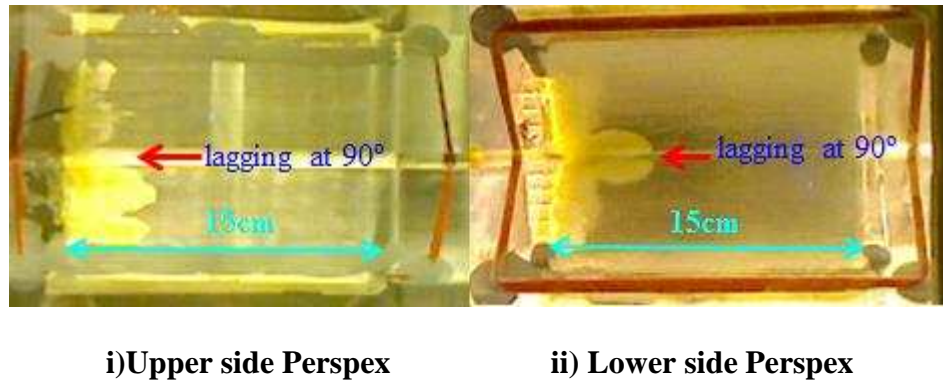
Fig. 6.20: Triaxial warp (K_1) flow behaviour with Perspex transparent tool. On the i) left image the top side (outward bend) of the 90° curved plate lagging is shown (red arrow), whereas on the ii) right image the bottom of the 90° curved plate lagging is shown (red arrow).

| i) Upper side Perspex | ii) Lower side Perspex |
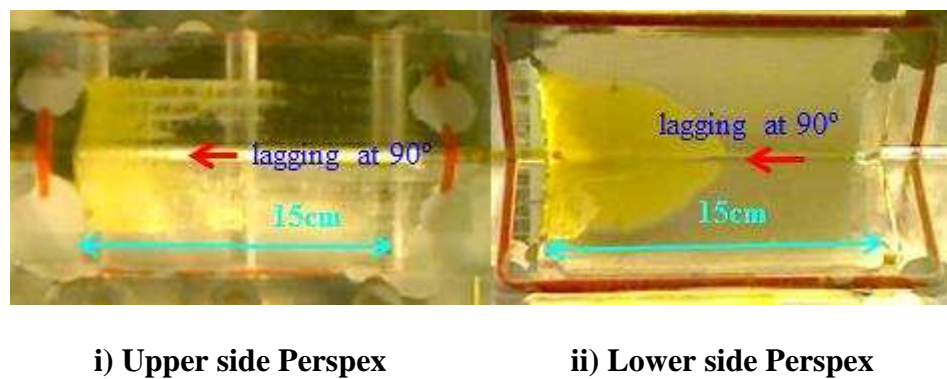
Fig. 6.21: Triaxial weft (K_2) flow behaviour with Perspex transparent tool. On the i) left image the top side (outer bend) of the 90° curved plate lagging is shown (red arrow), whereas on the ii) right image the bottom of the 90° curved plate lagging is shown (red arrow).

In order to model the aforementioned behaviour the triaxial preform V_f was decreased purposely down to 0.20 from the value of 0.503, which gave a similar behaviour to that measured experimentally, Fig 6.22 shows the 0.35

mm gap size, of the 3D FE CAD 90° curved plate model, having a volume fraction $V_f = 0.20$.

| i) Upper side FE model | ii) Lower side FE model |
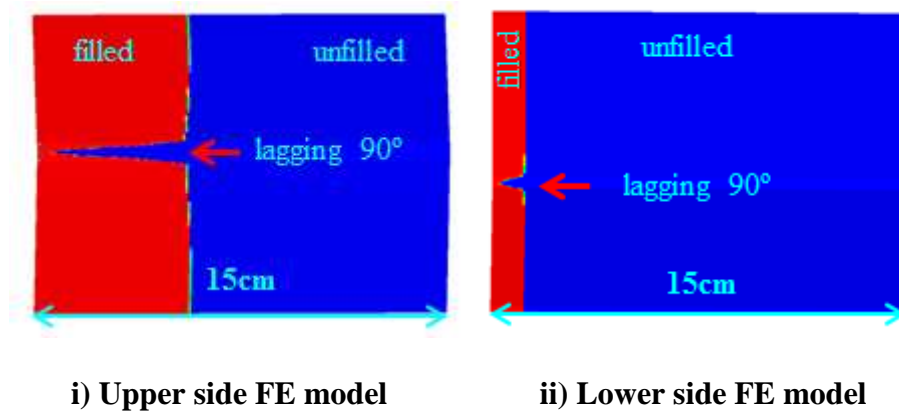
Fig. 6.22: Triaxial flow behaviour modelling with PAM-RTM software 3D FE CAD model for a 0.35 mm gap curved plate (with $V_f = 0.20$). On the left image, i) the top side of the 90° curved plate is displayed while on the ii) right image the bottom (inner side) of the 90°curved plate image is shown.

Due to the variable behaviour of the triaxial fabric it was suggested not to generate any advanced composite truss structure with this preform as it will be difficult to predict the variability according to the information provided from this investigation. The study of the variability of the node with the worst case (scenario where the permeability of the radii is lower than the permeability of the fabric) at this point will provide useful information only for the ACTS node geometric structure variability.

6.5 Conclusion

In Chapter 6 the Control Volume/Finite Element Method (CV/FEM) has been applied to solve the partial differential equations that refer to Darcy's law eq. (1-1). This was essential in order to address the moving boundary problem such as resin flow front advancement through the fabric.

Resin Transfer Moulding (RTM) gaps between the reinforcement and the tool surface due to local compression at sharp edges in the component geometry were modelled firstly with 2D FE CAD and secondly with 3D FE CAD on a 90° curved plate geometry. The gap size is affected by the bend geometry (radius and angle) according to equation (5-11) and the reinforcement parameters such as compressibility and friction-compression (μf_p) coefficient (on the tool surface) according to equation (5-10).

The input for 2D flow simulations was the thickness-weighted average of the equivalent gap permeability and the permeability of the compressed fabric. These allowed the effective permeability for each segment of the bend to be estimated according to equations (6-1) to (6-3). 3D flow simulations used material properties for simulations which were determined experimentally and presented in tables 3.2, 4.7, Chapters 3, 4.

Experimental observations on a Perspex tool with a 90° bend suggested that, during resin injection, the gap between reinforcement and tool results in racetracking at the top radius of the bend, while at the opposite (inner) side the locally increased fibre volume fraction V_f of the compressed reinforcement, may result in lagging of the flow front at the bend according to the variation of V_f / K_3 as was shown in Fig. 6.11, 6.13, 6.15, 6.17, 6.19.

When examining the top radii, K_3 is high enough to allow effective fluid exchange, whereas the flow front shape on the opposite (inner) side was also dominated by the top racetracking as was shown in Fig. 6.10.

Furthermore the flow front shapes on top and opposite sides of a 90° preform bend during impregnation of the 2/2 twill plain weave carbon fibre fabric, 3D woven HTS40 F13 carbon fibre fabric and triaxial plain weave glass fibre fabric was observed.

By applying the model of Chapter 5, the preform bend was segmented into zones each of different average gap height and fabric thickness in both 2D, and 3D scenarios (see Fig. 6.5, 6.7 respectively). The equivalent permeability of the gaps can be estimated, and the permeability of the compressed reinforcement can be determined from interpolation of the permeability measured at different compaction heights. Experimental analysis of localised fabric compression indicated that the gap height along the bend can be modelled as a curve according to eq. (5-11).

All gap height values estimated by means of a transparent Perspex tool were within the range of the 3D FE CAD 90° curve plate models albeit slightly lower than the gaps measured with CMM on aluminium base curved plates in Chapter 3. This was generally expected as CMM measurements (shown in Fig. 3.12) have been conducted under some applied pressure. In CMM measurements, the fabric was fixed on both ends with an adhesive in order to hold it in place. The ACTS node is manufactured from one piece of 8-layer 3D woven HTS40 F13 preform, which is assembled with some pressure and stress on the mould nodes as shown in Fig.7.9 (a)-7.9 (d). Some cases with zero gap size on the Perspex tool were observed for the triaxial fabric as shown in Fig. 6.20, 6.21, which may be modelled as mentioned at the end of section 6.4.3 and shown in Fig. 6.22.

The key findings to be carried forward can be summarised as follows:

- Race-track flow first modelled in 2D and then in 3D. Experimental results derived with the use of a transparent rig fitted with reasonable accuracy to 3D modelling.

- Similar fluid behaviour of 3D FE modelling with transparent tool experiments verified that there is compaction along a 90° curved plate due to fabric bending. These Vf variations generates a gap between the preform and mould wall.

- Therefore height h (mm) of the gap between the reinforcement and mould can be estimated by matching experiments to equivalent simulations.

References

[**1**]Rudd, C.D., Long, A.C., Kendal, K.N., and Mangin, CGE., Liquid moulding technologies, *"Resin transfer m*oulding structural reaction injection *moulding and related processing techniques"* Woodhead Publishing limited, (1997); p 258, p 270-273, ISBN 1 885 73 242 4.

[**2**]Li, J., Zhang, C., Liang, Z., and Wang, B., "Stochastic Simulation Based Approach for Statistical Analysis and Characterization of Composites *Manufacturing Processes"*, Journal of Manufacturing Systems Vol. **25**/ No. 2

[**3**]Liu, B., Bickerton, S., and Advani, S., "Modelling and simulation of resin *transfer moulding (RTM) gate control, venting and dry spot prediction"*. Composites Part A: Vol **27**A Number 2: 1996; p 135-141.

[**4**]Schell, J.S.U., Deleglise, M., Binetruy, C., Krawczak, P., Ermanni, P., "Numerical prediction and experimental characterisation of meso-scale-voids *in liquid composite moulding"*, Composites: Part A: **38** (2007); p 2460–2470.

[**5**]Simacek, P., Advani, S G., "A numerical model to predict fiber tow *saturation during liquid composite molding"*, Composites Science and Technology **63**: (2003); p 1725–1736**.**

[**6**]Long, A. C., (Ed). "Design and manufacture of textile composites*"*, Woodhead Publishing Ltd, 2007, p 259-287, ISBN-13: 978-1-85573-744-0.

[**7**]Lawrence, J.M., Barr, J., Karmakar, R., and Advani, S.G., "*Characterization of preform permeability in the presence of race tracking"*, Compos Part A: Applied Science Manufacturing **35**: (2004); p 1393–1405.

[8]Bickerton, S., Sozer, E. M., Graham, P. J. and Advani, S. G., "Fabric structure and mold curvature effects on preform permeability and mold filling in the RTM p*rocess Part I. Experiments"*. Composites: Part A **31:** (2000); p 423–438.

[9]Bickerton, S., Sozer, E. M., Graham, P. J. and Advani, S. G. "Fabric structure and mold curvature effects on preform permeability and mold filling in the RTM process *Part II. Experiment"*. Composites: Part A **36**: (2005); p 1128–1141.

[10]Endruweit, A., Long, A. C., Robitaille, F., Rudd. C. D., "Influence of stochastic fibre angle variations on the permeability of bi-directional textile *fabrics"*. Composites: Part A **37**: (2006); p 122–132.

[11]Babu, Z. B., and Pillai, K. M., "Experimental Investigation of the Effect of Fiber-mat Architecture on the Unsaturated Flow in Liquid Composite *Molding"* Journal of Composite Materials **38**: 2004; p 57.

[12]Hieber, C.A., and Shen, S.F., *"A finite e*lement/finite difference simulation *of the injection mold filling process",* Journal Non-Newtonian Fluid Mesh **7**(1): (1980); p 1-31.

[**13**]Frederick, R., Phelan, JR., *"Simulation of the injection process in resin transfer molding"*. Polymer Composites **18**(4): 1997; p 460–476.

[**14**]Trochu, F., Gauvin, R., and Gao, D-M., *"Numerical analysis of the resin transfer molding process by the Finite Elements method"*. Advantages in Polymer Technology **12**: (1993); p 329-342.

[15] Long, A. C., (Ed). "Composites forming technologies", Woodhead

Publishing Ltd, 2007; p 344, ISBN 1 84569 033 8.

[16] Devillard, M., Hsiao, K-T, Gokce, A., and Advani, S. G., "On-line

Characterization of Bulk Permeability and Race-Tracking during the Filling

Stage in Resin Transfer Molding Process". Journal of Composite Materials **37**:

(2003); p 1525, DOI: 10.1177/0021998303034459.

[17] Andersson, H.M., Lundstrom, T.S., and Gebart, B.R., "Numerical model

for vacuum infusion manufacturing of polym*er composites".* Polymer

Composites **13** (2-3): (2003); p 383-394.

[18] Hammami, A., Gauvin, R., and Trochu, F., "Modelling the edge effect in

liquid composites molding". Composites: Part A, **29** (5-6): (1998); p 603-609.

[19] Hammami, A., and Gebart, B.R., *"Analysis of the vacuum infusion

moulding process. Polymer Composites",* **21**(1): (2000); p 28-40.

[20] Lawrence, J. M., Fried, P., Advani, S. G., "Automated manufacturing

environment to address bulk permeability variations and race tracking in resin

transfer molding by redirecting flow with auxiliary gates". Composites: Part A

36: (2005); p 1128–1141.

[21] Weimer, C., Preller, T., Mitschang, P., Drechsler, K., "Approach to net-

shape preforming using textile technologies Part I: edges". Composites: Part

A **31**: (2000); p 1261–1268.

[22] Endruweit, A., Harper, L.T., Turner, T.A.,. Warrior, N.A, Long, A.C.,

"Random discontinuous carbon fibre preform: Permeability modelling and

resin injection simu*lation",* Composites Part A **39**: (2008); p 1660-1669.

[23]Pillai, K.M., Luce, T.L., Bruschke, M.V., Parnas, R.S., and Advani, S. G., "Modelling the Heterogeneities present in Preforms during Mold Filling in *RTM"*, 25th International SAMPLE Conference paper, 26-28 October 1993; p 279-293.

[24]www.esi-group.com. "Last accessed 19.09.2014".

Chapter 7

Node modelling

7.1 Introduction

The objective of this chapter is to model the liquid infusion process in order to develop a macro-scale flow simulation technique able to predict possible manufacturing defects during RTM. To achieve this, firstly the isotropic FE node behaviour was studied with the 3D woven HTS40 F13 fabric. Secondly, the anisotropic behaviour with and without void formation was investigated. Thirdly, we generated a new 3D FE generic node model with mesh refinement.

7.2 Background

An important aspect of the design process of any composite component is computational modelling. Predictive modelling for material and geometric characteristics of the generic node are essential in order to avoid low quality components due to defects (e.g. void formation) in the final composite material. There are a wide range of techniques available for the simulation of various manufacturing processes. Computational resources, it gives a visualisation of how the component is infused during RTM processing. It also provides an indication of any potentially critical areas inside the composite where a converging flow front may lead to void formations. This theoretical insight allows optimised design of injection gates and venting configurations for the generic node based on predicted resin flow paths and any highlighted dry spots or resin rich regions as reported in study on void formation in multi-layer woven fabrics by Jinlian, H.et al [1]. Devillard, M. et al [2] studied on-line

characterization of bulk permeability and race-tracking during the filling stage in RTM process, while a numerical model for vacuum infusion manufacturing of polymer composites was presented by Anderson, H.M et al [3]. Hammami, A., et al [4] on modelled the edge effect in liquid composites moulding while Sozera, E.M., et al [5] studied with on-line control the liquid composite mould filling process.

A successful prediction of the node fluid flow can yield substantial savings for high quality and volume production components. The paper by Anderson, H.M, et al [6] focused on measuring composite textiles thickness variations in the Vacuum Infusion Process with digital speckle photography. Gokce, A., and Advani S. G., [7] provided a paper on vent location optimization using map-based exhaustive search in LCM processes. Lawrence, J. M., Fried, P., Advani, S. G., [8] provided a research paper on automated manufacturing environment in order to address bulk permeability variations and race tracking in RTM by redirecting flow with auxiliary gates. Lawrence, J. M., et al [9] research made an approach to couple mould design and on-line control to manufacture complex composite parts by RTM. Weimer, C., et al [10] on his part I edges paper: reported an approach to net-shape preforming using textile technologies for use in LCM processes. While Devillard, M., Hsiao, K-T., Advani, S. G., [11] on their paper studied flow sensing and control strategies in order to address race-tracking disturbances in RTM process. Bickerton, S., Advani, S. G., [12] provided a paper on composites with the characterization and modelling of race-tracking in liquid composite moulding processes. Endruweit, A., et al [13] studied random discontinuous carbon fibre preforms by

permeability modelling and resin injection simulations for the LCM process reported by Rudd, C. D., et al [15].

7.3 Isotropic flow simulations

Firstly an isotropic scenario, that pertains to permeability values, injections and venting gates for the 3D woven HTS40 F13 preform, was studied in order to extract information about the isotropic 2D and 3D flow behaviour of the generic node as shown in Fig. 7.1 (a), (b) which also indicates 3D trial injection gate and vent locations as proposed by the tooling manufacturer. The same gates and venting was used for the 2D injection simulations.
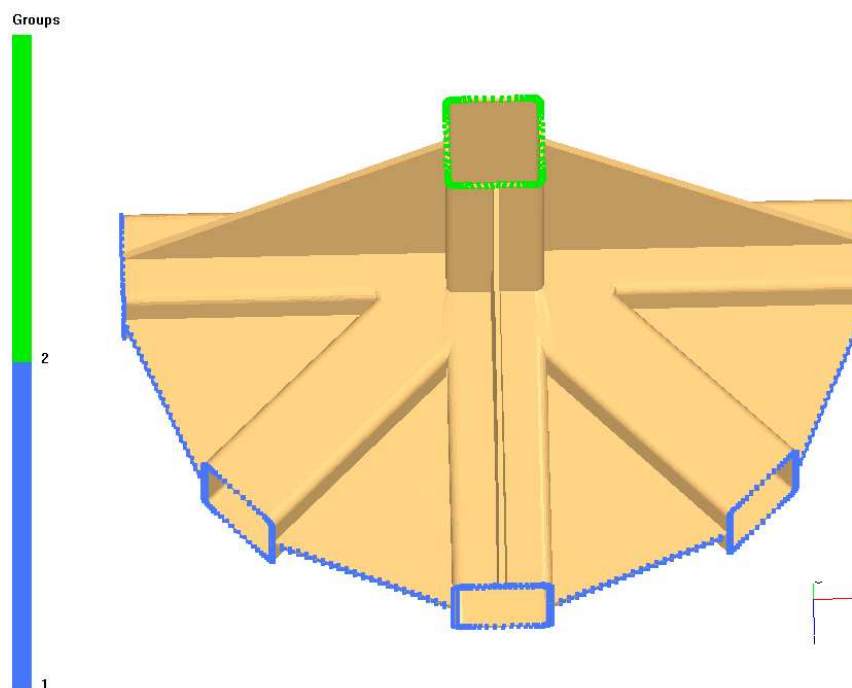
**Fig. 7.1 (a): 3D scenario of injection gate (blue) and venting (green) locations used for 3D simulations (top view) done with PAM-RTM®
software [14].**
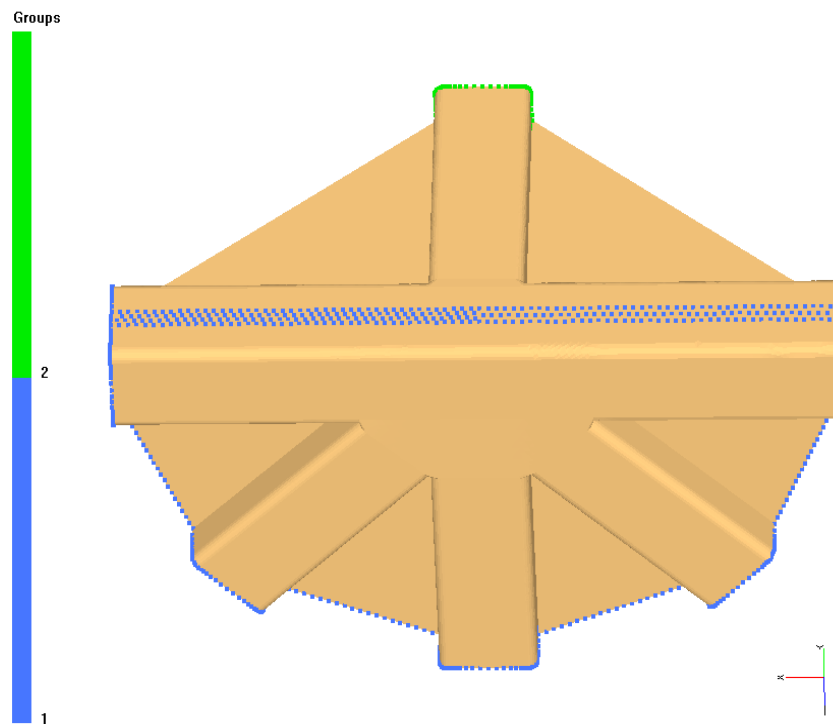
Fig. 7.1 (b): 3D scenario of injection gate (blue) and venting (green) locations used for 3D simulations (other side view).

The material properties used in isotropic and anisotropic simulations with HTS40 F13 3D woven preform are presented in Tables 3.2, 4.7 and their numerical values are as follows: Mean Permeability value reported by Endruweit, A., et al, [13] : $K_e = \sqrt{K_1 K_2}$, K_e= 3.4 x10^{-10} m^2 (Assumed Isotropic), K_1=5.207x10^{-10} m^2, K_2=2.221x10^{-10} m^2, K_3=5.207x10^{-12} m^2, μ(MVR 444 resin viscosity)=0.1 Pa s, P_i(injection pressure)=3 bar, P_v(vent pressure)=0 bar, d (density of carbon fibre)=1760 Kg/m^3, V_f =0.55, Φ(porosity)=0.45.

7.3.1 Isotropic 2D Node flow simulation

Firstly the flow behaviour of the node was modelled with a 2D CAD model, which was created and meshed with 6424 triangular elements as shown in Fig. 7.2.
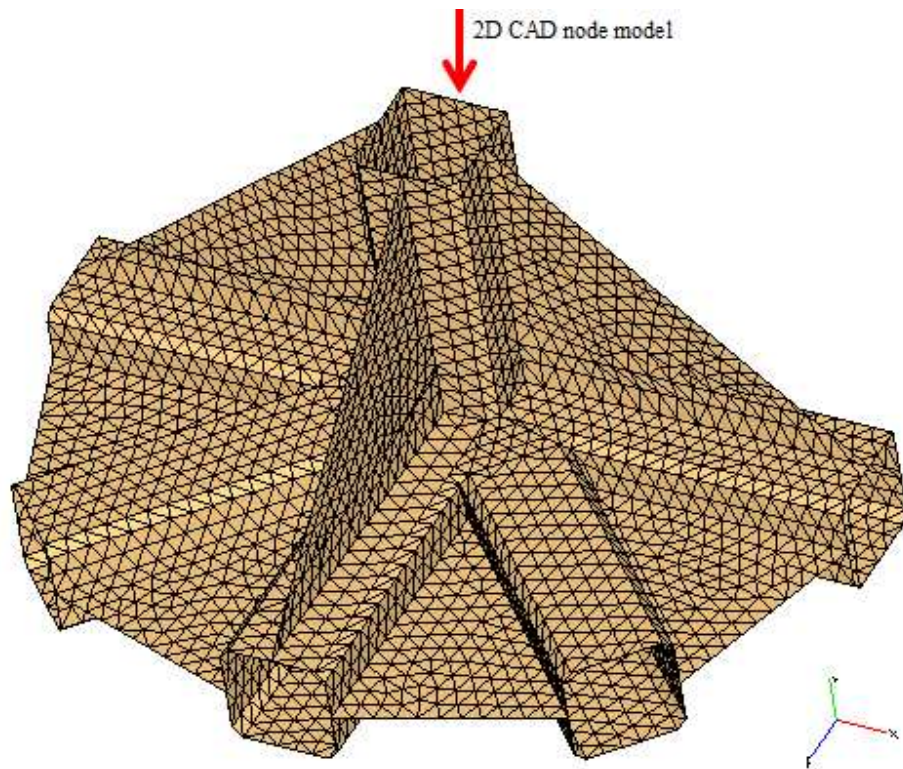
Fig. 7.2: 2D CAD node model meshed with 6426 triangular elements (red arrow shows 2D geometry of the node).

The flow behaviour of the node was simulated thereafter with the PAM-RTM

software shown in Fig. 7.3 (a), (b).
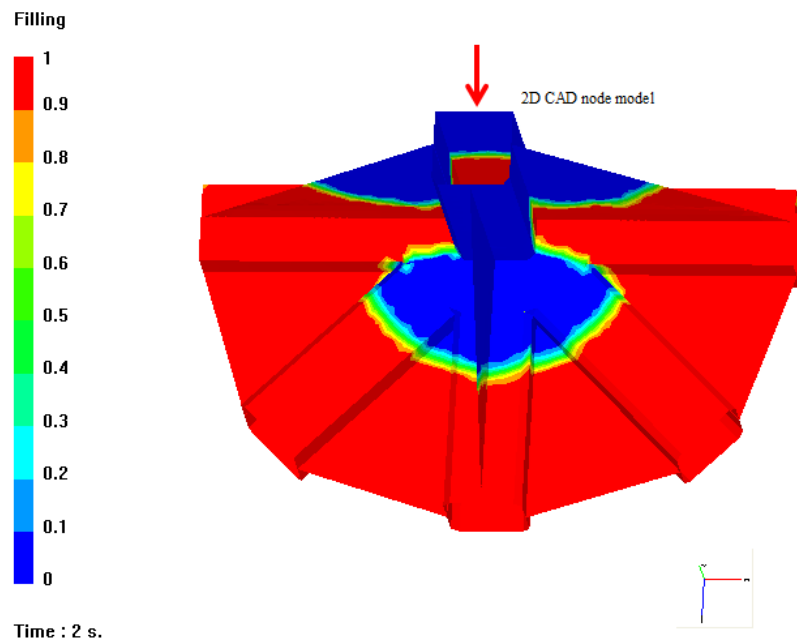
Fig. 7.3 (a): 2D node isotropic filling simulation (after 2 s.) top red colour filled area, blue unfilled, half-filled area any other colour.
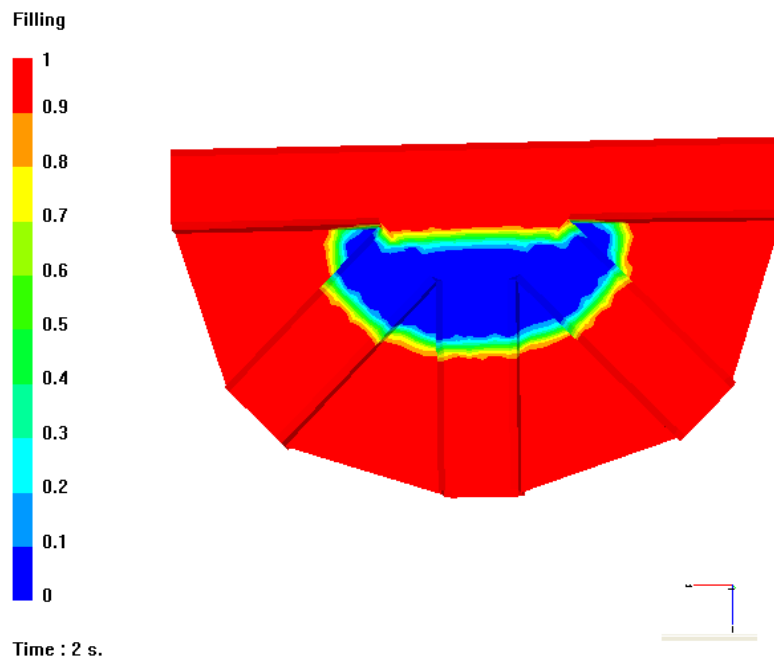
Fig. 7.3 (b): 2D node isotropic filling simulation (after 2 s.) opposite side (down) red colour filled area, blue unfilled, half-filled area any other colour.
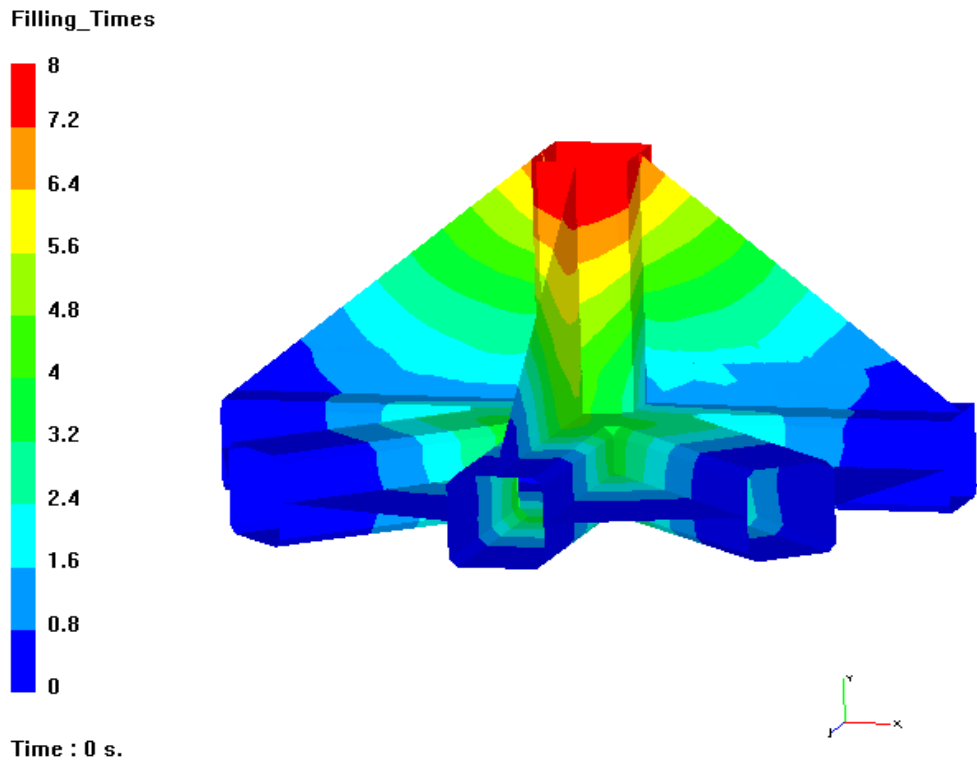
Fig. 7.4: 2D filling times simulation of the node.

The 2D FE model filling time simulation was 8 seconds as presented on Fig. 7.4. Filling and filling times simulations was then compared with the 3D FE node in order to verify flow behaviour and filling times.

7.3.2 Isotropic 3D Node flow simulation

A series of 3D CAD model of the node generated with different mesh density and the isotropic case scenario was simulated for each model. Two 3D CAD model of the node as shown in Fig. 7.5 (a) and Fig. 7.5 (b) was meshed with 16377 and 111240 tetrahedral elements.
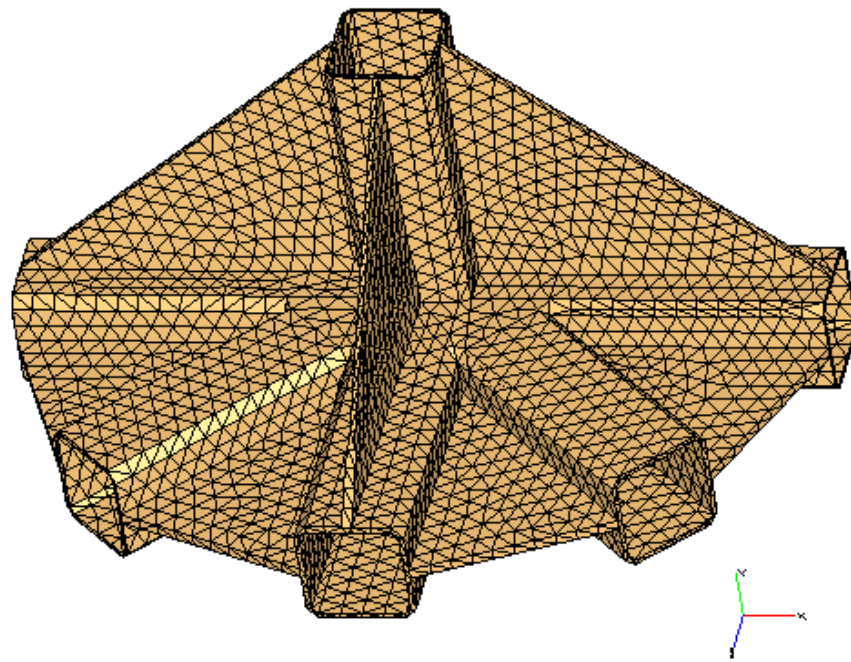
Fig. 7.5 (a): ACTS node coarse mesh with 16377 tetrahedral elements.
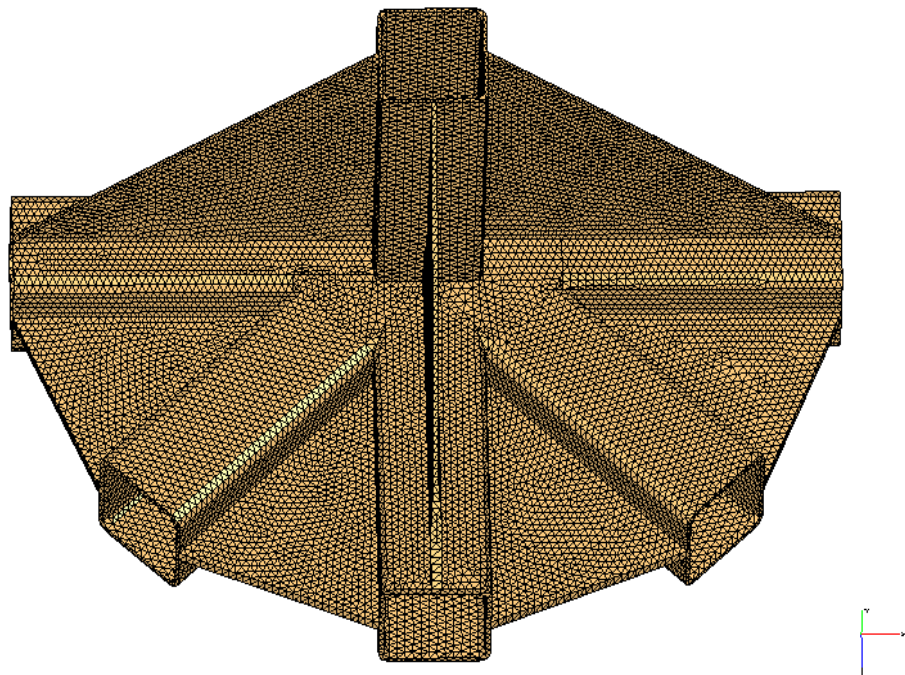
Fig. 7.5 (b): ACTS node fine mesh with 111240 tetrahedral elements.

The flow behaviour of the node as shown in Fig. 7.6 (a), Fig. 7.6 (b), was studied with the PAM-RTM$^{®}$ software for the same preform material properties (Tables 3.2 and 4.3) following the method as of section 7.3.1.
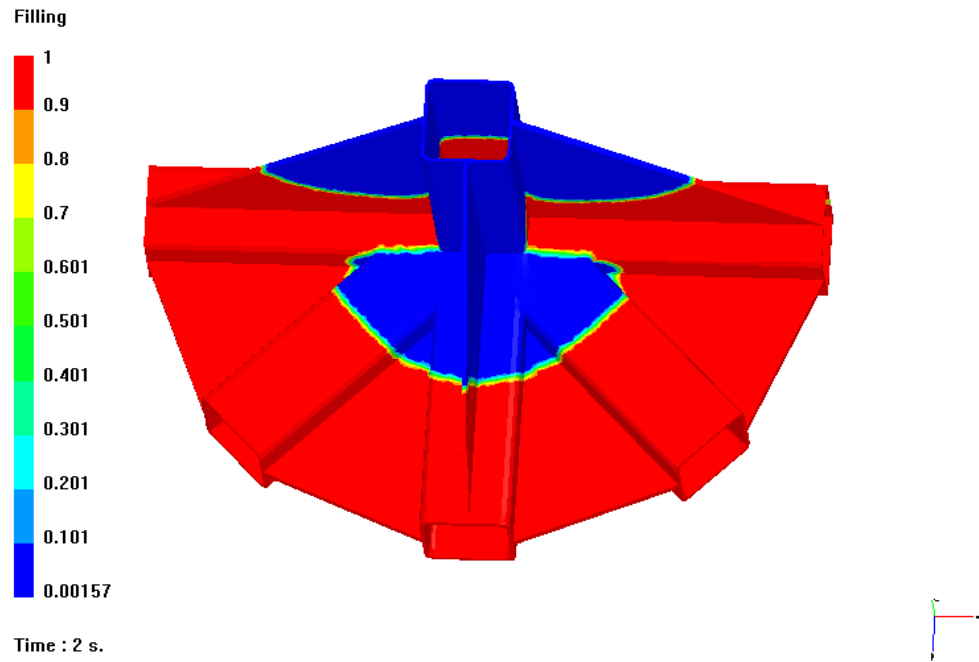
Fig. 7.6 (a): 3D node isotropic filling simulation (after 2 s.) top view red colour filled area, blue unfilled.
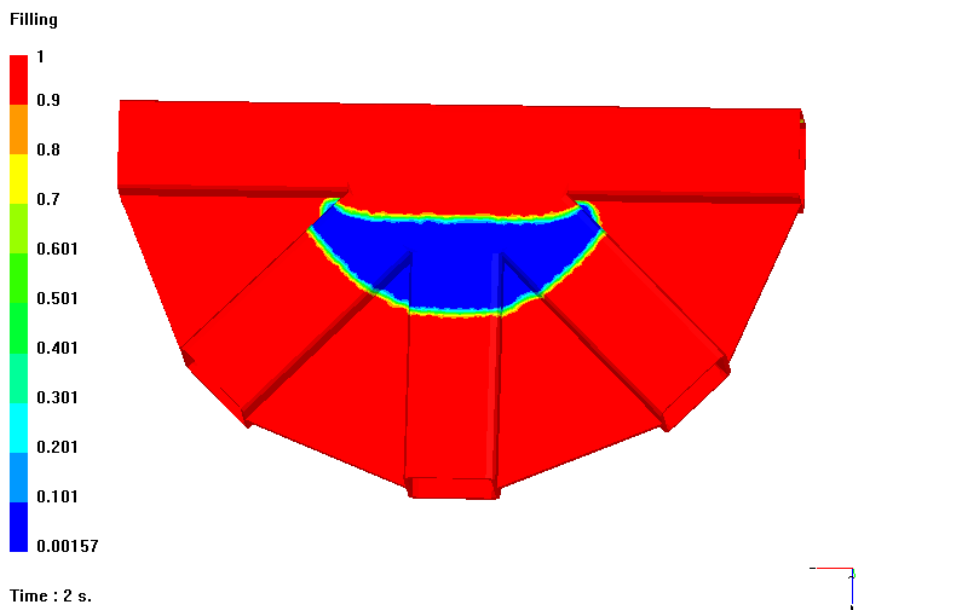
Fig. 7.6 (b): 3D node isotropic filling simulation (after 2 s.) opposite side red colour filled area, blue unfilled.

3D FE model filling time simulation presented on Fig. 7.6 (c), Fig. 7.6 (d).
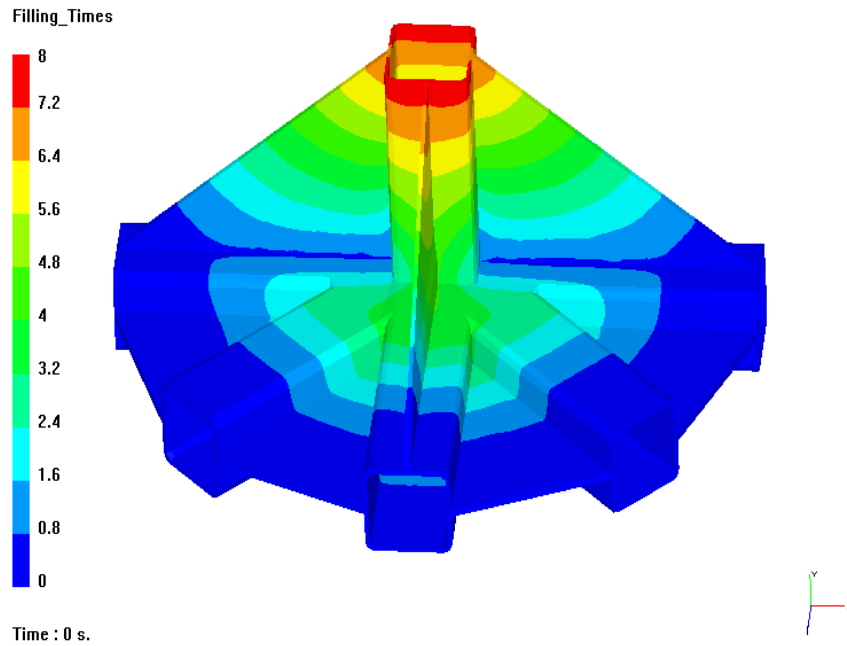
Fig. 7.6 (c): Filling times, for the upper view of the node.
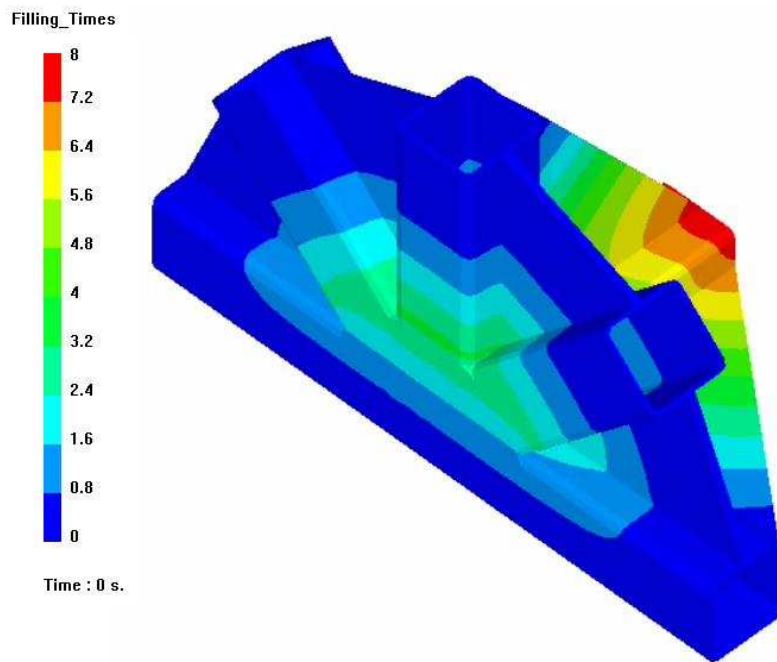
Fig. 7.6 (d): Filling times, for the lower view of the node.

7.3.2.1 3D isotropic mesh sensitivity

In this section 3D numerical simulations of the RTM process were performed with PAM-RTM® in order to validate the 3D sensitivity of the generic node for the isotropic case. Filling times results against number of tetrahedral elements from each 3D node model simulation are presented in Table 7.1.

Table 7.1: Filling times results against number of tetrahedral elements for the 3D node model.

3D node model (Num. of tetrahedral elem.)	Filling times(s)
16377	8.52
37777	7.81
50671	7.72
111240	7.7

The above table 7.1 shown that by increasing the mesh density of the 3D node model there is convergence of filling time (s) at 7.7 (s) for 111240 tetrahedral elements. Due to the fact that for the node is of complex geometry there is no analytical solution for comparison with the FE/CV method.

7.3.3 Discussion 2D, 3D isotropic case

From the whole investigation came out that 2D, 3D node simulations predicted nearly the same filling time 8 and 7.7 seconds respectively.

Both the 2D and 3D FE CAD node models revealed similar isotropic behaviour. Comparison between Figures 7.3(a), (b), 7.4 and Fig. 7.6 (a), (b), (c), (d), suggested that the flow fronts converge in the centre of the component on upper and opposite side. As a result air entrapment may be observed in this

region of the node. This may lead to void formation in what is bound to be a critical area within the node complex geometry.

7.4 Node anisotropic flow behaviour

In order to simulate the anisotropic flow behaviour with RTM of the ACTS node in a more realistic way, a new 3D model of the node was generated with mesh refinement in the zones of interest (23 node radii) for 280728 tetrahedral elements as shown in Fig. 7.7 (a) and (b). The orientations of warp and weft yarns shown in Fig. 7.8 have been used with the experimental compaction data of Chapter 3, to generate the stochastic variability simulation tables of the node that are presented in Appendix D.
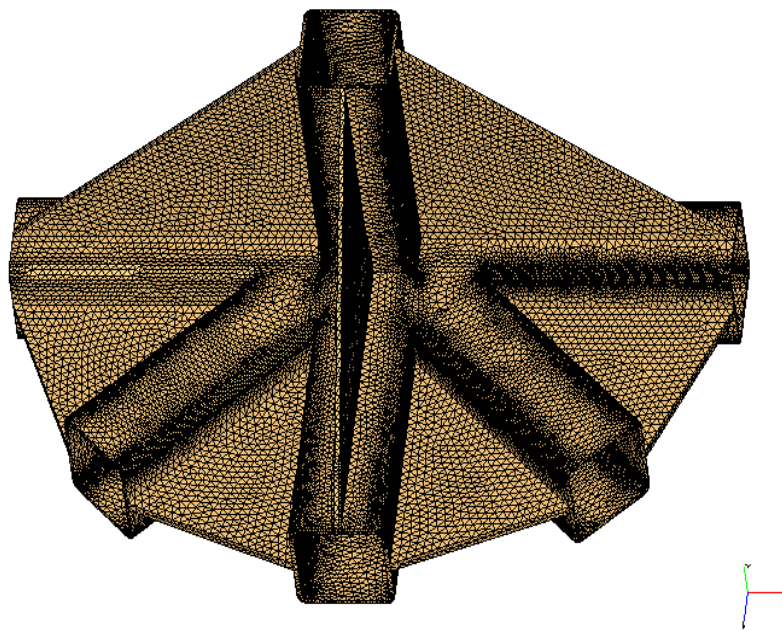
Fig. 7.7 (a): 3D FE CAD node model. The upper side of the node mesh with 280728 tetrahedral elements.
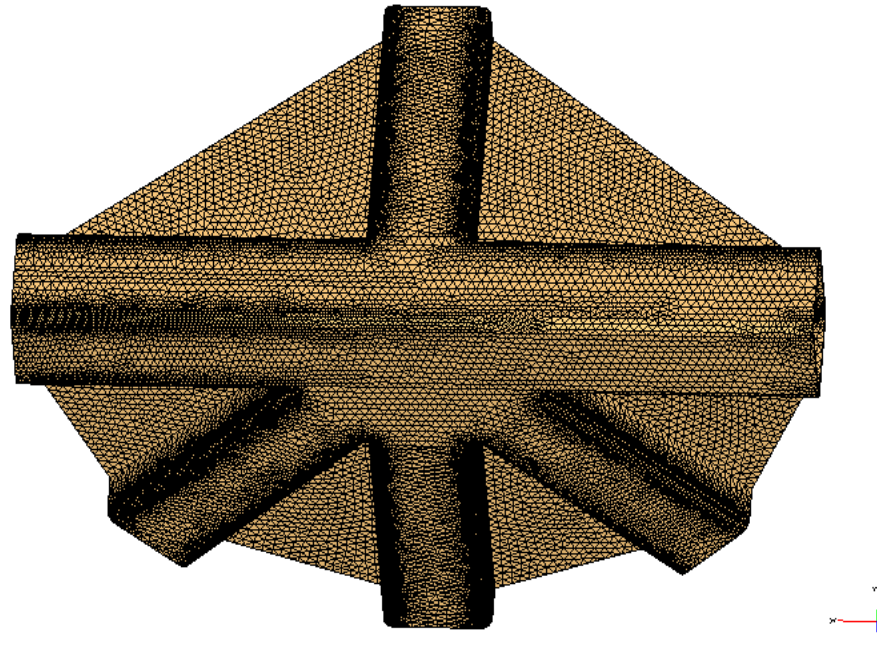
Fig. 7.7 (b): The lower side of the 3D FE CAD node model mesh with 280728 tetrahedral elements.

7.4.1 Assignment of fibre orientation in FE model

Assignment of fibre orientation is an important application, in resin injection for fibre reinforced composite materials. Fibre orientation needed to be placed correctly on CAD model in order to predict computationally resin flows and then optimise the manufacturing process of the composite. Interaction between flow and fibre orientation has been the subject of extensive study by Papathanasiou, T. D., et al [16] on his research paper flow-induced alignment in composite materials. Tucker, C. L., Advani, S. G., [17] provided a paper for the assignment of fibre orientation during flow in Polymer Composites Manufacturing. Therefore assignment of warp, weft material directions is an important step for RTM simulations. The distribution of the fibre orientation in a composite can be predicted by knowing the architecture of the textile that will be used as well as the direction (warp or weft) that this

208

fabric will be placed on the mould. For complicated components like the ACTS node the deformation and the changes of fibres orientations near the mould walls, across and along the 90° edges of the mould where the fabric is placed should be taken into account, as shown in Figs. 7.9 (a) - 7.9 (d).

Provided that the input fibre distribution has been assigned correctly, for the aims and purposes of the RTM process (Fig 7.8) the easiest way to verify this prediction, was by taking real time images (shown in Figs. 7.9 (a) - 7.9 (d) of the node in laboratory conditions. Comparison of the real time images with the modelled ones showed a satisfactory agreement, verifying the assumption made regarding the local fibre orientations.
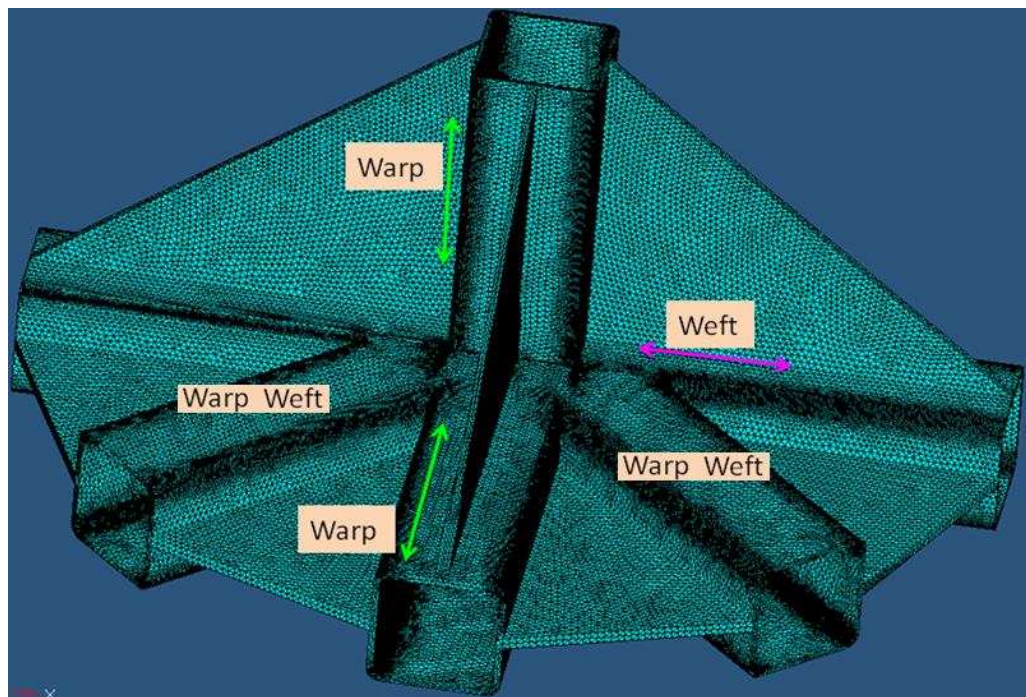
Fig. 7.8: Orientation of warp and weft preform directions in generic node 3D FE model.

Then the actual set of orientations (Fig 7.9 a, b, c, d) was compared to 3D FE CAD node model (Fig. 7.8) in order to simulate the node flow behaviour. The 3D FE CAD model did not take into account local fabric deformation and any excess fabric, which changed the orientations of the textile locally in each moulding. This meant that the finite element solution was developed at macroscale without taking into account the local process induced micro, meso scale change of the textile. For the node model of Fig. 7.8 the vector orientations were incorporated in each tetrahedral element as described in section 6.3.3 and shown in Fig. 6.8 for the curved plate model. The incorporated orientations in the 3D FE CAD node model are shown in Fig. 7.8.
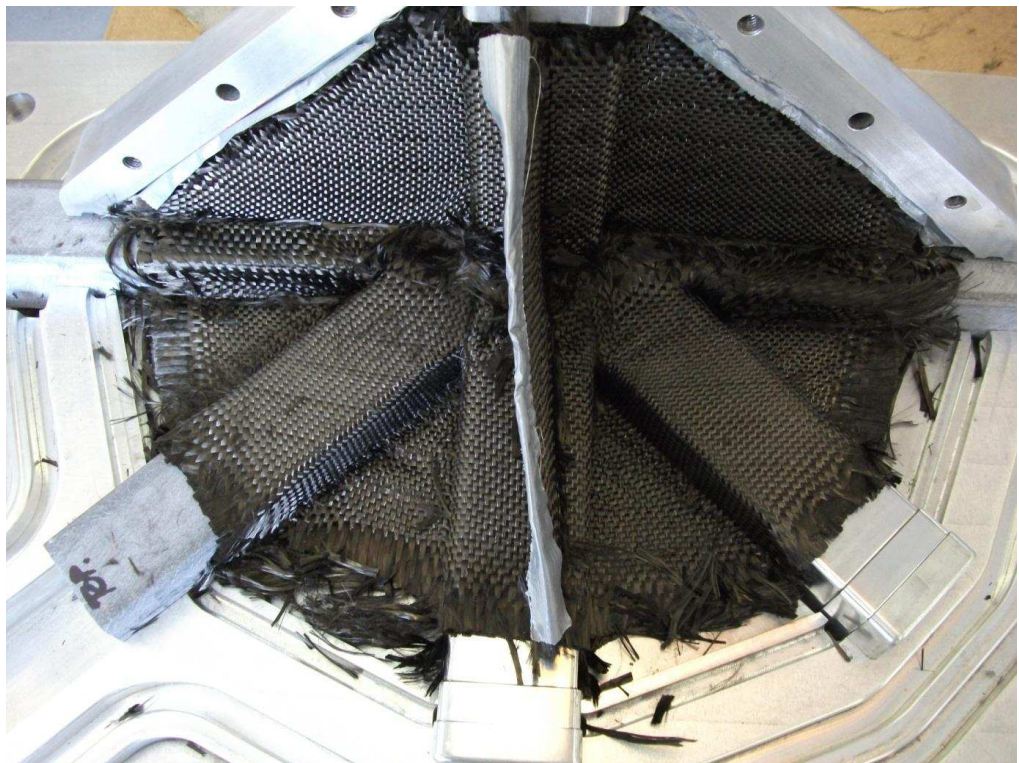
Fig. 7.9(a): Analysis of fibre orientations, top view. (Composites Integration Ltd laboratories, part of Cytec group).

Fig. 7.9 (b): Analysis of fibre orientations, right side view.
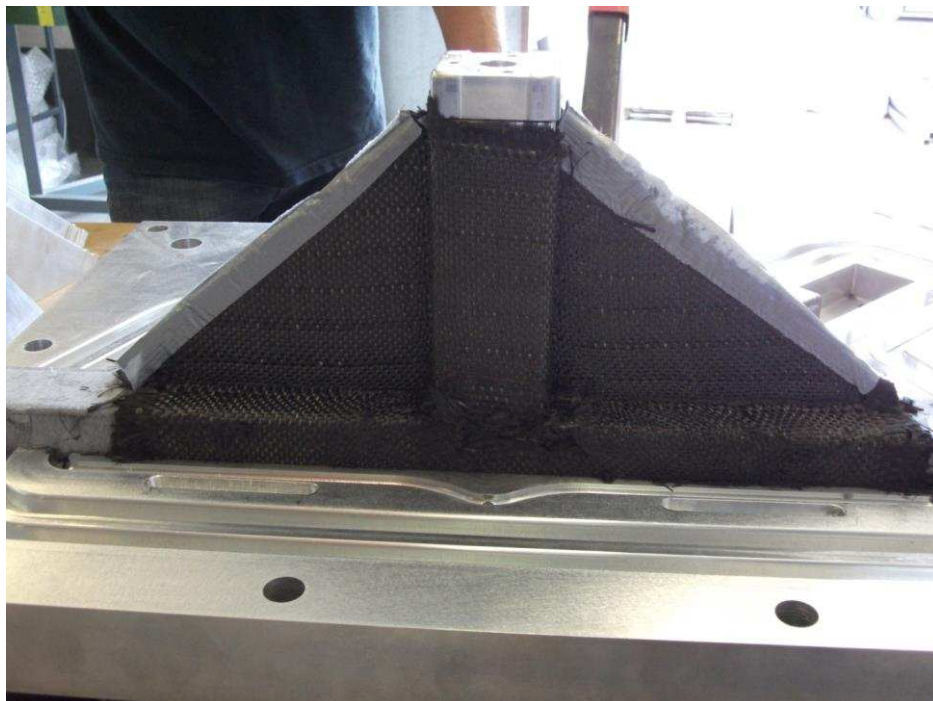
Fig. 7.9 (c): Analysis of fibre orientations, rear view.
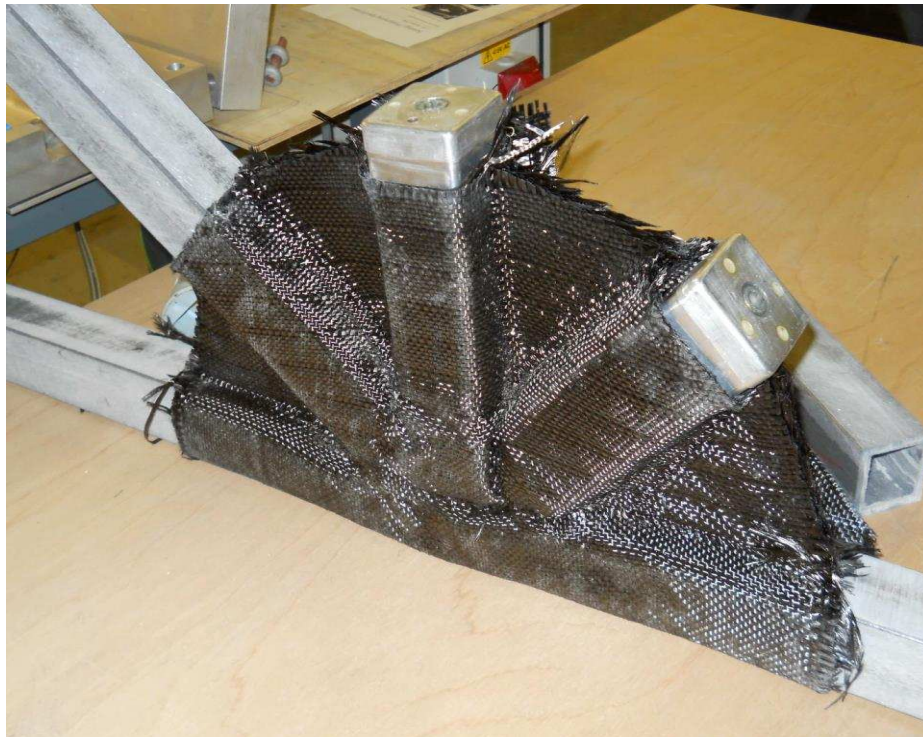
Fig. 7.9 (d): Analysis of fibre orientations, lower surface view.

7.4.1.1 2/2 twill, triaxial, ACTS fabric Volume fractions for simulations with node

Fabric volume fractions for simulations has been used by taking on to account the tested fabrics (Fig. 3.3) and the average aerial density of each preform that was evaluated previously as shown in Tables 6.1-6.3 section 6.3.4. With the use of equation (3-2) the material properties and mould height, the fibre volume fraction was calculated as function of mould thickness.

i) 2/2 twill preform

Volume fraction eq. (3-2) numerical calculation for 2/2 twill 2-layer preform for 2mm thickness: $V_{f\,2layer} = 39.02\%$.

ii) ACTS 3D woven HTS40 F13 preform

Volume fraction eq. (3-2) numerical calculation for 3-layers ACTS 3D woven HTS40 F13 preform d (m/A) = 1.713 Kg/m^2 for 2mm thickness: $V_{f\,3layer} = 48.7\%$.

iii) Triaxial preform

Volume fraction eq. (3-2) numerical calculation for triaxial 2-layer preform for 2mm thickness: $V_{f\,2layer} = 46.1\%$.

Fibre volume fractions calculated have been used as simulation input data with PAM-RTM in this chapter for FE CAD generic node (strut elements F) model Fig. 1.5.

7.4.2 3D simulation case of the node

The anisotropic 3D FE CAD node simulation with 3D woven HTS40 preform material properties provided more realistic information of what may happen during the resin infusion process. Figures 7.10 (a), (b) suggested that the flow fronts converge in the centre of the component on the upper and opposite side in a similar way as the 2D, 3D isotropic cases. However the converging front in the central region has a different shape than that of Fig. 7.6 (a), (b).

Therefore it was decided to study the void formation in the 3D CAD FE node model with the PAM-RTM$^®$ void formation algorithm described in the following section.

Filling_Times

Time : 0 s.
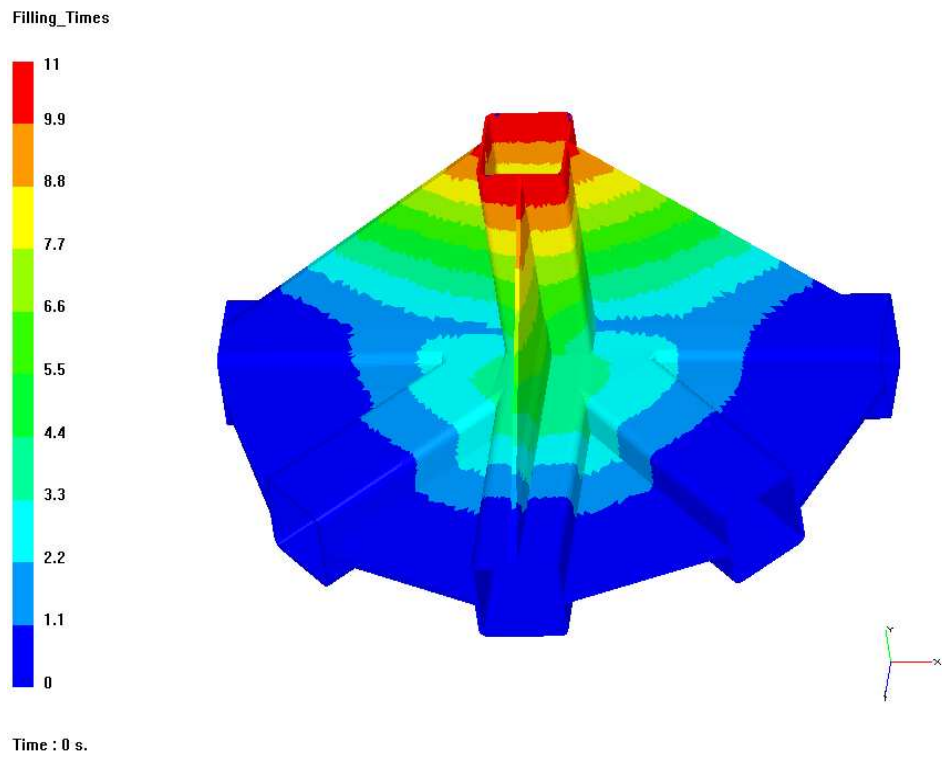
Fig. 7.10 (a): Anisotropic simulation of the node filling times.

Filling_Times

Time : 0 s.
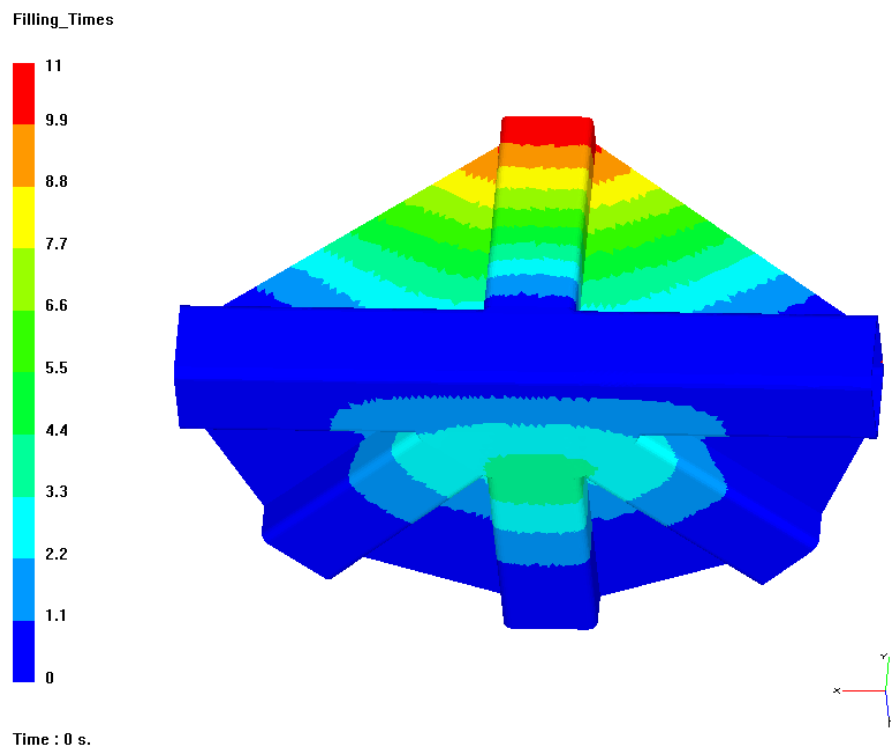
Fig. 7.10 (b): Anisotropic simulation of the node filling times.

Anisotropic simulation gave higher filling time of 11seconds from 8 and 7.7 seconds in 2D, 3D isotropic case as presented in section 7.3.4. This is due to the fact that on the anisotropic filling the permeabilities have different values ($K_1 \neq K_2 \neq K_3$) therefore the complete filling of the node in xyz directions needs more time.

7.4.3 PAM-RTM® void formation algorithm

The study on void formation in RTM in the FE/CV method is well addressed by Jinlian, H., Yi L., Xueming, S., [1] and many other researchers mentioned previously on section 7.2 of this Chapter. The PAM-RTM void formation algorithm that was used is based on the ideal gas equation:

$$\frac{PV}{T} = k \qquad (7\text{-}1)$$

Where: P is the pressure (bar), V the Volume (m^3), T is the Temperature (K) and the constant k is nR (n = number of moles, R = 8.314 J/mol K from Avogadro's law). Considering that T is constant equation (7-1) can be written:

$$PV = const. \qquad (7\text{-}2)$$

Equation (7-2) is used to manage the pressure increase as the volume of the air trap changes. After some time, the pressure in the air trap becomes equal to the injection pressure. This means that pressure difference is zero and the resin becomes stagnant. The simulation therefore stops and elements are not filled with resin. These voids are represented by the blue region in fig. 7.11 as presented on ESI PAM-RTM 2010 User's Guide [14], (the red region represents the resin filled area, blue the unfilled).
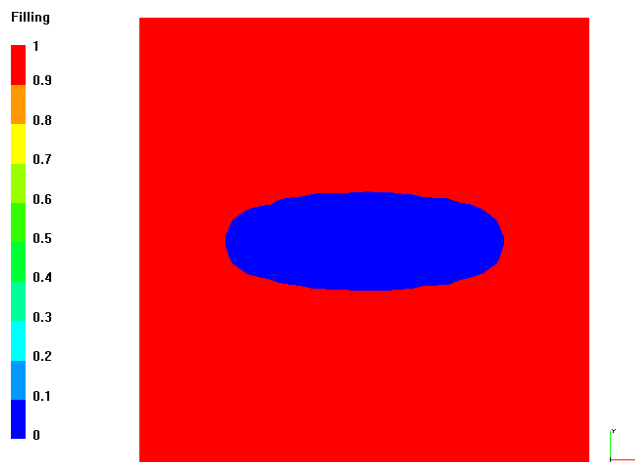
Fig. 7.11: Example of void formation with PAM-RTM software for infusion of a flat plate from the edges [14] red area filled, blue unfilled.

7.4.4 Anisotropic 3D simulation with void formation

The anisotropic 3D FE CAD node was simulated by PAM-RTM® with the void formation application switched "on" as mentioned in section 7.4.3.

In this way it is possible to detect voids during simulation of the filling and/or suggest additional vents in order to eliminate converging flow fronts and unfilled regions inside the node.

The dimensions of any voids formed may also be estimated. For example in Fig. 7.12 the simulation revealed an elliptic void formation, (indicated by the red arrow), with dimensions 4.7 cm in length horizontally and 1.4 cm vertically.
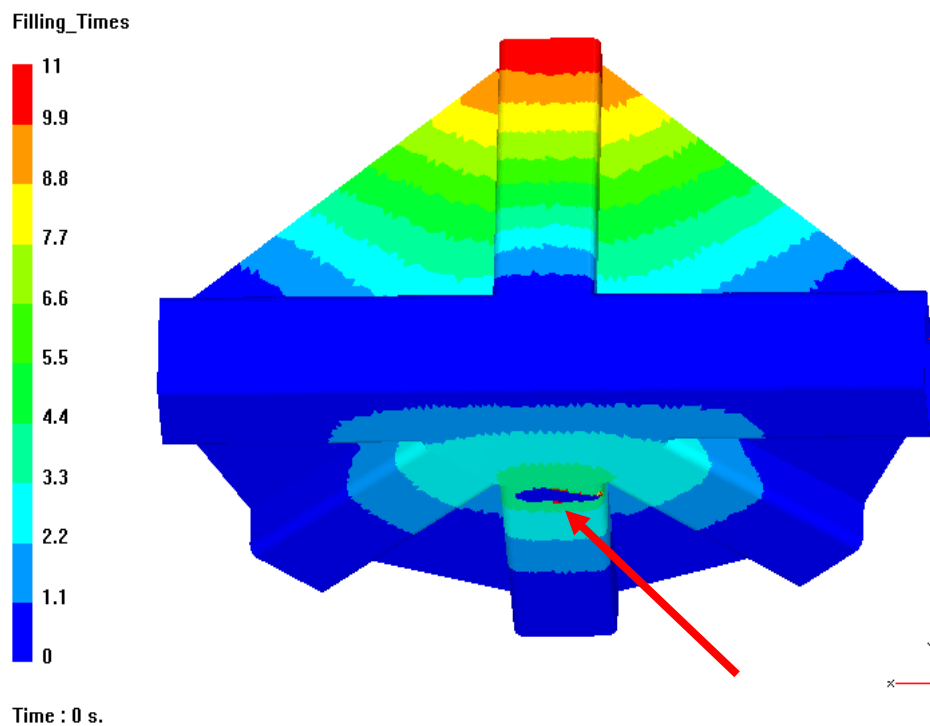
Fig. 7.12: Prediction of elliptic void formation with 4.7 cm in length horizontally and 1.4 cm vertically, indicated by red arrow.

By taking into account the modelling results of section 7.4.4 the node mould was modified with three extra vents on the opposite side of the HTS40 F13 3D woven preform. In order to evaluate the flow in the mould a number of pressure transducers were included to monitor the experimental filling pattern as well.

7.5 Conclusion

In this chapter 2D CAD and 3D CAD node models have been studied for isotropic and anisotropic cases with and without void formation. The flow pattern in the isotropic scenario for the 2D case was the same as the 3D case. The filling scenario for the 2D case with 6426 triangular elements and for the 3D case with 111240 tetrahedral elements indicated a converging flow towards the centre of the generic node in both top and opposite sides. Vector

217

orientations were incorporated on the node for the more realistic filling of the anisotropic case, of the node, during RTM.

A new 3D model of the node meshed with 280728 tetrahedral elements has been tested with PAM-RTM® software for the above anisotropic filling case. The 3D model of the node was tested with the use of PAM-RTM® air entrapment "on" for predicting void formation. By taking into account the simulation results the generic node moulder must modified in order to avoid void formation on the lower side at the centre of the node as shown Fig. 7.12.

The key findings to be carried forward can be summarised as follows:

- 3D anisotropic case modelling is possible to predict the fluid flow of a complex geometry in a more realistic way than 2D, 3D isotropic cases.

- 3D anisotropic case modelling with complex geometries may predict converging flow and so void formation during liquid infusion on component scale. This allows the modification of node mould in order to avoid macro-scale void formation.

References

[1] Jinlian, H., Yi L., Xueming, S., *"Study on void formation in multi-*layer *woven fabrics"*. Composites: Part A **35**: (2004); p 595–603.

[2] Devillard, M., Hsiao, K-T, Gokce, A., and Advani S. G., "On-line Characterization of Bulk Permeability and Race-Tracking during the Filling *Stage in Resin Transfer Molding Process"*. Journal of Composite Materials 37: 2003; p 1525, DOI: 10.1177/0021998303034459.

[3] Anderson, H.M, Lundstrom, T.S., and Gebart, B.R., "Numerical model for *vacuum infusion manufacturing of polymer composites"*. Polymer composites **13** (2-3): (2003); p 383-394.

[4] Hammami, A., Gauvin, R., and Trochu, F., *"Modelling the edge effect in liquid composites molding"*. Composites: Part A, **29** (5-6): (1998); p 603-609.

[5] Sozera, E.M., Bickerton, S., Advani, S.G., "On-line strategic control of liquid composite mould fillin*g process"*, Composites: Part A **31**: (2000); p 1383–1394.

[6] Anderson, H.M, Lundstrom, T.S., and Gebart, B.R., Synnergren, P., "Application of Digital Speckle Photography To Measure Thickness Variations in the Vacuum *Infusion Process"*. Polymer composites **24** (3): (2003); p 448-455.

[7] Gokce, A., and Advani S. G., "Vent Location Optimization Using Map-*Based Exhausive Search in Liquid Composite Moulding Processes"*, Materials and Manufacturing Processes Vol. **19**, No.3: 2004; p 523-548.

[8]Lawrence, J. M., Fried, P., Advani, S. G., "Automated manufacturing environment to address bulk permeability variations and race tracking in resin *transfer molding by redirecting flow with auxiliary gates"*. Composites: Part A **36**: (2005); p 1128–1141.

[9]Lawrence, J. M., Hsiao, K-T., Don, R. C., Simacek, P., Estrada, G., Sozer, E. M., Stadtfeld, H. C., Advani, S. G., "An approach to couple mold design and on-line control to manufacture complex composite parts by resin transfer *molding"*. Composites: Part A **33**: (2002); p 981–990.

[10]Weimer, C., Preller, T., Mitschang, P., Drechsler, K., *"Approach to net-*shape preforming using textile technologies. Part I: edges". Composites: Part A **31**: (2000); p 1261–1268.

[11]Devillard, M., Hsiao, K-T., Advani, S. G., "Flow sensing and control strategies to address race-tracking disturbances in resin transfer molding-part *II: automation and validation"*. Composites: Part A **36**: (2005); p 1581–1589.

[12]Bickerton, S., Advani, S. G., "Characterization and modelling of race-tracking in liqui*d composite molding processes"*. Composites Science and Technology **59**: (1999); p 2215-2229.

 [13]Endruweit, A., Harper, L.T., Turner, T.A., Warrior, N.A., Long, A.C., "Random discontinuous carbon fibre preform: Permeability modelling and resin injection *simulation",* Composites Part A 39: (2008); p 1660-1669.

[14]www.esi-group.com ESI PAM-RTM 2010 User's Guide.

[15]Rudd, C. D., Long, A. C., Kendall, K. N., Mangin, C., *"Liquid moulding technologies: Resin transfer moulding, structural reaction injection moulding and related processing techniques",* Woodhead Publishing Ltd: 1997; p.258, ISBN 1 85573 242 4.

[16]Papathanasiou, T. D., and Guell, D. C., *"Flow*-induced alignment in *composite materials".* Woodhead Publishing Ltd, Abington Hall, Abington, Cambridge DB16AH England: 1997; p 147–148, ISBN 1 85573 254 8.

[17]Tucker, C. L., Advani, S. G., "Processing of short-*fiber systems".* In: Advani S G (Ed.) Flow and Rheology in Polymer Composites Manufacturing. Technology & Engineering **87**: 1994**;** p 369–402.

Chapter 8

Node variability modelling

8.1 Introduction

The objective of this chapter is to use stochastic modelling simulations in order to predict the generic node variability during RTM process. Stochastic modelling is defined as a method in which one or more variables within the model are random. A novel approach to determine the probabilistic flow behaviour in RTM process by FE modelling with a stochastic methodology is presented in this Chapter. Node modelling on Chapter 8 shown that race-tracking may occur at the 90° curved plate radii node during infusion. Based on this information by including random race-tracking variability effects and changing the inlet and outlet in FE simulations the node variability is predicted on macro-scale.

Generic node variability was modelled with the probabilistic population gap distribution of the 3D woven HTS40 F13 fabric thickness by taking on to account the twenty three 90° curved plate radii of the node (which flow behaviour previously studied on Chapter 6) having the material properties of Tables 3.2, 4.7 and Appendix D. Based on the same 3D FE CAD generic node model introduced on Section 7.4, Fig. 7.7 (a), (b) for anisotropic flow behaviour.

Node variability was also studied for 2/2 twill and triaxial glass preforms in order to understand better the fluid behaviour of the composite node with different local permeability characteristics on the radii due to race-tracking.

Finally, the modelling results of the 3D woven HTS40 F13 were taken into account and the ACTS node mould was modified. Based on Chapters 7, 8 modelling work prototypes of generic node with a 3D woven HTS40 F13 preform was successfully manufactured subsequently, on Chapter 9, based on the assumption of race-tracking on the twenty three 90° edges of the generic node.

8.2 Background

Study of the variability modelling during mould filling is presented by Pillai, K.M., et al [1] on their research paper modelling the heterogeneities present in preforms during mould filling in RTM. Li, J., Zhang, et al [2] presented a paper on statistical characterization and robust design of RTM processes for the manufacturing of composites. Lawrence, J. M., et al [3] wrote an approach to couple mould design and on-line control to manufacture complex parts by RTM and Parnas, R. S., et al [4] based on a permeability database for composites manufacturing.

Stochastic Finite Elements Method was proposed by Berveiller M., [5], as the stochastic solver for studies in the field of liquid composite moulding simulation to predict influence of random parameters on the injection cycle time with an optimal number of simulations.

Material properties and their variations affect the composite part final quality and mechanical performance. Because composites are heterogeneous, variations may occur at the constituent level i.e. fibre and matrix.

Therefore variability affects ply orientation, fibre volume fraction, composite thickness and RTM process induce defects such as voids. The stochastic modelling of RTM manufacturing process, methodology has been used to address this problem. Stochastic processes can be found in Keese A., [6], Isukapalli, S.S., [7].

A non-intrusive method relying on deterministic computations has been proposed. In this case, the overall stochastic response is expanded in the method proposed by Puig et al., [8], onto Polynomial Chaos.

The coefficients are determined by using the orthogonality of the Hermite polynomials with respect to the Gaussian probability measure. Such a method then yields a multidimensional integration that can be performed by Monte-Carlo numerical simulations.

A review of techniques for representing stochastic processes can be found in Li C.C. and Der Kiureghian A., [9] with their paper "Optimal discretization of random fields", while Zhang J. and Ellingwood B., [10] research seems to provide the most accurate results among these techniques.

The late two methods require implementation within commercial Finite Element codes when dealing with large and complex problems.

8.3 Node variability modelling methodology

In this section stochastic modelling is used on RTM simulations in order to estimate the probability of void formation and predict the fluid flow behaviour of the composite generic node under different injection gates and vents scenarios. The random numerical variables are populated with experimental variability data, and random variable parameters assumed to be the measured gap distributions height from the variations of V_f on Chapter 3, Sections 3.7.1, 3.8.

In order to include the effect of variability in the 3D woven HTS40 F13 fabric, the 3D node model in Fig. 7.7 (a), (b) was segmented in twenty four zones. In the twenty three edge zones a different local permeability was generated with the use of probabilistic gap distributions. The twenty fourth zone (zero zone) was the zone out of the 90° angle curve plates with 3D woven HTS40 F13 fabric costant volume fraction and material properties as presented in Section 7.3. In regions where gap heights were necessary parameters, their values were taken from the bending tests performed on an aluminium 90° curved plate, through the CMM technique (Chapter 3).

To each one of the generic nodes shown in Fig. 8.1(a), 8.1(b) (from A to F, clockwise) a sub group of zones was assigned as follows: node member A - (zones 1, 2, 3, 4), node member B - (zones 5, 6, 7, 8), node member C - (zones 9, 10, 11, 12), node member D - (zones 13, 14, 15, 16), node member E - (zones 17, 18, 19) and node member F - (20, 21, 22, 23). Zone 0, refers to the

fixed permeability of the fabric (outside the 23 edge, gap variability zones).

These are shown in Figs. 8.1 and 8.2.
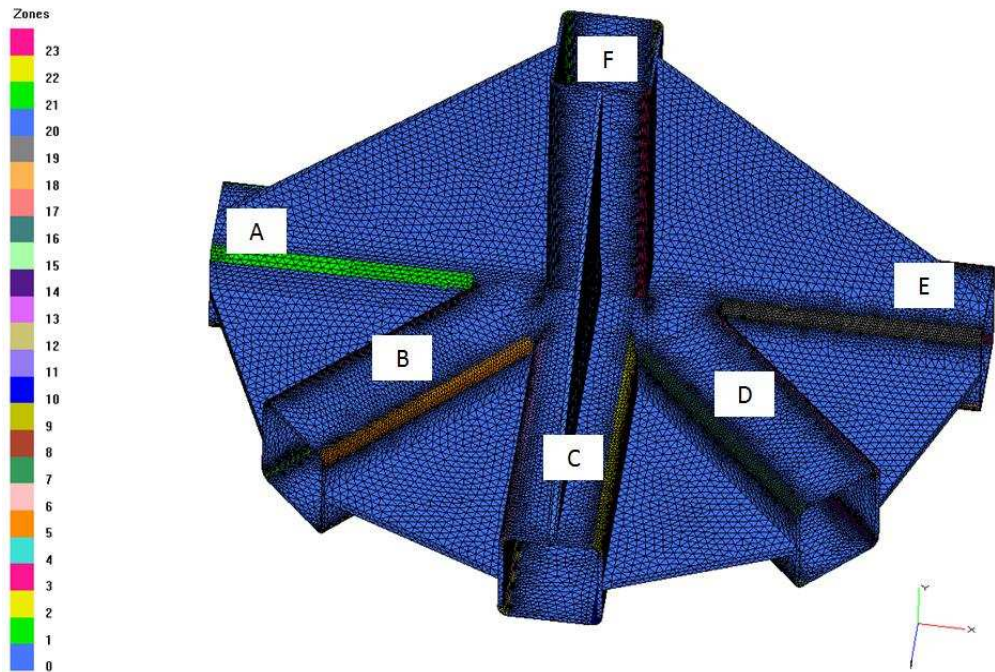
Fig. 8.1 (a): Generic node model for variability simulations Top view. A1 is the green zone, B5 the orange zone, C9 the dark-yellow zone etc.
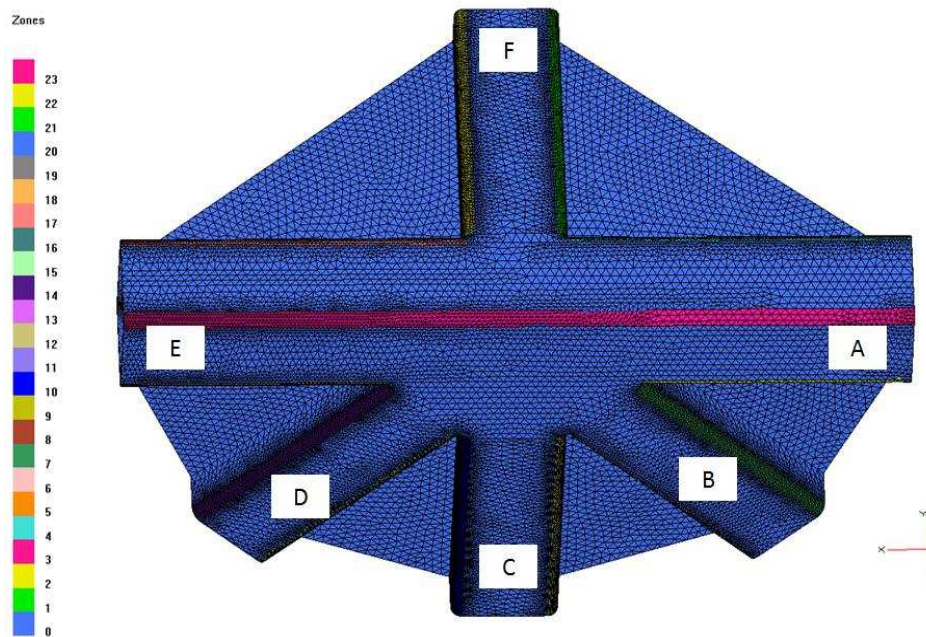
Fig. 8.1 (b): Generic node model for variability simulations. View of the opposite side.

A gap height was assigned randomly to each one of the twenty-three zones from A(1, 2, 3, 4) to F(20, 21, 22, 23,) (the zone 0 was the preform permeability therefore excluded). Each one of these zones represents a high probability of race-tracking indicating that resin rich zones may be observed in the final component. This was confirmed experimentally (Fig. 7.15 (b)).

The assignment of heights was achieved through a random number generator code that was written for this purpose. This was based on a simple Monte Carlo approach, using the measured fabric thickness on 90° bend in Figs. 3.13 (a) - 3.13 (g) then maximum gap heights calculated according to Section 3.8. The series of tables with random probabilistic distribution gap heights that was generated are presented in Appendix D.

All random numbers and corresponding gaps that used for the node simulations are presented in Tables D.1-D.10 Appendix D. generic node number of layers distribution considered as presented on Fig. 1.5.

Thereafter the random number generator code generated an N random number which corresponded to a gap height. The gap height properties assigned to the corresponding node zone as presented in Tables D.1-D.10 Appendix D. The same procedure was repeated twenty–three times and so random gaps were assigned to all node 90° radii edges.

In order to circumvent a software limitation with regards to the number of through-thickness elements at the edges of the node (the PAM-RTM 2010 software can run models with up to 600,000 tetrahedral elements at sharp

edges), and also minimize computational time, the following steps were followed:

i) For the values of the node permeability K_{fabric} at the twenty three edges the permeability $K_{fabric}= f(V_f)$ were used, (see table 4.3).

ii) For the values of the gap permeability K_{gap} at the twenty three edges, equation (6-1) $K_{gap}=h_i^2/12$ was used.

iii) The total permeability K_{total} for each zone at the compressed volume fraction was taken to be the weighted average presented by Endruweit, A., et al [11]

$$K_{total} = \frac{(h_{fabric}K_{fabric} + h_{gap}K_{gap})}{h_{fabric} + h_{gap}} \qquad \textbf{(8-1)}$$

The above permeability equation (8-1) for the 3D FE node anisotropic model is directional along the in-plane (K_{1total}, K_{2total}) and through thickness (K_{3total}) directions. This directionality is indicated in equations (8-2) and (8-3) below.

$$K_{1Total} = \frac{(h_{fabric}K_{1\,fabric} + h_{gap}K_{gap})}{h_{fabric} + h_{gap}}$$

$$\text{and} \qquad \textbf{(8-2)}$$

$$K_{2Total} = \frac{(h_{fabric}K_{2\,fabric} + h_{gap}K_{gap})}{h_{fabric} + h_{gap}}$$

$$K_{3Total} = (\frac{K_{3\,fabric}}{h_{fabric}}) \frac{(h_{av.gap} + h_{fabric})}{(1 + \frac{h_{av.gap}}{h_{fabric}} \frac{K_{3\,fabric}}{K_{gap}})} \qquad \textbf{(8-3)}$$

For in-plane parallel flow the h_{gap} and h_{fabric} values were taken from the case of 2D 90° curved plate racetrack modelling, (section 6.3.2).

For the through-thickness series flow the values of h_{gap} and h_{fabric} were calculated through eq. (8-3) as presented in Appendix G.

8.4   Simulations results and discussion

A series of thirty simulations (ten for each of the three tested fabrics) presented, i.e. ACTS HTS40 F13 3D woven, 2/2 twill in plane and triaxial with 280728 tetrahedral elements per simulation, was run with the generic node FE CAD model and PAM-RTM® software.

Simulations were conducted with the mode: "application of void formation - on" for material properties taken from Tables 3.2, and 4.3. An example of all node variability input values is presented in Table 8.1, (and in Appendix E).

Table 8.1: Input file to the simulation (case 1 for the ACTS fabric of generic node), showing the number of zones (left column) and layers per zone (second column), as well as the fibre directions per zone (third column) with the randomly selected gap heights and number of gaps, (last column).

ACTS Simulation 1			
Node zone	Number of layers	Node fabric direction	Random gap h(mm)
1	4	weft	0.15mm
2	4	weft	0.45 mm
3	4	weft	0.35 mm
4	4	weft	0.55mm
5	4	45^0 (warp/weft)	0.55mm
6	4	45^0 (warp/weft)	0.55mm
7	4	45^0 (warp/weft)	0.45mm
8	4	45^0 (warp/weft)	0.65mm
9	4	warp	0.55 mm
10	4	warp	0.75 mm
11	4	warp	0.55 mm
12	4	warp	0.55 mm
13	4	45^0 (warp/weft)	0.15mm
14	4	45^0 (warp/weft)	0.15mm
15	4	45^0 (warp/weft)	0.55mm
16	4	45^0 (warp/weft)	0.55mm
17	4	weft	0.45mm
18	4	weft	0.15mm
19	4	weft	0.45mm
20	3	warp	0.45 mm
21	3	warp	0.45 mm
22	3	warp	0.35mm
23	3	warp	0.45mm

From Table 8.1 and Appendix E a series of thirty output files was generated. The whole investigation gave useful information of the variability and void formation that may arise during the manufacturing process of the generic node with HTS40 F13 3D woven fabric, 2/2 twill and triaxial preforms.

8.4.1 HTS40 F13, 2/2 Twill, Triaxial fabric simulation for prediction of node void formation

Simulations of the variability with HTS40 F13 3D woven fabric predicted the frequency and the void volume that may arise during the node manufacturing process by RTM as shown in Tables 8.1, E1-E.29 Appendix E.

The probabilistic distributions of void formation that may arise during the node manufacturing process are presented in Figures 8.3 (a), (b), 8.5 (a), (b), 8.8 (a), (b), 8.10 (a), (b), 8.13 (a), (b), 8.15 (a), (b), 8.18 (a), (b), 8.21 (a), (b).

Thereafter worst case scenarios (i.e. those with higher n-frequency void content (defined as the number of voids per channel distribution) and the higher volume of voids (m^3) for each of the three tested fabrics) were chosen to be improved and optimized from all output files of the thirty simulations.

Optimization was achieved though injection gate and vent modifications by taking in to account mould's geometry and the existing injection lines and vents from original scenario.

Extra vents were implanted in the node for these cases and the simulations were repeated again with the worst case void formation scenarios.

As a result the total void volume decreased significantly from the order of tens of centimetres cubed to the order of millimetres cubed.

This will be demonstrated in the following sections, shown collectively for each preform simulation.

8.4.2 Pre-optimization and optimization processes for HTS40 F13 fabric based generic node

The FE node model in Fig. 8.1 (a), (b) was simulated ten times with the material properties of the HTS40 F13 3D woven preform. The input file tables used in simulations are presented in Appendix E.

The model revealed what may happen during resin filling of the node. Two of the worst case scenarios (referred to as cases 1 and 8), i.e. those with higher n-frequency voids content and the higher volume voids (m^3) will be discussed for this fabric in order to demonstrate the optimization process and to predict the node variability, frequency of void formation and void volume.

Figures 8.2 (a) and (b) show the pre-optimised simulation case 1, during resin filling for the ACTS fabric.

It is observed in Fig. 8.2 (a), that at the zone 8 in Table 8.1, the converging flow presents a peak (goes faster), as a result of the higher gap size (0.65 mm) that was chosen by the random number generator for this particular zone.
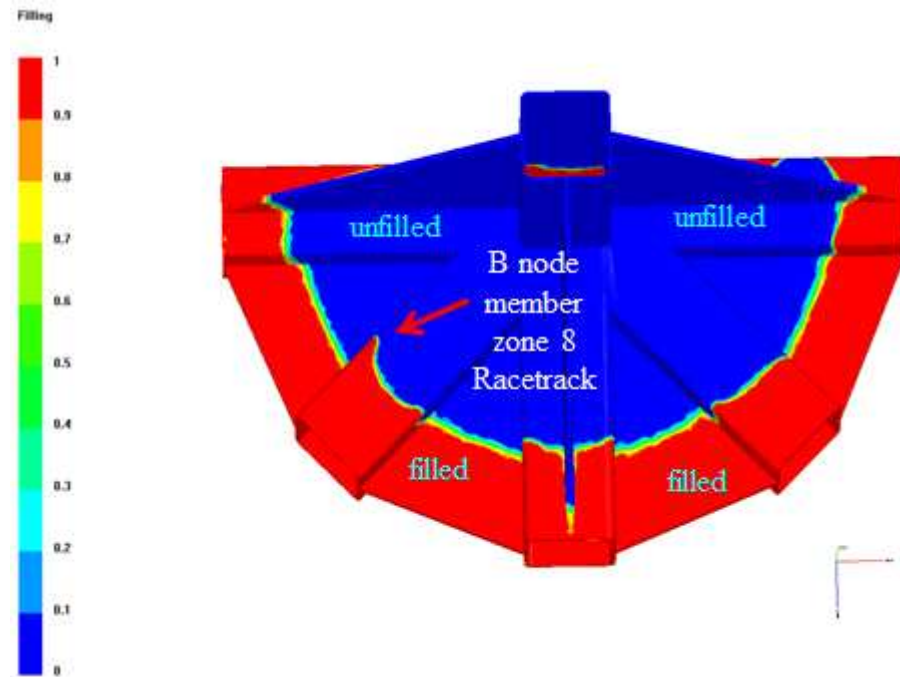
Fig. 8.2 (a): Case 1 simulation <u>during</u> filling and <u>before optimization</u> of ACTS HTS40 F13 3D woven fabric. Top surface view (red coloured filled area, blue unfilled, other colours half filled).
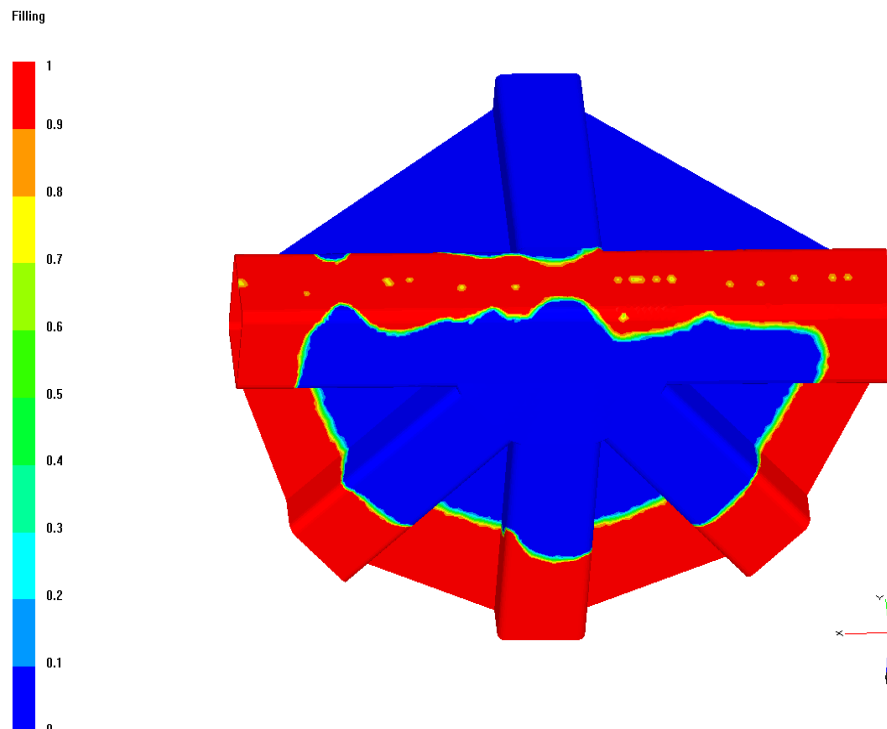
Fig. 8.2 (b): Case 1 simulation <u>during</u> filling and <u>before</u> <u>optimization</u> with ACTS HTS40 F13 3D woven fabric. View of the lower surface (red coloured filled area, blue unfilled, other colours half filled).

Upon completing the pre-optimization filling process with the simulation of case 1, a total of sixty seven voids were detected with PAM-RTM software and most of them were distributed randomly on the node's centre top part and underneath (opposite side) geometry. A large void of volume $2.57{\times}10^{-6}$ m^3 and 2.5 cm maximum length in the shear web on the top of the ACTS node connected to member F according to Fig. 8.1 (a) was observed (Fig 8.3 (a) blue unfilled area) input data used Table 8.1. On the centre of the opposite lower side of the node (Fig 8.3 (b)) a larger void formation with about 14 cm maximum horizontal length and 4.9 cm maximum vertical length, was observed. Its volume was $1.17{\times}10^{-5}$ m^3. The void was extended through the thickness of the composite.
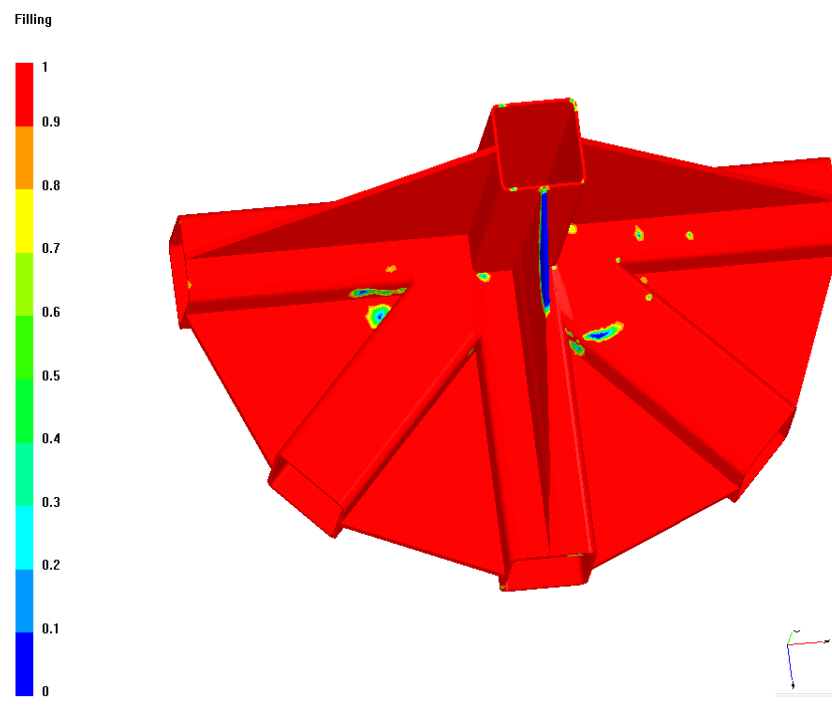
Fig. 8.3 (a): Case 1 <u>before</u> optimization and <u>after</u> filling has been completed. The image shows the upper surface of the node of the ACTS HTS40 F13 3D woven fabric (red coloured filled area, blue unfilled, other colours half filled).

234
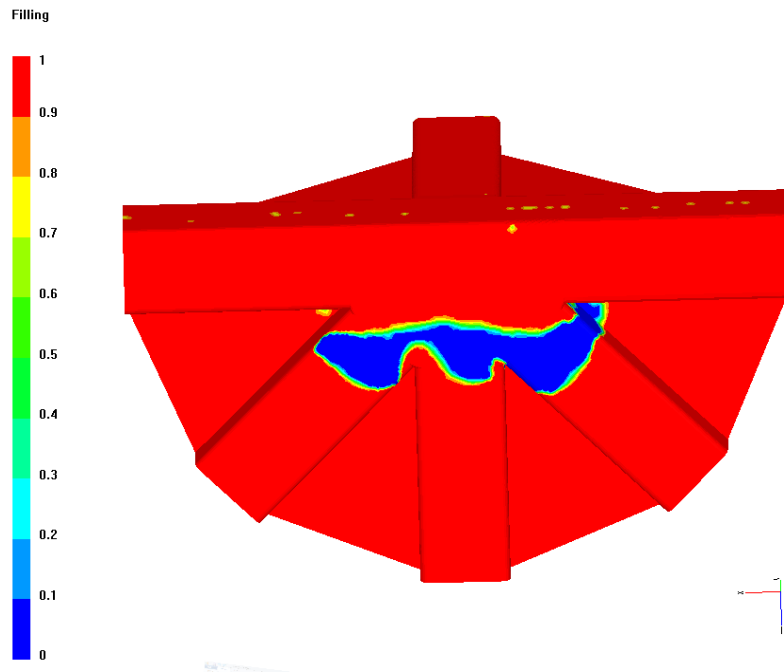
Fig. 8.3 (b) Case 1 <u>before</u> optimization, <u>after</u> filling has been completed. The image shows the lower surface of the ACTS HTS40 F13 3D woven fabric. These were the worst cases of void formation from 10 simulations with this preform (red coloured filled area, blue unfilled).

n-freq. void ACTS case 1	1	27	31	6	1	1
Max void vol. (m3)	2.43E-10	3.35E-09	2.88E-08	3.30E-07	2.57E-06	1.17E-05
Total node void vol. (m3)	2.43E-10	9.05E-08	8.93E-07	1.98E-06	2.57E-06	1.17E-05
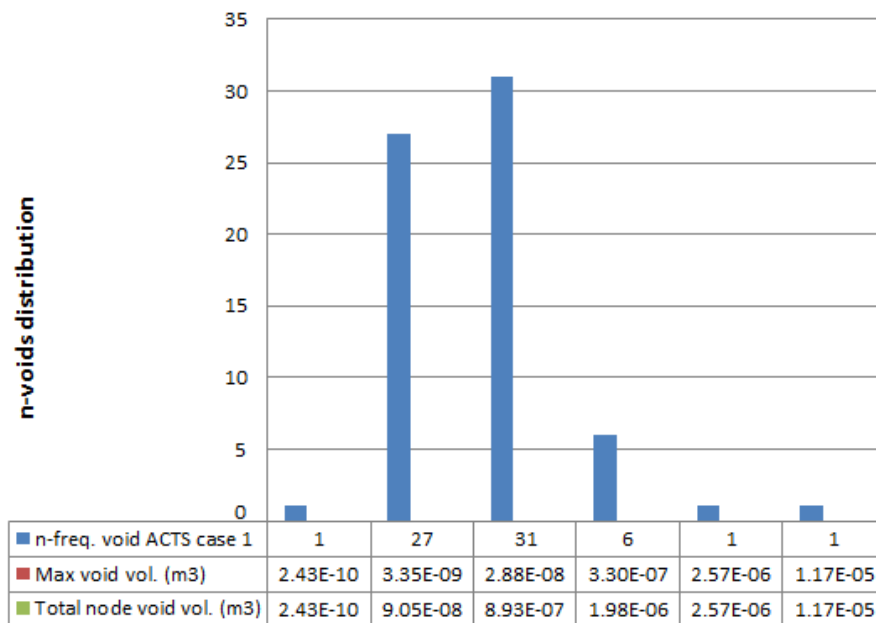
Figure 8.4: Case 1 ACTS HTS40 F13 3D woven fabric void distribution worst case out of 10 node simulations. Max void volume (m³), total voids volume (m³) at the indicated scale.

235

The defined terminology of the detected n-frequency of void formation i.e. number of voids per volume. The bar chart of the n-void distribution represented firstly against the max volume of voids and secondly against the total node void volume is shown on Fig. 8.4.

Carrying on with the pre-optimized simulation of case 8, a total of sixty four voids were detected, three of which had high volumes. The two most prominent were seen at the top surface (Fig. 8.5 (a)), had volumes of the order of 5.68×10^{-6} m^3, whereas the one at the lower surface (Fig. 8.5 (b)) had a volume of the order of 1.01×10^{-5} m^3.

One void was at the top of ACTS node member B, and was approximately of 2.4 cm maximum horizontal length and 4.7 cm maximum vertical length. The void was extended through the thickness in the composite with the same shape. At ACTS node member E a void of about 2.2 cm maximum horizontal length and 0.5 cm vertical length with the same through thickness shape was detected. A void with the same dimensions like member E in the shear web of the ACTS node was observed.
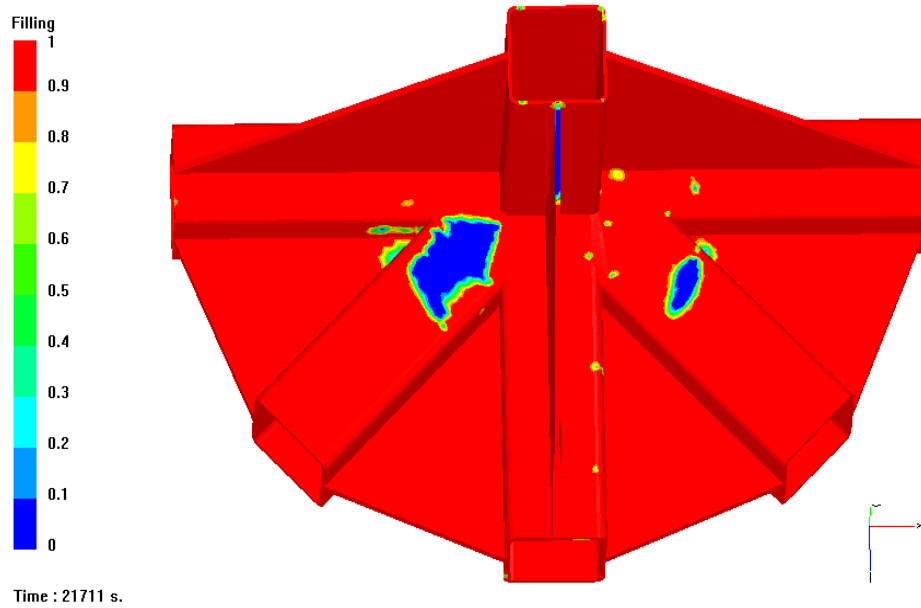
Fig. 8.5 (a): Case 8 <u>before</u> optimisation <u>after</u> filling has been completed in the ACTS HTS40 F13 3D woven fabric. The image shows the upper surface of the node (red coloured filled area, blue unfilled).
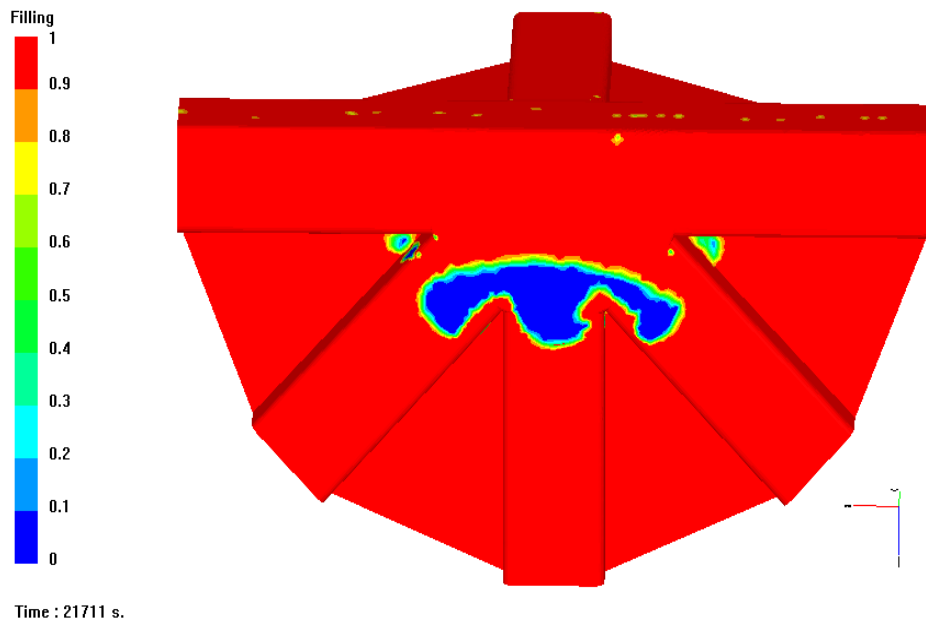
Fig. 8.5 (b): Case 8 <u>before</u> optimisation ACTS HTS40 F13 3D woven fabric <u>after</u> filling has been completed. The image shows the lower surface of the ACTS HTS40 F13 3D woven fabric (red coloured filled area, blue unfilled).

■ n-freq. void ACTS case 8	2	26	25	8	2	1
■ Max void vol. (m3)	8.72E-10	3.21E-09	2.80E-08	3.92E-07	2.84E-06	1.01E-05
■ Total node void vol. (m3)	1.74E-09	8.35E-08	7.00E-07	3.14E-06	5.68E-06	1.01E-05
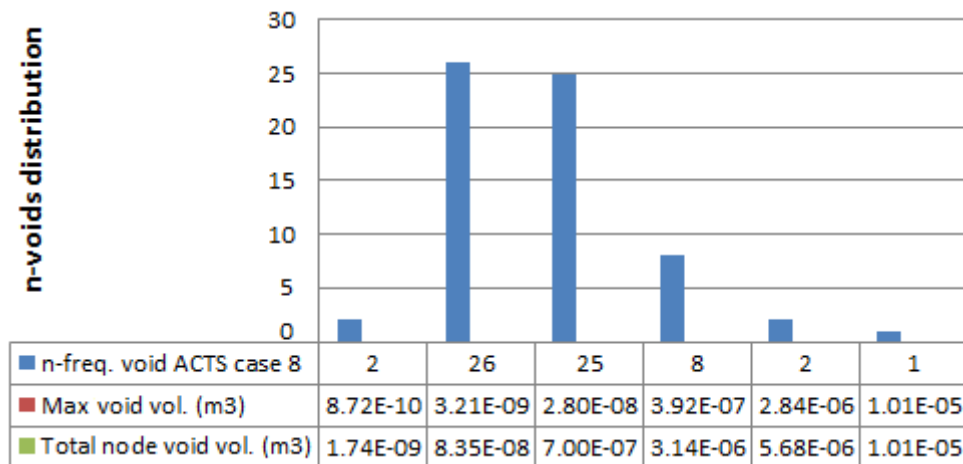
Fig. 8.6: The void distribution (out of 10 node simulations) case 8 (second worst scenario) of the ACTS HTS40 F13 3D woven fabric. Max void volume (m^3), total voids volume (m^3) at the indicated scale.

To summarise, critical areas in both cases 1 and 8, where void formation may potentially occur were identified to be situated:

(i)   in the shear web,

(ii)   on the opposite (lower) side central zone of the component and

(iii)   in the areas where the ACTS node members A, B, C, D, E and F are connected together on the centre of the node as shown in Fig 8.3 (a), (b) and 8.5 (a), (b).

The optimization process pertained to improving the process for manufacture of the node for cases 1 and 8 in such a way as to minimize the presence of high volume defects during the resin filling process.

To address this issue, the injection gates and vents of the node, were modified. In particular the injection gate running horizontally along node members A to E (presented on Chapter 7 Fig. 7.1, 7.2) was eliminated.

Secondly, one new vent was placed at the base of node F of 15 cm in length and 2.2 cm in height. An additional vent was placed at the top surface of the shear web, (green line in Fig. 8.7 (a) and three circular vents of 2.5 cm in diameter at the base of the node members C, D, E as viewed from the lower side (at the locations where the large volume voids were observed in Fig. 8.3 (b) and 8.5 (b)).
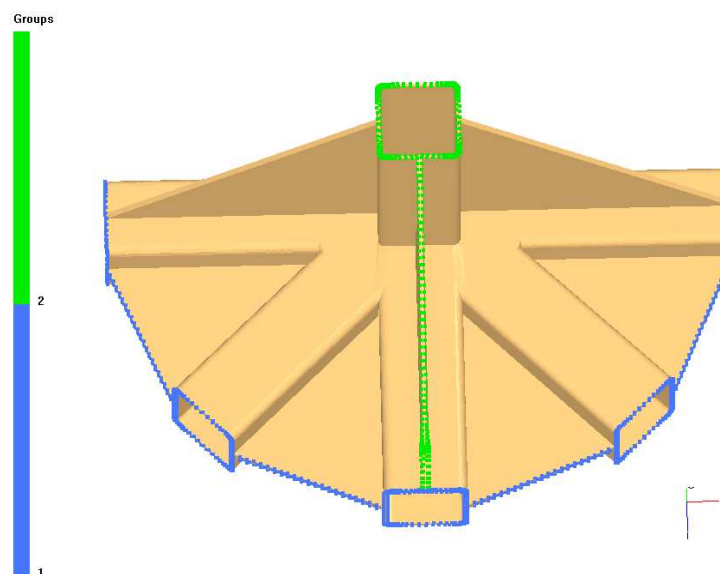
Fig. 8.7 (a): Node filling injection lines (blue), vents (green).
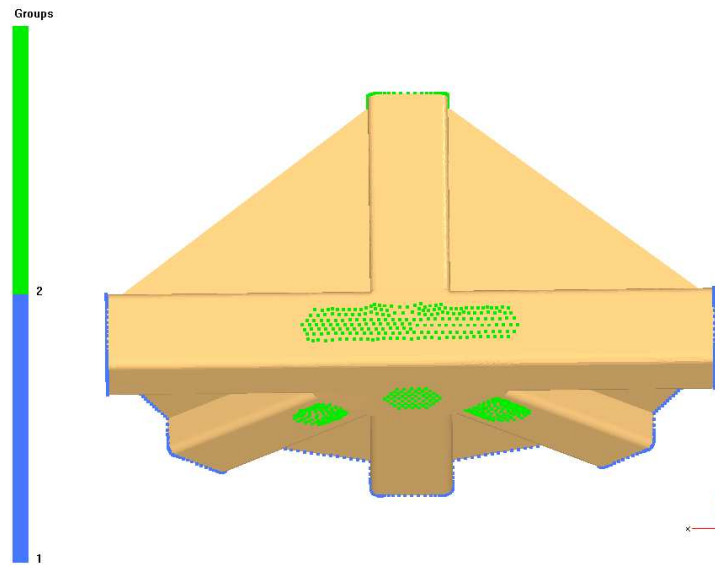
Fig. 8.7 (b): The green vent at the base of the F node and along A to E, has a height of 2.2 cm and length of 15 cm. The three lower circle shaped vents are of 2.5 cm in diameter.

Following these modifications, the simulation of the filling process for case 1

was repeated yielding the results in Fig. 8.8 (a) and (b).
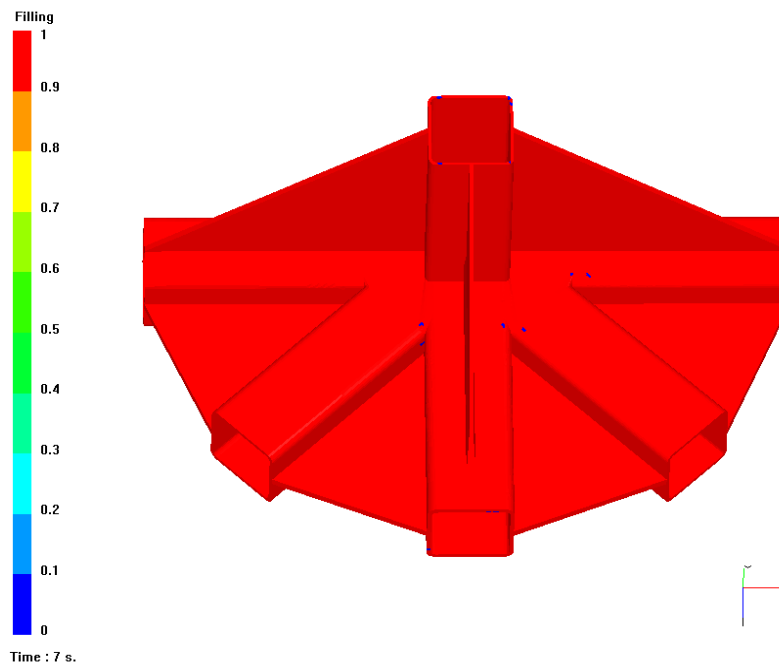
Fig. 8.8 (a): Case 1 ACTS HTS40 F13 3D woven fabric optimised with vents as per figure 8.7 (a), (b). The upper aspect of the node (red coloured filled area, blue unfilled).
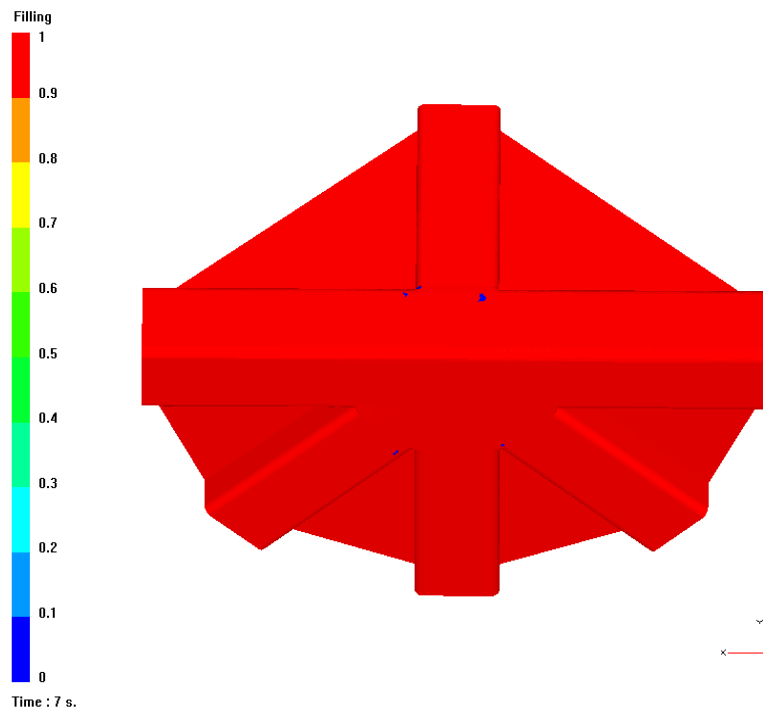
Fig. 8.8 (b): Case 1 ACTS HTS40 F13 3D woven fabric optimised with the new vents of figure 8.7 (a), (b). The lower aspect of the node (red coloured filled area, blue unfilled).

It is seen in the above figures that the top and bottom surfaces of the node were filled without any significant void formation at the critical areas observed previously for case 1.

The probabilistic distribution of void formation (Fig. 8.9) shifted significantly from its pre-optimized equivalent (Fig. 8.3 (a), (b)). This shift was both in number of voids (from a total number of 67 down to 36) as well as volume sizes (27 of the 36 voids had volumes approximately 3.38×10^{-9} m^3 and no voids of volume greater than 4.12×10^{-8} m^3 were observed). This is in sharp contrast with the distribution of Fig 8.4, where 39 out of the total 67 voids had volumes in the range 2.43×10^{-10} to 1.17×10^{-5} m^3.
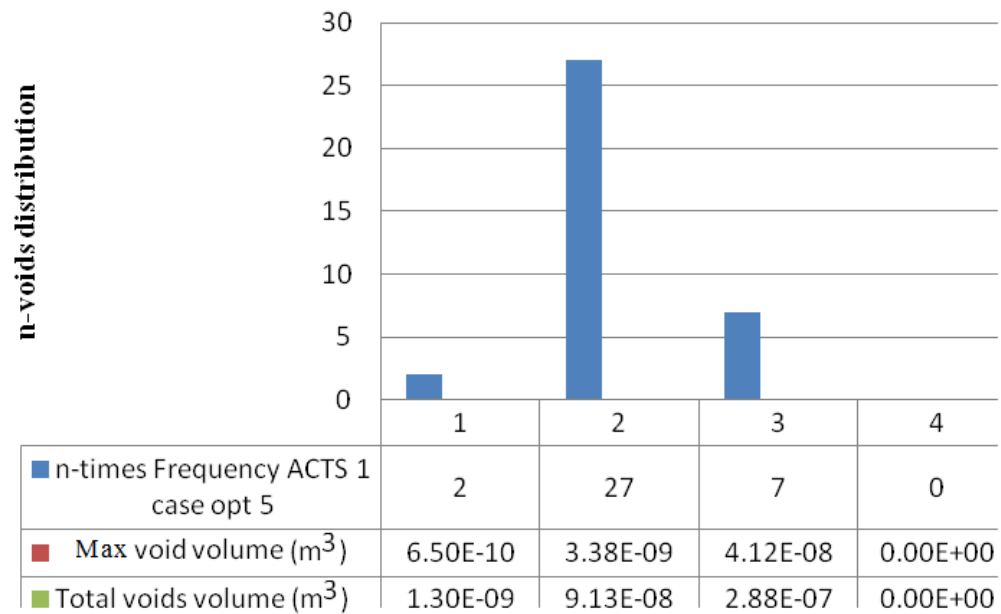
Fig. 8.9: Case 1 optimised ACTS HTS40 F13 3D woven fabric void distribution. Max void volume (m³), total voids volume (m³) at the indicated scale.

In a similar way the optimization process was repeated for case 8 and is presented in Figs. 8.10 (a) and (b). Both sides of the node were filled without any significant void formation in the critical areas mentioned previously for this case.
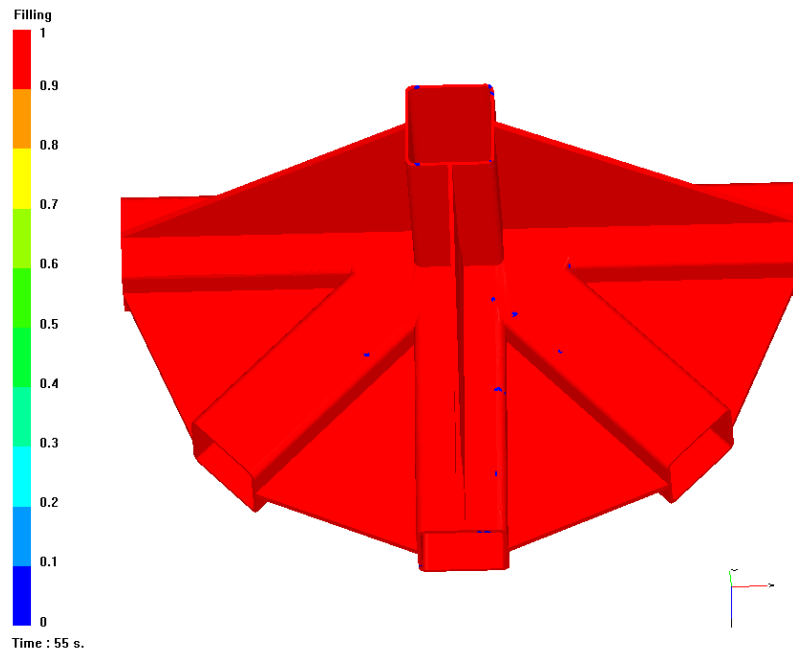
Fig. 8.10 (a): Case 8 ACTS HTS40 F13 3D woven fabric optimised with vents as per figure 8.7 (a), (b). Top surface view (red coloured filled area, blue unfilled).
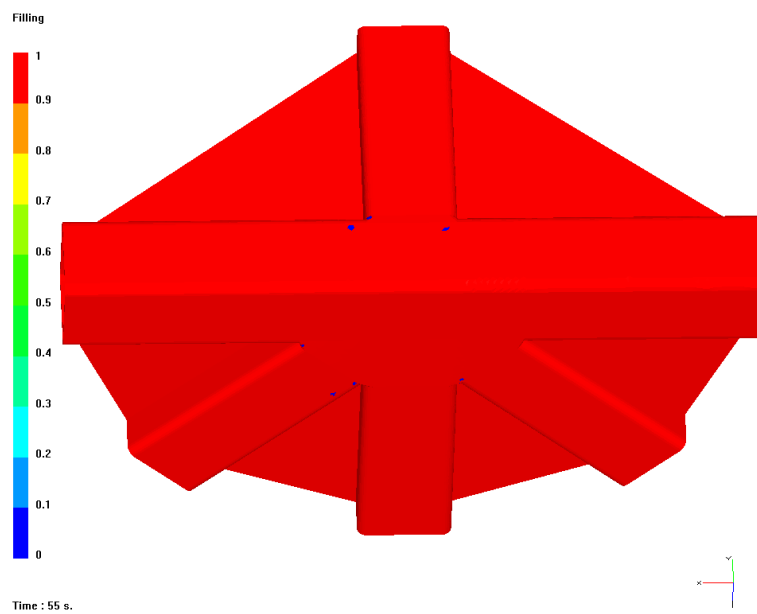
Fig. 8.10 (b): Case 8 ACTS HTS40 F13 3D woven fabric optimised with vents as per figure 8.7 (a), (b). View of the lower surface (red coloured filled area, blue unfilled).

243

The probabilistic distribution of void formation again decreased significantly in number (from 64 down to 32) and there were no voids of volume greater than 2.55×10^{-8} m^3 as shown in Fig. 8.11.

	1	2	3	4
■ n-times Frequency ACTS 8 case opt 1	5	19	8	0
■ Max void volume (m^3)	8.55E-10	2.50E-09	2.55E-08	0.00E+00
■ Total voids volum (m^3)	4.28E-09	4.75E-08	2.04E-07	0.00E+00
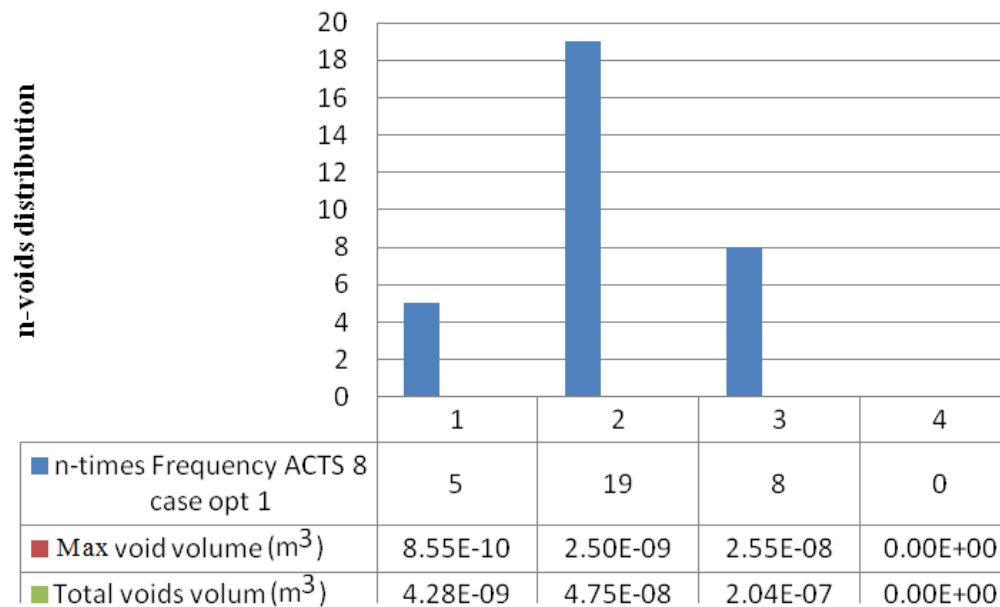
Fig. 8.11: Case 8 optimised ACTS HTS40 F13 3D woven fabric void distribution. Max void volume (m^3), total voids volume (m^3) at the incated scale.

Therefore these two cases demonstrate that the modifications (in injection and vents) introduced in the node for this fabric in Figures 8.7 (a) and (b) had the desired effects.

To summarise all ACTS HTS40 F13 node simulations with optimized cases 1, 8 are presented in Table 8.2, Appendix F, Figs. F.1-F.8. A similar approach will be used for the optimisation of the 2/2 twill and triaxial fabric based nodes.

Table 8.2: Summary of ACTS HTS40 F13 node simulations with detected probability for void formation and optimised cases.

Node simulation case	n-time Frequency voids	Max void volume (m^3)	Total node voids volume (m^3)	
1	67	1.17E-05	1.72E-05	
1 opt	36	4.12E-08	3.80E-07	optimised
2	73	2.57E-06	8.60E-06	
3	70	5.49E-06	1.40E-05	
4	75	2.18E-06	1.02E-05	
5	66	3.63E-06	1.41E-05	
6	72	1.08E-05	1.55E-05	
7	67	3.53E-06	1.39E-05	
8	64	1.01E-05	1.97E-05	
8 opt	32	2.55E-08	2.56E-07	optimised
9	71	4.95E-06	1.89E-05	
10	61	4.19E-06	1.44E-05	

8.4.3 Pre-optimization and optimization processes for the 2/2 twill fabric based generic node

The FE node model in Figures 8.1(a), (b) was simulated ten times with material properties of the 2/2 twill preform. All input data for simulations are presented in Appendix F, Figs. F.9-F.17. Figures 8.12 (a) and (b) show the filling process of case 3.

It may be observed again that at the edges of the nodes there are peaks of racetrack flow front similar to the one observed for the node of the ACTS woven fabric in Figure 8.2 (a), (b) due to similar flow behaviour (local gap permeability higher that fabric's permeability at radii).
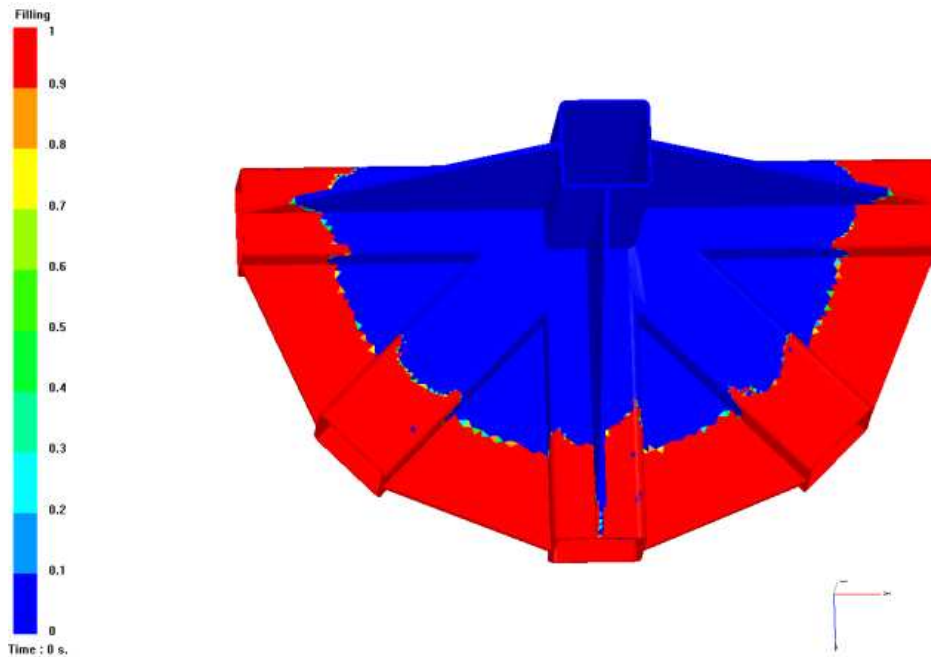
Fig. 8.12 (a): Case simulation 3 during filling of the 2/2 twill fabric. Clear peaks in the flow front are seen at the edges of nodes A to E on the upper surface (red coloured filled area, blue unfilled).
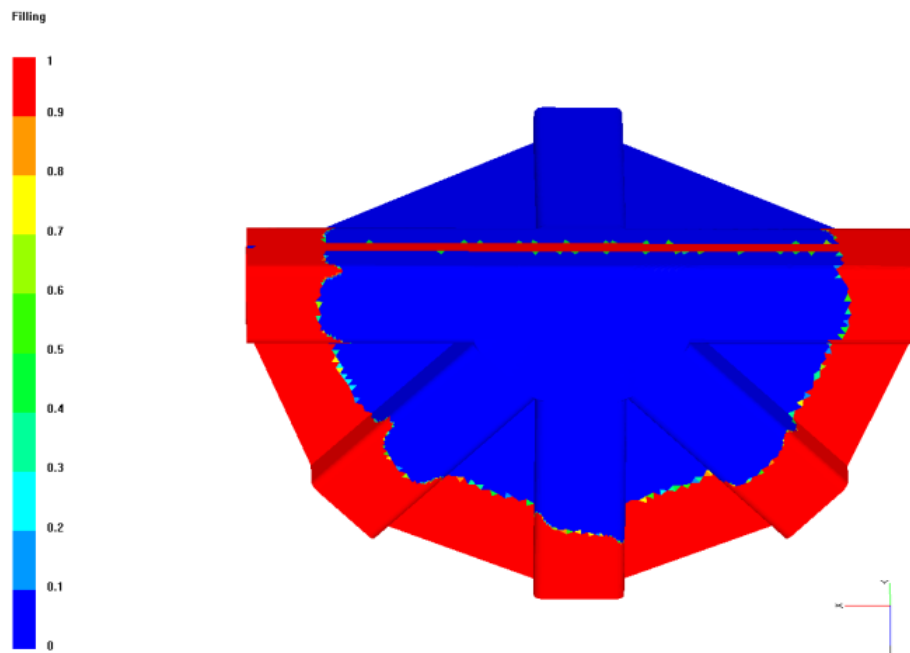
Fig. 8.12 (b): Case simulation 3 during filling of the 2/2 twill fabric. Less protruded peaks in the flow front are seen at the edges of the nodes A to E on the lower surface (red coloured filled area, blue unfilled).

For the 2/2 twill preform, case 8 presented the largest number of voids after the completion of the simulated filling. A total of 120 voids were detected with the PAM-RTM® software, with most of them grouped on node's centre top surface and lower side. Critical areas for void formation were identified to be near the areas where the node members A, B, C, D, E and F are connected together towards the centre of the upper surface as shown in Fig. 8.13 (a) and (b). In particular, a high number of large voids was observed between node members A and B, with the most predominant having a volume of 4.66×10^{-6} m^3 (Fig. 8.13 (a)).   Other voids of a smaller scale, less than 1mm in diameter were observed between the node members C and D and between the node members D and E. On the opposite side the largest volume void (1.90×10^{-5} m^3) (Fig. 8.13 (b)) occupied the centre and parts of the nodes B, C and D.
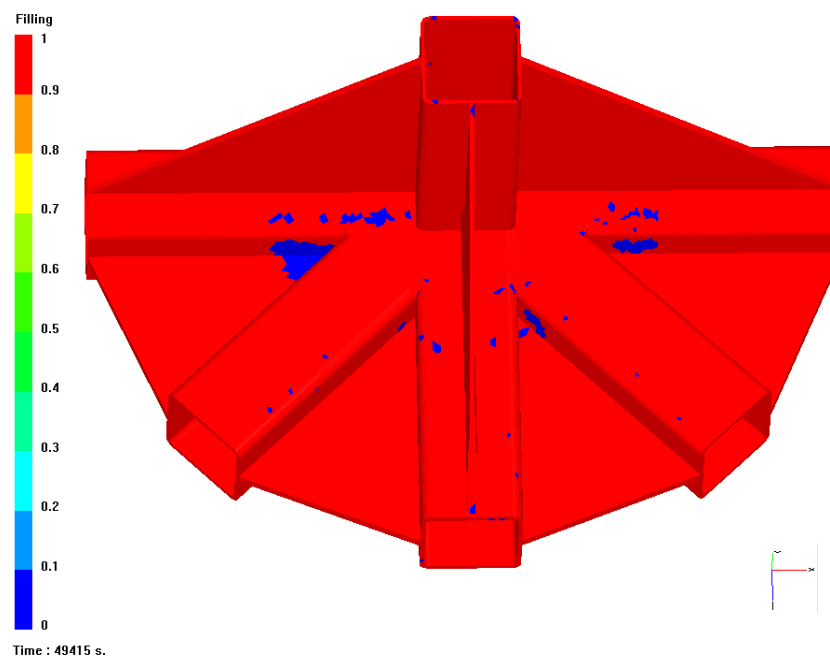
Fig. 8.13 (a): Case 8 for the 2/2 twill node before optimization. The void distribution for the upper surface is shown (red coloured filled area, blue unfilled).
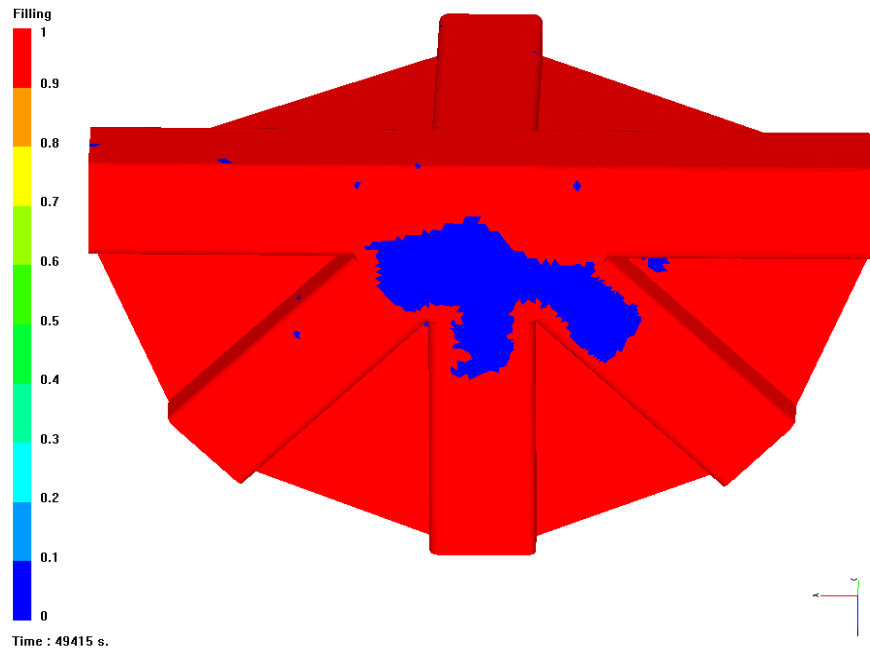
Fig. 8.13 (b): Case 8 for the 2/2 twill node before optimization. The void distribution and the central predominant void at the lower surface are seen (red coloured filled area, blue unfilled).

The pre-optimization probabilistic node distribution for the above case is presented in Fig. 8.14.

n-freq. void 2.2 twill case 8	11	70	31	6	1	1
Max void vol. (m3)	8.06E-10	3.38E-09	3.09E-08	2.97E-07	4.66E-06	1.90E-05
Total node void vol. (m3)	8.87E-09	2.37E-07	9.58E-07	1.78E-06	4.66E-06	1.90E-05
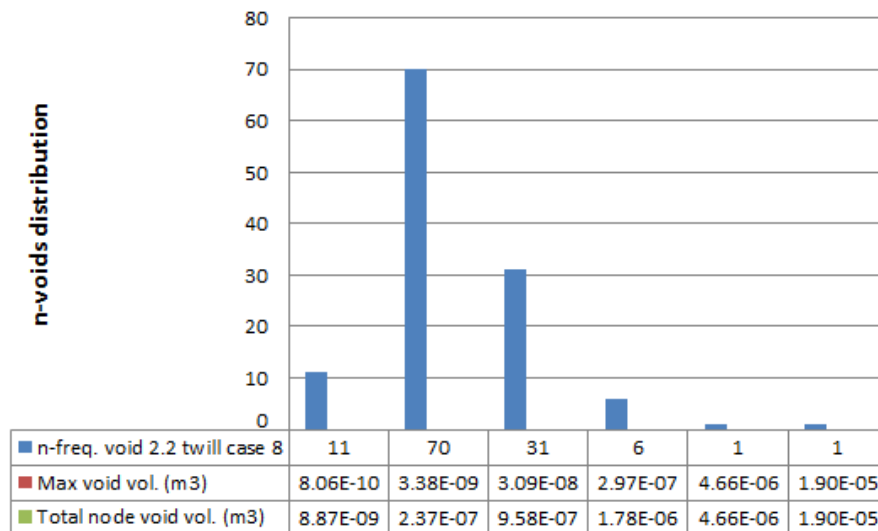
Fig. 8.14: Simulation case 8, for the 2/2 twill fabric void distribution prior to optimizing the node. 120 voids in total where detected. Max void volume (m^3), total voids volume (m^3) at the indicated scale.

The optimization process of the 2/2 twill preform was performed with the same new injection gates and vents that were also used for the ACTS HTS40 F13 3D woven fabric (Fig. 8.7 (a) and (b)). This was for three reasons:

(i)   the similarity of the flow front showing sharp peaks at the edges of both fabrics during filling,

(ii)   the fact that both materials showed a tendency to aggregate large volume voids near the central lower surface,

(iii)   the evident improvement of the ACTS fabric filling with these new injection gates and vents. Hence the simulation of the 2/2 twill case 8, was repeated under these conditions.

The output file results are presented in Fig. 8.15 (a) and (b). After optimization the high volume voids on top and lower sides were almost eliminated. Since these were occupying a dominant fraction of the total volume of voids their elimination led the total void volume to significantly decrease by two orders of magnitude. However, it is worth noting that the total number of voids has increased marginally to 126 (from 120) as shown by the probabilistic distribution in Fig. 8.16.

The formation of much smaller voids of the order 10^{-9} m^3 has increased in number from 70 (Fig. 8.14) to 101 (Fig. 8.16). Six voids each of maximum volume 2.88×10^{-7} m^3 were detected and no defects of higher volume were present (c.f. with 8 voids in the range 2.97×10^{-7} to 1.90×10^{-5} m^3 for the pre

optimized filling simulation). All these results are summarized in Figure 8.14 and Table 8.3.
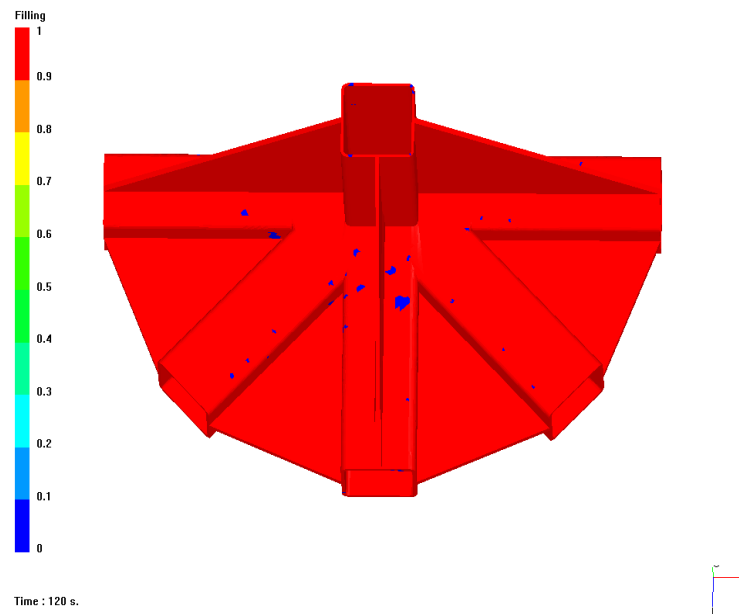
Fig. 8.15 (a): Optimised filling simulation for case 8 of the 2/2 twill fabric The large voids between node members A-B, C-D and D-E were eliminated at the upper surface, leaving only a minor number of smaller voids (red coloured filled area, blue unfilled).
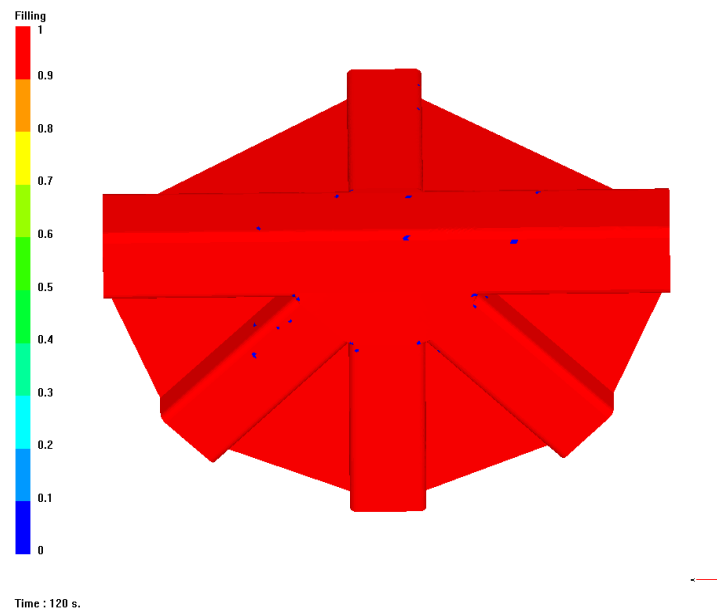
Fig. 8.15 (b): The central large void was eliminated at the lower surface leaving only a minor number of smaller voids (red coloured filled area, blue unfilled).
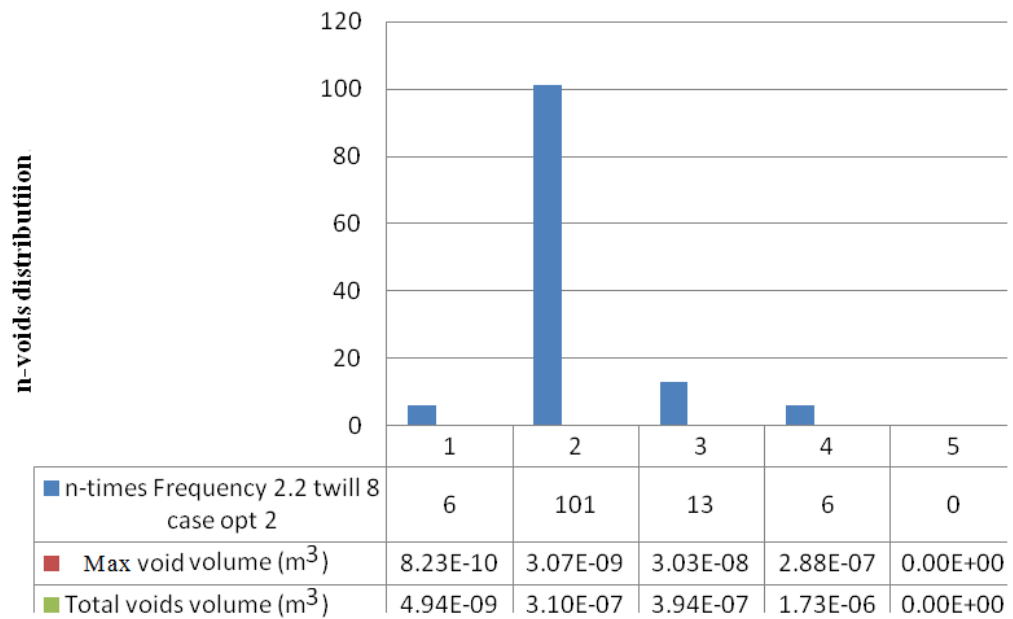
Fig. 8.16: Case 8 optimised 2/2 twill fabric void distribution. Max void
volume (m^3), total voids volume (m^3) at the indicated scale.

To summarise all 2/2 twill node simulations with optimized case 8 are

presented in Table 8.3. All frequencies presented on Appendix F, Tables voids

distributions in Figs F.9-F.17.

Table 8.3: Summary of 2/2 twill node simulations with detected
probability for void formation. The worst case scenario 8 has been
optimised by eliminating the high volume defects.

Node simulation case	n-time Frequency voids	Max void volume (m^3)	Total node voids volume (m^3)	
1	116	4.88E-06	1.20E-05	
2	120	1.01E-05	1.60E-05	
3	123	1.26E-05	1.62E-05	
4	125	1.79E-05	2.00E-05	
5	121	4.85E-06	1.22E-05	
6	118	5.83E-06	1.05E-05	
7	107	7.72E-06	1.16E-05	
8	120	1.90E-05	2.66E-05	
8 opt	126	2.88E-07	2.44E-06	optimised
9	130	1.43E-05	1.73E-05	
10	113	1.29E-05	1.59E-05	

8.4.4 Pre-optimization and optimization processes for triaxial fabric with generic node

The optimization process of the node geometry of a triaxial fabric was performed for the case where the local permeability of the twenty three right angle edges was lower than the permeability of the fabric. This behaviour was observed in experimentally in Chapter 6 (Fig. 6.19, 6.20). On the other hand the simulations with 3D woven HTS40 F13 fabric and 2/2 twill studied cases where the local permeability of the twenty three right angle radii, was higher than the permeability of the fabric. In both of those cases the problem of void formation that may arise during RTM, was addressed by applying the same vents and injection lines presented in Fig. 8.7 (a), (b).

Therefore it would be useful to explore what may happen to the variability of the node with a lagging random fluid behaviour (as observed experimentally on a single 90° curve plate bending was shown in Fig. 6.11, 6.13, 6.15, 6.17, 6.19.) at the twenty three edges as manifested in the triaxial fabric. In other words, would the node geometry generate voids in different critical areas than the 2/2 twill and ACTS fabrics and would additional vents and injection points be required to optimize the filling process for the triaxial fabric?

The FE node model (Fig. 8.1 (a), (b) was simulated ten times with material properties of the triaxial preform. All input data for simulations are presented in Appendix F, Figs F.18-F.26.

Figures 8.17 (a), (b) shows the simulated filling for case 2. In this case at the edges of the node unlike the one observed at ones presented above. These lags

indicated the lower local permeability at the radii and so the slower flow at the

node edges.
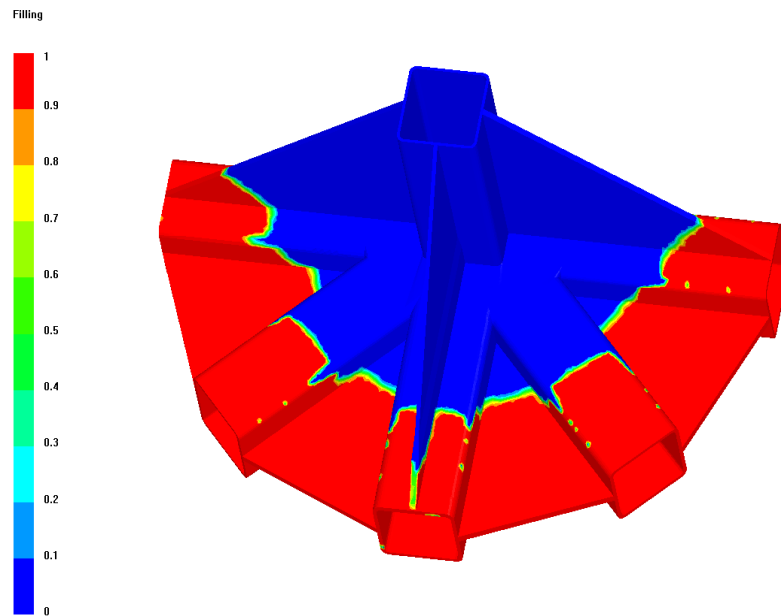
Fig. 8.17 (a): Case 2 filling with triaxial fabric. The flow front is lagging at the edges of the nodes (red coloured filled area, blue unfilled, other colours half filled).
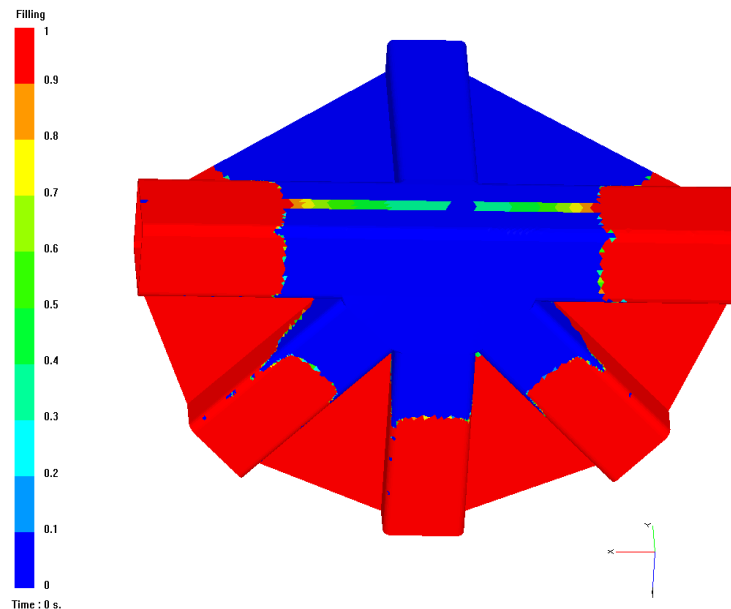
Fig. 8.17 (b): Case 2 filling with triaxial fabric. The flow front is lagging at the edges of the nodes (red coloured filled area, blue unfilled, other colours half filled).

Simulations revealed what may happen in the triaxial preform worse-case scenario 3, during resin filling of the node. Overall, 99 voids were identified with the PAM-RTM® software and most of them were distributed randomly on node's centre top part, rear and lower sides as shown in Fig. 8.18 (a) and (b). A high void formation on the shear web that connects node members C and F was observed (Fig. 8.18 (a)). The largest of them had a volume 1.11×10^{-5} m^3. On the surface underneath the node, a large unfilled region (like in the cases of ACTS HTS40 F13 3D woven and the 2/2 twill preform) was not observed (Fig.8.18 (b)). However another large void (8.81×10^{-7} m^3) was detected at the base of the rear side at the intersection between node members A, E and F. The probabilistic node distribution bar chart, for case 3 is shown in Fig. 8.19.
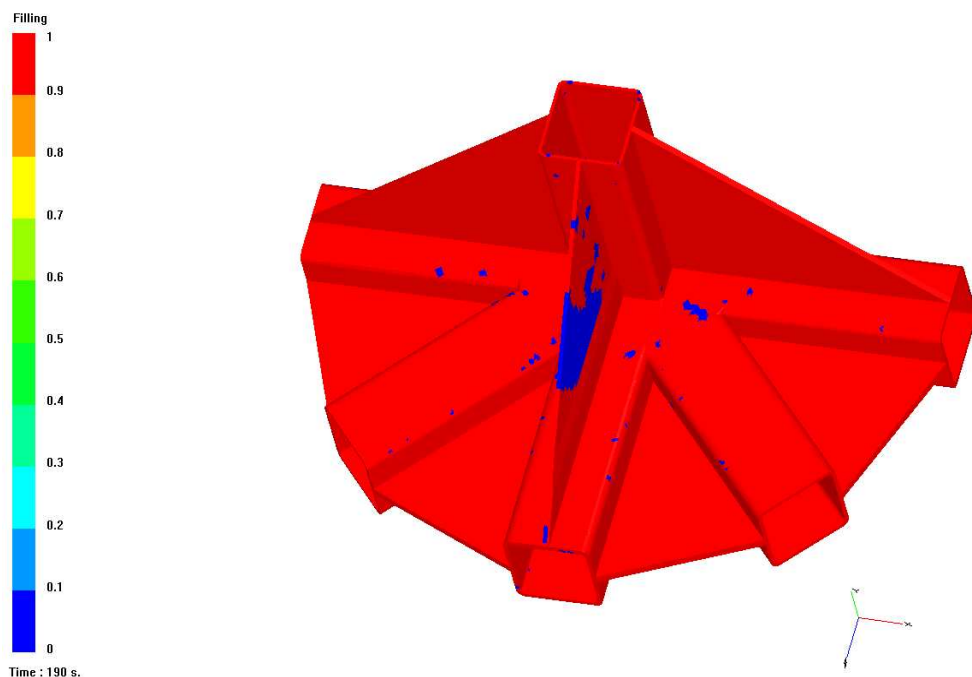
Fig. 8.18 (a): Simulation of case 3 for the triaxial glass fabric before optimization. A large unfilled region on the shear web on top of node C can be seen (red coloured filled area, blue unfilled, other colours half filled).
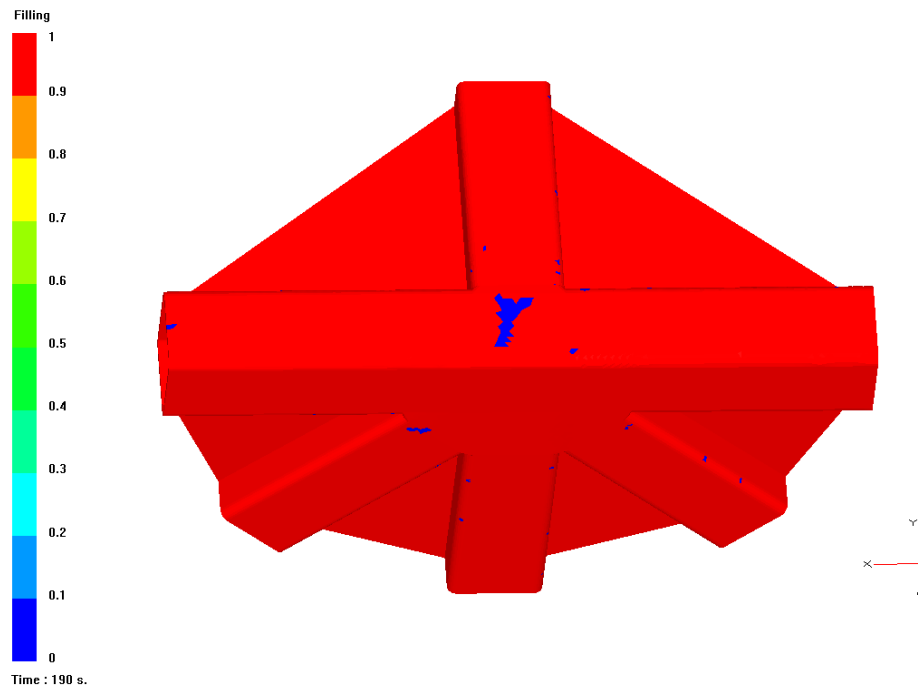
Fig. 8.18 (b): Simulation of case 3 with triaxial glass fabric before optimization. A void at the intersection of nodes A, E and F is seen (red coloured filled area, blue unfilled, other colours half filled).

■ n-freq. void triaxial case 3	3	71	20	4	0	1
■ Max void vol. (m3)	6.92E-10	4.14E-09	3.29E-08	3.55E-07	0.00E+00	1.11E-05
■ Total node void vol. (m3)	2.08E-09	2.94E-07	6.58E-07	1.42E-06	0.00E+00	1.11E-05
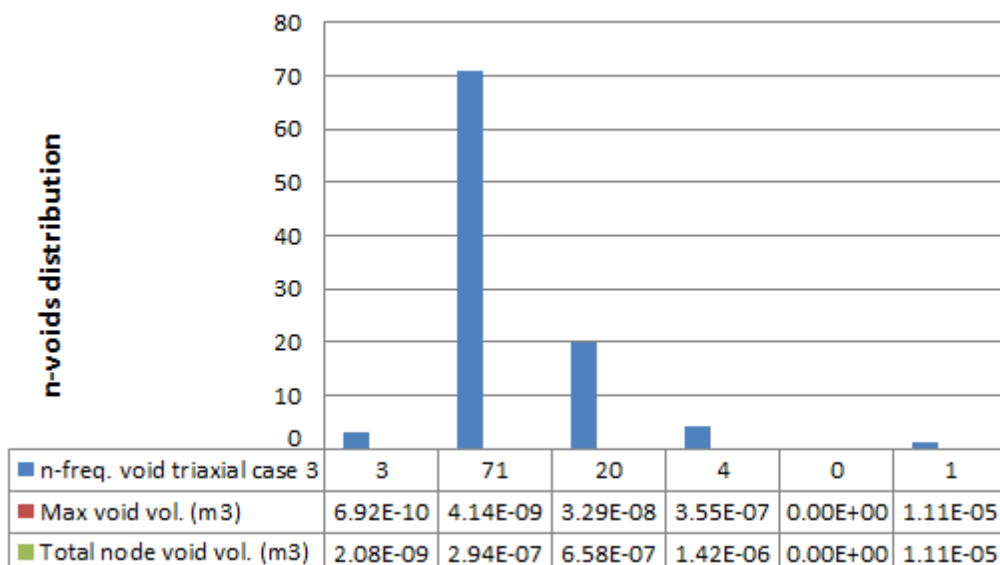
Fig. 8.19: Bar chart of void distribution for the pre-optimised simulation of the triaxial fabric, case 3, (worst case out of 10 node simulations). Max void volume (m^3), total voids volume (m^3) at the indicated scale.

In order to address the optimization of case 3, a different approach was implemented to the node of Fig 7.1 (a), (b). An additional vent was placed on the top of the shear web that connects nodes C and F (Fig. 8.20 (a)) and an injection gate was created, extending along the rear length from node A to E (Fig. 8.20 (b)), to tackle the observed voids in these regions.
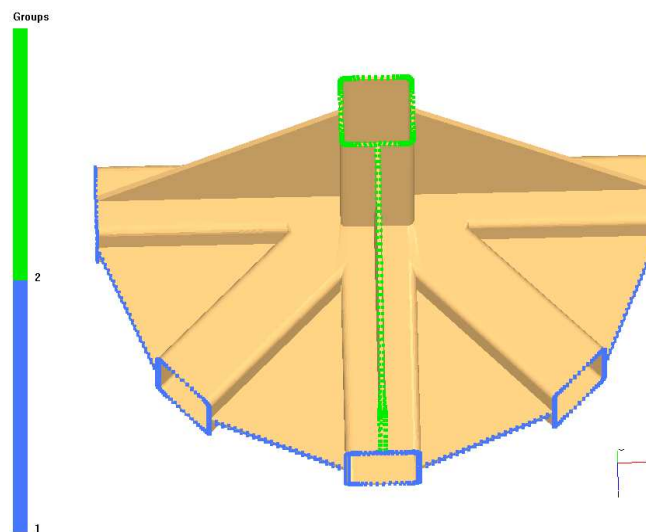
Fig. 8.20 (a): Top view of the node. Injection lines (blue) vents (green).
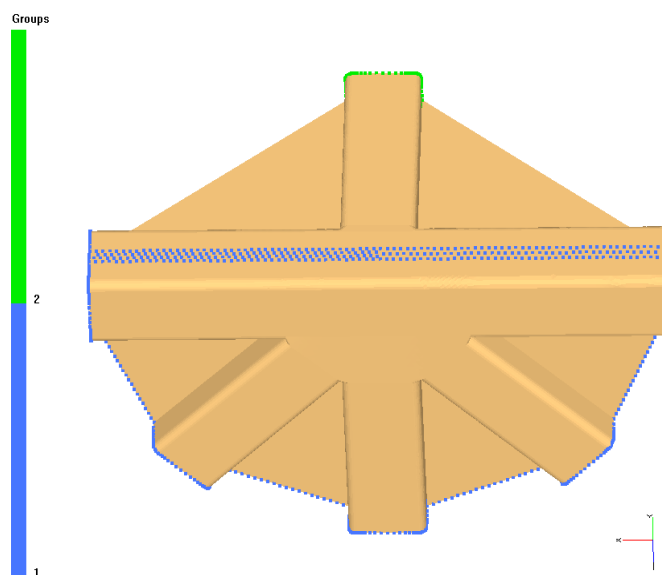
Fig. 8.20 (b): Injection lines (blue) vents (green) opposite side node.

Upon implementation of this new configuration of gates and vents, case 3 simulation was repeated and the results are presented in Fig. 8.21 (a) and (b). After simulation of the filling process the large voids on shear web and the rear side of the node were eliminated. The total void volume dropped significantly by two orders of magnitude.

The probabilistic distribution shows that voids formation increased in number but not significantly from 99 to 104 in this case as shown in the Fig. 8.22. Also the largest volume defect was predicted to be 1.3×10^{-7} m^3. All triaxial node simulations including the optimised case 3 are summarised in Table 8.4.
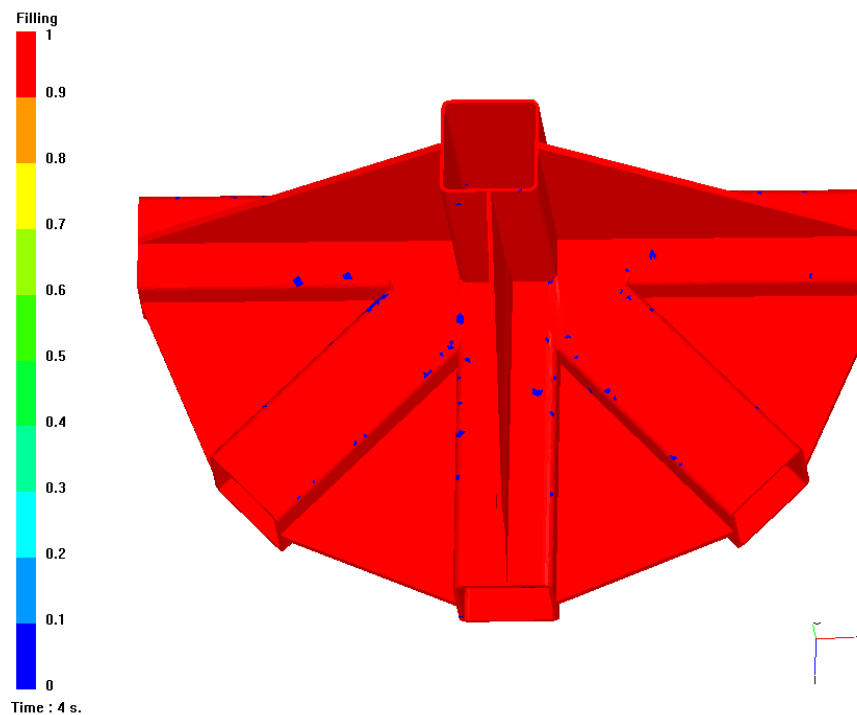
Fig. 8.21 (a): Case 3 triaxial fabric after optimization on node with new vents as per figure 7.65 (red coloured filled area, blue unfilled).
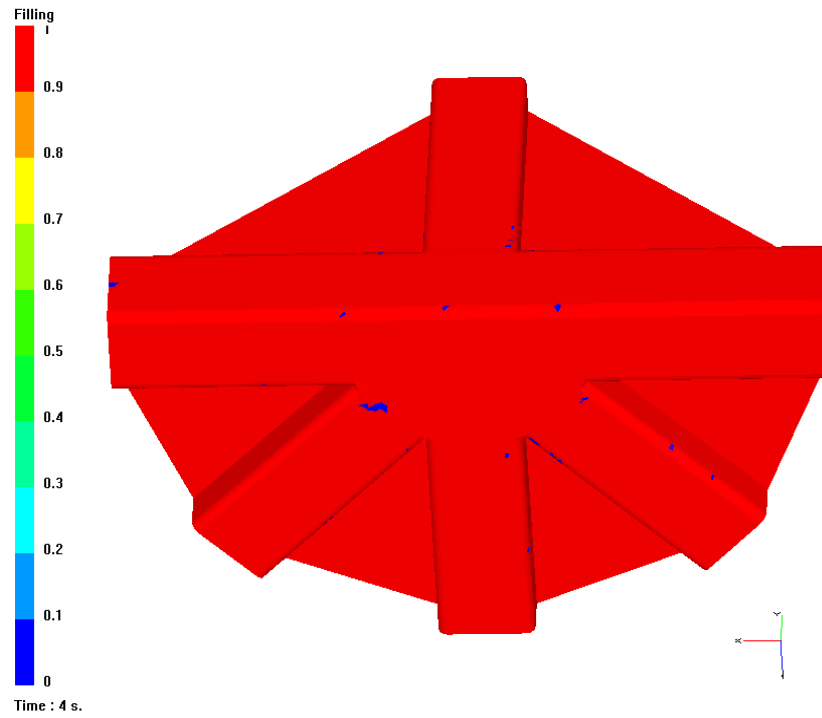
Fig. 8.21 (b): Case 3 triaxial fabric after optimization on node with vents as per figure 7.65 (red coloured filled area, blue unfilled).

	1	2	3	4	5	6
n-times Frequency triaxial 3 case optimised	4	80	19	1	0	0
Max void volume (m^3)	7.24E-10	3.69E-09	2.01E-08	1.30E-07	0.00E+00	0.00E+00
Total voids volume (m^3)	2.90E-09	2.95E-07	3.82E-07	1.30E-07	0.00E+00	0.00E+00
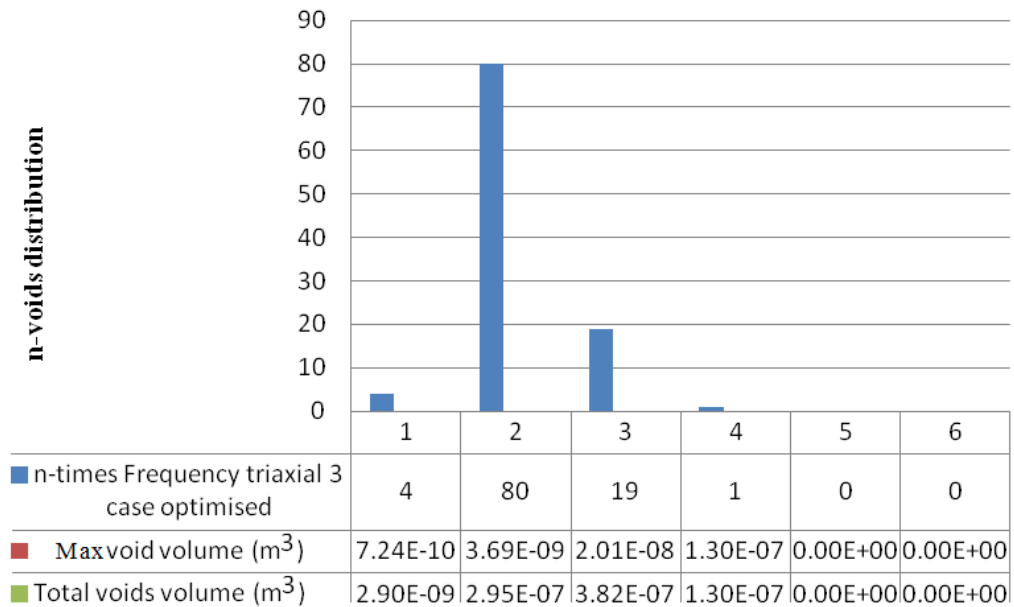
Fig. 8.22: Simulation for case 3 optimised triaxial fabric void distribution. Max void volume (m^3), total voids volume (m^3) at the indicated scale.

Table 8.4: Summary of triaxial node simulations with detected probability for void formation and case 3 optimization.

Node simulation case	n-time Frequency voids	Max void volume (m^3)	Total node voids volume (m^3)	
1	94	5.20E-06	6.37E-06	
2	122	4.91E-06	6.78E-06	
3	99	1.11E-05	1.35E-05	
3 opt	104	1.30E-07	8.10E-07	Optimised
4	107	2.05E-06	3.02E-06	
5	109	1.51E-07	9.56E-07	
6	108	5.21E-06	6.81E-06	
7	110	4.98E-06	5.98E-06	
8	104	5.11E-06	6.02E-06	
9	106	1.54E-07	9.32E-07	
10	91	1.68E-07	9.31E-07	

Simulations of the variability with the triaxial fabric shown in Appendix F, Figs F.18-F.26. The modelling results for the node showed the elimination of high volume voids on a design with a new vent at the shear web as shown in Fig. 8.20 (a), (b) the proposed mould modification.

8.5 Conclusion

The generic node variability was studied with a probabilistic distribution of the 3D woven HTS40 F13 fabric thickness along the edges with material properties from Chapter 3, 4 (tables 3.2, 4.7) and applied on each of the twenty three edges of the node. With the same 3D FE CAD generic node model the variability of 2/2 twill and triaxial glass preforms was studied in order to understand better the flow behaviour for the composite node with different local permeability behaviour.

- The node was modelled with 3D woven HTS40 F13 preform in order to investigate the variability and void formation and predict what may happen during the manufacturing process. It was found that after application of the injection gates and vents of Figure 8.7 (a) and (b) the total number of voids was reduced from 67 to 34 (case 1) and 64 to 32 (case 8), after the filling process (Table 8.2). Also the large volume defects were eliminated in both cases thus the total volume of defects after optimization decreased by two orders of magnitude from 10^{-5} m^3 to 10^{-7} m^3

- The node was also modelled in 3D to test the fluid behaviour of the advanced composite truss structure with different local permeability for the 2/2 twill and triaxial glass preform. The 2/2 twill was optimised by applying the same modifications as for the ACTS fabric i.e. Fig 8.7 (a) and (b), due to the similar flow front behaviour at the 23 edges, which exhibited a converging flow character. In this case, the total volume of defects was reduced by one order of magnitude from 10^{-5} to 10^{-6} m^3 (Table 8.3) and the larger defects were eliminated. However the total number of voids increased marginally from 120 to 126.

- Finally, for optimisation of the triaxial case a different modification was applied shown in Fig. 8.20 (a), (b). This was due to the different character of the flow front (with a lag in flow at the edges) giving rise to voids in different areas than the two previous studied fabrics. The total volume of voids was reduced again by two orders of magnitude

from 10^{-5} to 10^{-7} m^3 (as shown Table 8.4) for the optimised case. However the total number of voids increased slightly from 99 to 104.

The key findings to be carried forward can be summarised as follows:

- Generic node variability was studied with a probabilistic distribution on his twenty three 90° radii for three different fabrics.

- The different local permeability behaviour (i.e. V_f at 90° radii of the node) for each of the tested fabrics gave different void distribution.

- Worst case simulations were used to improve or optimise the manufacturing process.

- Defects after optimization decreased as reported in points i), ii), iii) of this section.

Because all simulations of the ACTS HTS40 F13 preform were based on the assumption of rich resin (race-track) edges, their experimental detection as shown in Chapter 9 Fig. 9.3 (b) can be taken as an indication that the generic node structure was optimised in terms of void defects with the above mentioned stochastic modelling optimization process.

References

[1]Pillai, K.M., Luce, T.L., Bruschke, M.V., Parnas, R.S., and Advani, S. G., "Modelling the Heterogeneities present in Preforms during Mold Filling in *RTM"*, 25th International SAMPLE Conference paper 26-28 October 1993; p 279-293.

[2]Li, J., Zhang, C., Liang, R., Wang, B., "Statistical characterization and *robust design of RTM processes",* Composites Part A **36**: (2005); p 564-580.

[3]Lawrence, J. M., Hsiao, K-T., Roderic, C. D., Simacek, P., Estrada, G., Sozer, E. M., Stadtfeld, H. C., Advani, S. G., "An approach to couple mold design and on-line control to manufacture complex parts by resin transfer *molding",* Composites: Part A **33**: (2002); p 981–990.

[4]Parnas, R. S., Flynn, K. M., and Dal Favero, M. E., *"A Permeability Database for Composites Manufacturing,"* Polymer Composites: Vol. **18**, No. 5: Oct. 1997; p 623-632.

[5] Berveiller M. "Elements Finis Stochastiques: approches intrusive et non intrusive pour des analyses de fiabilité", PhD Thesis, Université Blaise Pascal-Clermond Ferrand, 2005.

[6] Keese A. "A general purpose framework for stochastic finite elements", PhD Thesis, Technischen Universität Braunschweig, 2004.

[7] Isukapalli, S.S. "Uncertainty Analysis of Transport-Transformation Models", PhD Thesis, The State University of New Jersey, 1999.

 [8] Puig B., Poirion F. and Soize C. *"Non-*Gaussian simulation using Hermite *polynomial expansion: convergences"*. Prob. Eng. Mech., Vol. 17, 2002; pp. 253-264.

[9] Li C.C. and Der Kiureghian A. *"Optimal discretization of random fields"*. J. Eng. Mech., Vol. 119, No. 6, 1993; pp. 1136-1154.

[10] Zhang J. and Ellingwood B. *"Orthogonal series expansions of random fields in reliability analysis"*. J. Eng. Mech., ASCE, Vol. 120, No. 12, 1944; pp. 2660-2677.

[11]Endruweit, A., Harper, L.T., Turner, T.A., Warrior, N.A., Long, A.C., "Random discontinuous carbon fibre preform: Permeability modelling and *resin injection simulation",* Composites Part A 39: (2008); p 1660-1669.

Chapter 9

Node Manufacturing

9.1 Mould modification for generic node

By taking into account the modelling results of section 7.4.4 the node mould was modified with three extra vents on the opposite side of the HTS40 F13 3D woven preform. In order to evaluate the flow in the mould a number of pressure transducers were, also included to monitor the experimental filling pattern. All pressure transducers were perpendicular to the surface around the positions indicated in Fig. 9.1.

In particular:

1) Pressure Transducer B was perpendicular to the lower surface of section B at the position indicated in Fig. 9.1. Transducers B and D were at equal distances from the centre of the node.

2) Pressure Transducer G was perpendicular to the lower surface of the intersection on section G at the position indicated in Fig. 9.1.

3) Pressure Transducer D was perpendicular to the lower surface of section D.

The above positions allowed resin flow and any potential dry patch defects to be monitored during the manufacturing process.
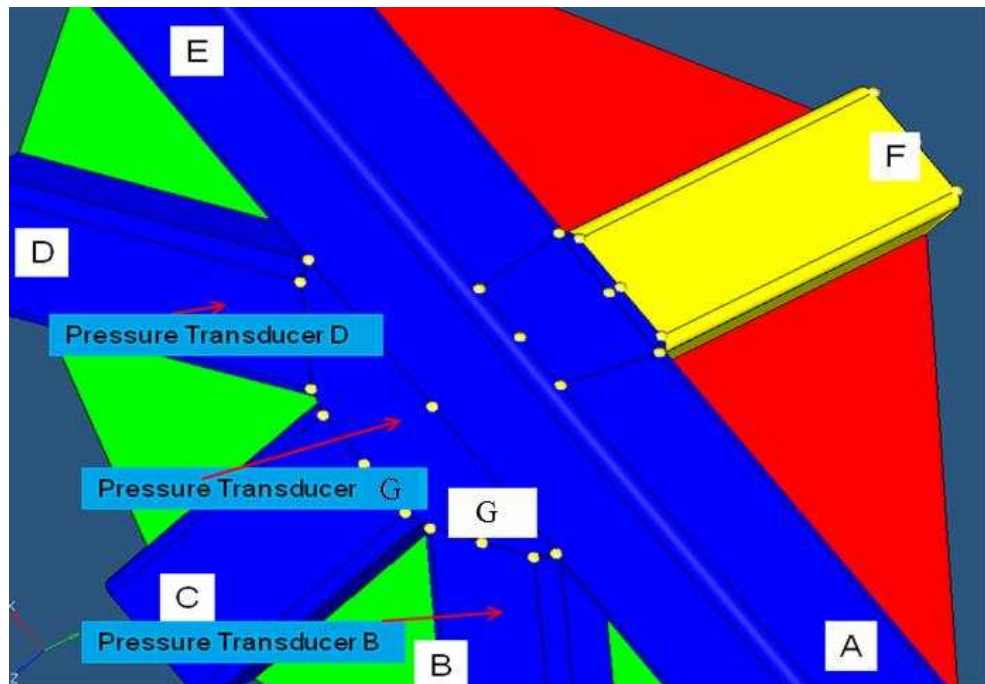
Fig. 9.1: Lower side of the node with the positions of the three pressure transducers D, G, B on area indicated with red arrows.
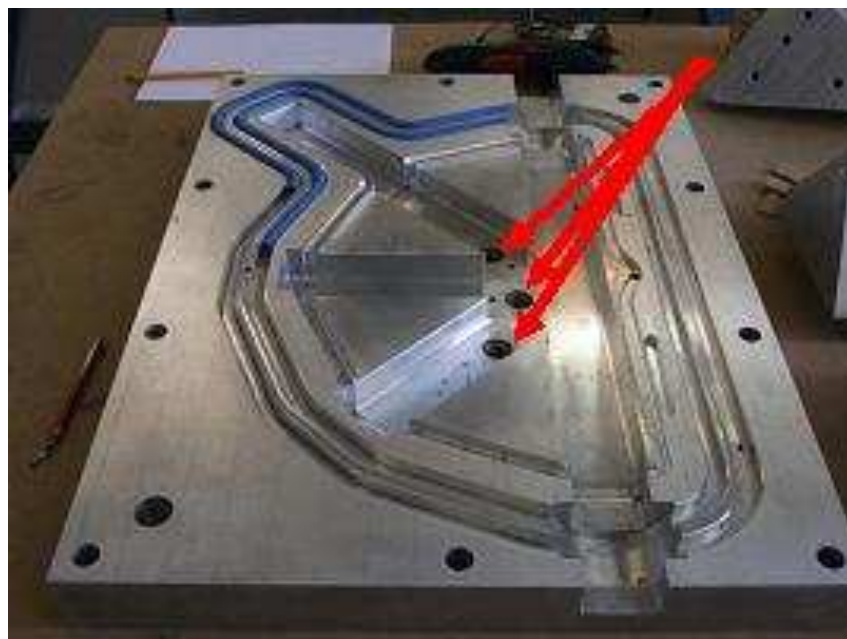
Fig. 9.2: 3 vents were placed on the base of the mould, see red arrows.

Taking into account the simulation results the three additional vents that have been included in the mould are shown in Fig. 9.2.

9.2 Manufacturing process of the ACTS node

Based on this research work overall a number of twenty prototype nodes were manufactured successfully (by Composites Integration Ltd), with the 3D woven HTS40 F13 preform and MVR444 resin. A prototype of the manufactured node is presented in Fig. 9.3 (a) and (b) as a sample. No void formation observed at the critical opposite site in any of the prototype manufactured nodes with RTM.

Futhermore it can be seen that the yellow zones (Fig. 9.3 (b)) at the corners of the node represent regions of higher concentration of resin which indicated resin rich zones on 90° bending angle of the textile.

This was one of the assumptions that the 3D variability modelling of the ACTS node was based upon as explained in following Chapter 8 section 8.3.

Thus although no direct non-destructive techniques for detecting and confirming the existence of voids in the main bulk of the final product was used, there is supportive evidence that the manufactured product of Figures 9.3 (a) and (b), should be optimized in terms of high volume defects.

Fig. 9.3 (a): Prototype manufactured node top surface view.
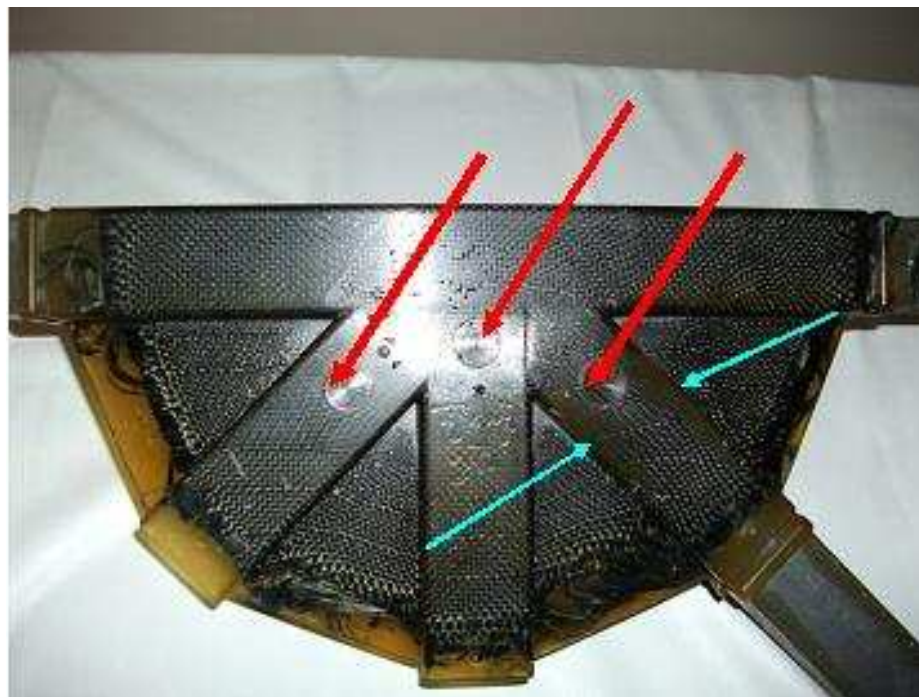
Fig. 9.3 (b): Prototype manufactured node with RTM. Other side view (red arrows show the 3 vents used).

9.3 Conclusion

On the manufacturing process, a series of twenty prototype generic nodes with 3D woven HTS40 F13 preform was manufactured incorporating three vents at the base (Fig.9.3 (a), (b)) as suggested by the computer based modelling optimisation. Although the bulk volume of the structure could not be probed for the detection of voids with NDT (Non Destructive Techniques) after the filling process with resin MVR444, no dry areas were observed and the edges (yellowish radii) showed clear signs of high resin concentrations (race-tracking) as shown by cyan arrows Fig. 9.3 (b) node member B zones (7, 8). Because all simulations of the ACTS preform were based on the assumption of rich resin edges, their experimental detection can be taken as an indication that the structure was optimised in terms of void defects.

Chapter 10

Conclusions and future work

10. Introduction

The objective of this chapter is to summarise all work presented previously in Chapters 1-9 of this thesis and propose the future direction of research.

All major conclusions drawn from this thesis are related to the research objectives presented in Chapter 1. Chapter 10 describes the motivation and details how this research study adds to the field of work, and explores what future work could be continued in order to complement the previous research on race-tracking and variability modelling.

10.1 Discussion

This research dealing with race-tracking and the variability modelling during the manufacturing process of RTM. Chapter 3 measured the compressibility and thickness variation of three different textiles as shown. Chapter 4 presented an empirical model able to calculate the in plane and through thickness permeability. New simulation tools were validated and applied to manufacturing process, modelling the flow behaviour of the resin as the node is manufactured. In particular the racetracking and the influence of the reinforcement structure and component geometry on the resin flow was analysed, developing fundamental understanding and a model in Chapter 5 that can predict the occurrence of phenomena such as "void formation" due to converging flows. This has involved stochastic modelling and the use of

commercial simulation tools such as PAM-RTM® (ESI group). From the other side experimental results in Chapter 6 showed that the racetrack behaviour on a 3D curved plate bend preform may be successfully modelled for each tested fabric.

Finally the node was modelled with a 3D woven HTS40 F13 preform in order to investigate the variability and void formation and predict what may happen during the manufacturing process.

The large volume defects were eliminated by addition and recombination of injection gates and vents on the generic node geometry. The optimization process was also preformed for the 2/2 twill and triaxial fabric.

On the experimental side, twenty prototypes of the generic node with 3D woven HTS40 F13 preform was manufactured incorporating three vents at the (opposite side) base as suggested by the modelling optimisation study.

10.2 Conclusions

In summary on Chapter 3 of this thesis quantified the compressibility of the tested fabrics. The determination of the height, H (mm), of the preforms against pressure, P (bar) was made possible with an empirically derived power law. With CMM contact technique the fabric thickness variation on a 90° bending angle for three different preforms was measured. Tables with measured preform thickness on the 90° bend from the samples of the tested preforms were presented.

On Chapter 4 in unsaturated radial flow the in-plane permeabilities (K_1, K_2) and flow orientation (θ) were measured and fitted with a power law curve. In saturated unidirectional flow at constant flow rate the through-thickness permeability K_3 was determined and fitted with a power law curve. This way it was possible to predict (K_1, K_2, K_3) at any volume fraction for modelling simulations.

Chapter 5 derived a model that may be used for FE modelling against the formation of resin rich zones along a 90° angle during infusion in RTM. The model predictions fitted well with experimental CMM contact technique data for samples of three tested fabrics.

Chapter 6 Race-track flow first modelled in 2D and then in 3D. Experimental results derived with the use of a transparent rig fitted with reasonable accuracy to 3D modelling.

Similar fluid behaviour of 3D FE modelling with transparent tool experiments verified that there is compaction along a 90° curved plate due to fabric bending. These Vf variations generates a gap between the preform and mould wall.

The height h (mm) of the gap between the reinforcement and mould may be simulated and thereafter matched with the equivalent experiments.

On Chapter 7 the use of 3D anisotropic modelling predicted the fluid flow of a complex geometry in a more realistic way than 2D, 3D isotropic cases. 3D anisotropic case modelling with complex geometries may predict converging flow and so void formation during liquid infusion on component scale. This

allowed the modification with three extra vents of node mould in order to avoid macro-scale void formation with HTS40 F13 preform.

On Chapter 8 the generic node variability was studied with a probabilistic distribution on his twenty three 90° radii for three different fabrics. The different local permeability behaviour (i.e. V_f at 90° radii of the node) for each of the tested fabrics gave different void distribution. Worst case simulations were used to improve or optimise the manufacturing process. Defects after optimization process decreased in volume.

Although the study of the node was done with 3D tetrahedral elements the through thickness flow (gates and vents) proposed for the manufacturing RTM process is equivalent to 2D flow.

3D flow behaviour study as presented on chapter 6 on this thesis (i.e. complete 3D modelling at a 90° curved plate by taking on to account the fabric's compressibility along the 90° radii for 3D study of race-tracking) required a higher mesh density. A much higher number of elements is therefore required in order to include all the twenty-three 90° curved plates fabric's compressibility of the node truss structure.

 These mesh sizes (tens of millions of tetrahedral elements) posed a serious restriction for the complete 3D modelling of the ACTS node. Due to fact that exceeded the actual practical capability of the software and hardware instalation.

Therefore it would be worthwhile if future 3D modelling research work on composites truss manufacturing with RTM will take in to account the present

developments in race-tracking and void formation and provide a complete study of the whole component where there are no software mesh limitations.

10.2.1 Major conclusions

- Experimental results showed that the racetrack behaviour on a 3D 90° curved plate bend preform may be successfully modelled and predict fluid flow behaviour for each fabric.

- Stochastic modelling simulation may be used for void optimization of any composite structure in RTM process.

10.3 Considerations for future work

While a significant amount of work was accomplished and a series of conclusions set forth in section 10.2, 10.2.1 of this study were reached there are still some areas that would benefit from additional study. These areas include:

- Evaluation of the existing bending model. Although the existing model of chapter 5 has been tested with three different fabrics (2/2 twill, 3D woven, triaxial), and two materials (carbon, glass fibres) on aluminium and Perspex 90° curved plate rigs, new experimental evaluation with different geometry textiles will be useful. This is due to the fact that the model does not account for inter-yarn racetracking (warp, weft directions) but only the preform compaction along the bending angle.

- Modelling macro-scale variability with flow simulations for other sharp shape edges geometries in order to predict manufacturing defects with

different 3D FE CAD would be beneficial to demonstrate the model

applicability of this work to generic composite structures.

Appendix A : Publications and achivements

i) Publications:

[1]. ENDRUWEIT, A., GOMMER, F., HUTCHINSON, J., KOUTSONAS, S., LONG, A.C., SCHUBEL, P., XIAO, X. and ZENG, X., 2012. *"Resin flow* simulation based on advanced reinforcement geometry modelling from yarn-scale to component-*scale"* In: 11th International Conference on Flow Processes in Composite Materials. Auckland N. Zealand.

ii) Achievements:

This award was given for the manufacture of the 3D preform by Sigmatex, which studied in part on the analysis presented in this thesis as part of ACTS (Advanced Composites Truss Structures) project.

Appendix B: CMM measured fabric thickness on 90° bend

All CMM experimental results with the 3 tested fabrics are presented as shown in Tables B(a)-B(e).

Table B (a): Measured h_{min} thickness of 3D woven for HTS40 F13 fabric in warp direction.

Sample Num.	h_{min} fabric thickness on bend(mm)
Sample 1	2
Sample 2	2.2
Sample 3	2.2
Sample 4	2.1
Sample 5	2.2
Sample 6	2.1
Sample 7	2.1

Table B (b): Measured h_{min} thickness of 3D woven for HTS40 F13 fabric in weft direction.

Sample Num.	h_{min} fabric thickness on bend(mm)
Sample 1	2.3
Sample 2	2.4
Sample 3	2
Sample 4	2.6
Sample 5	2.2
Sample 6	2.3

Table B (c): Measured h_{min} thickness for 2/2 twill fabric.

Sample Num.	h_{min} fabric thickness on bend(mm)
Sample 1	1.7
Sample 2	1.8
Sample 3	1.6
Sample 4	1.7
Sample 5	1.7
Sample 6	1.7
Sample 7	1.7

Table B (d): Measured h_{min} thickness for triaxial fabric in warp direction.

Sample Num.	h_{min} fabric thickness on bend(mm)
Sample 1	2.2
Sample 2	2.6
Sample 3	2.3
Sample 4	2.1
Sample 5	2
Sample 6	2.2

Table B (e): Measured h_{min} thickness for triaxial fabric in weft direction.

Sample Num.	h_{min} fabric thickness on bend(mm)
Sample 1	2.3
Sample 2	2.2
Sample 3	2.2
Sample 4	2.5
Sample 5	2.1

Spiridon Koutsonas

Appendix C: Perspex tool experiments and shape analysis tables

In Appendix C the Perspex experiments from Chapter 6 are presented. Flow front propagation for each experiment on upper side and lower side of the Perspex is presented.
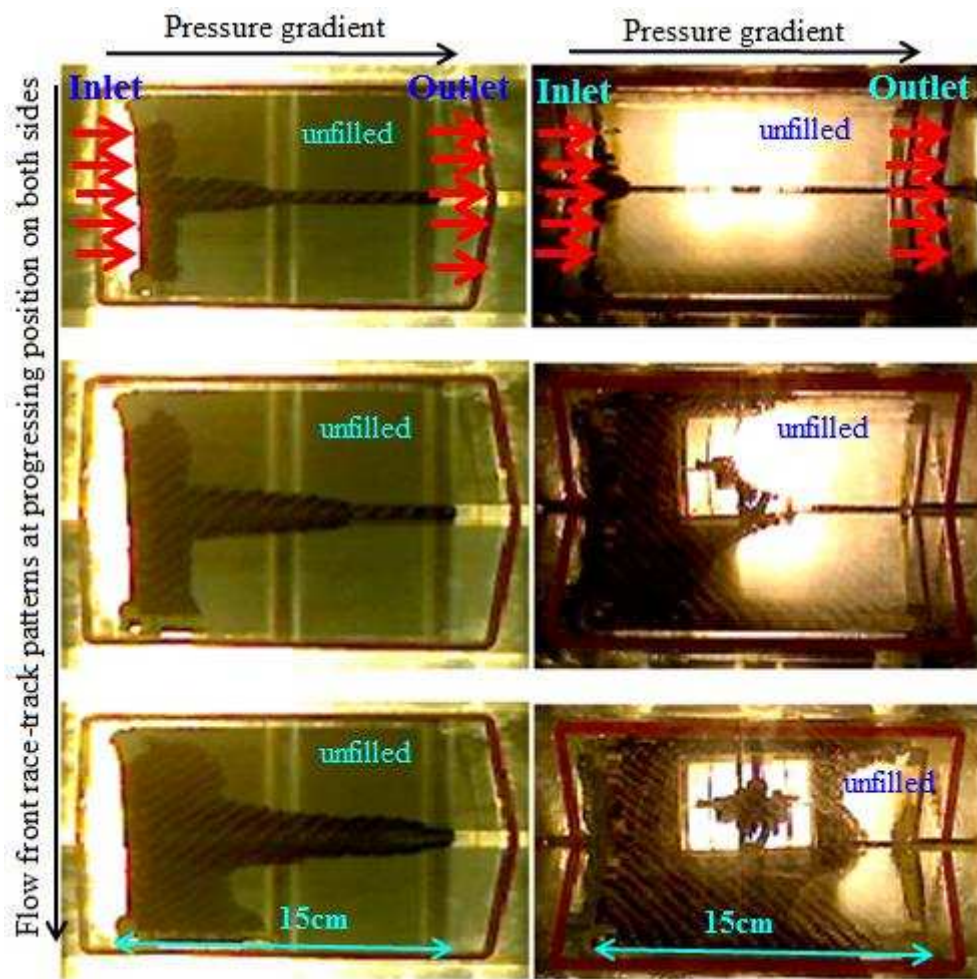
i) Upper side left (images)   **ii) Lower side right (images)**

Fig. C.1: Experiment 1, 2/2 twill racetrack evaluation of flow front on both sides with Perspex transparent tool (2rd line images shown on Fig. 6.10, shape analysis shown on section 6.4.1.3).
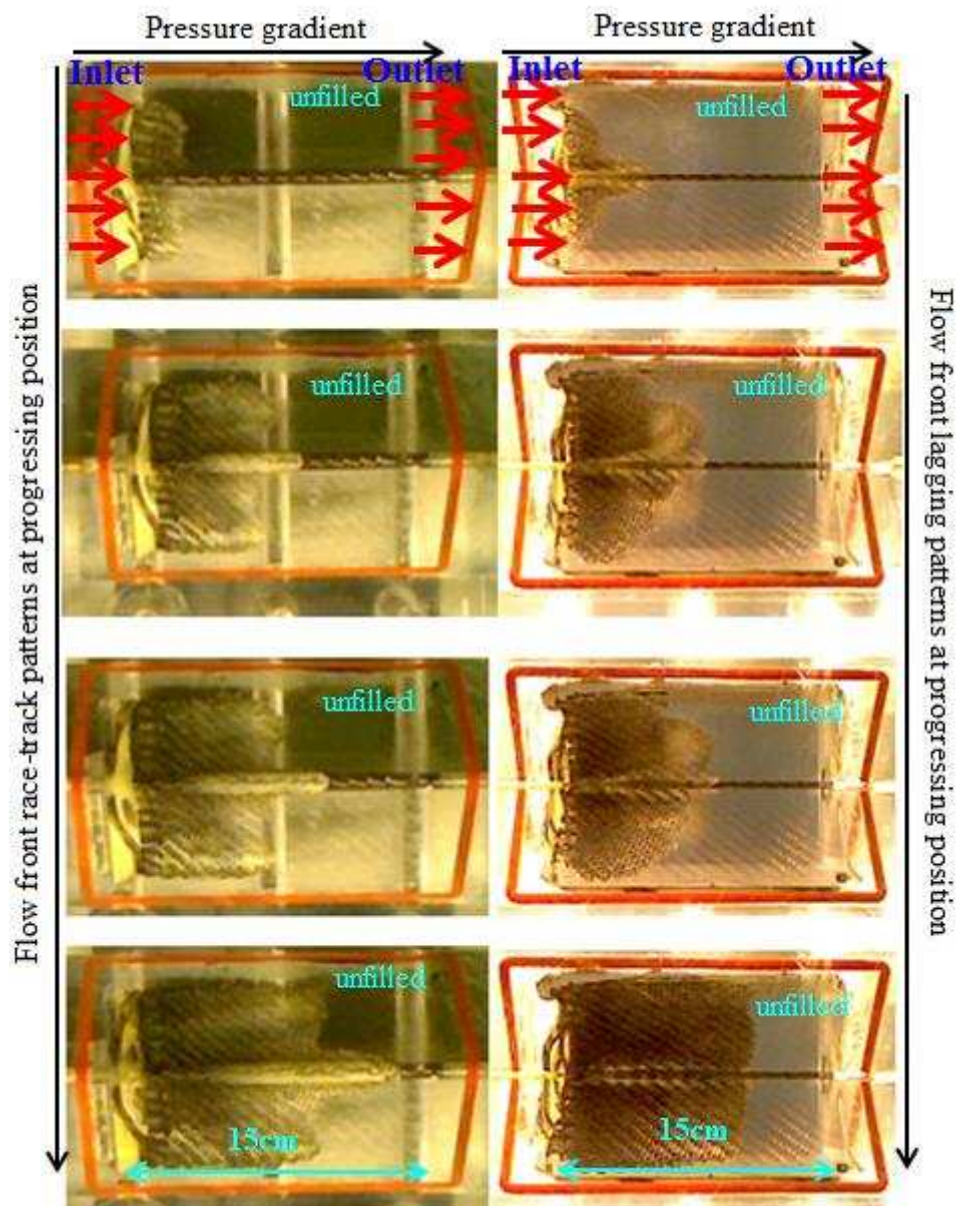
i) Upper side left (images)   **ii) Lower side right (images)**

Fig. C.2: Experiment 2, 2/2 twill racetrack evaluation (left)/lag evaluation (right) images with Perspex transparent tool (2rd line images shown on Fig. 6.11, shape analysis shown on section 6.4.1.5).
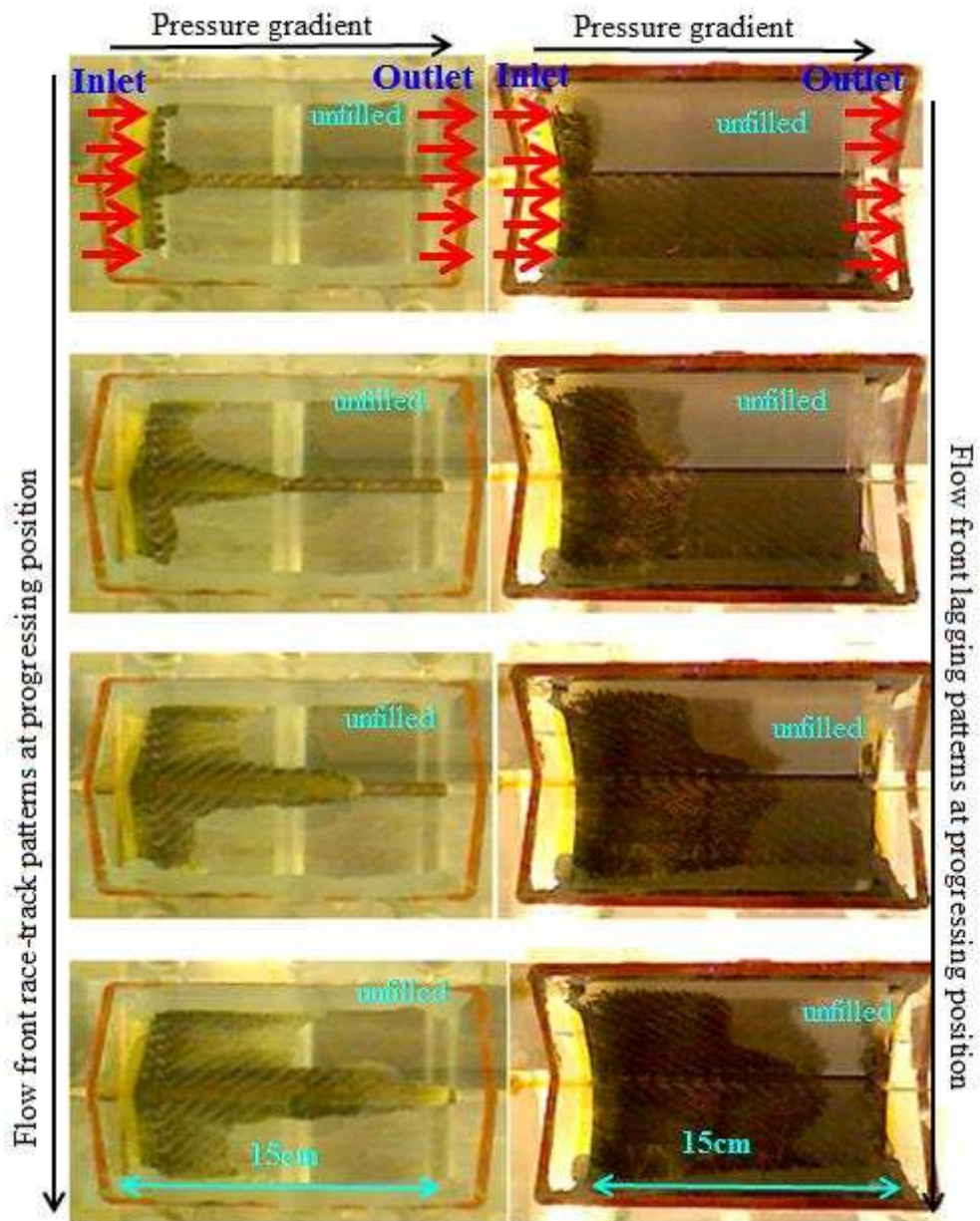
i) **Upper side left (images)**   ii) **Lower side right (images)**

Fig. C.3: Experiment 3, 2/2 twill racetrack evaluation (left)/lag evaluation (right) images with Perspex transparent tool.

Table C.1: 2/2 twill racetrack flow shape analysis Perspex exp. i) upper side ii) lower side from Fig. C.3.

i) 2/2 twill Perspex exp. shape analysis upper side:

y fill position 90° centre (cm)	y fill position upper (cm)	y fill position lower (cm)	Δy race-track (fill 90° centre (-) fill average upper/lower) (cm)
5	2.43	1.94	2.82
10	5.43	4.01	5.28
15	8.95	6.16	7.45

ii) 2/2 twill Perspex exp. shape analysis lower side:

y fill position 90° centre (cm)	y fill position upper (cm)	y fill position lower (cm)	Δy lag (fill 90° centre (-) fill average upper/lower) (cm)
5	5.98	6.19	-0.63
9.51	10.21	10.07	-0.64
13.45	14.93	15	-1.52

i) **Upper side left (images)**   ii) **Lower side right (images)**

Fig. C.4: Experiment 4, 2/2 twill racetrack evaluation (left)/lag evaluation (right) images with Perspex transparent tool.

Table C.2: 2/2 twill racetrack flow shape analysis Perspex exp. i) upper side ii) lower side from Fig. C.4.

i) 2/2 twill Perspex exp. shape analysis upper side:

y fill position 90° centre (cm)	y fill position upper (cm)	y fill position lower (cm)	Δy race-track (fill 90° centre (-) fill average upper/lower) (cm)
5	3.16	3.66	1.59
10	5.29	6.19	4.26
15	8.47	9.24	6.15

ii) 2/2 twill Perspex exp. shape analysis lower side:

y fill position 90° centre (cm)	y fill position upper (cm)	y fill position lower (cm)	Δy lag (fill 90° centre (-) fill average upper/lower) (cm)
3.93	4.96	5.02	-1.06
8.8	10	9.93	-1.17
13.41	14.85	15	-1.52

i) Upper side left (images)   ii) Lower side right (images)

Fig. C.5: Experiment 5, 2/2 twill racetrack evaluation (left)/lag evaluation (right) images with Perspex transparent tool.

Table C.3: 2/2 twill racetrack flow shape analysis Perspex exp. i) upper side ii) lower side from Fig. C.5.

i) 2/2 twill Perspex exp. shape analysis upper side:

y fill position 90° centre (cm)	y fill position upper (cm)	y fill position lower (cm)	Δy race-track (fill 90° centre (-) fill average upper/lower) (cm)
5	2.33	2.47	2.6
10	5.2	4.15	5.33
15	9.16	6.71	7.07

ii) 2/2 twill Perspex exp. shape analysis lower side:

y fill position 90° centre (cm)	y fill position upper (cm)	y fill position lower (cm)	Δy lag (fill 90° centre (-) fill average upper/lower) (cm)
4.58	5.07	5	-0.46
8.35	10	9.93	-1.62
13.73	14.35	15	-0.95

i) Upper side left (images)   ii) Lower side right (images)

Fig. C.6: Experiment 6, 2/2 twill racetrack evaluation (left)/lag evaluation (right) images with Perspex transparent tool.

Table C.4: 2/2 twill racetrack flow shape analysis Perspex exp. i) upper side ii) lower side from Fig. C.6.

i) 2/2 twill Perspex exp. shape analysis upper side:

y fill position 90° centre (cm)	y fill position upper (cm)	y fill position lower (cm)	Δy race-track (fill 90° centre (-) fill average upper/lower) (cm)
5	2.92	2.91	2.09
10	7.55	7.7	2.38
15	11.86	12.07	3.04

ii) 2/2 twill Perspex exp. shape analysis lower side:

y fill position 90° centre (cm)	y fill position upper (cm)	y fill position lower (cm)	Δy lag (fill 90° centre (-) fill average upper/lower) (cm)
5	5.41	5.41	-0.41
10	10.31	10.36	-0.34
13.67	14.39	14.59	-0.82

i) Upper side left (images)   **ii) Lower side right (images)**

Fig. C.7: Experiment 1, 3D woven HTS40 F13 warp racetrack evaluation (left)/lag evaluation (right) images with Perspex transparent tool (2rd line images shown on Fig. 6.13, shape analysis shown on section 6.4.2.3).
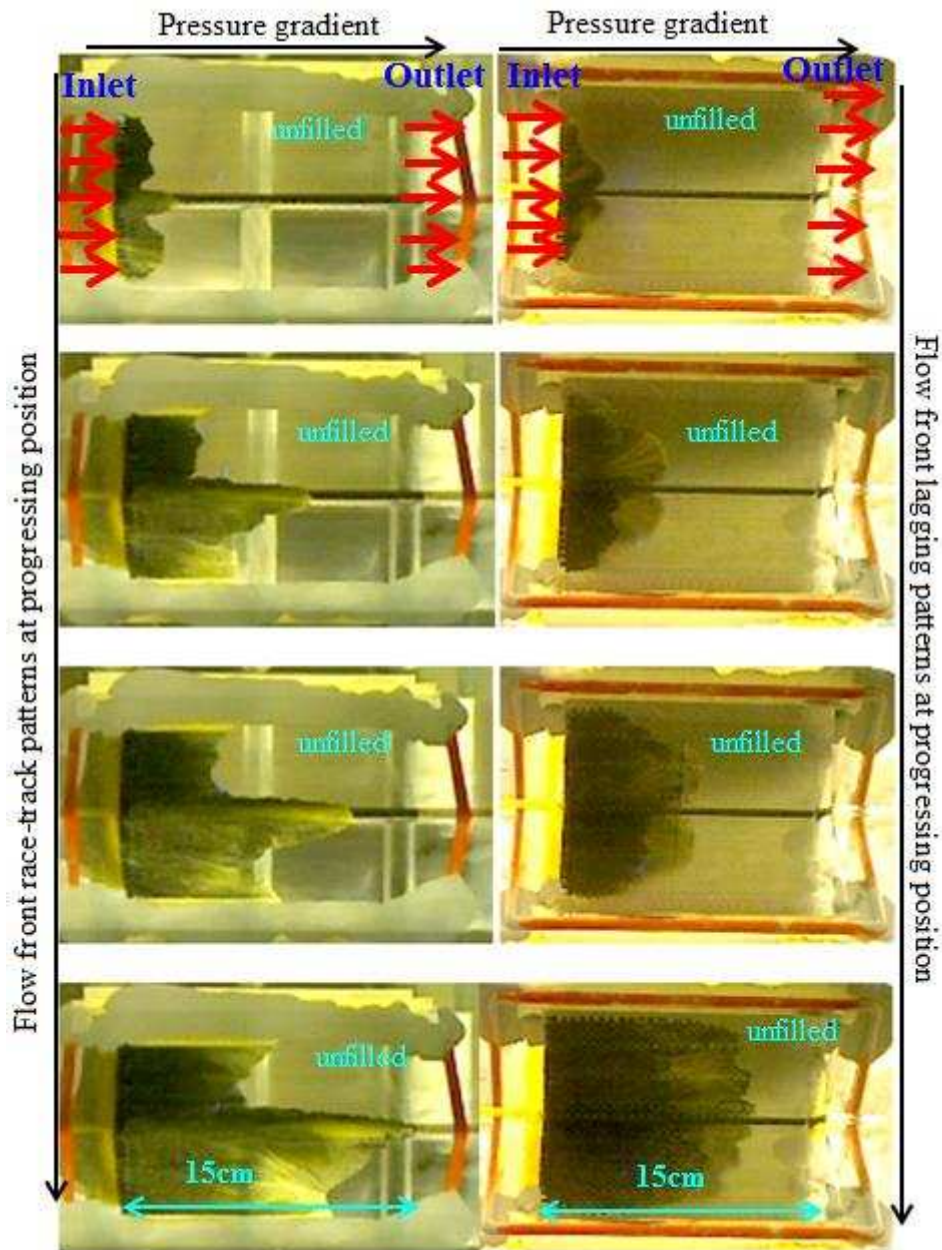
i) Upper side left (images)   **ii) Lower side right (images)**

Fig. C.8: Experiment 2, 3D woven HTS40 F13 weft racetrack evaluation (left)/lag evaluation (right) images with Perspex transparent tool (2rd line images shown on Fig. 6.15, shape analysis shown on section 6.4.2.6).
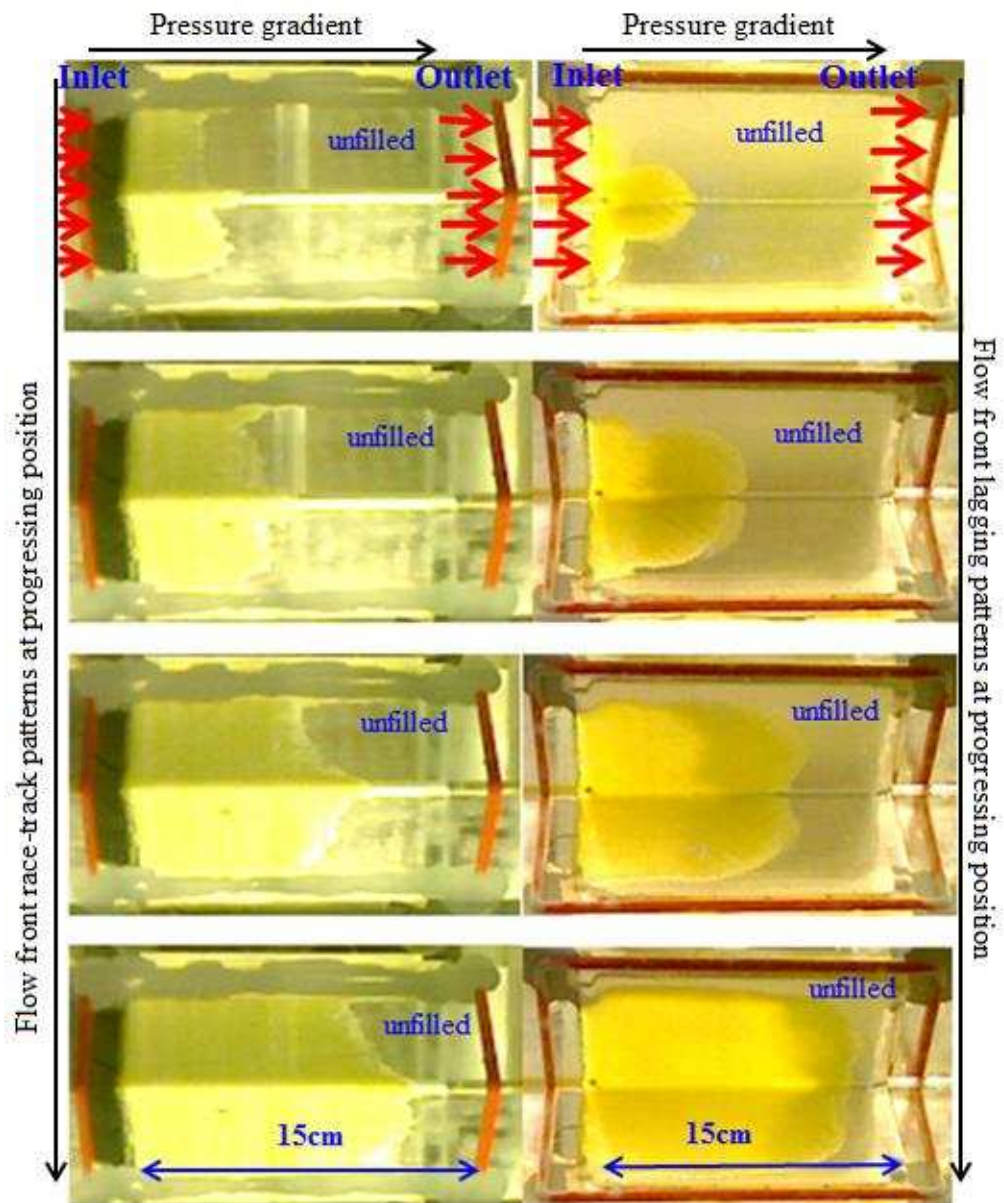
i) Upper side left (images) **ii) Lower side right (images)**

Fig. C.9: Experiment 1, triaxial warp racetrack evaluation (left)/lag evaluation (right) with Perspex transparent tool (3rd line images shown on Fig. 6.17, shape analysis shown on section 6.4.3.3).
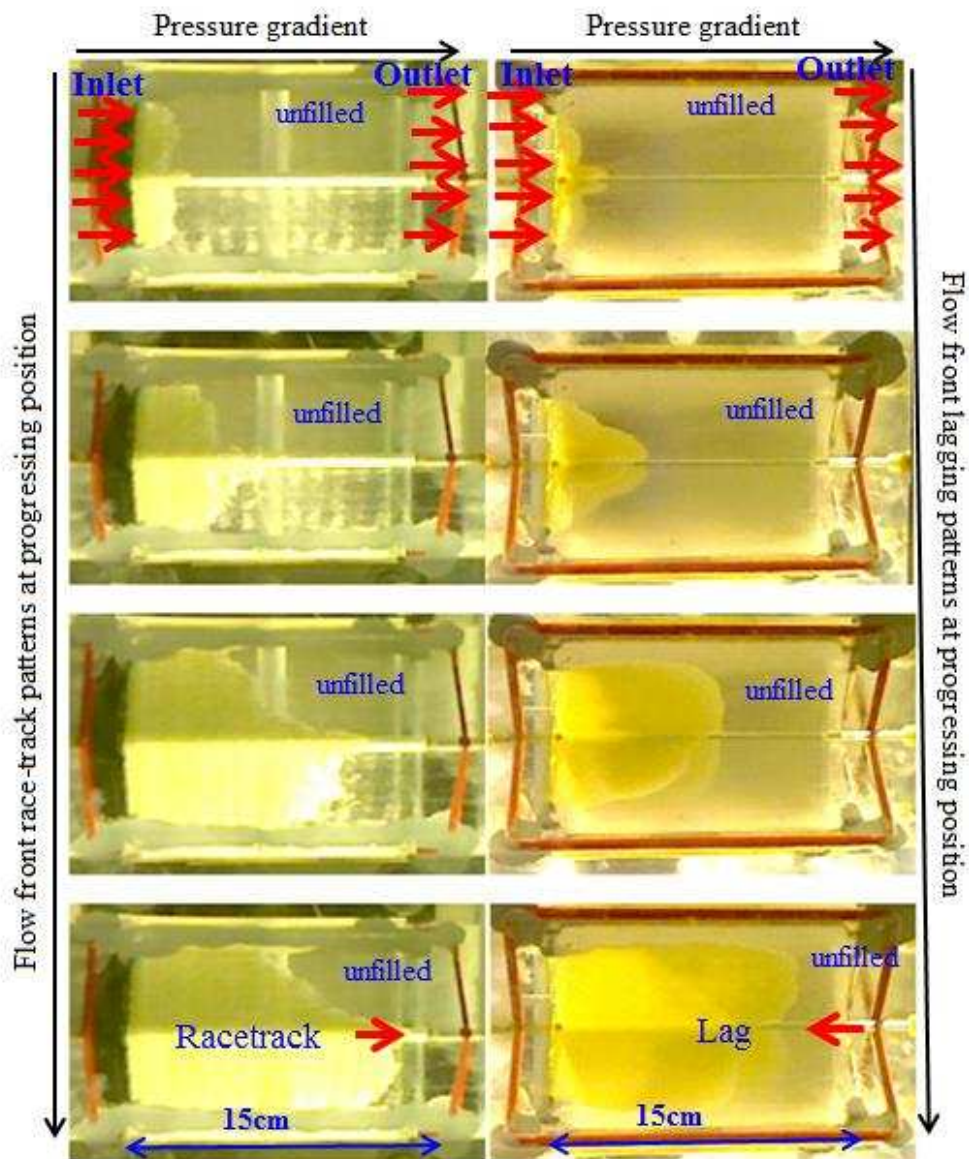
i) **Upper side left (images)**   ii) **Lower side right (images)**

Fig. C.10: Experiment 2, triaxial warp racetrack evaluation (left)/lag evaluation (right) with Perspex transparent tool.

Table C.5: 2/2 twill racetrack flow shape analysis Perspex exp. i) upper side ii) lower side from Fig. C.10.

i) 2/2 twill Perspex exp. shape analysis upper side:

y fill position 90° centre (cm)	y fill position upper (cm)	y fill position lower (cm)	Δy race-track (fill 90° centre (-) fill average upper/lower) (cm)
5	3.35	3.56	1.55
10	5.66	7.53	3.41
15	9.61	12.99	3.70

ii) 2/2 twill Perspex exp. shape analysis lower side:

y fill position 90° centre (cm)	y fill position upper (cm)	y fill position lower (cm)	Δy lag (fill 90° centre (-) fill average upper/lower) (cm)
5	5.86	5.86	-0.86
10	11.03	10.81	-0.92
13.18	14.49	14.34	-1.24
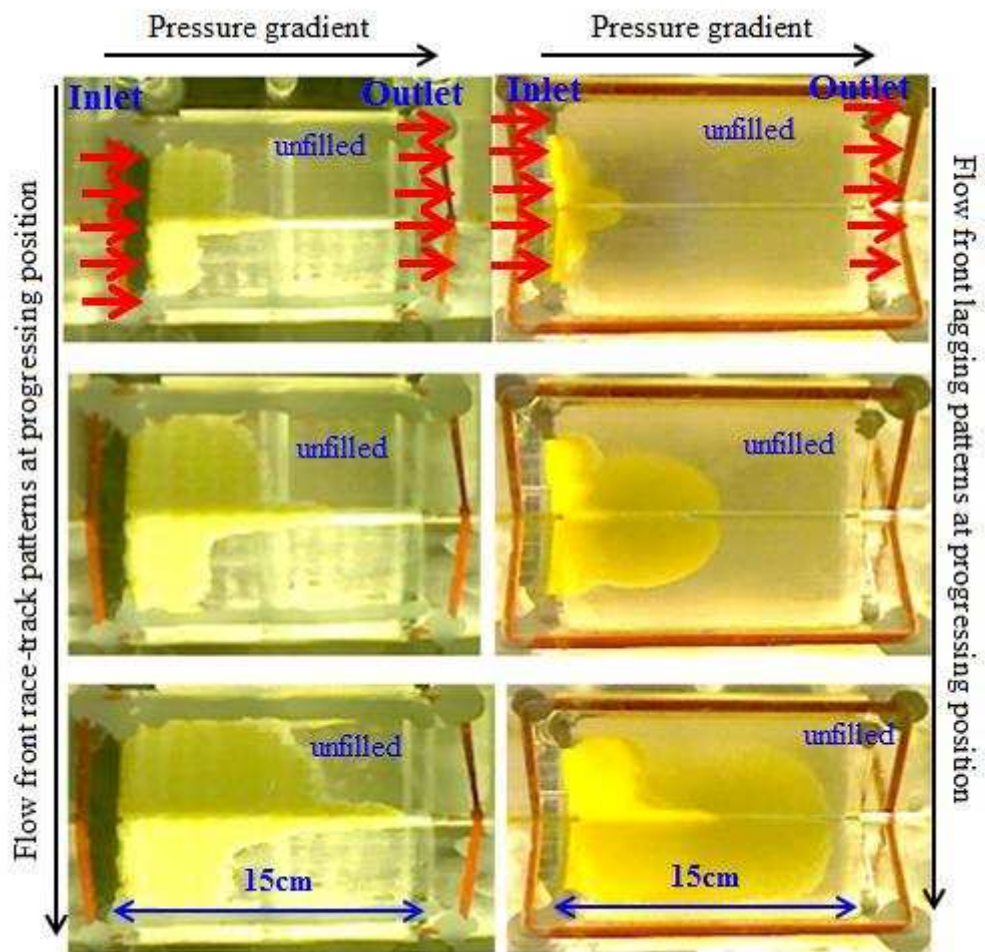
i) Upper side left (images)   **ii) Lower side right (images)**

Fig. C.11: Experiment 3, triaxial warp racetrack evaluation (left)/lag evaluation (right) with Perspex transparent tool.

Table C.6: 2/2 twill racetrack flow shape analysis Perspex exp. i) upper side ii) lower side from Fig. C.11.

i)   2/2 twill Perspex exp. shape analysis upper side:

y fill position 90° centre (cm)	y fill position upper (cm)	y fill position lower (cm)	Δy race-track (fill 90° centre (-) fill average upper/lower) (cm)
5	3.42	2.33	2.13
10	6.52	4.13	4.68
15	10.15	7.41	6.22

ii) 2/2 twill Perspex exp. shape analysis lower side:

y fill position 90° centre (cm)	y fill position upper (cm)	y fill position lower (cm)	Δy lag (fill 90° centre (-) fill average upper/lower) (cm)
4.23	5	5	-0.77
8.79	9.85	10.11	-1.19
13.46	14.44	14.58	-1.05
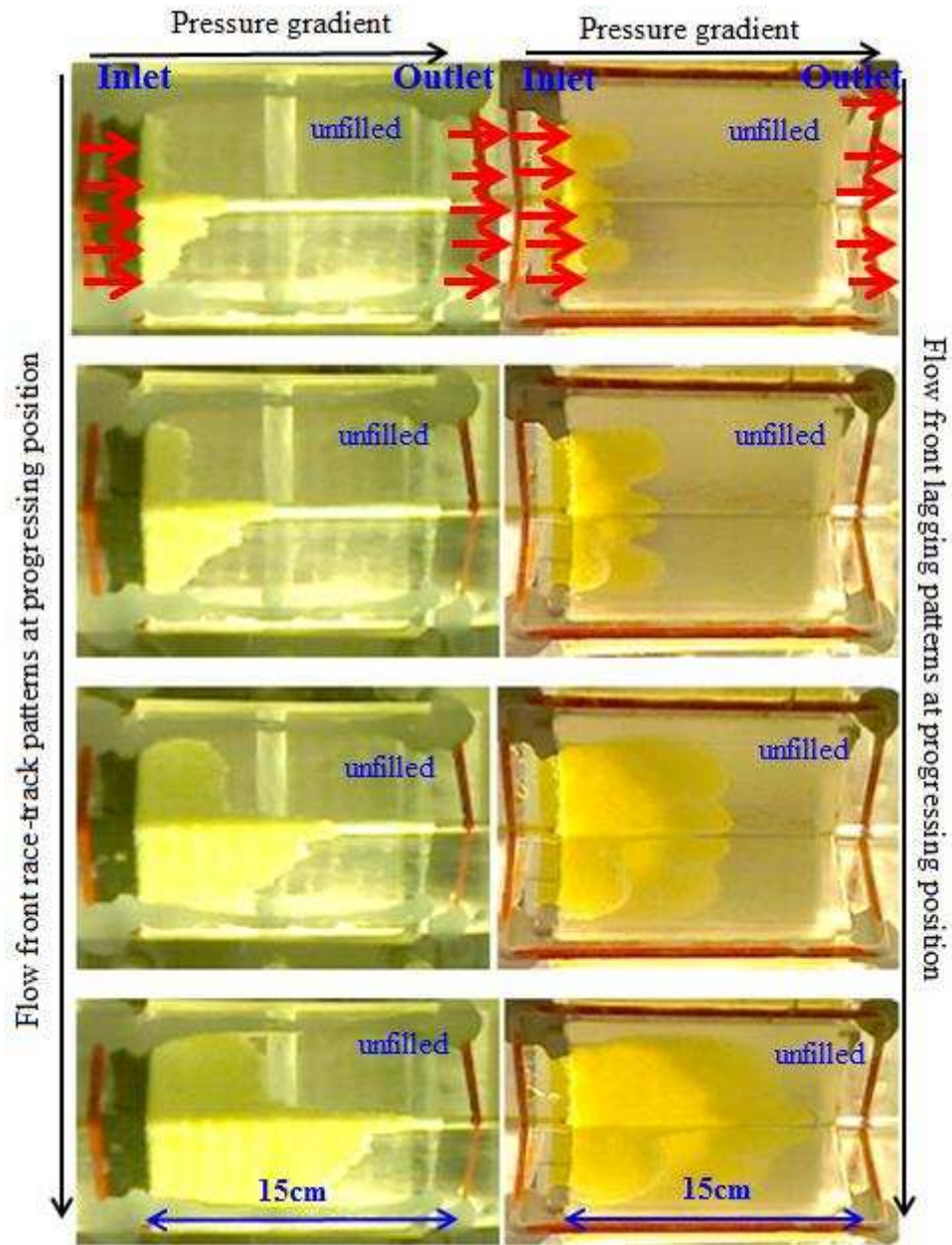
i) Upper side left (images)   ii) Lower side right (images)

Fig C.12: Experiment 4, triaxial warp racetrack evaluation (left)/lag evaluation (right)with Perspex transparent tool.

Table C.7: 2/2 twill racetrack flow shape analysis Perspex exp. i) upper side ii) lower side from Fig. C.12.

i) 2/2 twill Perspex exp. shape analysis upper side:

y fill position 90° centre (cm)	y fill position upper (cm)	y fill position lower (cm)	Δy race-track (fill 90° centre (-) fill average upper/lower) (cm)
5	1.75	2.5	2.88
10	4.61	7.07	4.16
15	6.83	11.44	5.87

ii) 2/2 twill Perspex exp. shape analysis lower side:

y fill position 90° centre (cm)	y fill position upper (cm)	y fill position lower (cm)	Δy lag (fill 90° centre (-) fill average upper/lower) (cm)
3.75	5.05	4.9	-1.23
9.06	10.19	10.05	-1.63
13.41	14.93	14.87	-1.49
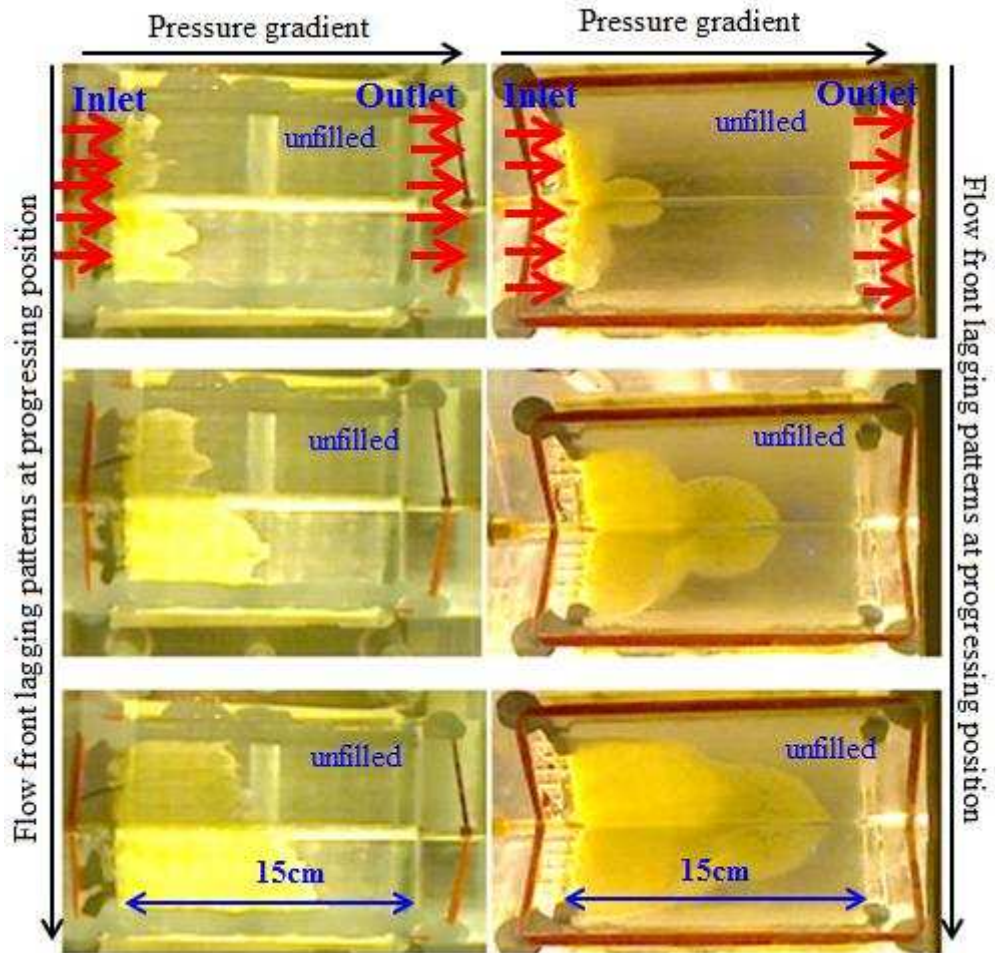
i) Upper side left (images)   **ii) Lower side right (images)**

Fig. C.13: Experiment 5, triaxial warp lag evaluation (left)/lag evaluation (right) with Perspex transparent tool (1st line images shown on Fig. 6.20).

Table C.8: 2/2 twill racetrack flow shape analysis Perspex exp. i) upper side ii) lower side from Fig. C.13.

i) 2/2 twill Perspex exp. shape analysis upper side:

y fill position 90° centre (cm)	y fill position upper (cm)	y fill position lower (cm)	Δy race-track (fill 90° centre (-) fill average upper/lower) (cm)
5	2.15	3.93	1.96
10	6.69	10.93	1.19
15	9.56	13.15	3.65

ii) 2/2 twill Perspex exp. shape analysis lower side:

y fill position 90° centre (cm)	y fill position upper (cm)	y fill position lower (cm)	Δy lag (fill 90° centre (-) fill average upper/lower) (cm)
4.2	5.39	5.47	-1.23
8.94	9.83	9.94	-0.95
13.34	14.7	14.25	-1.14
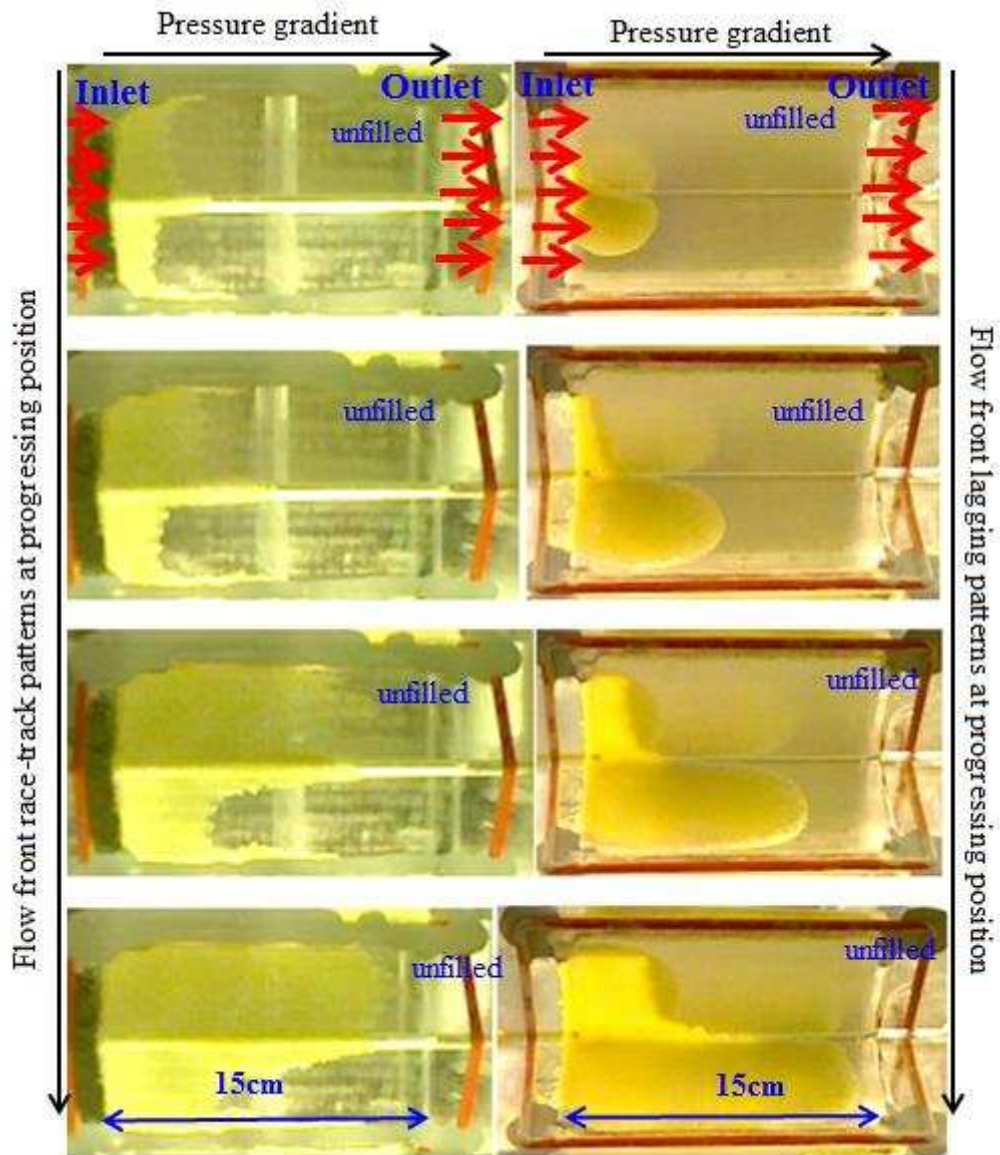
i) **Upper side left (images)**　　　　ii) **Lower side right (images)**

Fig. C.14: Experiment 1, triaxial weft racetrack evaluation (left)/lag evaluation (right) with Perspex transparent tool (2rd line images shown on Fig. 6.19, shape analysis shown on section 6.4.3.7).
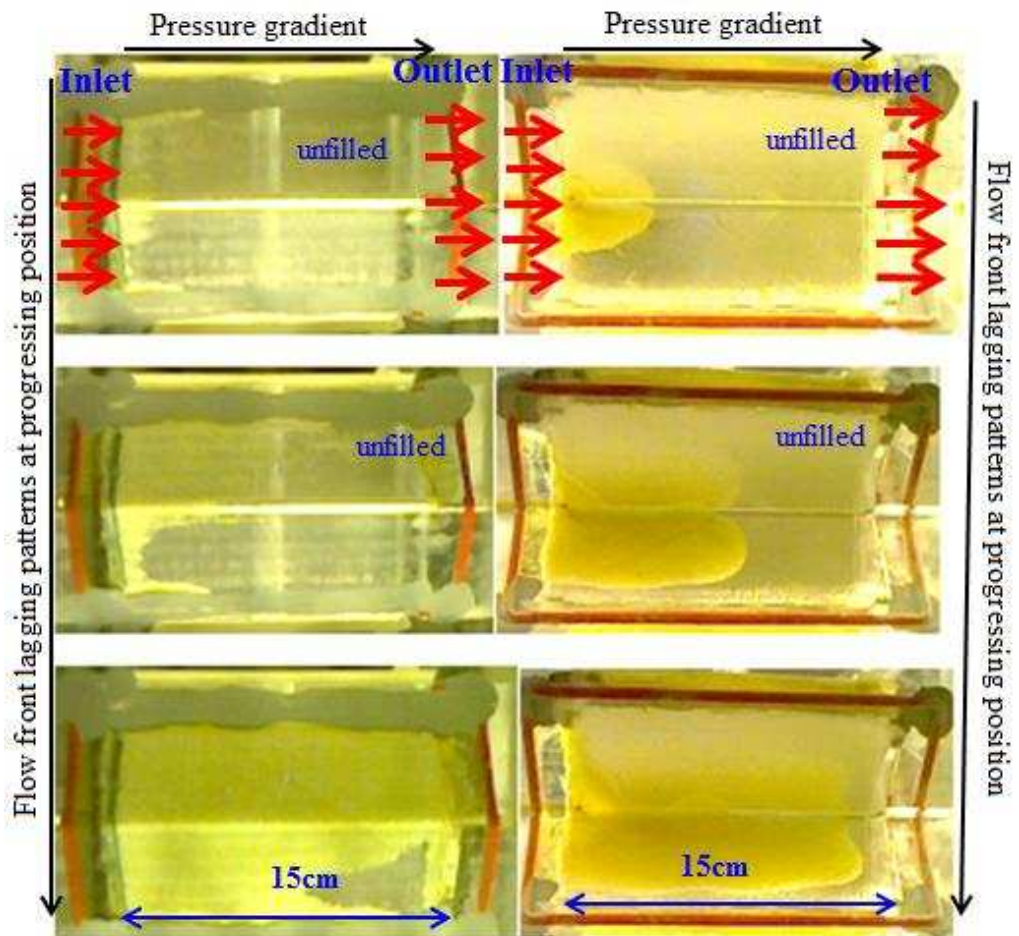
i) Upper side left (images)   ii) Lower side right (images)

Fig. C.15: Experiment 2, triaxial weft racetrack evaluation (left)/lag evaluation (right) with Perspex transparent tool.

Table C.9: 2/2 twill racetrack flow shape analysis Perspex exp. i) upper side ii) lower side from Fig. C.15.

i) 2/2 twill Perspex exp. shape analysis upper side:

y fill position 90° centre (cm)	y fill position upper (cm)	y fill position lower (cm)	Δy race-track (fill 90° centre (-) fill average upper/lower) (cm)
5	5.69	1.47	1.42
8	8.15	2.65	2.6
13.45	13.12	4.62	4.58

ii) 2/2 twill Perspex exp. shape analysis lower side:

y fill position 90° centre (cm)	y fill position upper (cm)	y fill position lower (cm)	Δy lag (fill 90° centre (-) fill average upper/lower) (cm)
3.97	4.91	5.04	-1.01
7.63	9.28	9.67	-1.85
13.56	14.38	14.52	-0.89
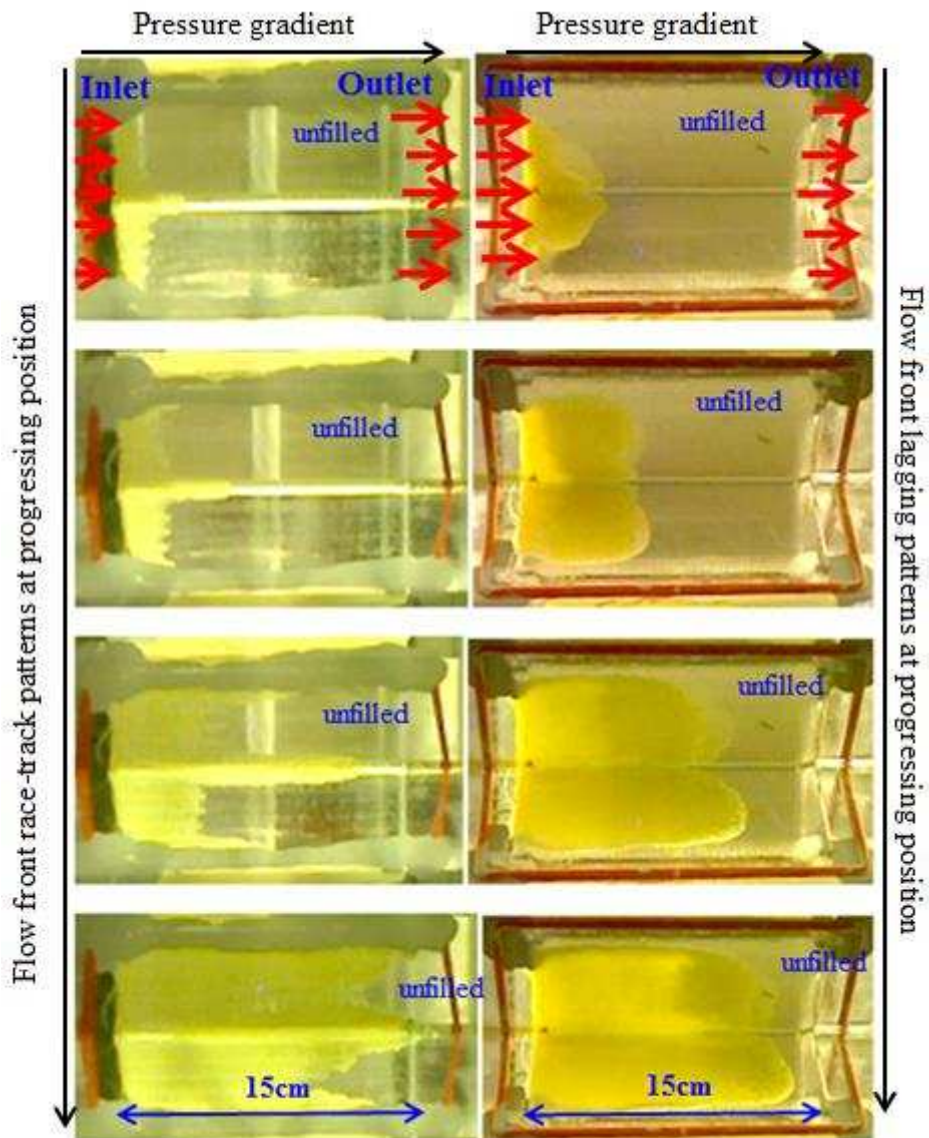
i) Upper side left (images)   **ii) Lower side right (images)**

Fig. C.16: Experiment 3, triaxial weft racetrack evaluation (left)/lag evaluation (right) with Perspex transparent tool.
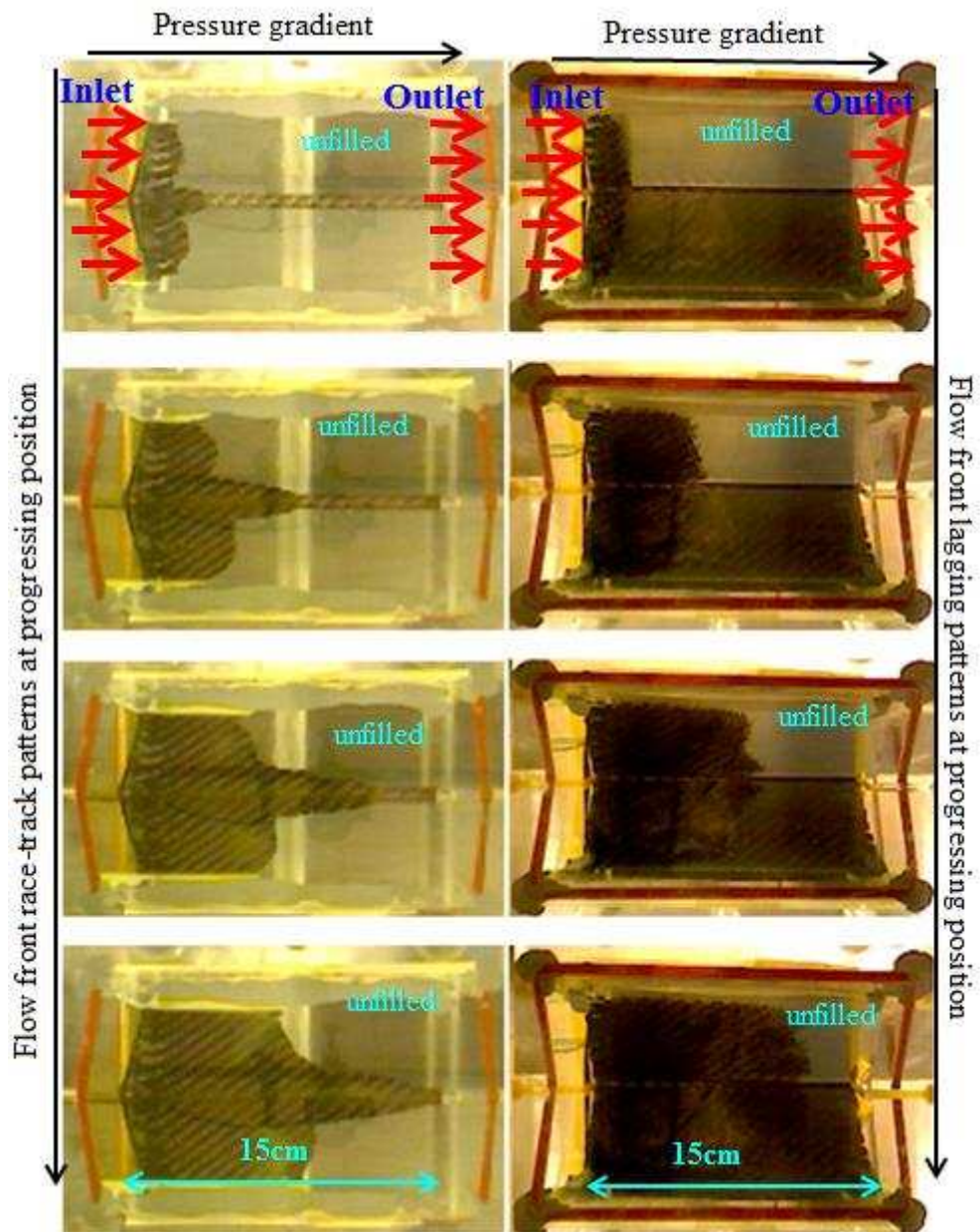
Table C.10: 2/2 twill racetrack flow shape analysis Perspex exp. i) upper side ii) lower side from Fig. C.16.

i)   2/2 twill Perspex exp. shape analysis upper side:

y fill position 90° centre (cm)	y fill position upper (cm)	y fill position lower (cm)	Δy race-track (fill 90° centre (-) fill average upper/lower) (cm)
5	1.82	1.94	3.12
10	4.29	4.31	5.7
15	11.86	10.91	3.61

ii)   2/2 twill Perspex exp. shape analysis lower side:

y fill position 90° centre (cm)	y fill position upper (cm)	y fill position lower (cm)	Δy lag (fill 90° centre (-) fill average upper/lower) (cm)
4.13	5.03	5.03	-0.9
8.77	9.43	9.97	-0.93
12.71	12.71	13.72	-1.1
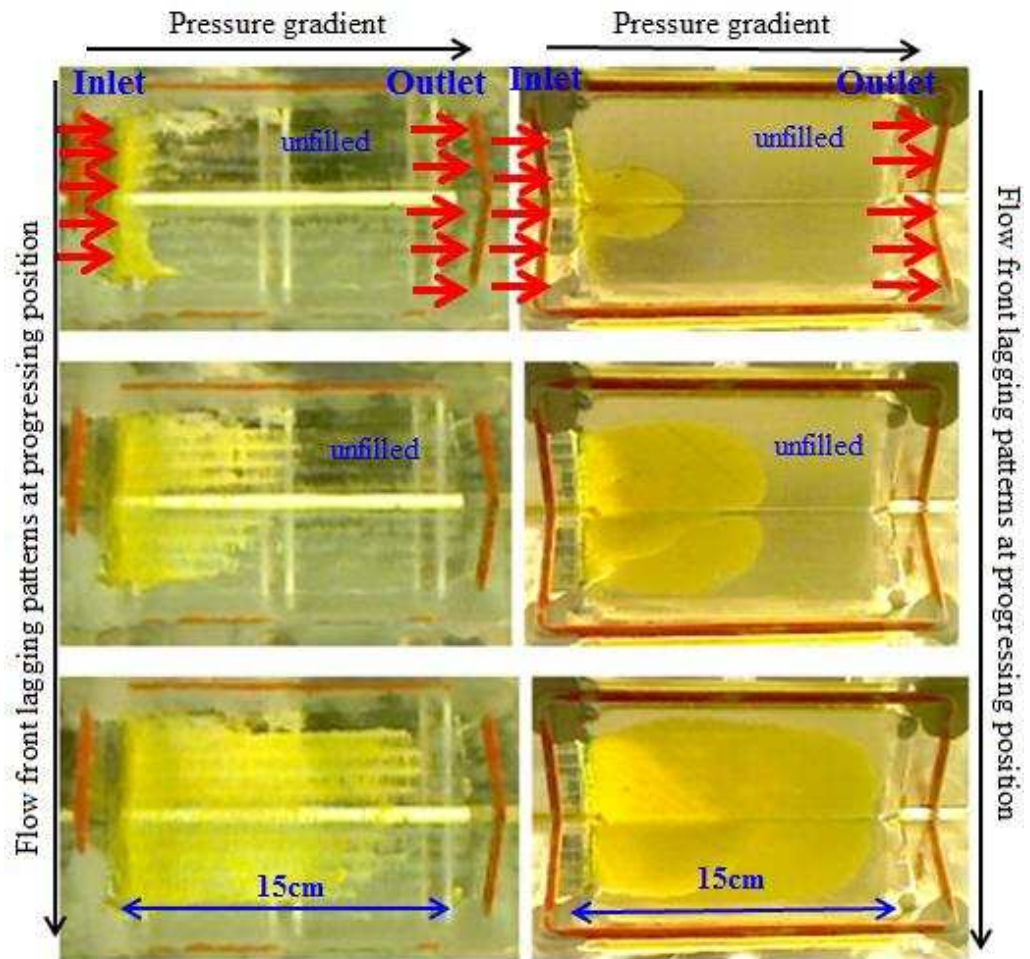
i) Upper side left (images)   **ii) Lower side right (images)**

Fig. C.17: Experiment 4, triaxial weft lag evaluation (left)/lag evaluation (right) with Perspex transparent tool.
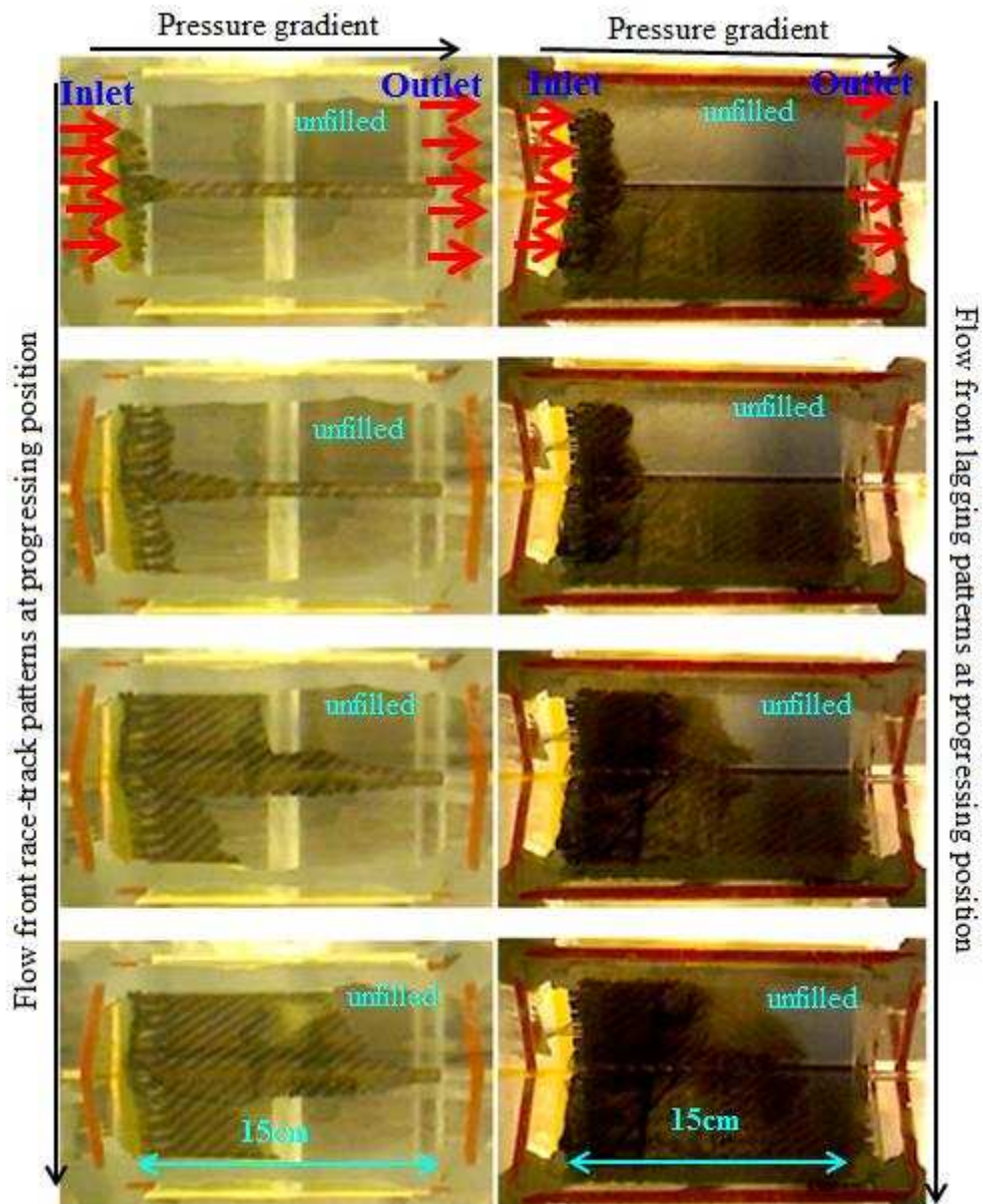
Table C.11: 2/2 twill racetrack flow shape analysis Perspex exp. i) upper side ii) lower side from Fig. C.17.

i)   2/2 twill Perspex exp. shape analysis upper side:

y fill position 90° centre (cm)	y fill position upper (cm)	y fill position lower (cm)	Δy lag (fill 90° centre (-) fill average upper/lower) (cm)
1.34	5.03	1.73	-2.04
2.47	8.64	6.38	-5.04
8.07	12.01	11.66	-3.77

ii)   2/2 twill Perspex exp. shape analysis lower side:

y fill position 90° centre (cm)	y fill position upper (cm)	y fill position lower (cm)	Δy lag (fill 90° centre (-) fill average upper/lower) (cm)
3.11	5.03	5.03	-1.92
6.73	8.85	8.85	-2.12
12.25	14.34	14.15	-2
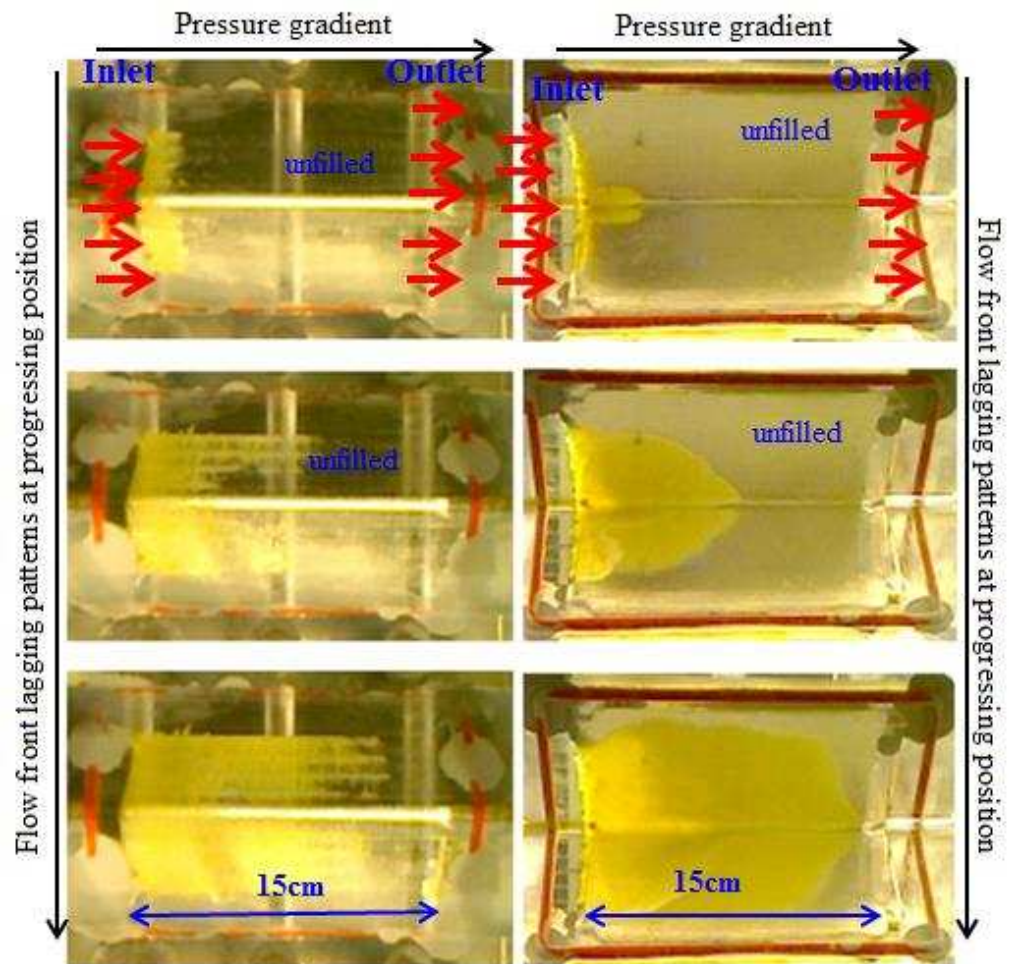
i) **Upper side left (images)**   ii) **Lower side right (images)**

Fig. C.18: Experiment 5, triaxial weft racetrack with Perspex transparent tool (3rd line images shown on Fig. 6.21).
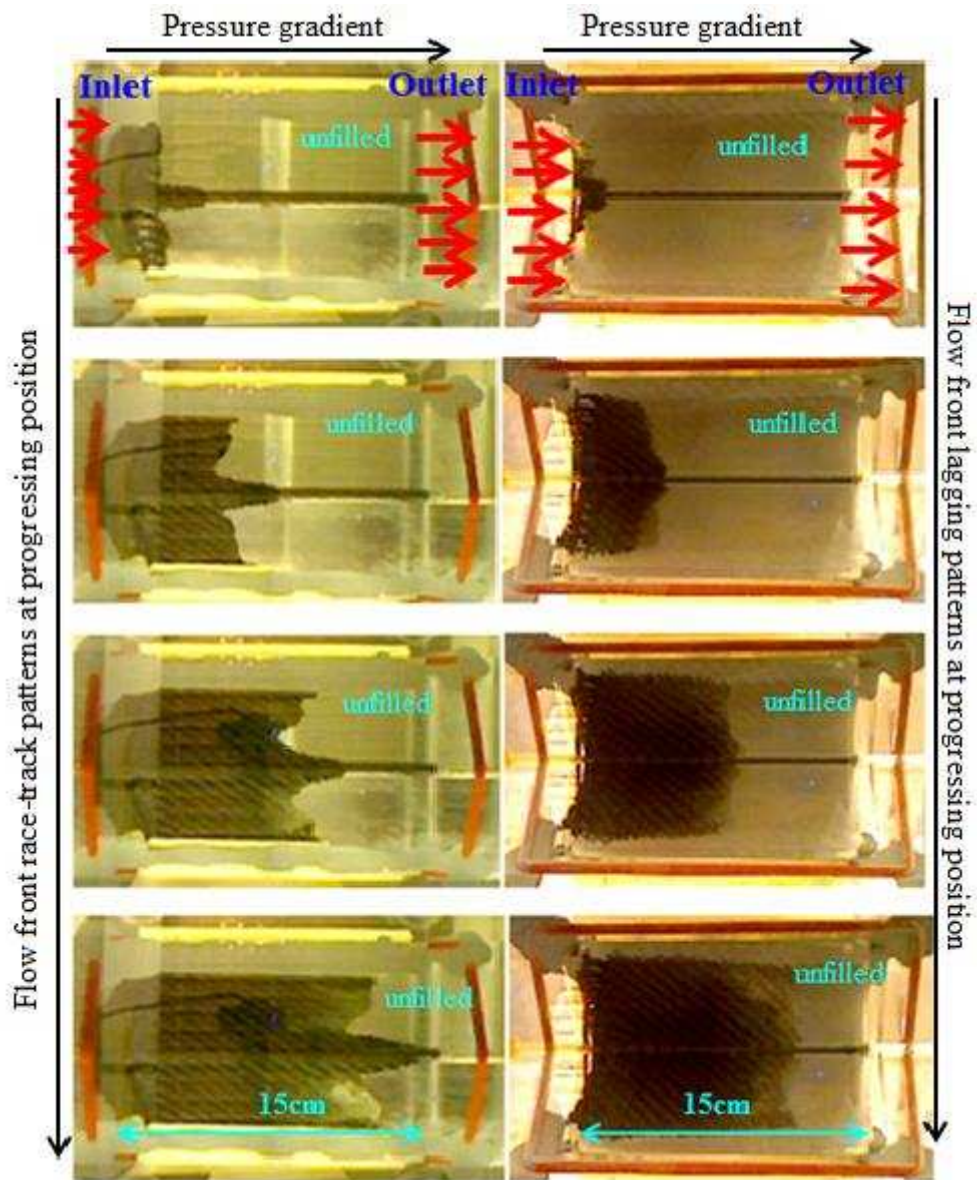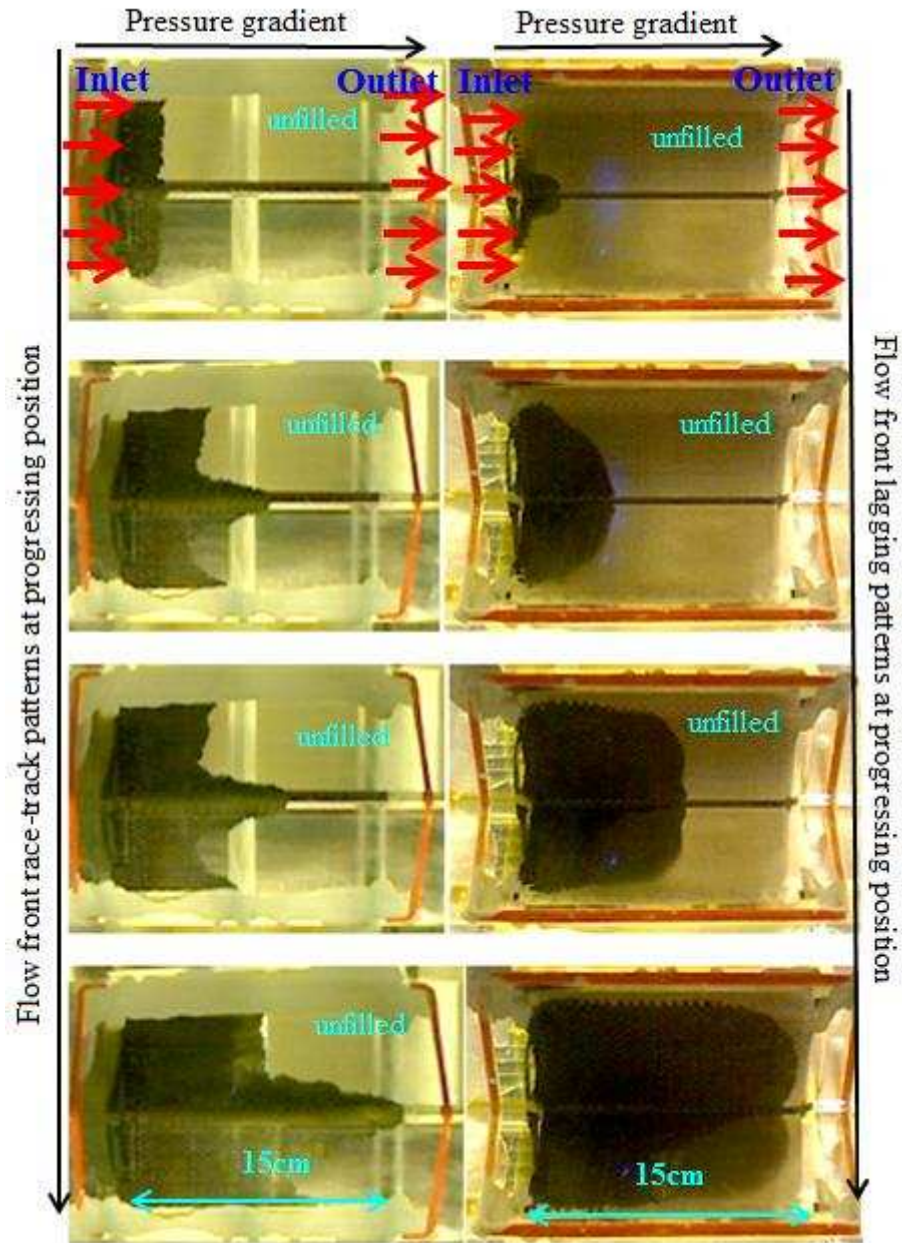
Table C.12: 2/2 twill racetrack flow shape analysis Perspex exp. i) upper side ii) lower side from Fig. C.18.

i)   2/2 twill Perspex exp. shape analysis upper side:

| y fill position 90° centre (cm)	y fill position upper (cm)	y fill position lower (cm)	Δy lag (fill 90° centre (-) fill average upper/lower) (cm)
1.54	2.02	2.04	-0.49
3.68	8.61	6.39	-3.82
4.37	11.97	11.11	-7.17

ii)   2/2 twill Perspex exp. shape analysis lower side:

y fill position 90° centre (cm)	y fill position upper (cm)	y fill position lower (cm)	Δy lag (fill 90° centre (-) fill average upper/lower) (cm)
2.89	3.68	3.86	-0.88
7.11	8.42	8.33	-1.27
12.38	14.44	14.34	-2.01

Appendix D: Gap distributions for use in simulation

i) 3D woven HTS40 F13 fabric random gaps

Firstly for the 3D woven HTS40 F13 fabric a series of tables was generated in order to study the node variability taking into account the gaps distribution in warp, weft directions for this preform according to the CMM measurements. For each N Random number (tested preform sample) a gap was assigned according to the probabilistic distribution as shown Tables D.1-D.4. Gap tables on this Appendix derived from fabric thickness with subtraction from the moulder height of the node (2.75mm).

Table D.1: HTS40 F13 fabric made of 3 layers gap in warp.

N Random number 3-layers	h_{max} gap warp(mm)
1, 2, 3	0.35
4, 5, 6	0.45
7	0.55

Edges HTS40 F13 fabric made of 3 layers gap in weft are not presented in ACTS generic node as shown Figs. 1.3-1.5, 7.8, 7.9 (a)-(d) and therefore no gap measurements has been done.

Table D.2: HTS40 F13 fabric made of 4 layers gap in warp.

N Random number 4-layers	h_{max} gap warp(mm)
1, 2, 3	0.55
4, 5, 6	0.65
7	0.75

Table D.3: HTS40 F13 fabric made of 4 layers gap in weft.

N Random number 4-layers	h_{max} gap weft(mm)
1	0.05
2	0.15
3	0.35
4, 5	0.45
6	0.55
7	0.75

Table D.4: HTS40 F13 fabric made of 4 layers gap at 45° to warp/weft.

N Random number 4-layers	h_{max} gap warp/weft(mm)
1	0.05
2	0.15
3	0.35
4, 5	0.45
6, 7, 8, 9	0.55
10, 11, 12	0.65
13, 14	0.75

ii) 2/2 twill fabric random gaps

The same technique as for HTS40 F13 fabric was repeated for the 2/2 twill fabric as shown in Tables D.5-D.6, assuming warp and weft permeability to be equal in this case.

Table D.5: 2/2 twill fabric 2 layers gap.

N Random number 2-layers	h_{max} gap(mm)
1	0.75
2, 3, 4, 5, 6	0.85
7	0.95

Table D.6: 2/2 twill fabric 3 layers gap.

N Random number 3-layers	h_{max} gap (mm)
1	0.95
2, 3, 4, 5, 6	1.05
7	1.15

iii) Triaxial fabric random gaps

Triaxial fabric variability was studied in the same way as HTS40 F13 and 2/2 twill fabric as shown in Tables D.7-D.10.

Table D.7: Triaxial fabric 2 layers gap in warp.

N Random number 2-layers	h_{max} gap warp(mm)
1	0.05
2	0.25
3, 4	0.35
5	0.45
6	0.55

Table D.8: Triaxial fabric 3 layers gap in warp.

N Random number 3-layers	h_{max} gap warp(mm)
1	0.15
2	0.45
3, 4	0.55
5	0.65
6	0.75

Table D.9: Triaxial fabric 2 layers gap in weft.

N Random number 3-layers	h_{max} gap weft(mm)
1	0.25
2	0.45
3, 4	0.55
5	0.65

Table D.10: Triaxial fabric 3 layers gap at 45° to warp/weft.

N Random number 3-layers	h_{max} gap warp/weft(mm)
1	0.15
2	0.25
3. 4	0.45
5, 6, 7, 8	0.55
9, 10	0.65
11	0.75

Appendix E: Simulation tables for generic node

i) ACTS Fabric Simulations:

Table E.1: Input file to the simulation case 2 for the ACTS fabric for generic node.

ACTS Simulation 2 Node zone	Number of layers	Node fabric direction	Random gap h(mm)
1	4	weft	0.15mm
2	4	weft	0.15mm
3	4	weft	0.45 mm
4	4	weft	0.15mm
5	4	45^0 (warp/weft)	0.75mm
6	4	45^0 (warp/weft)	0.65mm
7	4	45^0 (warp/weft)	0.65mm
8	4	45^0 (warp/weft)	0.65mm
9	4	warp	0.65mm
10	4	warp	0.75mm
11	4	warp	0.55mm
12	4	warp	0.65mm
13	4	45^0 (warp/weft)	0.75mm
14	4	45^0 (warp/weft)	0.55mm
15	4	45^0 (warp/weft)	0.55mm
16	4	45^0 (warp/weft)	0.55mm
17	4	weft	0.45mm
18	4	weft	0.75mm
19	4	weft	0.75mm
20	3	warp	0.35mm
21	3	warp	0.45mm
22	3	warp	0.45mm
23	3	warp	0.35mm

Table E.2: Input file to the simulation case 3 for the ACTS fabric for generic node.

ACTS Simulation 3 Node zone	Number of layers	Node fabric direction	Random gap h(mm)
1	4	weft	0.45 mm
2	4	weft	0.45 mm
3	4	weft	0.35 mm
4	4	weft	0.15mm
5	4	45^0 (warp/weft)	0.65mm
6	4	45^0 (warp/weft)	0.45 mm
7	4	45^0 (warp/weft)	0.65mm
8	4	45^0 (warp/weft)	0.15mm
9	4	warp	0.65mm
10	4	warp	0.55mm
11	4	warp	0.55 mm
12	4	warp	0.75 mm
13	4	45^0 (warp/weft)	0.65mm
14	4	45^0 (warp/weft)	0.55mm
15	4	45^0 (warp/weft)	0.35 mm
16	4	45^0 (warp/weft)	0.75 mm
17	4	weft	0.35 mm
18	4	weft	0.75mm
19	4	weft	0.55mm
20	3	warp	0.55 mm
21	3	warp	0.55 mm
22	3	warp	0.45 mm
23	3	warp	0.45mm

Table E.3: Input file to the simulation case 4 for the ACTS fabric for generic node.

ACTS Simulation 4 Node zone	Number of layers	Node fabric direction	Random gap h(mm)
1	4	weft	0.45 mm
2	4	weft	0.55 mm
3	4	weft	0.55 mm
4	4	weft	0.45 mm
5	4	45^0 (warp/weft)	0.15 mm
6	4	45^0 (warp/weft)	0.45 mm
7	4	45^0 (warp/weft)	0.75 mm
8	4	45^0 (warp/weft)	0.55 mm
9	4	warp	0.65 mm
10	4	warp	0.65 mm
11	4	warp	0.55 mm
12	4	warp	0.55 mm
13	4	45^0 (warp/weft)	0.55 mm
14	4	45^0 (warp/weft)	0.05 mm
15	4	45^0 (warp/weft)	0.65 mm
16	4	45^0 (warp/weft)	0.15 mm
17	4	weft	0.45 mm
18	4	weft	0.05 mm
19	4	weft	0.45 mm
20	3	warp	0.55 mm
21	3	warp	0.35 mm
22	3	warp	0.55 mm
23	3	warp	0.35 mm

Table E.4: Input file to the simulation case 5 for the ACTS fabric for generic node.

ACTS Simulation 5 Node zone	Number of layers	Node fabric direction	Random gap h(mm)
1	4	weft	0.05 mm
2	4	weft	0.45 mm
3	4	weft	0.45 mm
4	4	weft	0.45 mm
5	4	45^0 (warp/weft)	0.45 mm
6	4	45^0 (warp/weft)	0.35 mm
7	4	45^0 (warp/weft)	0.75 mm
8	4	45^0 (warp/weft)	0.65 mm
9	4	warp	0.55 mm
10	4	warp	0.55 mm
11	4	warp	0.75 mm
12	4	warp	0.75 mm
13	4	45^0 (warp/weft)	0.45 mm
14	4	45^0 (warp/weft)	0.55 mm
15	4	45^0 (warp/weft)	0.15 mm
16	4	45^0 (warp/weft)	0.65 mm
17	4	weft	0.05 mm
18	4	weft	0.45 mm
19	4	weft	0.05 mm
20	3	warp	0.35 mm
21	3	warp	0.55 mm
22	3	warp	0.55 mm
23	3	warp	0.35 mm

Table E.5: Input file to the simulation case 6 for the ACTS fabric for generic node.

ACTS Simulation 6			
Node zone	Number of layers	Node fabric direction	Random gap h(mm)
1	4	weft	0.35 mm
2	4	weft	0.45 mm
3	4	weft	0.45 mm
4	4	weft	0.05 mm
5	4	45^0 (warp/weft)	0.75 mm
6	4	45^0 (warp/weft)	0.55 mm
7	4	45^0 (warp/weft)	0.55 mm
8	4	45^0 (warp/weft)	0.75 mm
9	4	warp	0.65 mm
10	4	warp	0.55 mm
11	4	warp	0.65 mm
12	4	warp	0.65 mm
13	4	45^0 (warp/weft)	0.55 mm
14	4	45^0 (warp/weft)	0.65 mm
15	4	45^0 (warp/weft)	0.55 mm
16	4	45^0 (warp/weft)	0.75 mm
17	4	weft	0.45 mm
18	4	weft	0.55 mm
19	4	weft	0.75 mm
20	3	warp	0.35 mm
21	3	warp	0.45 mm
22	3	warp	0.55 mm
23	3	warp	0.35 mm

Table E.6: Input file to the simulation case 7 for the ACTS fabric for generic node.

ACTS Simulation 7			
Node zone	Number of layers	Node fabric direction	Random gap h(mm)
1	4	weft	0.45 mm
2	4	weft	0.05 mm
3	4	weft	0.35 mm
4	4	weft	0.55 mm
5	4	45^0 (warp/weft)	0.55 mm
6	4	45^0 (warp/weft)	0.45 mm
7	4	45^0 (warp/weft)	0.75 mm
8	4	45^0 (warp/weft)	0.75 mm
9	4	warp	0.75 mm
10	4	warp	0.55 mm
11	4	warp	0.75 mm
12	4	warp	0.65 mm
13	4	45^0 (warp/weft)	0.55 mm
14	4	45^0 (warp/weft)	0.55 mm
15	4	45^0 (warp/weft)	0.75 mm
16	4	45^0 (warp/weft)	0.65 mm
17	4	weft	0.35 mm
18	4	weft	0.55 mm
19	4	weft	0.75 mm
20	3	warp	0.35 mm
21	3	warp	0.55 mm
22	3	warp	0.35 mm
23	3	warp	0.45 mm

Table E.7: Input file to the simulation case 8 for the ACTS fabric for generic node.

ACTS Simulation 8			
Node zone	Number of layers	Node fabric direction	Random gap h(mm)
1	4	weft	0.45 mm
2	4	weft	0.15 mm
3	4	weft	0.45 mm
4	4	weft	0.45 mm
5	4	45^0 (warp/weft)	0.35 mm
6	4	45^0 (warp/weft)	0.65 mm
7	4	45^0 (warp/weft)	0.65 mm
8	4	45^0 (warp/weft)	0.55 mm
9	4	warp	0.75 mm
10	4	warp	0.55 mm
11	4	warp	0.65 mm
12	4	warp	0.65 mm
13	4	45^0 (warp/weft)	0.75 mm
14	4	45^0 (warp/weft)	0.65 mm
15	4	45^0 (warp/weft)	0.55 mm
16	4	45^0 (warp/weft)	0.45 mm
17	4	weft	0.15 mm
18	4	weft	0.45 mm
19	4	weft	0.75 mm
20	3	warp	0.35 mm
21	3	warp	0.35 mm
22	3	warp	0.45 mm
23	3	warp	0.45 mm

Table E.8: Input file to the simulation case 9 for the ACTS fabric for generic node.

ACTS Simulation 9			
Node zone	Number of layers	Node fabric direction	Random gap h(mm)
1	4	weft	0.45 mm
2	4	weft	0.45 mm
3	4	weft	0.35 mm
4	4	weft	0.35 mm
5	4	45^0 (warp/weft)	0.75 mm
6	4	45^0 (warp/weft)	0.65 mm
7	4	45^0 (warp/weft)	0.65 mm
8	4	45^0 (warp/weft)	0.65 mm
9	4	warp	0.65 mm
10	4	warp	0.75 mm
11	4	warp	0.65 mm
12	4	warp	0.55 mm
13	4	45^0 (warp/weft)	0.45 mm
14	4	45^0 (warp/weft)	0.45 mm
15	4	45^0 (warp/weft)	0.55 mm
16	4	45^0 (warp/weft)	0.55 mm
17	4	weft	0.75 mm
18	4	weft	0.45 mm
19	4	weft	0.35 mm
20	3	warp	0.45 mm
21	3	warp	0.45 mm
22	3	warp	0.35 mm
23	3	warp	0.55 mm

Table E.9: Input file to the simulation case 10 for the ACTS fabric for generic node.

ACTS Simulation 10			
Node zone	Number of layers	Node fabric direction	Random gap h(mm)
1	4	weft	0.75 mm
2	4	weft	0.45 mm
3	4	weft	0.05 mm
4	4	weft	0.35 mm
5	4	45^0 (warp/weft)	0.35 mm
6	4	45^0 (warp/weft)	0.15 mm
7	4	45^0 (warp/weft)	0.55 mm
8	4	45^0 (warp/weft)	0.05 mm
9	4	warp	0.75 mm
10	4	warp	0.65 mm
11	4	warp	0.55 mm
12	4	warp	0.65 mm
13	4	45^0 (warp/weft)	0.15 mm
14	4	45^0 (warp/weft)	0.55 mm
15	4	45^0 (warp/weft)	0.45 mm
16	4	45^0 (warp/weft)	0.55 mm
17	4	weft	0.45 mm
18	4	weft	0.45 mm
19	4	weft	0.45 mm
20	3	warp	0.45 mm
21	3	warp	0.35 mm
22	3	warp	0.35 mm
23	3	warp	0.45 mm

ii) 2/2 Twill Fabric Simulations:

Table E.10: Input file to the simulation case 1 for the 2/2 Twill fabric for generic node.

2.2 twill Simulation 1			
Node zone	Number of layers	Node fabric direction	Random gap h(mm)
1	3	weft	1.05mm
2	3	weft	1.05mm
3	3	weft	1.05mm
4	3	weft	0.95mm
5	3	45^0 (warp/weft)	1.05mm
6	3	45^0 (warp/weft)	1.15mm
7	3	45^0 (warp/weft)	1.05mm
8	3	45^0 (warp/weft)	1.05mm
9	3	warp	1.05mm
10	3	warp	1.05mm
11	3	warp	1.05mm
12	3	warp	1.05mm
13	3	45^0 (warp/weft)	1.05mm
14	3	45^0 (warp/weft)	1.05mm
15	3	45^0 (warp/weft)	1.05mm
16	3	45^0 (warp/weft)	1.05mm
17	3	weft	1.05mm
18	3	weft	1.05mm
19	3	weft	1.05mm
20	2	warp	0.85mm
21	2	warp	0.85mm
22	2	warp	0.85mm
23	2	warp	0.85mm

Table E.11: Input file to the simulation case 2 for the 2/2 Twill fabric for generic node.

2.2 twill Simulation 2			
Node zone	Number of layers	Node fabric direction	Random gap h(mm)
1	3	weft	1.05mm
2	3	weft	1.05mm
3	3	weft	1.05mm
4	3	weft	1.05mm
5	3	45^0 (warp/weft)	1.05mm
6	3	45^0 (warp/weft)	1.05mm
7	3	45^0 (warp/weft)	1.05mm
8	3	45^0 (warp/weft)	0.95mm
9	3	warp	1.05mm
10	3	warp	1.05mm
11	3	warp	1.05mm
12	3	warp	1.05mm
13	3	45^0 (warp/weft)	1.05mm
14	3	45^0 (warp/weft)	1.15mm
15	3	45^0 (warp/weft)	1.05mm
16	3	45^0 (warp/weft)	1.05mm
17	3	weft	1.05mm
18	3	weft	1.15mm
19	3	weft	1.05mm
20	2	warp	0.85mm
21	2	warp	0.85mm
22	2	warp	0.85mm
23	2	warp	0.85mm

Table E.12: Input file to the simulation case 3 for the 2/2 Twill fabric for generic node.

2.2 twill Simulation 3			
Node zone	Number of layers	Node fabric direction	Random gap h(mm)
1	3	weft	1.05mm
2	3	weft	1.05mm
3	3	weft	1.05mm
4	3	weft	1.15mm
5	3	45^0 (warp/weft)	1.05mm
6	3	45^0 (warp/weft)	1.05mm
7	3	45^0 (warp/weft)	0.95mm
8	3	45^0 (warp/weft)	1.05mm
9	3	warp	1.05mm
10	3	warp	1.05mm
11	3	warp	1.05mm
12	3	warp	1.05mm
13	3	45^0 (warp/weft)	1.05mm
14	3	45^0 (warp/weft)	1.15mm
15	3	45^0 (warp/weft)	1.05mm
16	3	45^0 (warp/weft)	1.05mm
17	3	weft	1.05mm
18	3	weft	1.05mm
19	3	weft	1.05mm
20	2	warp	0.75mm
21	2	warp	0.75mm
22	2	warp	0.95mm
23	2	warp	0.85mm

Table E.13: Input file to the simulation case 4 for the 2/2 Twill fabric for generic node.

2.2 twill Simulation 4			
Node zone	Number of layers	Node fabric direction	Random gap h(mm)
1	3	weft	1.05mm
2	3	weft	1.05mm
3	3	weft	1.05mm
4	3	weft	1.05mm
5	3	45^0 (warp/weft)	1.05mm
6	3	45^0 (warp/weft)	1.15mm
7	3	45^0 (warp/weft)	1.05mm
8	3	45^0 (warp/weft)	1.05mm
9	3	warp	1.05mm
10	3	warp	1.05mm
11	3	warp	1.05mm
12	3	warp	1.05mm
13	3	45^0 (warp/weft)	1.05mm
14	3	45^0 (warp/weft)	1.05mm
15	3	45^0 (warp/weft)	1.05mm
16	3	45^0 (warp/weft)	1.15mm
17	3	weft	1.05mm
18	3	weft	1.05mm
19	3	weft	1.05mm
20	2	warp	0.85mm
21	2	warp	0.85mm
22	2	warp	0.85mm
23	2	warp	0.85mm

Table E.14: Input file to the simulation case 5 for the 2/2 Twill fabric for generic node.

2.2 twill Simulation 5			
Node zone	Number of layers	Node fabric direction	Random gap h(mm)
1	3	weft	0.95mm
2	3	weft	1.15mm
3	3	weft	1.05mm
4	3	weft	1.15mm
5	3	45^0 (warp/weft)	1.05mm
6	3	45^0 (warp/weft)	1.05mm
7	3	45^0 (warp/weft)	1.05mm
8	3	45^0 (warp/weft)	1.05mm
9	3	warp	1.15mm
10	3	warp	1.05mm
11	3	warp	1.05mm
12	3	warp	1.05mm
13	3	45^0 (warp/weft)	1.05mm
14	3	45^0 (warp/weft)	1.05mm
15	3	45^0 (warp/weft)	1.05mm
16	3	45^0 (warp/weft)	1.05mm
17	3	weft	1.05mm
18	3	weft	1.05mm
19	3	weft	1.05mm
20	2	warp	0.95mm
21	2	warp	0.85mm
22	2	warp	0.85mm
23	2	warp	0.85mm

Table E.15: Input file to the simulation case 6 for the 2/2 Twill fabric for generic node.

2.2 twill Simulation 6			
Node zone	Number of layers	Node fabric direction	Random gap h(mm)
1	3	weft	1.15mm
2	3	weft	1.05mm
3	3	weft	1.05mm
4	3	weft	1.05mm
5	3	45^0 (warp/weft)	1.05mm
6	3	45^0 (warp/weft)	1.05mm
7	3	45^0 (warp/weft)	1.05mm
8	3	45^0 (warp/weft)	1.05mm
9	3	warp	1.05mm
10	3	warp	1.05mm
11	3	warp	1.05mm
12	3	warp	0.95mm
13	3	45^0 (warp/weft)	0.95mm
14	3	45^0 (warp/weft)	1.15mm
15	3	45^0 (warp/weft)	1.05mm
16	3	45^0 (warp/weft)	0.95mm
17	3	weft	1.05mm
18	3	weft	1.05mm
19	3	weft	1.05mm
20	2	warp	0.85mm
21	2	warp	0.85mm
22	2	warp	0.75mm
23	2	warp	0.85mm

Table E.16: Input file to the simulation case 7 for the 2/2 Twill fabric for generic node.

Node zone	Number of layers	Node fabric direction	Random gap h(mm)
2.2 twill Simulation 7			
1	3	weft	1.05mm
2	3	weft	1.15mm
3	3	weft	1.05mm
4	3	weft	1.05mm
5	3	45^0 (warp/weft)	1.05mm
6	3	45^0 (warp/weft)	1.05mm
7	3	45^0 (warp/weft)	0.95mm
8	3	45^0 (warp/weft)	1.05mm
9	3	warp	1.05mm
10	3	warp	0.95mm
11	3	warp	1.05mm
12	3	warp	1.05mm
13	3	45^0 (warp/weft)	1.05mm
14	3	45^0 (warp/weft)	1.05mm
15	3	45^0 (warp/weft)	1.15mm
16	3	45^0 (warp/weft)	1.05mm
17	3	weft	1.05mm
18	3	weft	1.05mm
19	3	weft	1.05mm
20	2	warp	0.85mm
21	2	warp	0.85mm
22	2	warp	0.95mm
23	2	warp	0.75mm

Table E.17: Input file to the simulation case 8 for the 2/2 Twill fabric for generic node.

2.2 twill Simulation 8			
Node zone	Number of layers	Node fabric direction	Random gap h(mm)
1	3	weft	1.05mm
2	3	weft	1.05mm
3	3	weft	1.05mm
4	3	weft	1.05mm
5	3	45^0 (warp/weft)	1.15mm
6	3	45^0 (warp/weft)	1.05mm
7	3	45^0 (warp/weft)	1.05mm
8	3	45^0 (warp/weft)	1.05mm
9	3	warp	1.05mm
10	3	warp	1.05mm
11	3	warp	1.05mm
12	3	warp	1.05mm
13	3	45^0 (warp/weft)	1.05mm
14	3	45^0 (warp/weft)	1.15mm
15	3	45^0 (warp/weft)	1.05mm
16	3	45^0 (warp/weft)	1.15mm
17	3	weft	0.95mm
18	3	weft	1.05mm
19	3	weft	0.95mm
20	2	warp	0.95mm
21	2	warp	0.85mm
22	2	warp	0.85mm
23	2	warp	0.85mm

Table E.18: Input file to the simulation case 9 for the 2/2 Twill fabric for generic node.

2.2 twill Simulation 9			
Node zone	Number of layers	Node fabric direction	Random gap h(mm)
1	3	weft	1.05mm
2	3	weft	1.05mm
3	3	weft	1.05mm
4	3	weft	1.15mm
5	3	45^0 (warp/weft)	1.05mm
6	3	45^0 (warp/weft)	1.05mm
7	3	45^0 (warp/weft)	1.05mm
8	3	45^0 (warp/weft)	1.05mm
9	3	warp	1.05mm
10	3	warp	1.05mm
11	3	warp	1.05mm
12	3	warp	1.15mm
13	3	45^0 (warp/weft)	1.05mm
14	3	45^0 (warp/weft)	1.05mm
15	3	45^0 (warp/weft)	1.05mm
16	3	45^0 (warp/weft)	1.05mm
17	3	weft	1.05mm
18	3	weft	1.05mm
19	3	weft	1.05mm
20	2	warp	0.85mm
21	2	warp	0.85mm
22	2	warp	0.85mm
23	2	warp	0.85mm

Table E.19: Input file to the simulation case 10 for the 2/2 Twill fabric for generic node.

2.2 twill Simulation 10			
Node zone	Number of layers	Node fabric direction	Random gap h(mm)
1	3	weft	1.05mm
2	3	weft	1.05mm
3	3	weft	1.05mm
4	3	weft	1.05mm
5	3	45^0 (warp/weft)	0.95mm
6	3	45^0 (warp/weft)	1.15mm
7	3	45^0 (warp/weft)	1.05mm
8	3	45^0 (warp/weft)	0.95mm
9	3	warp	1.15mm
10	3	warp	1.05mm
11	3	warp	1.05mm
12	3	warp	1.05mm
13	3	45^0 (warp/weft)	1.05mm
14	3	45^0 (warp/weft)	1.05mm
15	3	45^0 (warp/weft)	1.05mm
16	3	45^0 (warp/weft)	1.05mm
17	3	weft	1.05mm
18	3	weft	1.05mm
19	3	weft	1.05mm
20	2	warp	0.85mm
21	2	warp	0.85mm
22	2	warp	0.85mm
23	2	warp	0.85mm

iii)   Triaxial Fabric Simulations:

Table E.20: Input file to the simulation case 1 for the Triaxial fabric for generic node.

Triaxial Simulation 1			
Node zone	Number of layers	Node fabric direction	Random gap h(mm)
1	3	weft	0.45 mm
2	3	weft	0.45 mm
3	3	weft	0.25 mm
4	3	weft	0.65 mm
5	3	45^0 (warp/weft)	0.55 mm
6	3	45^0 (warp/weft)	0.75 mm
7	3	45^0 (warp/weft)	0.55 mm
8	3	45^0 (warp/weft)	0.55 mm
9	3	warp	0.45 mm
10	3	warp	0.45 mm
11	3	warp	0.65 mm
12	3	warp	0.55 mm
13	3	45^0 (warp/weft)	0.55 mm
14	3	45^0 (warp/weft)	0.45 mm
15	3	45^0 (warp/weft)	0.45 mm
16	3	45^0 (warp/weft)	0.25 mm
17	3	weft	0.55 mm
18	3	weft	0.55 mm
19	3	weft	0.25 mm
20	2	warp	0.45 mm
21	2	warp	0.25 mm
22	2	warp	0.45 mm
23	2	warp	0.35 mm

Table E.21: Input file to the simulation case 2 for the Triaxial fabric for generic node.

Triaxial Simulation 2 Node zone	Number of layers	Node fabric direction	Random gap h(mm)
1	3	weft	0.55 mm
2	3	weft	0.55 mm
3	3	weft	0.25 mm
4	3	weft	0.55 mm
5	3	45^0 (warp/weft)	0.55 mm
6	3	45^0 (warp/weft)	0.55 mm
7	3	45^0 (warp/weft)	0.55 mm
8	3	45^0 (warp/weft)	0.55 mm
9	3	warp	0.45 mm
10	3	warp	0.55 mm
11	3	warp	0.55 mm
12	3	warp	0.15 mm
13	3	45^0 (warp/weft)	0.65 mm
14	3	45^0 (warp/weft)	0.75 mm
15	3	45^0 (warp/weft)	0.45 mm
16	3	45^0 (warp/weft)	0.65 mm
17	3	weft	0.55 mm
18	3	weft	0.55 mm
19	3	weft	0.45 mm
20	2	warp	0.35 mm
21	2	warp	0.05 mm
22	2	warp	0.25 mm
23	2	warp	0.35 mm

Table E.22: Input file to the simulation case 3 for the Triaxial fabric for generic node.

Triaxial Simulation 3 Node zone	Number of layers	Node fabric direction	Random gap h(mm)
1	3	weft	0.65 mm
2	3	weft	0.55 mm
3	3	weft	0.45 mm
4	3	weft	0.55 mm
5	3	45^0 (warp/weft)	0.65 mm
6	3	45^0 (warp/weft)	0.75 mm
7	3	45^0 (warp/weft)	0.55 mm
8	3	45^0 (warp/weft)	0.75 mm
9	3	warp	0.15 mm
10	3	warp	0.45 mm
11	3	warp	0.45 mm
12	3	warp	0.55 mm
13	3	45^0 (warp/weft)	0.45 mm
14	3	45^0 (warp/weft)	0.45 mm
15	3	45^0 (warp/weft)	0.45 mm
16	3	45^0 (warp/weft)	0.55 mm
17	3	weft	0.45 mm
18	3	weft	0.45 mm
19	3	weft	0.25 mm
20	2	warp	0.05 mm
21	2	warp	0.45 mm
22	2	warp	0.25 mm
23	2	warp	0.35 mm

Table E.23: Input file to the simulation case 4 for the Triaxial fabric for generic node.

Triaxial Simulation 4 Node zone	Number of layers	Node fabric direction	Random gap h(mm)
1	3	weft	0.55 mm
2	3	weft	0.55 mm
3	3	weft	0.55 mm
4	3	weft	0.45 mm
5	3	45^0 (warp/weft)	0.45 mm
6	3	45^0 (warp/weft)	0.65 mm
7	3	45^0 (warp/weft)	0.55 mm
8	3	45^0 (warp/weft)	0.65 mm
9	3	warp	0.15 mm
10	3	warp	0.55 mm
11	3	warp	0.55 mm
12	3	warp	0.55 mm
13	3	45^0 (warp/weft)	0.45 mm
14	3	45^0 (warp/weft)	0.75 mm
15	3	45^0 (warp/weft)	0.65 mm
16	3	45^0 (warp/weft)	0.45 mm
17	3	weft	0.55 mm
18	3	weft	0.55 mm
19	3	weft	0.55 mm
20	2	warp	0.25 mm
21	2	warp	0.35 mm
22	2	warp	0.55 mm
23	2	warp	0.35 mm

Table E.24: Input file to the simulation case 5 for the Triaxial fabric for generic node.

Triaxial Simulation 5 Node zone	Number of layers	Node fabric direction	Random gap h(mm)
1	3	weft	0.55 mm
2	3	weft	0.55 mm
3	3	weft	0.55 mm
4	3	weft	0.65 mm
5	3	45^0 (warp/weft)	0.55 mm
6	3	45^0 (warp/weft)	0.55 mm
7	3	45^0 (warp/weft)	0.75 mm
8	3	45^0 (warp/weft)	0.75 mm
9	3	warp	0.55 mm
10	3	warp	0.15 mm
11	3	warp	0.75 mm
12	3	warp	0.45 mm
13	3	45^0 (warp/weft)	0.55 mm
14	3	45^0 (warp/weft)	0.55 mm
15	3	45^0 (warp/weft)	0.65 mm
16	3	45^0 (warp/weft)	0.75 mm
17	3	weft	0.55 mm
18	3	weft	0.55 mm
19	3	weft	0.45 mm
20	2	warp	0.45 mm
21	2	warp	0.05 mm
22	2	warp	0.35 mm
23	2	warp	0.35 mm

Table E.25: Input file to the simulation case 6 for the Triaxial fabric for generic node.

Triaxial Simulation 6 Node zone	Number of layers	Node fabric direction	Random gap h(mm)
1	3	weft	0.55 mm
2	3	weft	0.25 mm
3	3	weft	0.25 mm
4	3	weft	0.55 mm
5	3	45^0 (warp/weft)	0.75 mm
6	3	45^0 (warp/weft)	0.75 mm
7	3	45^0 (warp/weft)	0.15 mm
8	3	45^0 (warp/weft)	0.55 mm
9	3	warp	0.75 mm
10	3	warp	0.75 mm
11	3	warp	0.55 mm
12	3	warp	0.55 mm
13	3	45^0 (warp/weft)	0.55 mm
14	3	45^0 (warp/weft)	0.75 mm
15	3	45^0 (warp/weft)	0.75 mm
16	3	45^0 (warp/weft)	0.25 mm
17	3	weft	0.25 mm
18	3	weft	0.45 mm
19	3	weft	0.55 mm
20	2	warp	0.35 mm
21	2	warp	0.25 mm
22	2	warp	0.45 mm
23	2	warp	0.35 mm

Table E.26: Input file to the simulation case 7 for the Triaxial fabric for generic node.

Triaxial Simulation 7			
Node zone	Number of layers	Node fabric direction	Random gap h(mm)
1	3	weft	0.55 mm
2	3	weft	0.55 mm
3	3	weft	0.25 mm
4	3	weft	0.55 mm
5	3	45^0 (warp/weft)	0.15 mm
6	3	45^0 (warp/weft)	0.15 mm
7	3	45^0 (warp/weft)	0.55 mm
8	3	45^0 (warp/weft)	0.55 mm
9	3	warp	0.55 mm
10	3	warp	0.55 mm
11	3	warp	0.55 mm
12	3	warp	0.75 mm
13	3	45^0 (warp/weft)	0.75 mm
14	3	45^0 (warp/weft)	0.65 mm
15	3	45^0 (warp/weft)	0.25 mm
16	3	45^0 (warp/weft)	0.65 mm
17	3	weft	0.45 mm
18	3	weft	0.55 mm
19	3	weft	0.55 mm
20	2	warp	0.35 mm
21	2	warp	0.45 mm
22	2	warp	0.35 mm
23	2	warp	0.35 mm

Table E.27: Input file to the simulation case 8 for the Triaxial fabric for generic node.

Triaxial Simulation 8			
Node zone	Number of layers	Node fabric direction	Random gap h(mm)
1	3	weft	0.55 mm
2	3	weft	0.55 mm
3	3	weft	0.55 mm
4	3	weft	0.55 mm
5	3	45^0 (warp/weft)	0.75 mm
6	3	45^0 (warp/weft)	0.45 mm
7	3	45^0 (warp/weft)	0.25 mm
8	3	45^0 (warp/weft)	0.65 mm
9	3	warp	0.55 mm
10	3	warp	0.55 mm
11	3	warp	0.65 mm
12	3	warp	0.65 mm
13	3	45^0 (warp/weft)	0.25 mm
14	3	45^0 (warp/weft)	0.55 mm
15	3	45^0 (warp/weft)	0.55 mm
16	3	45^0 (warp/weft)	0.25 mm
17	3	weft	0.45 mm
18	3	weft	0.55 mm
19	3	weft	0.55 mm
20	2	warp	0.35 mm
21	2	warp	0.35 mm
22	2	warp	0.25 mm
23	2	warp	0.55 mm

Table E.28: Input file to the simulation case 9 for the Triaxial fabric for generic node.

Triaxial Simulation 9 Node zone	Number of layers	Node fabric direction	Random gap h(mm)
1	3	weft	0.55 mm
2	3	weft	0.65 mm
3	3	weft	0.55 mm
4	3	weft	0.45 mm
5	3	45^0 (warp/weft)	0.75 mm
6	3	45^0 (warp/weft)	0.75 mm
7	3	45^0 (warp/weft)	0.55 mm
8	3	45^0 (warp/weft)	0.25 mm
9	3	warp	0.65 mm
10	3	warp	0.55 mm
11	3	warp	0.15 mm
12	3	warp	0.15 mm
13	3	45^0 (warp/weft)	0.65 mm
14	3	45^0 (warp/weft)	0.45 mm
15	3	45^0 (warp/weft)	0.75 mm
16	3	45^0 (warp/weft)	0.15 mm
17	3	weft	0.45 mm
18	3	weft	0.55 mm
19	3	weft	0.45 mm
20	2	warp	0.05 mm
21	2	warp	0.35 mm
22	2	warp	0.35 mm
23	2	warp	0.35 mm

Table E.29: Input file to the simulation case 10 for the Triaxial fabric for generic node.

Triaxial Simulation 10			
Node zone	Number of layers	Node fabric direction	Random gap h(mm)
1	3	weft	0.25 mm
2	3	weft	0.55 mm
3	3	weft	0.55 mm
4	3	weft	0.55 mm
5	3	45^0 (warp/weft)	0.55 mm
6	3	45^0 (warp/weft)	0.45 mm
7	3	45^0 (warp/weft)	0.55 mm
8	3	45^0 (warp/weft)	0.65 mm
9	3	warp	0.65 mm
10	3	warp	0.55 mm
11	3	warp	0.45 mm
12	3	warp	0.45 mm
13	3	45^0 (warp/weft)	0.45 mm
14	3	45^0 (warp/weft)	0.55 mm
15	3	45^0 (warp/weft)	0.65 mm
16	3	45^0 (warp/weft)	0.45 mm
17	3	weft	0.25 mm
18	3	weft	0.25 mm
19	3	weft	0.45 mm
20	2	warp	0.35 mm
21	2	warp	0.25 mm
22	2	warp	0.35 mm
23	2	warp	0.55 mm

Appendix F: Frequency of voids and distribution

i) ACTS HTS40 F13 fabric simulation for prediction of node void formation

Defined terminology of the detected n-frequency of void formation i.e. number of voids per volume. The bar chart of the n-void distribution represented firstly against the max volume of voids and secondly against the total node void volume is shown on void distribution Figs. F.1-F.8.

(The distribution case 1 here presented on Fig. 8.4).

n-voids distribution	1	36	25	9	2
■ n-freq. void ACTS case 2	1	36	25	9	2
■ Max void vol. (m3)	4.03E-10	2.83E-09	2.90E-08	2.93E-07	2.57E-06
■ Total node void vol. (m3)	4.03E-10	1.02E-07	7.25E-07	2.64E-06	5.14E-06
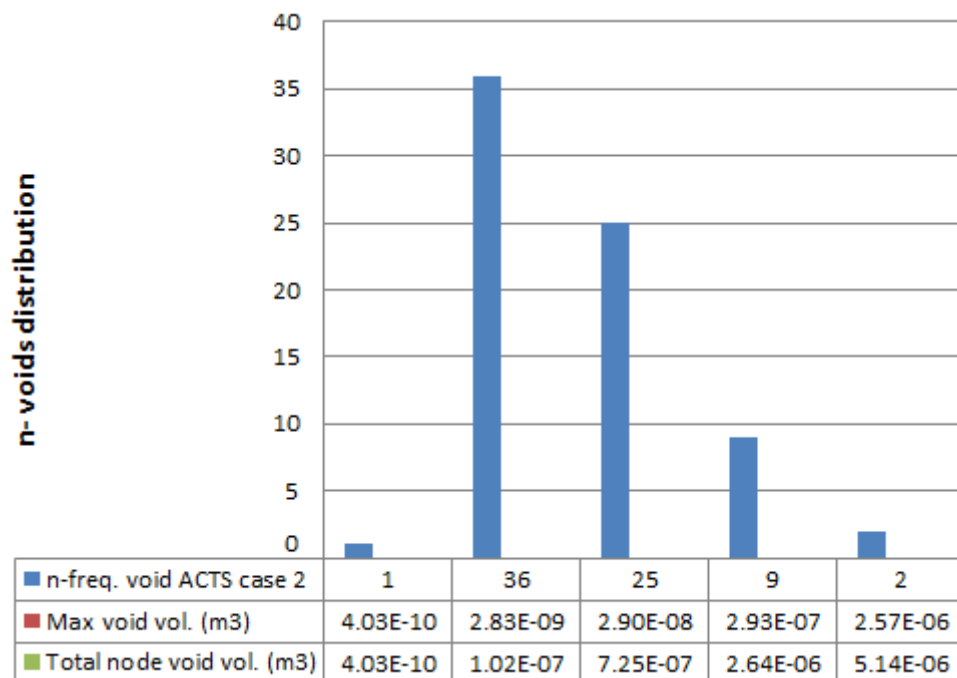
Figure F.1: Void distribution for node simulation case 2 with ACTS HTS40 F13 fabric.

Spiridon Koutsonas

n-freq. void ACTS case 3	1	30	29	8	2
Max void vol. (m3)	7.06E-10	2.97E-09	3.32E-08	2.40E-07	5.49E-06
Total node void vol. (m3)	7.06E-10	8.91E-08	9.63E-07	1.92E-06	1.10E-05
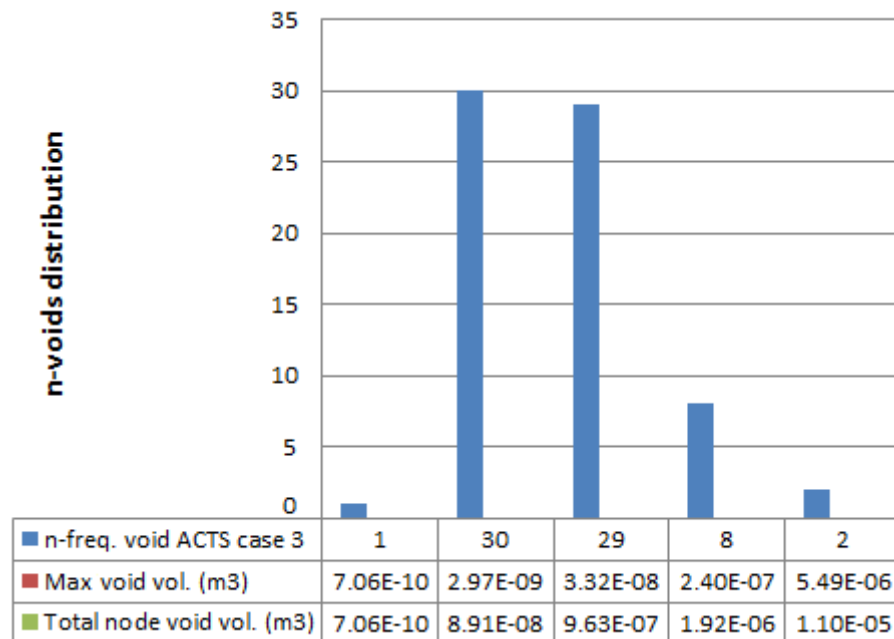
Figure F.2: Void distribution for node simulation case 3 with ACTS HTS40 F13 fabric.

n-freq. void ACTS case 4	5	30	30	7	3
Max void vol. (m3)	8.40E-10	3.40E-09	2.62E-08	3.97E-07	2.18E-06
Total node void vol. (m3)	4.20E-09	1.02E-07	7.86E-07	2.78E-06	6.54E-06
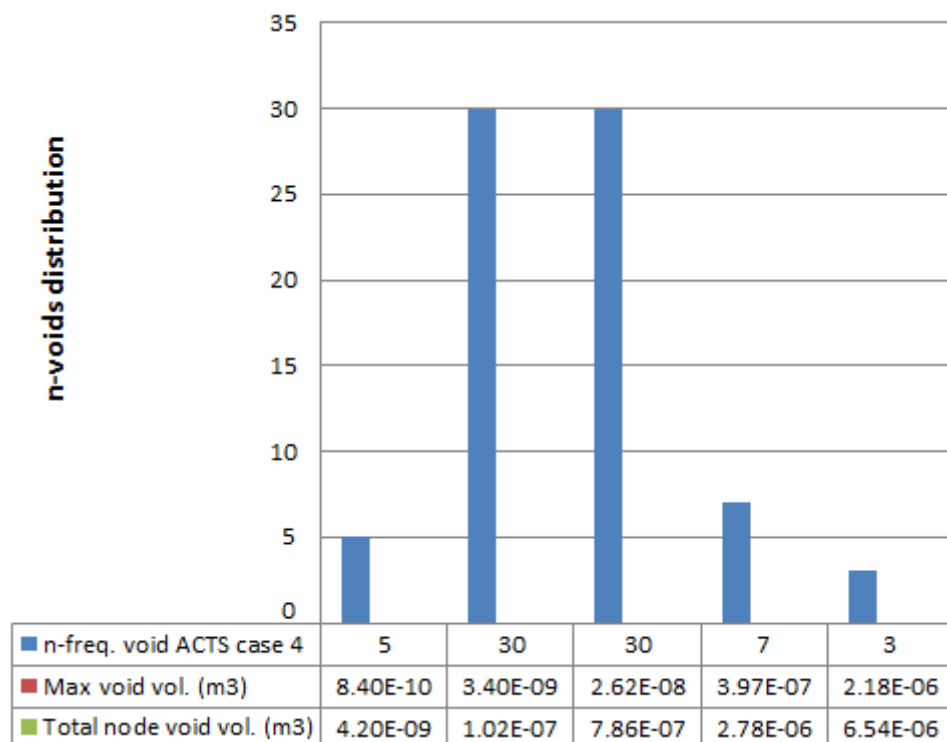
Figure F.3: Void distribution for node simulation case 4 with ACTS HTS40 F13 fabric.

342

n-freq. void ACTS case 5	1	30	26	6	3
Max void vol. (m3)	2.11E-10	4.05E-09	2.79E-08	3.94E-07	3.63E-06
Total node void vol. (m3)	2.11E-10	1.22E-07	7.25E-07	2.36E-06	1.09E-05

Figure F.4: Void distribution for node simulation case 5 with ACTS HTS40 F13 fabric.

n-freq. void ACTS case 6	4	29	31	6	1	1
Max void vol. (m3)	7.95E-10	3.67E-09	2.77E-08	3.00E-07	1.89E-06	1.08E-05
Total node void vol. (m3)	3.18E-09	1.06E-07	8.59E-07	1.80E-06	1.89E-06	1.08E-05

Figure F.5: Void distribution for node simulation case 6 with ACTS HTS40 F13 fabric.

	1	31	27	5	3
n-freq. void ACTS case 7	1	31	27	5	3
Max void vol. (m3)	4.52E-10	3.40E-09	2.87E-08	4.93E-07	3.53E-06
Total node void vol. (m3)	4.52E-10	1.05E-07	7.75E-07	2.47E-06	1.06E-05
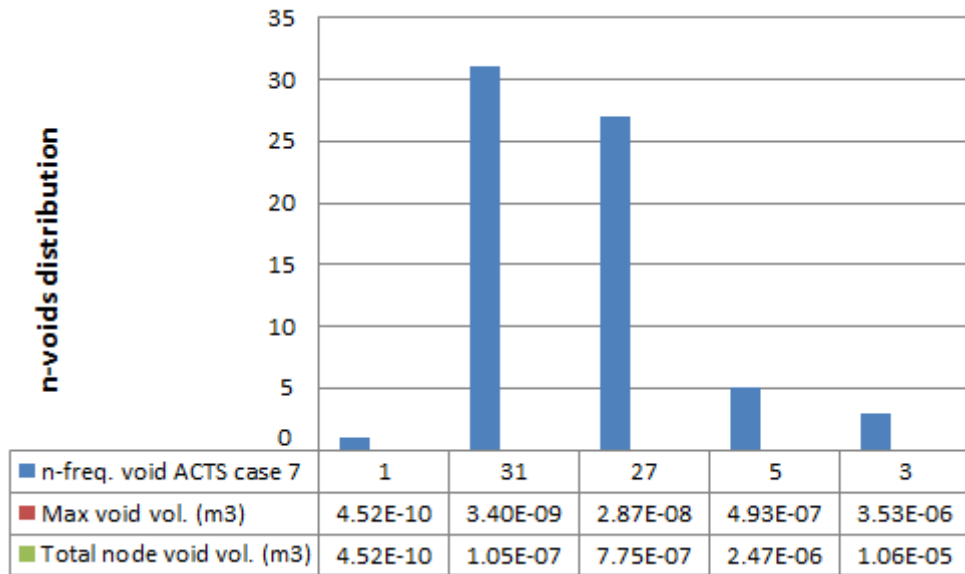
Figure F.6: Void distribution for node simulation case 7 with ACTS HTS40 F13 fabric.

(The distribution case 8 here presented on Fig. 8.6).

	3	27	31	7	3
n-freq. void ACTS case 9	3	27	31	7	3
Max void vol. (m3)	7.44E-10	3.22E-09	3.10E-08	4.24E-07	4.95E-06
Total node void vol. (m3)	2.23E-09	8.69E-08	9.61E-07	2.97E-06	1.49E-05
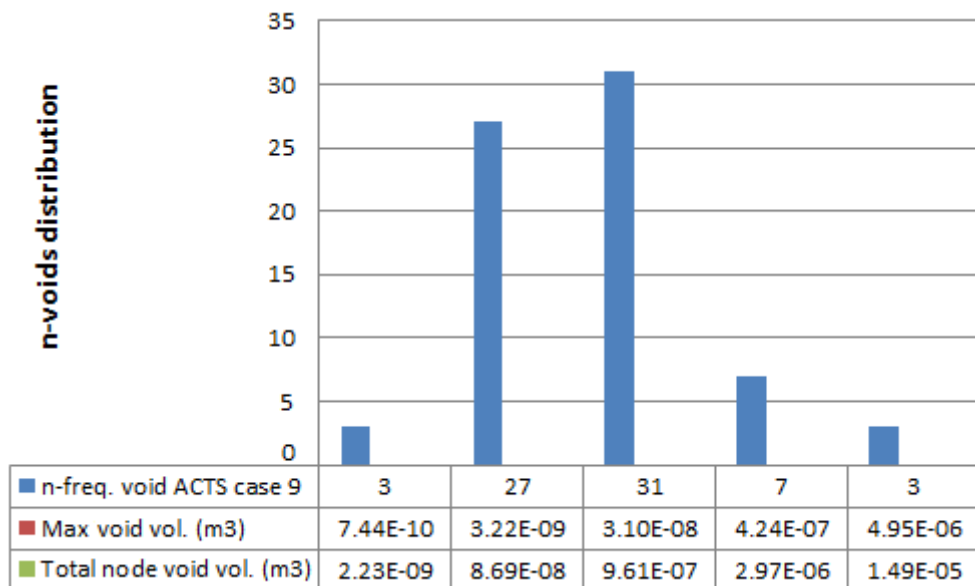
Figure F.7: Void distribution for node simulation case 9 with ACTS HTS40 F13 fabric.

	n-freq. void ACTS case 10	1	30	24	3	3
	Max void vol. (m3)	6.50E-10	3.32E-09	2.67E-08	3.63E-07	4.19E-06
	Total node void vol. (m3)	6.50E-10	9.96E-08	6.41E-07	1.09E-06	1.26E-05
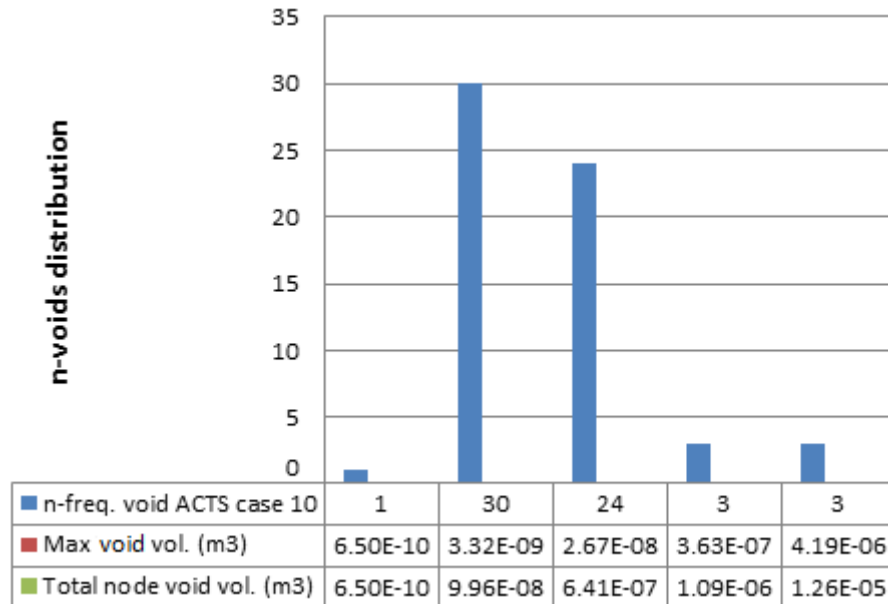
Figure F.8: Void distribution for node simulation case 10 with ACTS HTS40 F13 fabric.

ii) 2/2 twill fabric simulation for prediction of node void formation

Simulations of the variability with 2/2 twill in-plain carbon fabric predicted the frequency and the void volume that may arise during the node manufacturing process by RTM. The probabilistic distributions of void formation that may arise during the node manufacturing process are presented in Figs F.9-F.17.

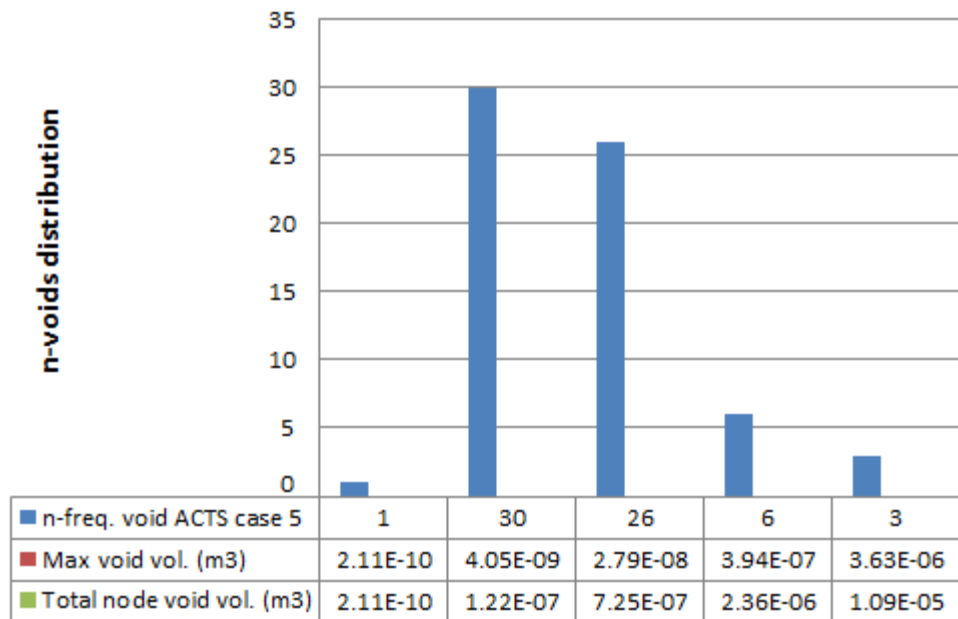|					
■ n-freq. void 2.2 twill case 1	6	74	28	6	2
■ Max Void vol. (m3)	8.29E-10	2.94E-09	3.12E-08	1.89E-07	4.88E-06
■ Total node void vol. (m3)	4.97E-09	2.18E-07	8.74E-07	1.13E-06	9.76E-06
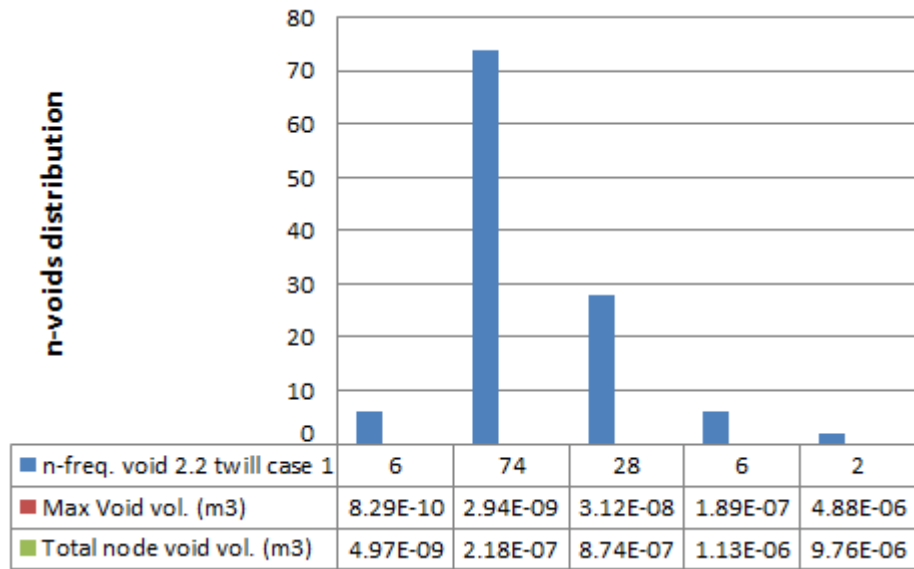
Figure F.9: Void distribution for node simulation case 1 with 2/2 twill fabric.

■ n-freq. void 2.2 twill case 2	10	71	29	8	1	1
■ Max void vol. (m3)	8.46E-10	3.17E-09	3.03E-08	3.56E-07	1.92E-06	1.01E-05
■ Total node void vol. (m3)	8.46E-09	2.25E-07	8.79E-07	2.85E-06	1.92E-06	1.01E-05

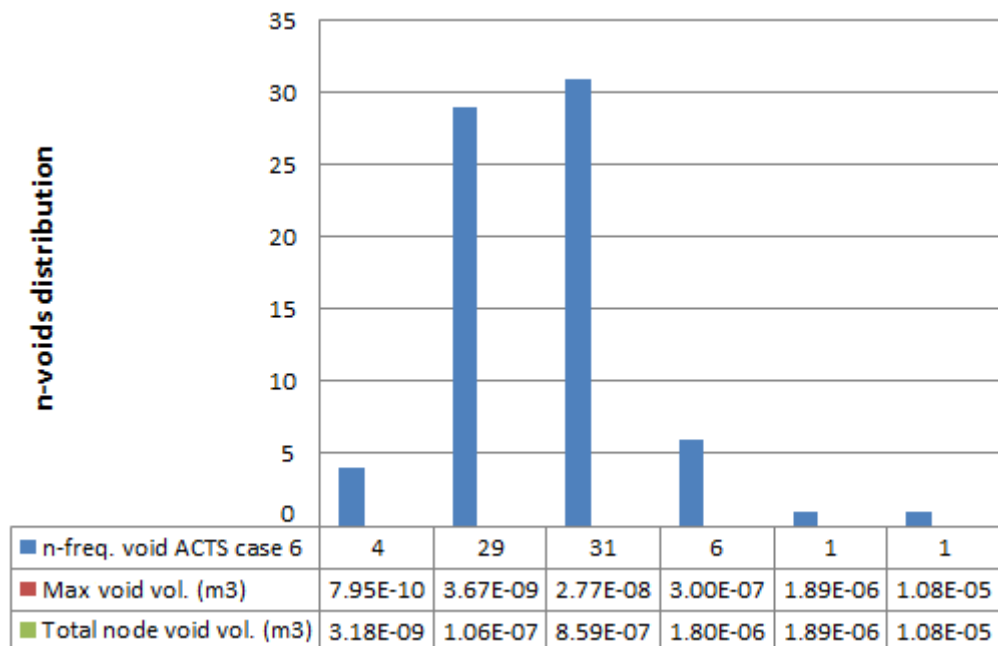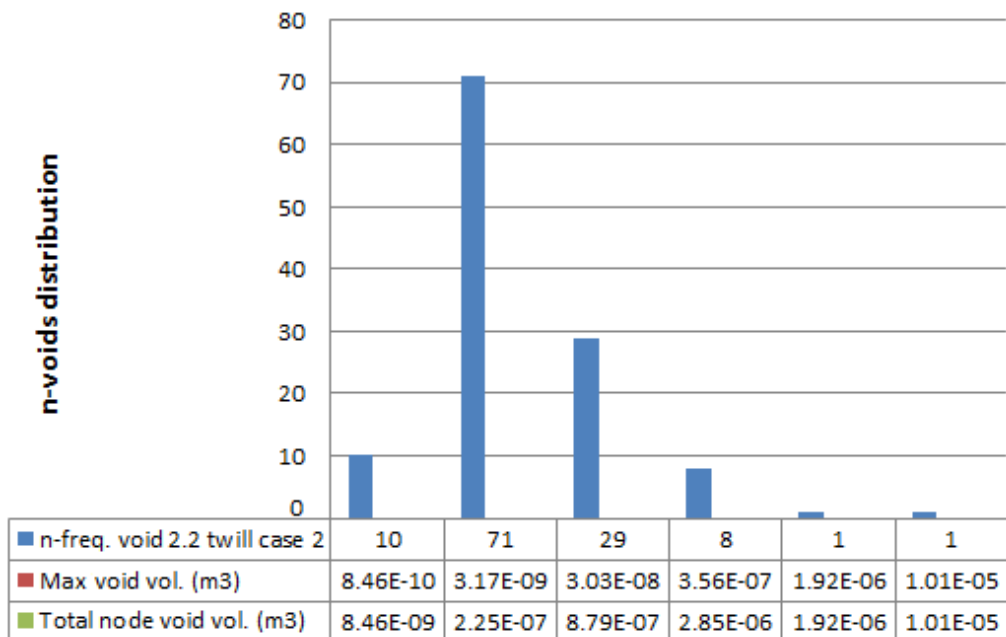**Figure F.10: Void distribution for node simulation case 2 with 2/2 twill fabric.**

n-freq. void 2.2 twill case 3	8	81	25	8	0	1
Max void vol. (m3)	7.65E-10	3.35E-09	2.70E-08	3.28E-07	0.00E+00	1.26E-05
Total node void vol. (m3)	6.12E-09	2.71E-07	6.75E-07	2.62E-06	0.00E+00	1.26E-05
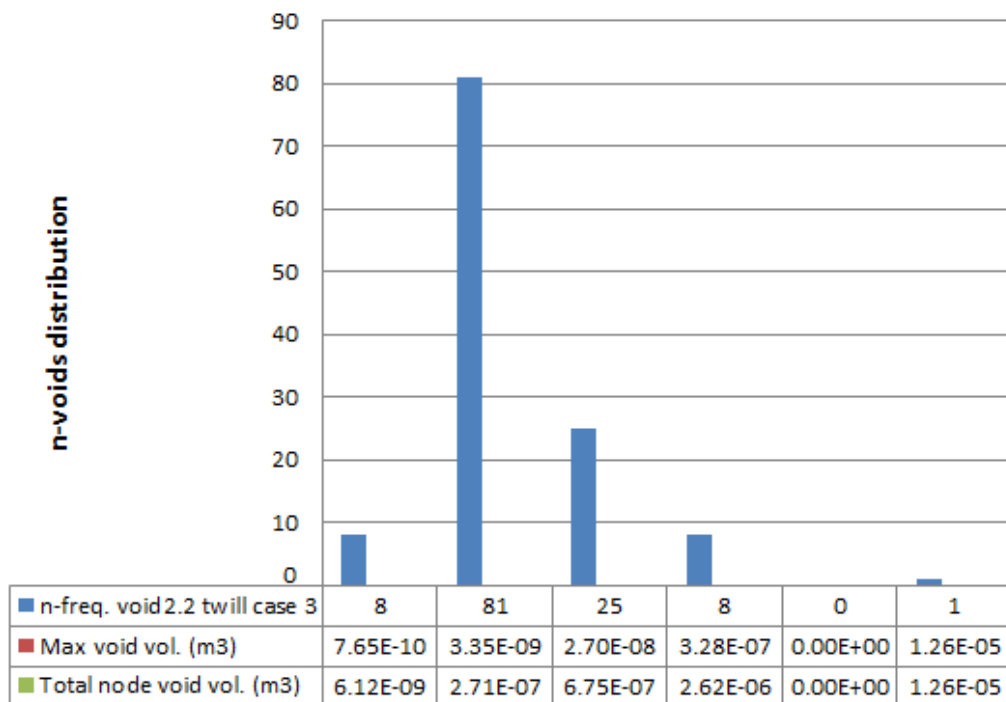
Figure F.11: Void distribution for node simulation case 3 with 2/2 twill fabric.

n-freq. void 2.2 twill case 4	10	79	30	5	0	1
Max void vol. (m3)	8.44E-10	2.93E-09	2.80E-08	2.08E-07	0.00E+00	1.79E-05
Total node void vol. (m3)	8.44E-09	2.31E-07	8.40E-07	1.04E-06	0.00E+00	1.79E-05
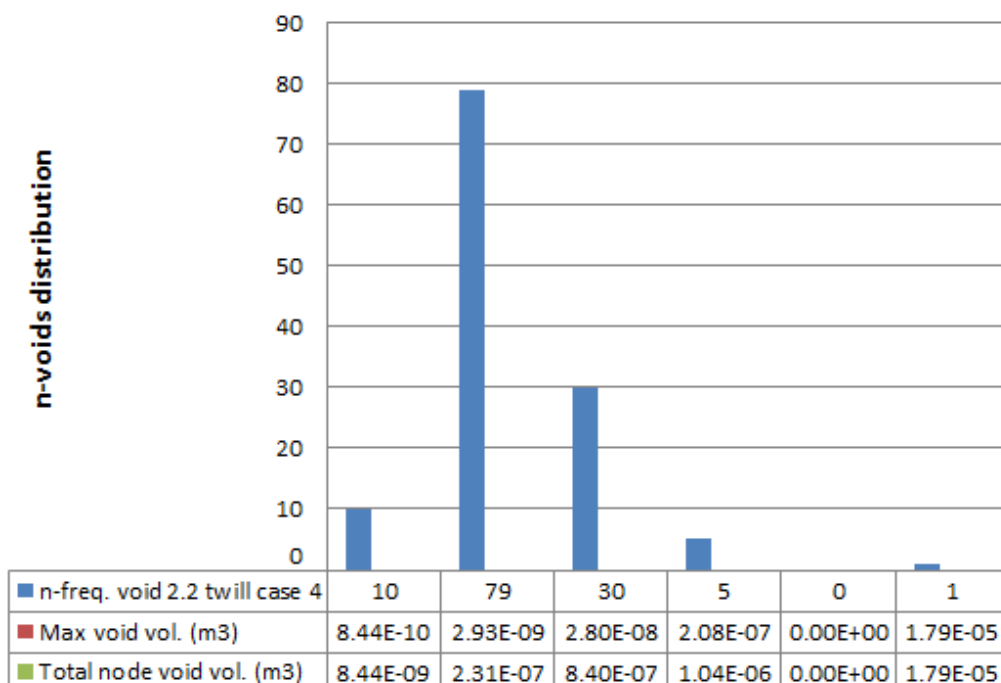
Figure F.12: Void distribution for node simulation case 4 with 2/2 twill fabric.

■ n-freq. void 2.2 twill case 5	7	71	38	3	2
■ Max void vol. (m3)	8.16E-10	3.23E-09	2.93E-08	3.68E-07	4.85E-06
■ Total node void vol. (m3)	5.71E-09	2.29E-07	1.11E-06	1.10E-06	9.70E-06

Figure F.13: Void distribution for node simulation case 5 with 2/2 twill fabric.

■ n-freq. void 2.2 twill case 6	7	72	29	9	1
■ Max void vol. (m3)	7.32E-10	3.05E-09	2.73E-08	4.05E-07	5.83E-06
■ Total node void vol. (m3)	5.12E-09	2.20E-07	7.92E-07	3.65E-06	5.83E-06

Figure F.14: Void distribution for node simulation case 6 with 2/2 twill fabric.

n-voids distribution					
■ n-freq. void 2.2 twill case 7	7	68	24	7	1
■ Max void vol. (m3)	8.41E-10	3.12E-09	3.00E-08	4.19E-07	7.73E-06
■ Total node void vol. (m3)	5.89E-09	2.12E-07	7.20E-07	2.93E-06	7.73E-06
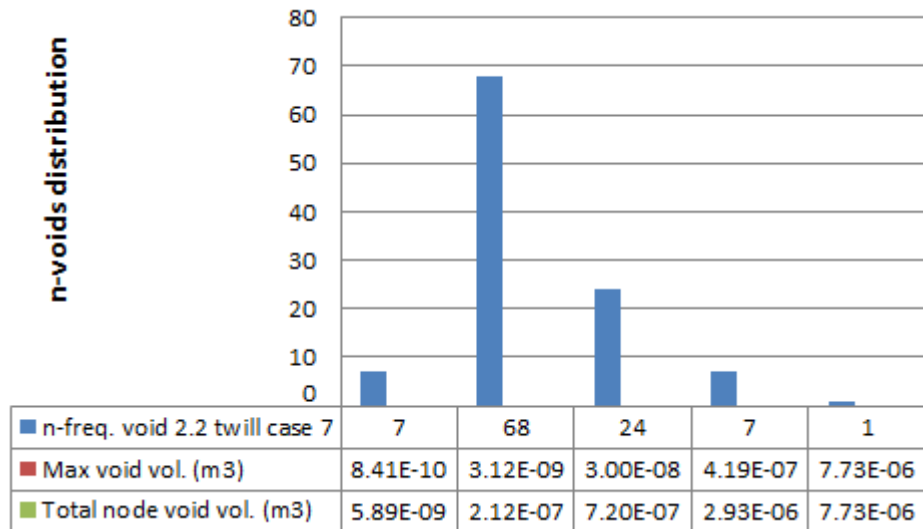
Figure F.15: Void distribution for node simulation case 7 with 2/2 twill fabric.

(The distribution case 8 here presented on Fig. 8.14).

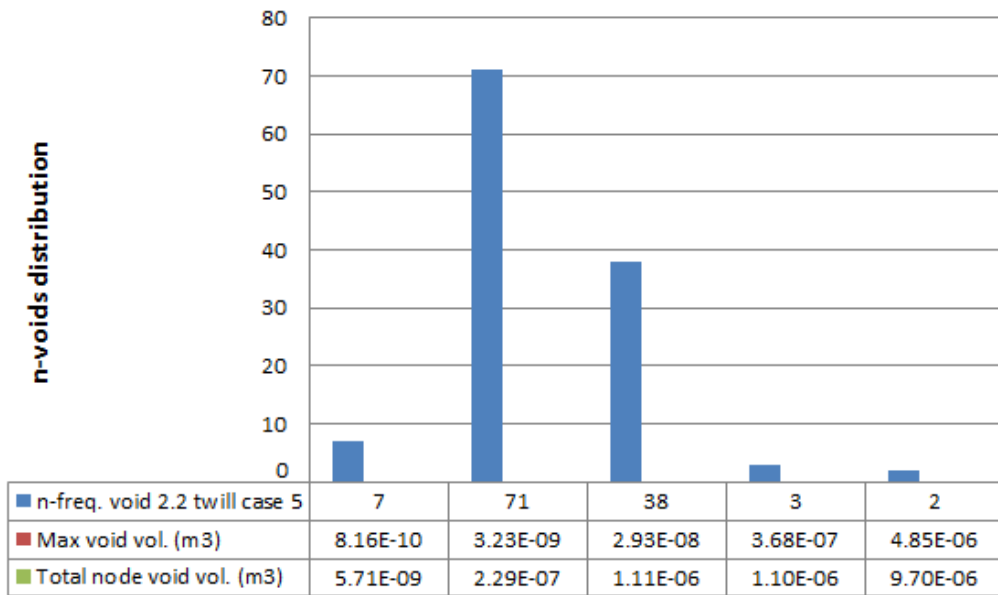| n-voids distribution					
■ n-freq. void 2.2 twill case 9	7	88	28	6	0	1
■ Max void vol. (m3)	7.95E-10	3.21E-09	2.50E-08	3.28E-07	0.00E+00	1.43E-05
■ Total node void vol. (m3)	5.57E-09	2.82E-07	7.00E-07	1.97E-06	0.00E+00	1.43E-05

Figure F.16: Void distribution for node simulation case 9 with 2/2 twill fabric.

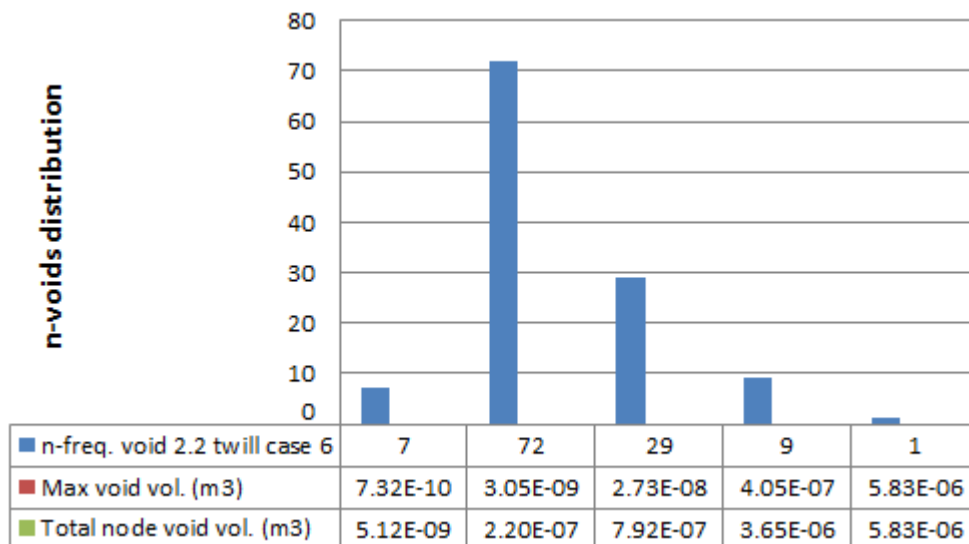|	10	67	31	4	0	1
■ n-freq. void 2.2 twill case 10	10	67	31	4	0	1
■ Max void vol. (m3)	8.21E-10	3.16E-09	2.61E-08	4.85E-07	0.00E+00	1.29E-05
■ Total node void vol. (m3)	8.21E-09	2.12E-07	8.09E-07	1.94E-06	0.00E+00	1.29E-05

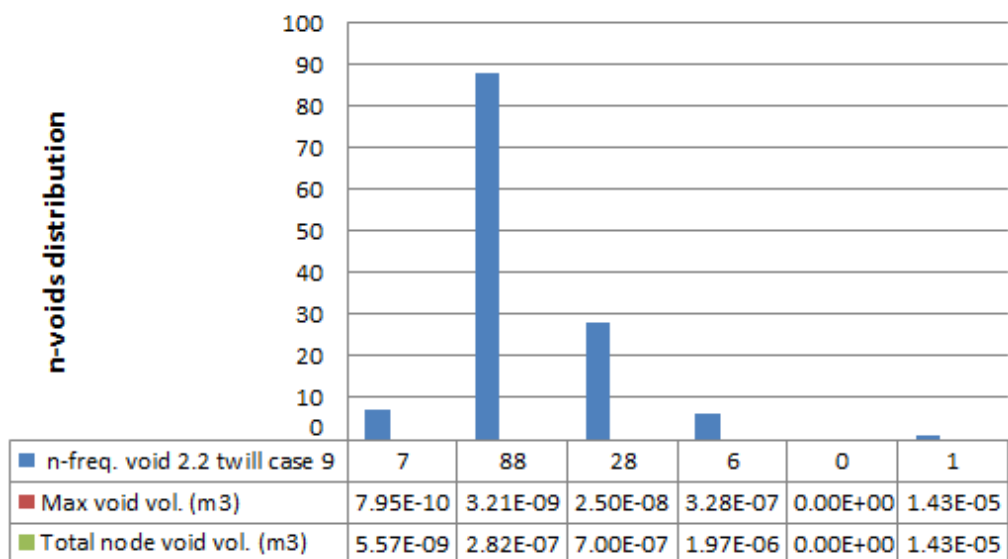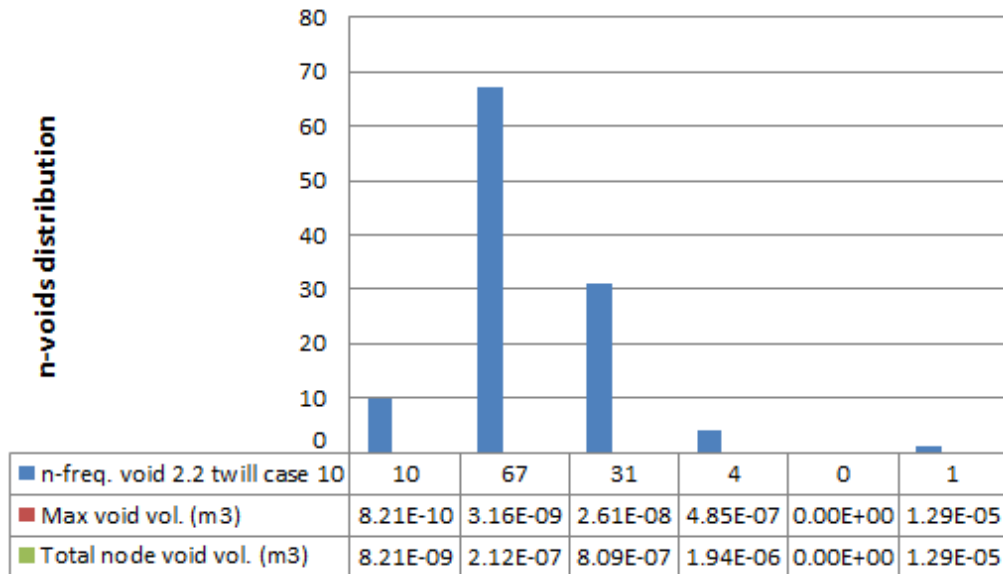**Figure F.17: Void distribution for node simulation case 10 with 2/2 twill fabric.**

iii) Triaxial fabric simulations for prediction of node void formation

Simulations of the variability with the triaxial glass fabric predicted the frequency and the void volume that may arise during the node manufacturing process by RTM. The probabilistic distributions of void formation that may arise during the node manufacturing process are presented in Figs F.18-F.26.

■ n-freq. void triaxial case 1	2	67	23	1	1
■ Max void vol. (m3)	8.91E-10	4.14E-09	2.48E-08	3.18E-07	5.20E-06
■ Total node void vol. (m3)	1.78E-09	2.77E-07	5.70E-07	3.18E-07	5.20E-06

Figure F.18: Void distribution for node simulation case 1 with triaxial fabric.

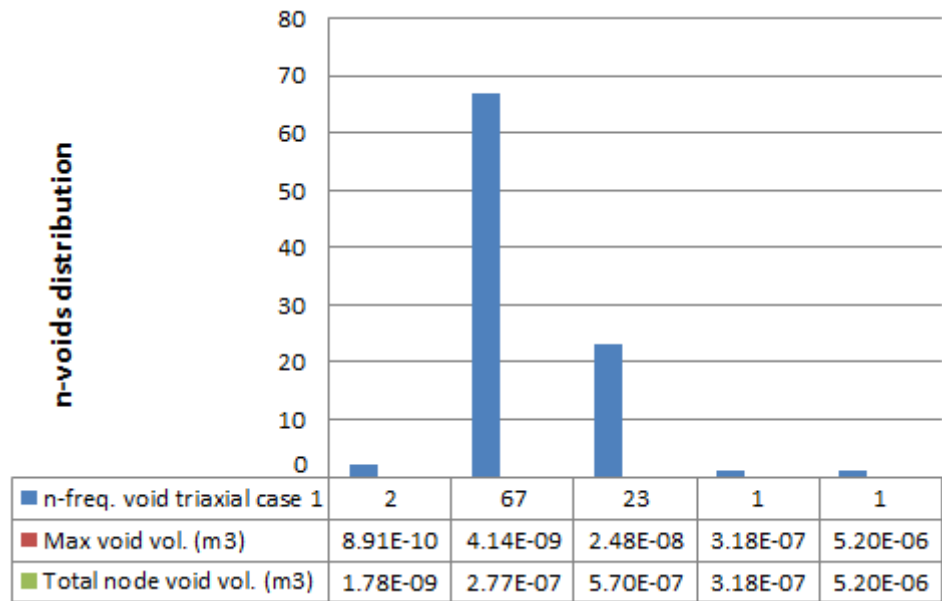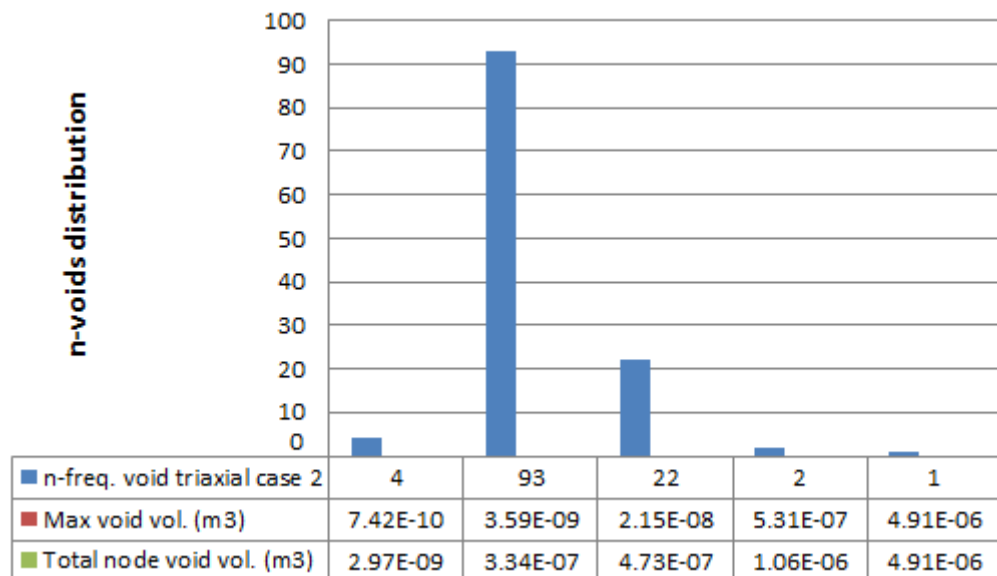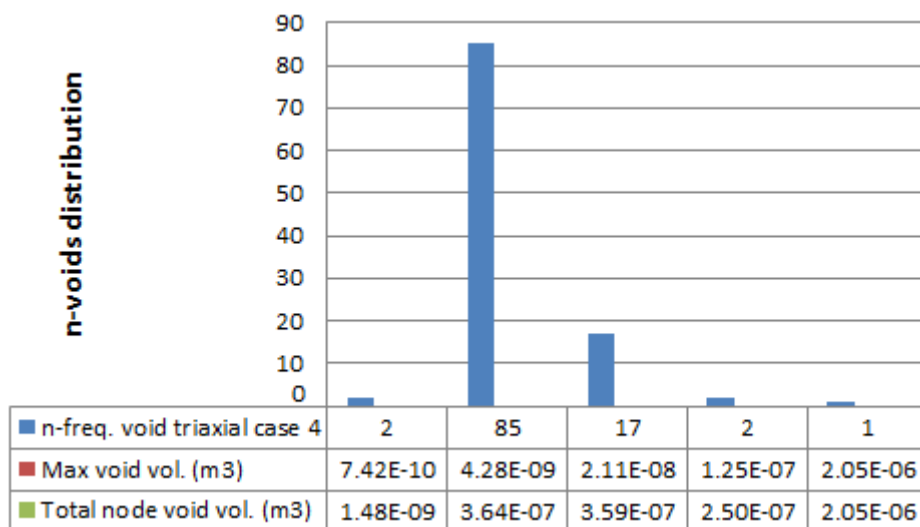|					
■ n-freq. void triaxial case 2	4	93	22	2	1
■ Max void vol. (m3)	7.42E-10	3.59E-09	2.15E-08	5.31E-07	4.91E-06
■ Total node void vol. (m3)	2.97E-09	3.34E-07	4.73E-07	1.06E-06	4.91E-06

Figure F.19: Void distribution for node simulation case 2 with triaxial fabric.

(The distribution case 3 here presented on Fig. 8.19).

n-freq. void triaxial case 4	2	85	17	2	1
Max void vol. (m3)	7.42E-10	4.28E-09	2.11E-08	1.25E-07	2.05E-06
Total node void vol. (m3)	1.48E-09	3.64E-07	3.59E-07	2.50E-07	2.05E-06

Figure F.20: Void distribution for node simulation case 4 with triaxial fabric.

n-freq. void triaxial case 5	6	84	18	1
Max void vol. (m3)	8.51E-10	3.84E-09	2.65E-08	1.51E-07
Total node void vol. (m3)	5.11E-09	3.23E-07	4.77E-07	1.51E-07

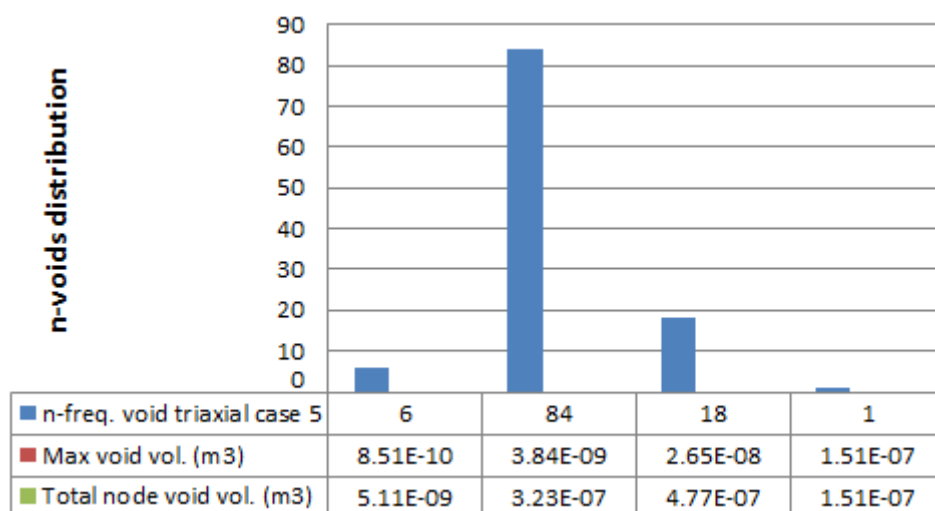**Figure F.21: Void distribution for node simulation case 5 with triaxial fabric.**

■ n-freq. void triaxial case 6	4	83	19	1	1
■ Max void vol. (m3)	8.15E-10	4.06E-09	2.13E-08	8.58E-07	5.21E-06
■ Total node void vol. (m3)	3.26E-09	3.37E-07	4.05E-07	8.58E-07	5.21E-06

Figure F.22: Void distribution for node simulation case 6 with triaxial fabric.

■ n-freq. void triaxial case 7	1	81	26	1	1
■ Max void vol. (m3)	8.43E-10	3.55E-09	1.94E-08	2.01E-07	4.98E-06
■ Total node void vol. (m3)	8.43E-10	2.88E-07	5.04E-07	2.01E-07	4.98E-06

Figure F.23: Void distribution for node simulation case 7 with triaxial fabric.

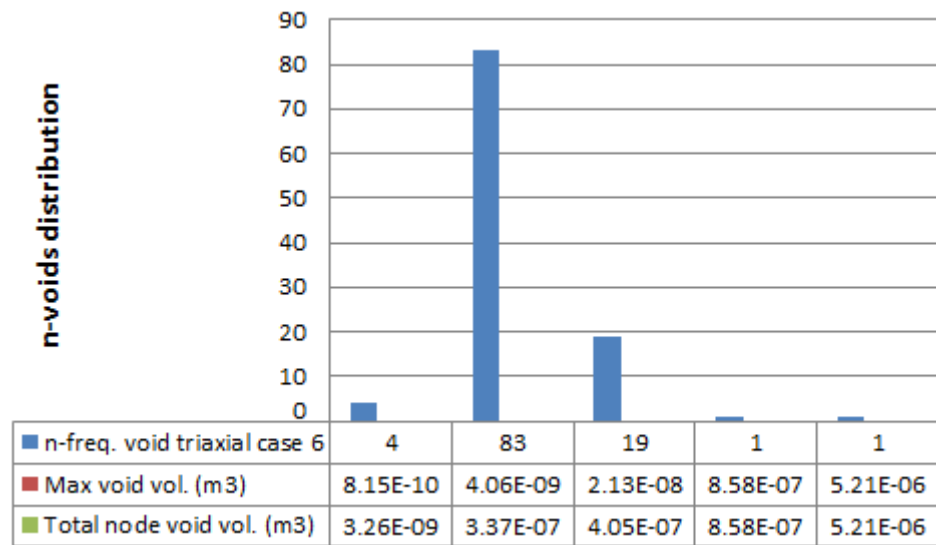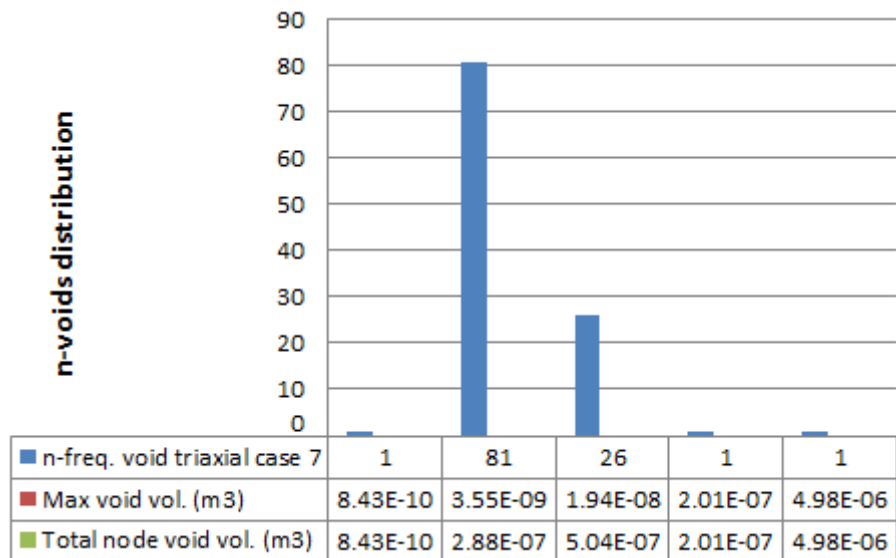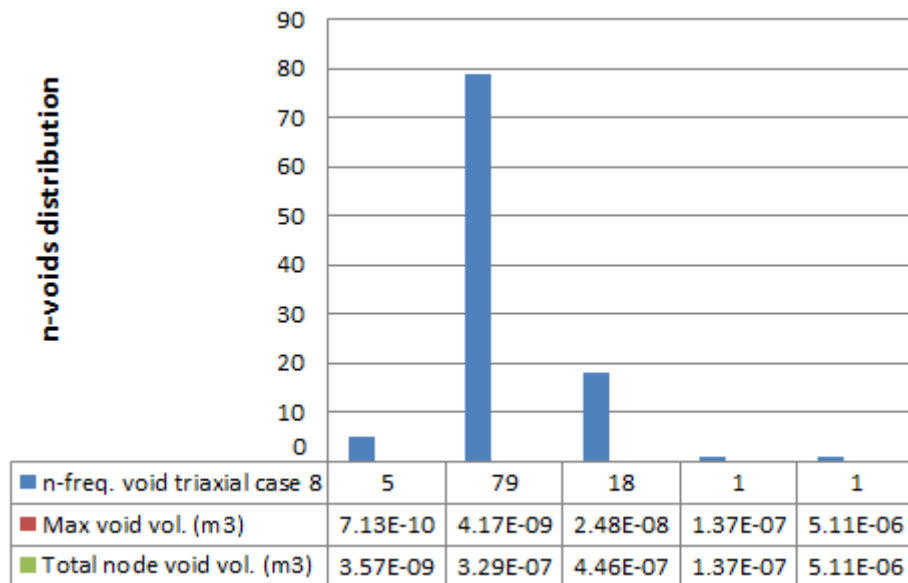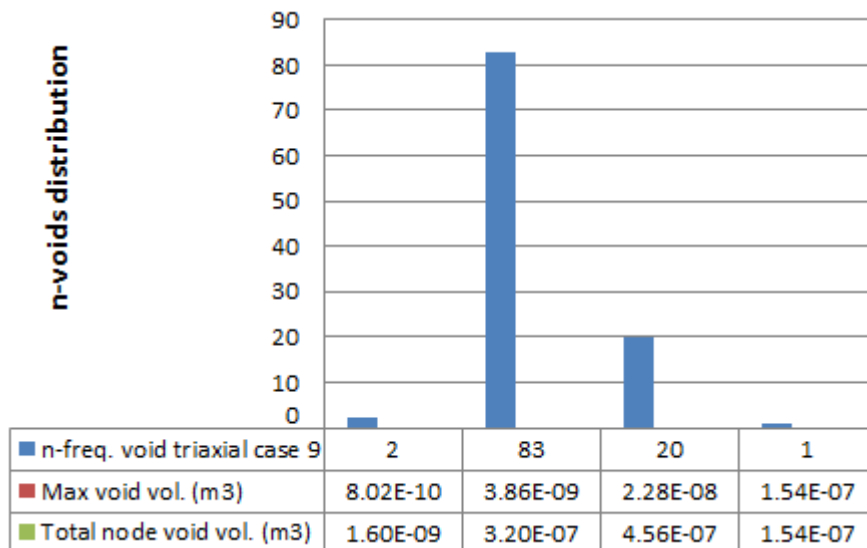Figure F.24: Void distribution for node simulation case 8 with triaxial fabric.

■ n-freq. void triaxial case 8	5	79	18	1	1
■ Max void vol. (m3)	7.13E-10	4.17E-09	2.48E-08	1.37E-07	5.11E-06
■ Total node void vol. (m3)	3.57E-09	3.29E-07	4.46E-07	1.37E-07	5.11E-06

■ n-freq. void triaxial case 9	2	83	20	1
■ Max void vol. (m3)	8.02E-10	3.86E-09	2.28E-08	1.54E-07
■ Total node void vol. (m3)	1.60E-09	3.20E-07	4.56E-07	1.54E-07

Figure F.25: Void distribution for node simulation case 9 with triaxial fabric.

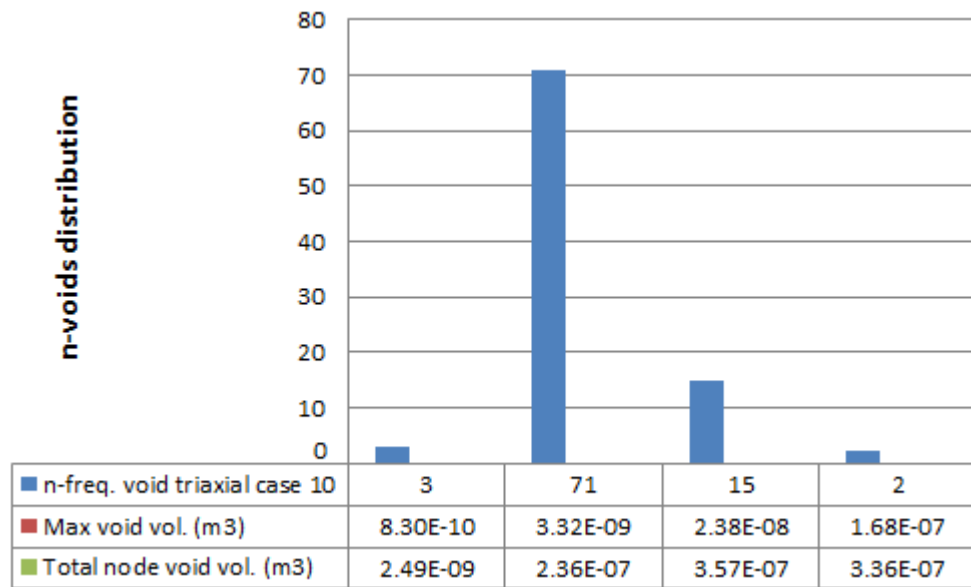|				
■ n-freq. void triaxial case 10	3	71	15	2
■ Max void vol. (m3)	8.30E-10	3.32E-09	2.38E-08	1.68E-07
■ Total node void vol. (m3)	2.49E-09	2.36E-07	3.57E-07	3.36E-07

Figure F.26: Void distribution for node simulation case 10 with triaxial fabric.

Appendix G: Series flow permeability

For series flow the permeability calculation was done from Darcy's law eq. (1-1) considering a pressure drop ΔP between mould's height H (i.e. gap height h_{gap} plus the fabric height h_{fabric}) across the flow direction as presented in Fig. G.1.
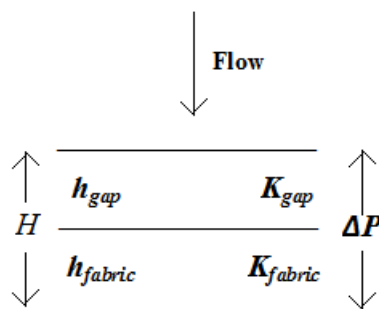
Fig. G 1: Schematic of permeability series flow.

From the above during steady-state flow the flow velocity be will equal to the gap and the fabric so:

$$u_{gap} = u_{fabric} \tag{G-1}$$

Substitution into Darcy's law eq. (1-1) (at both sides in equilibrium) where gap flow velocity will equal to the fabric flow velocity gives eq. (G-2)

$$-\frac{K_{gap}}{\mu}\frac{\Delta P_{gap}}{h_{gap}} = -\frac{K_{fabric}}{\mu}\frac{\Delta P_{fabric}}{h_{fabric}} \tag{G-2}$$

Solving the twice applied Darcy's law eq. (1-1) for ΔP_{gap} gives eq. (G-3)

$$\Delta P_{gap} = \frac{h_{gap}}{h_{fabric}}\frac{K_{fabric}}{K_{gap}}\Delta P_{fabric} \tag{G-3}$$

356

Therefore the total pressure will be the sum of the gap pressure plus the fabric pressure so:

$$\Delta P_{Tot} = \Delta P_{gap} + \Delta P_{fabric} = \Delta P_{fabric}(1 + \frac{h_{gap}}{h_{fabric}} \frac{K_{fabric}}{K_{gap}}) \qquad \textbf{(G-4)}$$

reconsidering Darcy's law the total flow velocity will be as per eq. (G-5)

$$u_{Tot} = -\frac{K_{Tot}}{\mu} \frac{\Delta P_{Tot}}{H} \qquad \textbf{(G-5)}$$

which with substitution of (D-4) and $H = h_{gap} + h_{fabric}$ gives:

$$u_{Tot} = -\frac{K_{Tot}}{\mu} \frac{(1 + \dfrac{h_{gap}}{h_{fabric}} \dfrac{K_{fabric}}{K_{gap}})\Delta P_{fabric}}{h_{gap} + h_{fabric}} \qquad \textbf{(G-6)}$$

but for series flow the total velocity will be equal to fabric velocity eq. (G-7)

$$u_{Tot} = u_{fabric} \qquad \textbf{(G-7)}$$

by rearranging (G-6) with (G-7):

$$-\frac{K_{Tot}}{\mu} \frac{(1 + \dfrac{h_{gap}}{h_{fabric}} \dfrac{K_{fabric}}{K_{gap}})\Delta P_{fabric}}{h_{gap} + h_{fabric}} = -\frac{K_{fabric}}{\mu} \frac{\Delta P_{fabric}}{h_{fabric}} \qquad \textbf{(G-8)}$$

This equation with simplification will give K_{Total} as shown in eq. (G-9):

$$K_{Total} = (\frac{K_{fabric}}{h_{fabric}}) \frac{(h_{gap} + h_{fabric})}{(1 + \dfrac{h_{gap}}{h_{fabric}} \dfrac{K_{fabric}}{K_{gap}})} \qquad \textbf{(G-9)}$$

therefore the through thickness permeability K_{3Total} for series flow on each of the 23 edges of the node may be written as shown in eq. (8-3).

$$K_{3Total} = (\frac{K_3}{h_{fabric}}) \frac{(h_{av.arc.gap} + h_{fabric})}{(1 + \frac{h_{av.arc.gap}}{h_{fabric}} \frac{K_3}{K_{gap}})} \qquad \textbf{(8-3)}$$

where the average gap ($h_{av.arc.gap}$) height was calculated from numerical modelling data.

Spiridon Koutsonas

## Appendix H: HDX30, Trent Oil Ltd viscosity

In appendix H the viscosity variation against temperature of the HDX30 oil used for the experiments with Perspex tool on Chapter 6 is presented as shown Fig. H1.

The oil viscosity, is obtained as a function of the temperature, by using a Brookfield rheometer (model DV-II). The Brookfield rheometer (model DV-II) uses a temperature controlled vessel equipped with a thermostat which maintained the temperature with an accuracy ±0.1°C.

The error in the viscosity determination with the above apparatus is less than 0.5% according to the manufacturer. Density of oil against temperature is measured using a pycnometer immersed in a temperature with controlled circulating water bath.

The kinematic viscosity values (centimetres-squared per second measured in Stokes) at each temperature are determined by multiplying the measured flow time of the oil through the rheometer capillary with the calibration constant of the used rheometer.

Finally the absolute viscosity μ (Pa.s) calculated numerically as the product of kinematic viscosity and the density of the tested oil, both at the same temperature.
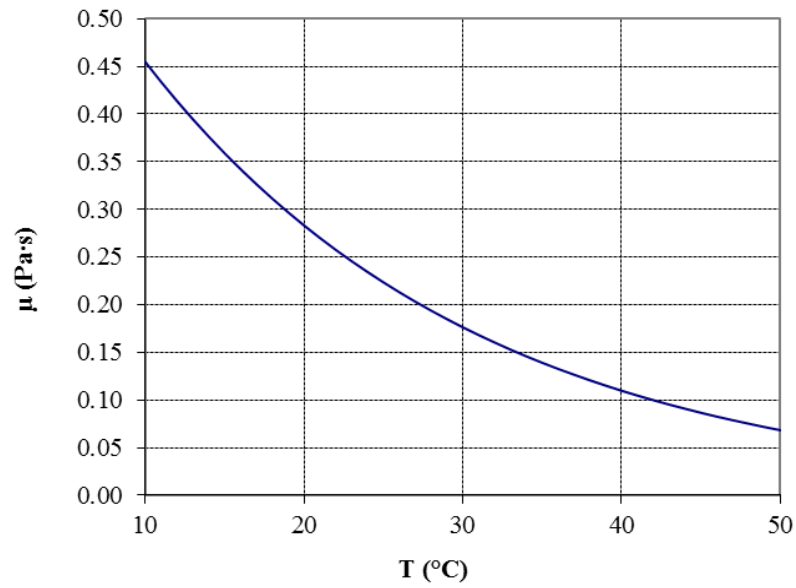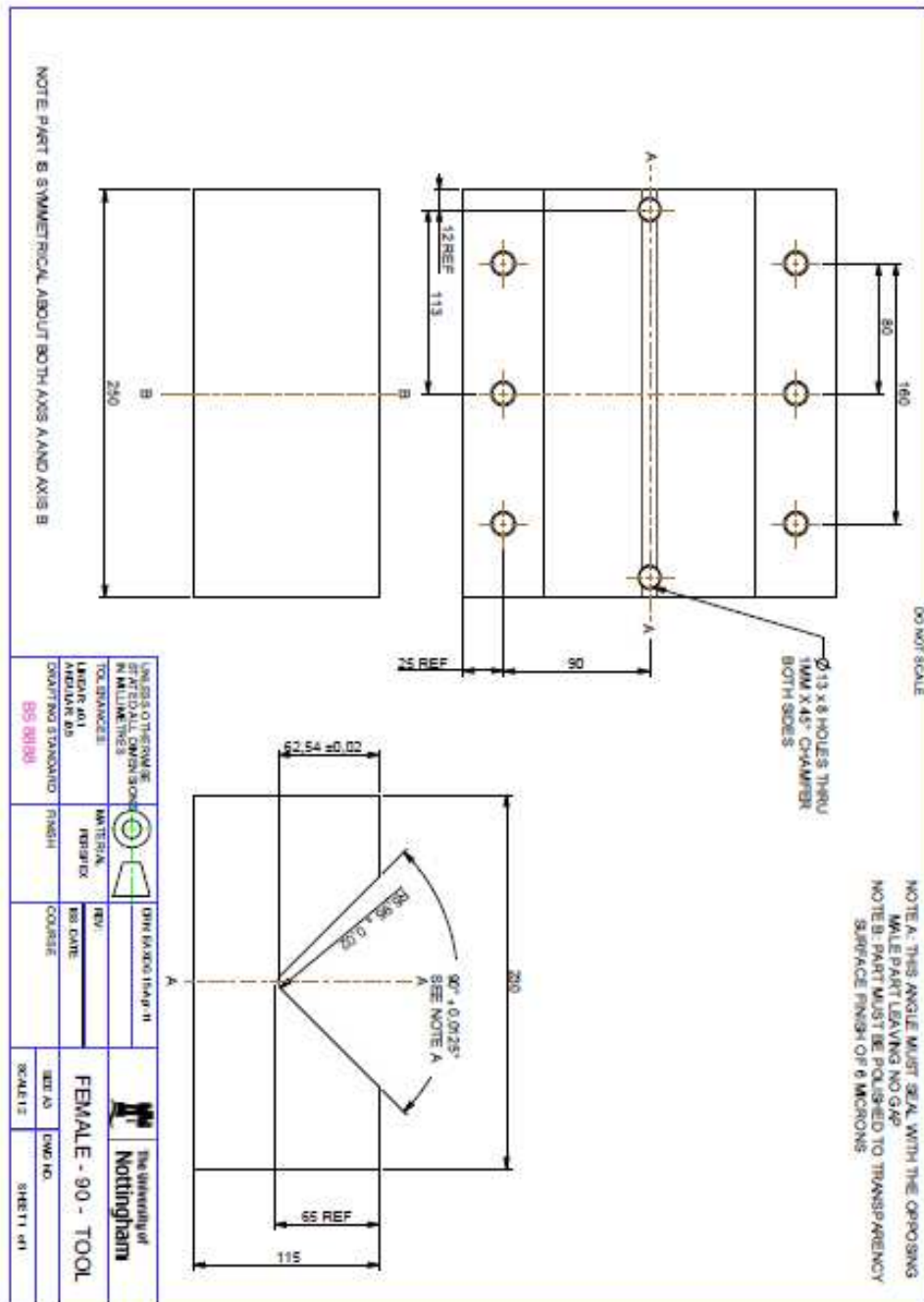
Fig. H1: HDX30 oil viscosity (μ) variation against Temperature.

For the experiments it was measured an average costant laboratory temperature of 19°C. Therefore the oil viscosity used in simulations was 0.3 (Pa s) as shown Fig. H1.

Appendix I: Perspex tool design

Appendix J: Programming codes

J.1 Images acquisition with 2 web cams (Mat lab)

```
%20.01.2011 Spiridon Koutsonas
%test video input of two installed webcams

%based on Matlab demo "Logging Data To Disk"

function video_input()
close all
clc

%*************************************************************
***
%Input:
s=90; %input in seconds
video1 = 'video_1.A'; %name of video 1
video2 = 'video_2.A'; %name if video 2
fgi = 1; % FrameGrabInterval - capture every fgi frame only
%*************************************************************
***

t=s*15; %total number of frames to capture -> camera has nominal 15fps
video1=sprintf([video1, '.avi']);
video2=sprintf([video2, '.avi']);

imaqhwinfo;
info=imaqhwinfo('winvideo');
disp('')
disp('***************  Supported Formats: ***************')
info.DeviceInfo.SupportedFormats
info.DeviceIDs

%Construct a video input object.
vid1 = videoinput('winvideo', 2,'YUY2_320x240'); %'YUY2_1024x768'
'YUY2_800x600' 'YUY2_320x240'
vid2 = videoinput('winvideo', 3, 'YUY2_320x240'); %'YUY2_320x240'

% %Select the source to use for acquisition.
set(vid1, 'FramesPerTrigger', t);
set(vid1, 'ReturnedColorSpace', 'gray');
set(vid1, 'FrameGrabInterval', fgi);
```

```
disp('')
disp('***************  Video Input 1 settings: ***************')
get(vid1)
set(vid2, 'FramesPerTrigger', t);
set(vid2, 'ReturnedColorSpace', 'gray');
set(vid2, 'FrameGrabInterval', fgi);
disp('')
disp('***************  Video Input 2 settings: ***************')
get(vid2)


%
% %View the properties for the selected video source object.
disp('***************  Video stream 1 properties: ***************')
src_vid1 = getselectedsource(vid1);
get(src_vid1)
disp('***************  Video stream 2 properties: ***************')
src_vid2 = getselectedsource(vid2);
get(src_vid2)


%
% %Preview a stream of image frames.
preview(vid1);
preview(vid2);


% Configure the logging mode to disk.
set(vid1, 'LoggingMode', 'Disk'); %Disk&Memory
set(vid2, 'LoggingMode', 'Disk');



% Create an AVI file object.
disp('***************  AVI parameters: ***************')
logfile1 = avifile(video1)
logfile2 = avifile(video2);
% Select a codec for the AVI file.
logfile1.Compression = 'none';
logfile2.Compression = logfile1.Compression ;
%logfile.Fps=1;
logfile1.Quality=100;
logfile2.Quality=logfile1.Quality;
% Since grayscale images will be acquired, a colormap is required.
logfile1.Colormap = gray(256);
logfile2.Colormap = gray(256) ;
% Configure the video input object to use the AVI file object.
vid1.DiskLogger = logfile1;
vid2.DiskLogger = logfile2;

disp('')
```

```
disp('**************   Start acuisition... ***************')
%read:
http://www.mathworks.com/matlabcentral/newsreader/view_thread/100745
start(vid1);
start(vid2);
tic

% Wait for the acquisition to finish.
wait(vid1,t);
%data = getdata(vid1,2); %read out time stamp
stop(vid1);
stop(vid2);
t1=toc %total acquiring time
disp('***************   End acuisition.     ***************')

% % Determine the number of frames acquired.
f1=vid1.FramesAcquired
f2=vid2.FramesAcquired
% % Ensure that all acquired frames were written to disk.
% vid1.DiskLoggerFrameCount

% Once all frames have been written, close the file.
aviobj1 = vid1.Disklogger;
file = close(aviobj1);
aviobj2 = vid2.Disklogger;
file = close(aviobj2);

% Once the video input object is no longer needed, delete
% it and clear it from the workspace.
delete(vid1);
delete(vid2);
clear vid1 vid2

%*************************************************************
**********
%Playback movie (just by grabbing frames - not possible to play two movies
%in the same window???

pvid1=MMREADER(video1); %load video file to play back
pvid2=MMREADER(video2);

%determine the number of frames
if pvid1.NumberOfFrames<= pvid2.NumberOfFrames
   nFrames = pvid1.NumberOfFrames;
else
   nFrames = pvid2.NumberOfFrames;
end
```

366

```
h=figure;
df=0; %offset
for i = 1+df : nFrames
   subplot(1,2,1)
   imshow(read(pvid1, i))
   %axis equal
   i2=round(i)-df;%corresponding frame sec movie (based on 1st movie)
t1,f1,f2
   subplot(1,2,2)
   imshow(read(pvid2, i2))
   %axis equal
%    h2=figure;
%    imshow(read(pvid1, i))
%    filename=(['vid1 ',num2str(i),'.bmp'])
%    saveas(h2, filename)
%    %close(h2)
%    h2=figure;
%    imshow(read(pvid2, i))
%    filename=(['vid1 ',num2str(i),'.bmp'])
%    saveas(h2, filename)
%    %close(h2)
end
close(h);
% Check for playing movies:
% - example from: mmreader class for plying movies
% - implay(video1)
```

J.2 Random numbers generator (C-prog.)

```c
#include <stdio.h>

#include <stdlib.h>

#include<math.h>

int GetRand(int min, int max);

int main(void)

{

 int i, rgap;

 for (i = 0; i < 23; i++)

 {

  rgap = GetRand(1,7);
```

```c
    printf ("Gap case %d\n", rgap);

  }

  return(0);

}

int GetRand(int min, int max)

{

  static int Init = 0;

  int rgapc;

  if (Init == 0)

  {

    /*

     * As Init is static, it will remember it's value between

     * function calls.  We only want srand() run once, so this

     * is a simple way to ensure that happens.

     */

    srand(time(NULL));

    Init = 1;

  }

  /*

   * Formula:

   *   rand() % N   <- To get a number between 0 - N-1

   *   Then add the result to min, giving you

   *   a random number between min - max.

   */

  rgapc = (rand() % (max - min + 1) + min);

  return (rgapc);

}
```